FEASIBILITY STUDY FOR YELLOW OLEANDER BIODIESEL PRODUCTION USING EGGSHELL-DERIVED NANOCATALYST SYNTHESIZED BY *BOTTOM-UP* TECHNIQUE

JEREMIAH ODHEK MASIME
B.Ed Sc. (KU), MSc. (KU)
(SSCX/06462P/2015)

A Thesis Submitted in Partial Fulfilment of the Requirements for the Award of the Degree of Doctor of Philosophy in Chemistry,

in

The School of Chemistry and Material Science

of

The Technical University of Kenya

(DECEMBER, 2023)

DECLARATION

This thesis is my original work and has not been presented in any other institute for a degree award or any other qualification.

Signature…… Date……

JEREMIAH ODHEK MASIME **PHD/ SSCX/06462P/2015**

Supervisors:

This thesis has been submitted with the approval as supervisors:

Signature……..……Date ……..……

DR. GEOFFREY OTIENO
TECHNICAL UNIVERSITY OF KENYA
SCHOOL OF CHEMISTRY AND MATERIAL SCIENCE

Signature……Date ……

PROFESSOR BETTY N. MBATIA
UNITED STATES INTERNATIONAL UNIVERSITY - AFRICA
SCHOOL OF PHARMACY AND HEALTH SCIENCES

Signature……Date ……

PROFESSOR ERICH OKOTH OGUR
TECHNICAL UNIVERSITY OF KENYA
DEPARTMENT OF MECHANICAL AND MECHATRONIC ENGINEERING

ACKNOWLEDGEMENT

First, let me take this opportunity to thank Dr. Geoffrey Otieno, my supervisor and Director of the School of Chemistry and Material Science, for agreeing to work with me for the past seven years. I would like to thank you for introducing me to the field of nanocatalysis and materials science, which brought me into contact with materials chemistry and industrial chemistry. I learned a lot from your comments, feedback, and constant guidance throughout this PhD course. Without your valuable insights and contributions, as well as your extensive expertise, this work might never have come to fruition. I appreciate the intellectual freedom you have granted and the encouragement to take the direction of nanotechnology research. I cannot avoid thanking the members of the Thesis Committee Prof. Erich Ogur, Prof. Betty Njeri Mbatia, and Dr. Geoffrey Otieno for their helpful suggestions, encouragement, and support and for putting up with my many mistakes in preparing this study. My thanks also go to the entire staff of the School of Chemistry and Materials Science at the Technical University of Kenya.

I appreciate Prof. Betty Njeri Mbatia's support in preparing significant publications as well as her thought-provoking requests regarding the preparation of the final report and manuscripts. The discussions played an important role in encouraging me to think creatively and from different angles in order to develop thorough and impartial criticism. And special thanks to Professor Austin Aluoch for guiding me in preparing slides for research presentations, Professor Lalah for guiding me in conducting the life cycle analysis, and Dr. Ruth Omole for teaching me how to reference using Mendeley software. I would also like to appreciate, Dr. George Oindo, Dr. James Owuor, Dr. Shem Musyoki, and Dr. Peter Ndangili.

I thank my colleagues, and friends, Dr. George Oindo, Dr. James Owuor, and Dr. Ruth Omole, for their support. We started as work colleagues and somehow became close friends. I am grateful for your endless support and valuable advice. Throughout my studies, you made the environment of the department intellectually stimulating. I have always had great respect for your creativity, originality, and work ethic. This opportunity has undoubtedly made me a well-rounded scientist and an open-minded person. Special thanks to my friend George Oindo for his valuable friendship and personal support. My thanks also go to our laboratory assistants, Mr. Samson Gurema, Mr. George Okonji, Mr. Allan Wicks, Mr. Thomas Mwaiwa, Ms. Hellen Nchore, and Mr. Daniel Ouma. They supported me in setting up the machines and provided practical help where needed.

Grants from the National Research Fund of Kenya (2016-2017) helped fund this research. I also thank the Royal Society of Chemistry for sponsoring me for a GC/MS training course at Jomo Kenyatta University of Agriculture and Technology (JKUAT) in 2018. I also attended a Malvern-sponsored Advanced Material Characterization session at KEMRI that same year.

DEDICATION

I dedicate this work to my Loving father Mr. Stephen Masime Angugo who struggled to see me through my education in spite of financial constraints.

TABLE OF CONTENTS

LIST OF TABLES

LIST OF FIGURES

ABBREVIATIONS AND ACRONYMS

ANOVA	Analysis of Variance
ASTM	American Standards Testing for Materials
API	American Petroleum Index
APC	Auxillary Plant Cost
ASE	Accelerated solvent extraction
AV	Acid Value
AEOE	Aqueous enzymatic oil extraction
BET	Brunauer-Emmett-Teller
BJH	Barrett-Joyner-Halenda
BP	Brake Power
BPC	Biodiesel Production Cost
BTE	Brake Thermal Efficiency
BSE	Backscattered electrons
BSFC	Brake Specific Fuel Consumption
CCD	Central composition design
CI	Combustion injection
CV	Calorific value
DI	Diesel Index (DI)
DPC	Direct Production Cost
DOE	Design-of-experiments
DSC	Differential Scanning Calorimetry

DTG	Diffential Thermal Gravemetric Analysis
EBSD	Diffracted backscattered electrons
EDX	Energy Dispersive X-ray analysis
EIOLCA	Economic input– output Life Cycle Analysis
EMs	Electron Microscopes
FCI	Fixed Capital Cost
FFA	Free Fatty Acid
FTIR	Fourier transform-infrared
GCMS	Gas Chromatography - Mass Spectrometry
HHR	Heat Release Rate
IMEP	Indicated Mean effective pressure
IV	Iodine Value
IP	Indicative Power
IPC	Indirect Production Cost
LCA	Life-cycle analysis or assessment
LCIA	The life cycle impact assessment
LCI	Life Cycle Inventory
IUPAC	International Units of Pure and Applied Chemistry
MAE	Microwave-assisted extraction
MAAEE	Microwave-assisted aqueous enzymatic extraction
Meff.	Mechanical Efficiency
MSD	Mass Selective Detector

NP	Net Profit
Pm	Mean effective pressure
PPC	Physical Plant Cost
PV	Peroxide Value
ROI	Return of Investment
RSM	Response Surface Methodology
SEM	Scanning Electron Microscopy
SIC	Specific Investment Cost
SFE	Supercritical fluid extraction
SOC	Start of Combustion
SV	Saponification Value
TCI	Total Capital Investment
TEC	Total Equipmet Cost
Vol. Eff.	Volumetric Efficiency
WCI	Working Capital Inestment
XRD	X-ray Powder Diffraction
XRF	X-Ray Fluorescence Spectroscopy
YOO	Yellow Oleander Oil
YOBD	Yellow Oleander Biodiesel

ABSTRACT

The global energy demand is expected to rise by 53% by 2030, depleting crude oil reserves by 2052. This increase in energy demand growth has led to increased CO_2 emissions, environmental degradation, and the need for alternative fuels. Researchers are exploring biofuel production using Yellow Oleander seeds, a non-edible plant with high oil content. Heterogeneous base catalysts are preferred for biodiesel production due to their non-toxic, high surface area, reusable, and superior stability, while nanocatalysis increases catalytic activity. The eggshell-derived nanocatalyst was prepared using the *bottom-up* technique and characterized using TG/DTG/DSC, BET/BJH, XRD, FTIR, XRF, TEM, SEM, and EDX. Response surface methodology was used to optimize biodiesel production from yellow oleander by analyzing physicochemical properties, performance, combustion, and emission characteristics in a 4-stroke engine and life cycle analysis.

Yellow oleander oil yielded 64.53 ± 0.53 % under optimal conditions, including 80°C temperature, a petroleum ether solvent, 180 minutes, oilseed particle size, and 1:6 solid-to-solvent ratio, following second-order kinetics. The activation energy, enthalpy of extraction, and entropy were ΔEa = + 33.03 kJ/mol, ΔH = + 38.27 kJ kg-1, and ΔS = + 0.097 kJ/mol.K, respectively. The Gibbs free energy decreases at high temperatures, causing the extraction process to become spontaneous. Using XRD diffractograms, the particle size was determined to be 13.86 ± 0.987 nm. The spherical nature of the nanocatalyst particles was revealed by the SEM and TEM images. From BET analysis, the surface area, average pore diameter, and pore volume were; 5.54 ± 0.48 m^2g^{-1}, 18.57 ± 2.16 nm, and ≈ 0.016 ± 0.0 to 0.017 ± 0.0 cm g^{-1}, respectively. The eggshell-derived nanocatalyst, a mesoporous material with a large specific surface area, was found to be beneficial for the transesterification reaction process. The response surface methodology yielded 93.70% of yellow

oleander biodiesel under optimal conditions, including a reaction time of 40 minutes, a mild temperature of 60°C, and a 3.68 wt% catalyst loading. The FTIR spectrum of yellow oleander oil and biodiesel showed consistent carboxylate regions. The oil and biodiesel's physical and chemical properties align with ASTM D6751 standards. Engine performance, combustion, and emission behavior were evaluated. B20 was found to be the blend with properties close to that of petrodiesel. The study assessed the production costs and energy balance of a biodiesel plant, revealing an energy balance of 6.94 and an estimated production cost of KES 99.90/L (US$ 0.68)/L). The market price for a biodiesel blend of yellow oleander with 20% biodiesel (B20) was 186.75 KES/L (US$ 1.27 /L). This study synthesized a cost-effective, long-lasting nanocatalyst using waste egg shells to produce yellow oleander biodiesel, which meets ASTM D 6751 specifications and can be used in diesel engines.

CHAPTER ONE

1.0. INTRODUCTION

The world's largest source of energy is fossil fuels such as coal, liquefied petroleum gas (LPG) and crude oil (Energy, 2017). Fuel consumption in the transport sector is responsible for the release of 57% of carbon dioxide emissions, 45% of nitrogen oxide (N_2O) emissions, and 8% of particulate matter emissions (Olanrewaju & Olubusoye, 2020). The environmental impact of fuel emissions is also devastating as it has led to heart disease, lung cancer, and lung malfunctions (Quinn *et al.*, 2020). Due to rising energy prices, several nations around the world do not have enough energy to meet their needs (Ouedraogo, 2017).

The total energy sources worldwide as of 2020 are presented below in Figure 1.

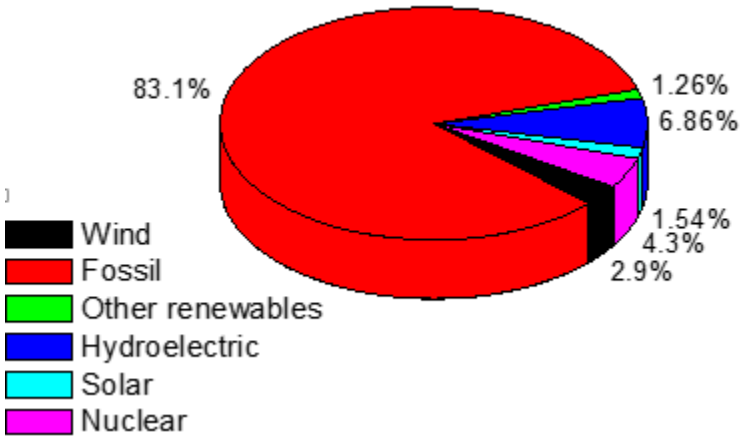

Figure 1: World-Wide Total Energy Sources (Geli *et al.*, 2022)

Fossil fuels remain the most popular fuel, accounting for 83.1% of total energy consumption worldwide. 16.9% of energy is provided by other fuels, including hydropower, nuclear power, wind power, and other renewable energy sources. Most of the world's petroleum fuel, is used in

manufacturing, transportation, heating, agriculture, and a number of other sectors of the modern economy (Takase *et al.*, 2021). The main factors that influence this large use of petroleum fuel include population growth, increase in gross domestic product (GDP), and energy supply (Bauer *et al.*, 2017). The global population growth rate is around 200,000 people per day, resulting in a continuous increase in energy demand (Owusu & Asumadu-Sarkodie 2016; Pattanaik *et al.*, 2019). The world population grew from 7.1 billion in 2013, and it is expected to reach over 9 billion by 2040 (Energy, 2017).

In Africa, the population is projected to double by the year 2050 (Quinn *et al.*, 2020), and this will inevitably result in an increase in the energy demand. Global energy demand will rise by 30 % between 2018 and 2040 (Edomah, 2018). Fossil fuels account for about 88.6 % of the total global primary energy demand (Ashraful *et al.*, 2014), by 2035, the increase in global energy consumption will account for 90% of all demand growth. The international transportation sector will account for 63% of the growth in the consumption of oil and other liquid fuels by 2040 (Mofijur *et al.*, 2016). The rise in prices resulting from increased demand for petroleum and other liquid fuels is one of the biggest challenges. The need for industrial raw materials, such as crude oil, grows along with the size of the world economy, pushing up the price of oil (Baumeister & Kilian, 2016). As with any other commodity, crude oil prices, refining costs, and fuel demand also influence diesel prices. As a result, the world economy has also been impacted by the unpredictability of the global energy market, particularly the recent shifts in oil prices (Chai & Jin, 2020). When fuel prices rise, transportation costs also rise, which affects industrial production costs and the prices of industrial products. The cumulative effect of this situation is an increase in oil prices and global inflation. In 2011, the world produced 85.7 million barrels of liquids daily,

with 80.0% consisting of natural gas liquids, unconventional liquids, crude oil, and condensate.. Crude oil production increased by 1.5 % annually from 1995 to 2005 and is expected to be exhausted by 2042 (Raj & Singh, 2012; Murray, 2016).

Due to the rapid increase in the number of vehicles worldwide, the transport sector is responsible for around 22 % of the greenhouse gases emitted into the atmosphere (Mofijur *et al.*, 2016). This contributes to international climate change and leads to phenomena such as El Niño (Datta & Mandal, 2014; Perera, 2018a), frequent and prolonged periods of drought (Kiss *et al.*, 2018), and health and safety issues (Mofijur *et al.*, 2016).

Challenges related to fuel costs, supply and demand, and emissions, as well as the negative climate impact of fossil oil, have driven the search for alternative fuels (Perera, 2018b). To control these adverse climatic effects, the world needs to formulate sustainable green policies (Ozturk, 2016). After the Paris Energy Agreement for the energy sector at the 2015 Climate Change Conference (COP), the renewable energy sector has grown faster (Pickl, 2019). Switching from fossil fuels to low-carbon alternative fuel sources will help reduce greenhouse gas emissions. The need for green energy is increasing and there are various renewable energy sources to meet this need. This energy transition therefore requires technical innovations in the field of renewable energies (Gielen *et al.*, 2019). Excluding conventional biomass, renewable fuels account for only 12.6% of the world's total energy resources (Geli *et al.*, 2022). Some of the renewable energies include geothermal, hydroelectric, tidal, solar, wind and biofuels.

Biofuels are renewable energy sources derived from biomass. They include biodiesel, vegetable oil, biogas and bioalcohols (Bušić *et al.*, 2018). Biofuels fall into three classes, that is, first, second and third generation. Starch, sugar, animal fats, and vegetable oils serve as primary raw materials

for the first generation of biofuels. Waste resources such as waste food, waste vegetable oil, and non-edible vegetable oils are used to produce second-generation biofuels. Finally, algae are used to produce third-generation biofuels (Dutta *et al.,* 2014; Behera *et al.,* 2015; Aro, 2016). Different countries use different feedstocks depending on their local availability (Changmai *et al.*, 2020). Edible or non-edible oilseeds are used as feedstock for biodiesel. Palm oil produces 31% of the world's biodiesel, while soybean oil and rapeseed oil account for 27 % and 20% respectively (Changmai *et al*., 2020). Researchers have extensively explored biodiesel production from non-edible oilseeds due to increasing costs of food, fuel prices and global climatic changes (Ogunkunle & Ahmed, 2019). The use of non-edible oils and waste oil as feedstock for second-generation biodiesel is preferred as they do not compete with edible feedstocks in the food supply (Bušić *et al.*, 2018). The non-edible oil feedstocks explored by researchers include *Ailanthus altissima, Azadirachta indica, Hevea brasiliensis, Hura crepitans, Jatropha curcas, Simmondsia chinensis, Madhuca indica, Nicotiana tabacum, Pongamia pinnata, Ricinus communis* and *Thevetia peruviana*, among others (kumar & Sharma, 2016). Of all the non-edible oil feedstocks for biodiesel production, *Thevetia peruviana* (Yellow oleander) seed has the highest oil content of ~ 60 – 67 % (Dallatu *et al*., 2017a).

The physicochemical properties of standard biofuels include high flash point, low sulfur content, high cetane number, and low greenhouse gas emissions. The oxygen contained in the molecular structure of biodiesel promotes combustion. They also help reduce the amount of smoke particles released compared to diesel (Basumatary, 2014; Gaurav & Sharmac, 2018). Biodiesel is blended with petrodiesel fuel to improve the lubricating properties of petrodiesel, allowing it to be used directly in a diesel engine (Kathirvelu *et al.*, 2017).

Biodiesel can be produced using various methods including pyrolysis, enzymatic transesterification, acid transesterification, and alkaline catalysed transesterification. Catalysis offers superior performance, faster reaction time, milder reaction environment, reduced by-products, recycleability, and wide range of use in biodiesel production compared to other techniques (Maroa & Inambao, 2021). These advantages make catalytic transesterification a promising strategy for the production of environmentally friendly and sustainable biodiesel (Maroa & Inambao, 2021). Feedstock, reaction conditions, intended biodiesel yield and quality, and cost are just some of the variables affecting the catalyst option for biodiesel production. Both homogeneous and heterogeneous catalysts have been used successfully in the production of biodiesel.

Current research is focused on synthesizing catalysts that can increase process efficiency and sustainability (Mohiddin *et al.*, 2021). Compared to heterogeneous acid catalysts, heterogeneous base catalysts have higher catalytic activity (Gardy *et al.*, 2019). Biodiesel produced using alkaline-catalyzed transesterification reaction (Basumatary, 2014) results in high yields close to the theoretical values (Atabani *et al.*, 2013). In base-catalyzed transesterification, homogeneous or heterogeneous catalysts are used. Heterogeneous base catalysts are solid basic compounds in the transesterification reaction used to produce biodiesel. Such compounds include ZnO, CuO, zeolites, CaO, SrO, MgO, and BaO (Faruque *et al.*, 2020). Calcium oxide is preferably used as a heterogeneous base catalyst for the production of biodiesel. This is because it is readily available, affordable, has long shelf life, high base strength, and is recyclable (Gardy *et al.*, 2019). Calcium oxide is largely derived from limestone, other sources include incinerated waste bones and shells (Changmai *et al.*, 2020). CaO, which is obtained from bone waste and incinerated eggshells, can

be used for biodiesel production (Da Silva *et al.*, 2019). This catalyst is both nanocrystalline and has a specific surface area approximately 1.54 times larger than commercial CaO (Bharti *et al.*, 2019). Heterogeneous catalysts are preferred for biodiesel production due to their ability to promote cleaner, efficient chemical reactions, reduce waste, enable catalyst recovery and reuse, and operate under milder conditions. (Jamil *et al.*, 2017). Heterogeneous catalysis reduces biodiesel production cost since the catalysts can be recovered and recycled (Hassan *et al.*, 2018). This study prepared heterogeneous nanocatalysts from waste eggshells for the production of biodiesel from yellow oleander seeds. Response Surfaces Methodology (RSM) was used to optimize the transesterification reaction. Thereafter, the synthesized nanocatalyst and yellow oleander biodiesel were characterized. The engine performance, combustion, and emission characteristics of yellow oleander biodiesel and its blends were also examined on a four-stroke diesel engine. Finally, the life cycle of yellow oleander biodiesel was studied.

1.1 Problem Statement

Global energy demand is projected to increase by 71% between 2000 and 2030, exhausting the availability of fossil fuels (Energy, 2017). This will affect fuel supplies, cause fluctuations in crude oil prices and lead to inflation (Gershon *et al.*, 2019). Biodiesel is one of the best fuel options that can be used to meet increased energy demands (Ogunkunle & Ahmed, 2019b). The transportation industry was responsible for 73% of those emissions (Alhindawi *et al.*, 2020). The released greenhouse gases (GHGs) have led to global climate changes, which have caused several problems, such as global warming, *el-Ninos*, *la-Ninas*, and ecological imbalance (Abeydeera *et al.*, 2019). Biodiesel significantly reduces net carbon dioxide emissions by 78% compared to petrodiesel, making it an optimal method for meeting emissions limits (Acevedo *et al.*, 2015). In

addition, biodiesel is biodegradable, can reduce greenhouse gas emissions, solve energy security issues, and reduce the need for petroleum-based fuels.

The biggest challenge in biodiesel production is the high production costs. Raw material prices account for 60-80% of total biodiesel production costs. Using cooking oil as an ingredient also poses a risk to food safety. This led to the search for alternative raw materials to replace the use of cooking oil in biodiesel production. These are sustainable, more environmentally friendly, and financially viable methods (*Dallatu et al.*, , 2017a). One way to solve this problem is to produce biodiesel from non-food vegetable oils and used cooking oils (Pikula *et al.*, 2020). Yellow oleander (*Thevetia peruviana*) seed with a high oil content of ~ 60 to 67% is an example of a non-edible oil that is a potential feedstock for the production of biodiesel (Toldra-Reig *et al.*,2020).

Biodiesel production through the transesterification process of vegetable oils requires the use of alkalis, acids, and enzymes as catalysts. Homogeneous catalysts are corrosive, hygroscopic and undergo saponification reactions lowering the yield (Diamantopoulos, 2015). When using a homogeneous catalyst, a lot of water is also required to wash the biodiesel during production. Unfortunately, this ends up in the environment and pollutes waterways. The use of waste-based heterogeneous catalysts in biodiesel production is preffered (Yaşar, 2019). The use of heterogeneous CaO nanocatalysts obtained from eggshell waste in biodiesel production is a promising alternative that is safer and more environmentally friendly (Xing *et al.*, 2021).

Researching optimal biodiesel production conditions can reduce production costs, but process optimization can be costly and time-consuming due to considering one variable at a time.. To solve this problem, multiple variables are examined in a single experiment using experimental design

(DOE). This saves time, reduces production costs, and reduces the amount of data to be analysed (Toldra-Reig *et al.*, 2020).

1.2. Objectives

1.2.1. General Objective

To study biodiesel production from yellow oleander by transesterification of the oil with methanol using a synthesized nanocatalyst from eggshells and to assess the life cycle, and evaluate the diesel engine, performance, combustion, and emission characteristics.

1.2.2. Specific Objective

a) To study the kinetic and thermodynamic processes associated with the extraction of yellow oleander oil and to identify the physicochemical properties.

b) To synthesize eggshell-derived nano-catalysts with the bottom-up technique and study the physicochemical characteristics of the nano-catalyst.

c) To optimize the production of yellow oleander biodiesel using response surface methodology with central composite design, and determine the physicochemical and thermal properties of the biodiesel.

d) 4. To test the performance, combustion, and emission, characteristics of a 4-stroke engine using yellow oleander biodiesel and its blends with petrodiesel.

e) To perform a life cycle analysis (LCA) of yellow oleander biodiesel in Kenya

1.3 Justification

The increase in the use of fuels in transportation, industry, agriculture, and heating homes and businesses is driving the demand for fuels on a global scale. This increase in fuel demand has led to a decline in international crude oil reserves, higher oil prices, leading to inflation, and

higher costs for industrial products. The high energy demand and the use of petrodiesel have also resulted in excessive emissions of pollutants into the environment. The aim of this research is to reduce the environmental impact by using green fuels such as yellow oleander biodiesel. The cost of producing biodiesel depends on the raw materials and catalysts used. Raw materials account for between 60 and 80% of total production costs and the use of cooking oil for biodiesel production creates food insecurity. To overcome the disadvantages of homogeneous catalysts, this research aims to synthesize heterogeneous nanocatalysts with high catalytic activity, stability, and environmental friendliness for the transesterification of yellow oleander biodiesel with methanol. The use of heterogeneous basic catalysts and non-edible oils has gained importance. CaO nanocatalyst from waste eggshells in the production of yellow oleander biodiesel has gained popularity because it is inexpensive, recyclable, and environmentally friendly.

The yellow oleander biodiesel production was optimized using the response surface methodology (RSM) to determine the optimal variables for the highest biodiesel yield at the lowest cost.. The parameters used included catalyst loading, temperature, and time for biodiesel production. This study also considered the physicochemical properties of the biodiesel, the engine performance, combustion and emissions characteristics, and the life cycle analysis of the yellow oleander biodiesel in Kenya

.

CHAPTER TWO

2.0 LITERATURE REVIEW

2.1 Biodiesel

Biodiesel is an alkyl ester prepared by transesterifying vegetable oils with primary alcohols. It acts as a substitute for petroleum-based fuels (Zaher & Soliman, 2015). Biodiesel production utilizes various feedstocks, with over 350 oleaginous plants available for use. Some of the non-edible vegetable oil feedstocks in Kenya are presented in Table 2.1.

Table 2.1: Yield and oil content of some non-edible vegetable oil feedstocks in Kenya

Plant	Oil Seed Yield Kg/Ha	% Oil		References
		Seed	Kernel	
Castor	500 – 1000	45–50	64–71	(Atabani *et al.*, 2013; El-Hamidi & Zaher, 2018; Keneni & Marchetti, 2017)
Croton	50	30 - 45	50–60	(Atabani *et al*., 2013; Keneni & Marchetti, 2017)
Jatropha	1900 - 2500	20–60	40 - 60	(Atabani *et al*., 2013; Keneni & Marchetti, 2017)
Yellow oleander	3500	60 - 62	60 - 67	(Atabani *et al*., 2013; Basumatary, 2014)

The production of biodiesel from local, nonedible vegetable oil seeds with an oil content of over 40% is preferred (Demirbas *et al.*, 2016). Some of the feedstocks from non-edible vegetable oils include: Jatropha, castor, rubber (*Hevea brasiliensis*) and neem (*Azadirachta indica*) have been investigated as a potential feedstock for biodiesel due to their relatively high oil content (Mishra & Goswami, 2018). Vegetable oils are preferred biodiesel feedstocks since they are renewable, produce fuel on a large scale, and are environmentally friendly (Amin, 2019). Compared to other

oilseed crops, yellow oleander seeds and kernels have the highest oil yield of 3500 kg/ha. This plant is easily available, cheap, and environmentally friendly.

2.1.1. The yellow oleander (*Thevetia Peruviana*) in Kenya

Thevetia Peruviana, often known as the yellow oleander tree, is a drought-tolerant plant that can be found throughout Kenya and is a member of the *Apocynaceae* family. This plant is perennial, thrives in soil that would normally be unsuitable for conventional agriculture, and can be harvested continuously for years (Deka & Basumatary, 2011). It thrives very well in the western part of Kenya and is locally called 'Chamama' by the Luos (Kishan *et al.*, 2012).

The spiral, linear, and roughly 13–15 cm long leaves of the yellow oleander plant reach heights of 2–6 m. After one and a half years, it begins to bloom, and after that, it blooms three times a year. Depending on the pattern of rainfall and plant age, the plant produces 400–800 fruits per year, yielding a consistent supply of seeds. It produces funnel-shaped yellow blooms with petals wrapped in spirals. The 4-5 cm in diameter, almost spherical fruits of the yellow oleander shrub have a fleshy mesocarp. Each ripe fruit has two to four seeds per kernel, and the plant's entire organ system is covered with milky fluid (Basumatary, 2014). The plant's stem and fruit are dark reddish-black and contain a huge seed that is covered in wax to help it retain water (Kishan *et al.*, 2012). The yellow oleander tree, with its dark reddish-black stem and wax-covered seed, yields 40-50 kilograms of fruit annually (Yadav *et al*., 2017). The plant's kernel contains 67% oil, yielding 1750 L of oil per hectare of land with an annual seed production of 52.5 t/ha (Atabani *et al.*, 2013). Figure 2.1 (A to D) shows the plant, seeds, and kernel.

Figure 2.1 panel 1: Yellow oleander plant (A) and green fruit (B)

Figure 2.1 panel 2: Yellow oleander fruits with seeds (C) and kernels (D)

Protein and carbohydrate molecules are bonded in yellow oleander oil through covalent bonds, van der Waals attractions, electrostatic interactions, and hydrogen bonds. As a result, various chemical, biochemical, or mechanical processes are required to separate the oil molecules from the seed (Dong *et al.*, 2016).

Various techniques are used to optimize oil production and increase productivity while maintaining oil quality. These techniques are discussed next.

2.2. Methods of oil extraction

Extraction is an essential step in isolating identified valuable compounds from plants. Oil can be extracted using various mechanical and chemical techniques. These techniques include supercritical fluid extraction, chemical or solvent extraction, enzymatic extraction and mechanical extraction. The most popular commercial oil extraction techniques are mechanical pressing and solvent extraction (Bhargavi *et al.*, 2018; Diaby *et al.*, 2017). Any of these extraction methods can be used depending on the type of vegetable oil to be produced, the quality of the oil, and the cost of production.

2.2.1. Mechanical Extraction

Mechanical extraction is the process of pressing the oil out of seeds (Çakaloğlu *et al.*, 2018). High pressure is used depending on the temperature applied, a process referred to as hot or cold press extraction. Several machine types are available in the mechanical pressing method, such as hydraulic and screw press machines (Nde & Foncha, 2020; Santoso *et al.*, 2014). Raw materials with low oil content require heating for efficient extraction, using hot mechanical extraction. For raw materials that are fragile or have a higher oil content, mechanical cold extraction is used as it preserves the taste and nutritional value of the oil. The mechanical extraction method produces relatively pure oil because no chemicals are used (Bhargavi *et al.*, 2018; Keneni & Marchetti, 2017; Subroto *et al.*, 2015).

Mechanical extraction offers advantages such as solvent-free production, safer virgin oil production, continuous, faster oil expulsion, simplicity, and affordability (Laing & Taylor, 2013).

Mechanical extraction has some disadvantages, including that its extraction efficiency is affected by the moisture content of the seeds. It requires experienced operators to achieve better results, is also both more time-consuming and labor-intensive than solvent extraction, and the amount of oil extracted is less than that in solvent extraction (Zhang *et al.*, 2018). The vegetable oil extracted by mechanical extraction must first be filtered and then degummed, although this method is used on an industrial scale, mechanical extraction has a lower oil yield and suffers from significant oil loss (Keneni & Marchetti, 2017; Laing & Taylor, 2013). This is due to the low effectiveness of the mechanical extraction process and the high oil content in the residues. These factors make them unsuitable for the complete extraction of oil from low-oil-content seeds such as soybeans (Bhargavi *et al.*, 2018).

2.2.2. Solvent oil extraction (chemical extraction)

The traditional Soxhlet extraction method is a popular solid-liquid extraction method used in oil production studies, requiring minimal solvent to extract large amounts of organic extract from plant material. Soxhlet extraction, a popular technique used in many current extraction techniques, is facilitated by the presence of the target compound in the refluxing solution (Keneni *et al.*, 2020). This extraction method is used in fields such as chemistry, food science, environmental science, and pharmacology.

Franz Von Soxhlet invented a Soxhlet extractor apparatus in 1879 that was used to extract lipids from solid materials (Azmir *et al.*, 2013). Soxhlet extractors are available in different sizes, from 10 cm^3 to 5000 cm^3 depending on the extractor's capacity (Bhargavi *et al.*, 2018). Figure 2.2 illustrates the different parts of a Soxhlet extractor.

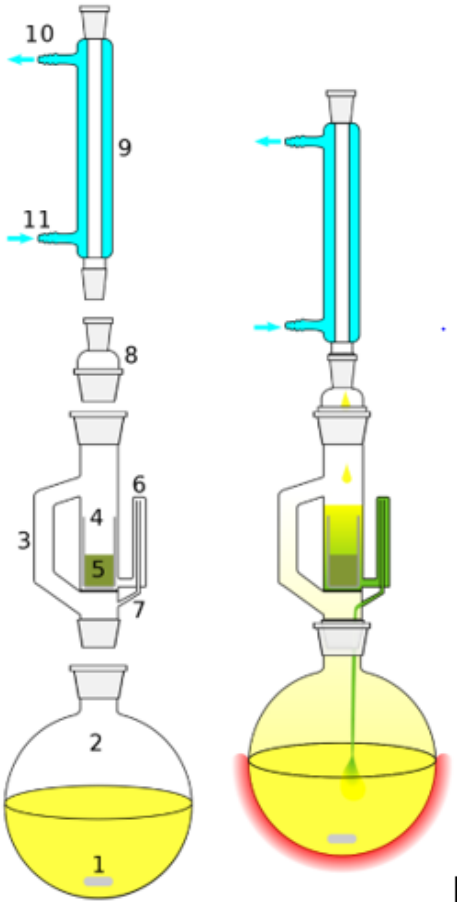

Figure 2.2: Soxhlet Apparatus

Key: 1) Stirrer bar or anti-bumping granules 2) Soxhlet extraction pot 3) Soxhlet distillation path 4) Soxhlet Thimble 5) Extraction meal 6) Syphon arm - inlet 7) Syphon arm - outlet 8) Soxhlet reduction adapter 9) Soxhlet condenser 10) Water out 11) Water in

The type of solvent used to extract the vegetable oil determines the quality of the oil. Non-polar organic solvents such as petroleum ether, hexane, and chloroform are used for this purpose. Other extraction methods include Soxhlet, hydro distillation, and maceration with alcohol (Danlami *et al.*, 2014).

The collected yellow oleander seeds were first dried, then crushed into powder, and then placed inside a thimble (Verran *et al.*, 2014). When the Soxhlet extraction pot is heated, the solvent evaporates and enters into the Soxhlet condenser. The liquid that results from the condensation process seeps into the extraction chamber that holds the extraction meal. The solvent in the sample overflows the extraction chamber and once it reaches a particular level trickle back down into the Soxhlet extraction pot. Lipid extraction takes four to eight hours for complete extraction (Gonfa & Mario, 2017). However, the specific number of cycles required depends on the sample and target analyte (Ntalikwa, 2021).

After extraction, the mixture of oil and solvent is collected and then separated using the rotary evaporator at the solvent's boiling point. The separated samples are then left under the fume hood for one hour to ensure that all remaining solvent evaporates into the environment and the pure oil remains (Niju *et al.*, 2019). N-hexane is used in the SE process as a solvent because it produces more oil than other solvents. However, although SE provides good results, its use at the industrial level is questionable because it generates toxic and flammable fumes (Khaw *et al.* 2017; Bhargavi *et al.*, 2018).

The conventional Soxhlet method of extraction is both economical and simple to use (Zhang *et al.*, 2018). High oil extraction efficiency is achieved by allowing many extractions to take place simultaneously. Soxhlet extractors have 90 to 98 % oil extraction efficiency (Nde & Foncha, 2020). Its efficiency is influenced by the oil's composition, solvent type, seed pretreatment conditions, seed particle size, temperature, and length of the extraction process (Oladipo & Betiku, 2019). High temperature improves oil solubility and diffusibility, which increases extraction yield (Premi & Sharma, 2013).

The disadvantage of SE is the insufficient extraction of polar lipids. Additionally, SE uses enormous amounts of solvents and is labor-intensive, time-consuming, and only economically and attractively at large-scale production (Hibbert *et al.*, 2019). However, it requires heating, making it costly, and the most preferred solvent (hexane) becomes hazardous with prolonged exposure (Nde & Foncha, 2020). Despite its disadvantages, hexane is still useful for research and some oil extraction processes. There are also possibilities of thermal decomposition of the vegetable oil because of very long hours of heating.

Soxhlet extraction is preferred because a small amount of solvent can extract a volume of oil. In addition, agitation promotes oil removal, making the solvent extraction process more manageable and less expensive. Agitation of the sample during extraction allows the solvent to better penetrate the solid matrix and come into contact with the oil sample, resulting in a more efficient extraction process (Zulqarnain *et al.*, 2021).

2.3. Kinetics of Extraction

The kinetics of solvent extraction systems is vital for the basic understanding of extraction processes. Understanding a system's extraction mechanism helps predict potential rate improvements, with high temperature being a key factor due to its ability to decrease viscosity (Kaya, 2020).

2.4. Kinetic models of extraction

Kinetic studies use the rate of extraction to determine whether a process is too slow or too fast to reach equilibrium. These investigations serve to understand the factors influencing the extraction rate, which is used to further develop the overall process and to prepare for future scaling. Since it establishes a connection between the concentration of the reactants and the rate of the reaction, the

order of the reactions is also crucial. To simulate the kinetics of plant extraction, mathematical techniques have produced a wide range of kinetic models. Models can be developed empirically or semi-empirically, or they can be constructed theoretically using Fick's law or chemical kinetic equations (rate law) (Motlagh *et al.*, 2022). The rate at which the oil dissolves in the solvent and reaches the equilibrium concentration in the combination determines how quickly the oil is extracted. The oil extraction process from seeds involves several mass transfer processes. The four main mass transfer processes during oil production include diffusion, desorption, solvent percolation, and solvent phase diffusion. The rate is determined when the oil in the solid diffuses into the solution (Kusuma & Mahfud, 2015; Dos Santos *et al.*, 2015).

Both conventional and unconventional extractions have been subjected to the use of kinetic extraction models based on chemical kinetic equations or rate laws (first order and second order). The second-order kinetic model is most commonly used because the empirical equations are used to express the concentration changes of the components in the extracted product, thus providing insight into the process (Motlagh *et al.*, 2022).

2.4.1. Thermodynamics of oil extraction

The thermodynamic studies of oil production also play a significant role in determining the feasibility of the process on an industrial scale. They provide information about the type of reaction that takes place during a production process. Thermodynamic modeling is used to determine the activation energy and thermodynamic state of the reactants involved in oil extraction. Parameters such as enthalpy (ΔH), entropy (ΔS), and Gibbs free energy (ΔG) in the extraction process are evaluated (Alves *et al.*, 2019). The enthalpy value indicates whether the process is exothermic or endothermic. The entropy value indicates that the reaction occurs spontaneously, while the Gibbs

free energy value determines whether the reaction is reversible or not. Whenever the Gibbs free energy is zero, the reaction can proceed in either a forward or reverse direction under equilibrium condition. From the above thermodynamic parameters data, the activation energy (E_a) of an extraction process can also be determined.

Jabar *et al.*, (2015) studied the thermodynamics of yellow oleander oil extraction. They found that the enthalpy value (ΔH = + 29.20 kJ/mol) and entropy value (ΔS = +91.84 J/mol) were positive, while ΔG was generally negative at high temperature. This indicated that the yellow oleander oil extraction process was endothermic, spontaneous and irreversible (Jabar *et al*., 2015).

Most researchers focused on the physico-chemical properties of yellow oleander oil, a few studied the kinetics and thermodynamics of oil extraction for biodiesel production. In this work, the kinetic and thermodynamic techniques for the extraction of yellow oleander oil from the seeds are studied. However, other research suggests that the commercial process for producing homogeneously catalyzed biodiesel is costly and environmentally harmful. This is because they can increase processing complexity, cost and waste due to their dissolved nature, susceptibility to deactivation and the need for efficient recovery and recycling methods (Kesic *et al.*, 2016).

2.5. Characterization of yellow oleander oil

This section focuses on the physicochemical properties of yellow oleander oil using the ASTM standards. These measurements include GC/MS and FTIR analysis of the chemical composition and structure of oils. The physicochemical analysis of oils typically involves the determination of several key properties, including moisture content, acid number, saponification number, peroxide number, iodine number, calorific value, specific gravity, kinematic viscosity, and a specific number (CN).

2.5.1. Spectroscopic methods of analysis of oil

Gas chromatography-mass spectroscopy (GC-MS) and Fourier transform infrared (FTIR) spectroscopy are the spectroscopic methods used to quantitatively and qualitatively analyse yellow oleander oil and biodiesel.

FTIR spectra illustrate absorption bands with characteristic frequencies assigned to different functional groups (Palencia, 2018). GCMS detects compounds eluted at different retention times, with mass spectra corresponding to the compounds present in the analyte, indicating fatty acid composition (Piechocka *et al.*, 2020).

2.5.1.1. Gas Chromatography-Mass Spectrometry (GCMS)

GC-MS is a combination of two analysis techniques: gas chromatography (GC) and mass spectrometry (MS). This technique is used to characterize and identify various organic compounds. Chromatography is a qualitative separation technique for organic compound analysis, while mass spectrometry provides quantitative analysis using retension times and mass spectra. These two methods are used together to study complex organic compounds (Hase *et al.*, 2017). In addition, GCMS provides quantitative data by measuring the abundance of specific ions corresponding to the target compounds. This gives detailed information about the concentration of the sample components.

GC parts include a carrier gas, an injection port, an oven, and a column. The temperature range for the GC oven was between 40 and 320 °C. Inside the furnace, the column is a thin tube with a unique polymer coating. The analyte molecules travel through the column due to the heating. First, chemical mixtures in the sample are divided based on how volatile they are. Then an inert gas carries them through the column. Highly volatile chemical compounds pass down the column

considerably faster than low volatile chemicals (Stashenko & René Martínez, 2014). The mass spectrometry instrument, the second component of the GC/MS, consists of three main components: an ion source, a filter, and a detector. The number of ions with a certain mass/charge ratio is counted by the detector. A mass spectrum is created by compiling the recorded data on a computer. The mass spectrum is a visual representation of how many ions of different masses pass through the filter. To identify chemical compounds, a computer compares spectra to other spectra in the library.

Suwari *et al.*, (2018) performed the GC-MS analysis of yellow oleander seed oil for biodiesel production. They found that the most important fatty acids in yellow oleander oil were oleic acid (41.91%), linoleic acid (11.89%), palmitic acid (17.02%), and stearic acid (6.23%). The high density of yellow oleander seed oil is due to the presence of saturated fatty acids. According to Adepoju, *et al.*, (2018), yellow oleander oil contained the following acids: palmitic acid (9.52%), stearic acid (7.02%), linoleic acid (37.91%), oleic acid (32.82%), linolenic acid (12.33%) and others (0.40%). The level of unsaturation was high at 70.73%.

Bora *et al.*, (2014) observed that yellow oleander oil contained 36.43% of total saturated fat and 63.57% of total unsaturated fat.

Despite the relatively lower sensitivity of FTIR in comparison to MS, FTIR detection provides a molecular "fingerprinting" capability that is not available to MS. FTIR Spectrophotometry is discussed next.

2.5.1.2. FTIR analysis of vegetable oil and biodiesel samples

FTIR spectroscopy is widely used to analyze many solid, liquid, and gaseous materials. This is because, it is easy to use, flexible, and allows for quick analysis (Gezici *et al.*, 2012). FTIR analysis

enables a comprehensive understanding of the chemical composition of vegetable oils by providing characteristic peaks that correspond to the functional groups present in the oil. It evaluates oil quality by ensuring that it meets desired standards for various purposes, including biodiesel production (McElroy *et al.*, 2015). This is because a functional group absorbs radiation at a specific frequency expressed as wave numbers between 4000 and 600 cm^{-1} (Sharma *et al.*, 2018). The magnitude of this absorption is directly related to the molecular weight of the functional group. This magnitude identifies the proportion of a functional group that makes up a given sample. Although distinguishing between certain bond configurations, such as ketone and carboxylic acid C=O, can be difficult. FTIR spectroscopy can quickly identify and quantify functional groups in mixtures using an infrared spectrum (George *et al.*, 2015). When the yellow oleander oil was subjected to FTIR analysis, the IR spectra showed two distinct bands at 2924.18 cm^{-1} which were assigned to the symmetric stretching vibration of the aliphatic CH_2 group. The symmetric stretching vibration was due to 20.26 % linolenic acid and 16.11 % oleic acid groups present in the oil (Dallatu *et al.*, 2017a).

FTIR spectrometry has the following advantages: greater signal-to-noise ratio, high energy throughput, high precision, and high stability (Faghihzadeh *et al.*, 2016). This procedure is quick, non-destructive, and requires little sample preparation. It makes it possible to evaluate the functional groups present in organic molecules on a qualitative level (Chen *et al.*, 2015)

The disadvantages of FTIR spectroscopy include that it does not have a grating and the acquisition costs are very high. The small size of the sampling chamber of an FTIR can also present some challenges. Installed components may block the IR beam; Therefore, they can often only evaluate

small objects such as rings. Finally, some materials completely absorb infrared radiation, so obtaining accurate data may be impossible (El Fels *et al.*, 2015).

The next section discusses the physicochemical properties of vegetable oils based on ASTM D6751, biodiesel standards, and other techniques.

2.5.2. Physicochemical properties of yellow oleander oil

These properties include the moisture content, saponification number (SV), acid number (AV), peroxide number (PV), iodine value(IV), calorific value (CV), specific gravity, kinematic viscosity, and cetane number, among others.

2.5.2.1. Moisture content (ASTM-D2709)

Moisture content in vegetable oils is a crucial factor in the production of biodiesel and affects the quality of the end product. The maximum allowable volumetric moisture content in a base oil is 0.05 % according to ASTM regulations (Ismail & Ali, 2015). High moisture content in the oil can lead to various issues, including water buildup and microbiological growth in equipment used for handling, storing, and transporting fuel. In addition, incorrect handling after processing or soaking up atmospheric moisture while storing is to contributes tor the moisture content (Fregolente *et al.*, 2015). Adepoju *et al*., (2018) studied the moisture content in the yellow oleander oil. They recorded 0.0131 % which was within the ASTM D2709 range of 0.05 % vol.

2.5.2.2. Saponification value (SV) ASTM-D 5558-95

Saponification value (SV) is the mass of potassium hydroxide needed to saponify 1 gram of oil, but cannot estimate oil's molecular weight, but triglycerides' molecular weight is inversely proportional. Oils with a higher saponification value have a lower average molecular weight. This means that the triglycerides in these oils and fats are made up of smaller fatty acid molecules. On

the other hand, oils with a lower saponification value have, on average, a higher molecular weight. The triglycerides in these oils and fats are made up of larger fatty acid molecules (Adepoju *et al.*, 2018). A higher saponification value also indicates the presence of free fatty acids, which lead to soap formation.

Suwari *et al.*, (2018) observed a saponification value of 140.52 mg KOH/g in yellow oleander oil which met the ASTM standard of 350 mg KOH/g (Sakthivel *et al.*, 2018). It suggested that the oil would work well as a feedstock for making biodiesel. According to observations by Dallatu *et al.*, (2017b), yellow oleander oil had a saponification number of 197.75 ± 0.72.

2.5.2.3. Acid value (AV) (ASTM – D 974 - 00)

The acid value (AV) of vegetable oil is crucial for evaluating biodiesel raw materials quality and free fatty acid content, indicating rancidity due to oxidation or hydrolysis activity. The AV is calculated as the mass in milligrams of KOH needed to neutralize all the acid in 1 gram of sample (Gul *et al.*, 2020). The maximum AV level for pure biodiesel is 0.8 mg KOH/g, as per ASTM standard D6751.

Adepoju *et al.*, (2018), observed an acid value of 3.8048 in yellow oleander oil, indicating that the oil was favourable for biodiesel production. Godson & Bassey, (2015) observed that the yellow oleander biodiesel had an AV of 0.441 mg KOH/g. This means that it did not experience any oxidative deterioration at the time of testing.

2.5.2.4. Peroxide value (PV) (ASTM D-1563)

In vegetable oil and biodiesel samples, the peroxide value determines the amount of oxidative moieties present. These oxidative molecules are hydroperoxides produced when fatty esters and oxygen from the air interact (de Almeida *et al.*, 2019). The maximum ASTM peroxide value for

vegetable oil is normally set at 4.8 meq/kg (milliliquivalents per kilogram). It may be an indication that the oil is severely oxidized and unusable when the biodiesel peroxide level exceeds this threshold (Jonas *et al.*, 2020).

Bora *et al.*, (2014) observed a low peroxide value of 4.8 mEq. O_2/kg oil in yellow oleander oil indicates that the oil will stay longer without turning rancid. However, Adepoju *et al.* (2018), observed a PV of 23.8 mEq. O_2/kg in yellow oleander oil indicates that the oil has undergone significant oxidation. Dallatu *et al.*, (2017) observed a peroxide value of 3.20 mEq. O_2/kg for yellow oleander oil. Confirming that it was of good quality, with a lower tendency to go rancid on long-time storage.

2.5.2.5. Iodine value (IV) (ASTM D445)

Iodine value (IV) is crucial for analyzing chemical stability, oxidative rancidity, and unsaturation levels in oil and biodiesel fuels. It measures the amount of iodine absorbed by 100 mL of a given oil or biodiesel (Zuleta *et al.*, 2012). The ASTM standard iodine value is 115 I_2/100 g. Higher IV in an oil sample indicates higher double bond content, affecting stability, oxidation resistance, and potential polymerization (Esfarjani *et al.*, 2019). Low-iodine biodiesel tends to be more flammable than higher-iodine biodiesel, while it may have less favorable cold flow characteristics. Heat leads to the polymerization of glycerides, which reduces the lubricity of the fuel and leads to the formation of deposits in biodiesel that contains more unsaturated fatty acids (Folayan *et al.*, 2019). An IV in yellow oleander oil of 97.60 gI_2/100 g indicated both a low triglyceride iodine content and a high level of unsaturation (Adepoju *et al.*, 2018).

Bora *et al.*, (2014) observed an iodine value of 34.56 g I_2/100 g in yellow oleander oil met the ASTM requirements This means that the degree of unsaturation in yellow oleander oil was low.

2.5.2.6. Calorific value (ASTM D240)

Calorific value (CV) measures fuel energy content, with unsaturated vegetable oils having lower CV compared to petrodiesel, while biofuels with higher oxygen content burn completely and produce fewer emissions. However, because biofuels contain oxygen in their molecular structure, they have lower calorific values, resulting in a significant loss of performance (Reddy *et al.*, 2018). The lower heating value (LHV), also known as the average CV of vegetable oils is 38.4 MJ/kg, while the heating value (HHV) of vegetable oil is 39.45 MJ/kg (Mairizal *et al.,* 2020).

2.5.2.7. Specific gravity (ASTM D1298)

Fuel density is a critical fuel property as fuel injection systems, pumps and injectors must deliver a precise amount of fuel for complete combustion. For optimal combustion, a certain amount of fuel has to be pumped through injection systems, pumps, and injectors. The fuel must maintain density values within acceptable ranges to permit ideal air-to-fuel ratios and complete combustion. Particulate matter emissions and incomplete combustion are risks associated with high-density fuels (Ajani *et al.*, 2019). The total volume of the fuel is compared to water at 15 °C to determine its specific gravity. Using a hydrometer, the ASTM D 1298 test technique is used to determine the density of oil and water (Rupasianghe & Gunathilaka, 2018). In the analysis of yellow oleander oil, the specific gravity was 0.88 ± 0.02 (Dallatu *et al.,* 2017a). According to European standards (ENISO 3675 and EN ISO 12185), biodiesel must have a density of 0.86 to 0.9 g/cm^3. However, the American Society for Testing and Material (ASTM) standard does not set limits on biodiesel density (Jonas *et al.*, 2020). Plant oils with a specific gravity of 0.8200 to 1.0714 at 30 °C are considered suitable for use as biofuel (Dallatu *et al.,* 2017a). Yellow oleander oil is a yellow liquid with a specific gravity of 0.898, and a density of 0.887 g/cm^3 (Adepoju *et al.*, 2018). This value

is within the EN ISO 12185 range of 0.86 - 0.90 g/cm^3. The density of vegetable oil depends on the fatty acid composition and the purity of the raw materials, and the lower-density value indicated that yellow oleander oil contains fewer unsaturated fatty acids (Suwari *et al.*, 2018).

2.5.2.8. Kinematic Viscosity (ASTM-D445)

The viscosity of a liquid is considered to be its resistance to flow, it has an ASTM D445 standard value for KV of 1.9 to 6.0 mm^2/s. KV is determined by the time it takes for a given volume of liquid to flow through a calibrated glass capillary viscometer (Al-Mashhadani & Fernando, 2017). According to research, vegetable oils can be used as fuel in diesel engines (Hellier *et al.*, 2015). However, vegetable oils have high viscosity and low volatility. These impede fuel atomization and spray pattern, resulting in excessive carbon deposits, injector clogging and piston ring sticking (Adaileh & Alqdah, 2012; Che Mat *et al.*, 2018). A high viscosity value will also cause oxidized polymeric compounds, which can result in the growth of gums and sediments that clog the engine's filters. Calculating the ideal conditions for storage, handling, and operation of fuels depends on their viscosity. The length of the fatty acid chain correlates with an increase in kinematic viscosity. The kinematic viscosity of unsaturated vegetable oils is significantly influenced by the type and amount of double bonds, with the position of the double bond having a lesser influence (Mairizal *et al.*, 2020).

Dallatu *et al.*,(2017b) observed a kinematic viscosity of 23.23 mm^2/s in yellow oleander oil. This high viscosity was reduced by the oil's transesterification reaction. Yarkasuwa *et al.,* (2013) observed that the viscosity of yellow oleander oil dropped from 47 to 5.21 mm^2/s as a result of transesterification. Suwari *et al,* (2018) observed a KV of 2.18 mm^2/s in yellow oleander oil.

Vegetable oils become viscous due to the presence of unsaturated fatty acids in their structures (Patel *et al.,* 2017).

2.5.2.9. Cetane number (ASTM D613)

The cetane number measures how fast ignition occurs and combustion's smoothness, and a higher cetane value indicate better ignition properties (Giakoumis & Sarakatsanis, 2019). A fuel with a higher cetane number then results in a shorter deceleration time and smoother engine operation. Biodiesel has a higher CN than petrodiesel because it contains more oxygen than petrodiesel (Shah *et al.*, 2018).

Dallatu *et al.*, (2017b) oberved a CN of 48 in yellow oleander oil, which was within the ASTM range of 47 to 51. However, Adepoju *et al.,* (2018) observed that the cetane number for yellow oleander oil and biodiesel were 99.1216 and 99.6228 respectively. These values were higher than the biodiesel ASTM standard. The next section looks at the synthesis and characterization of nanocatalyst.

2.6. Synthesis and characterization of eggshells nanocatalyst

Nanoparticles are particles with sizes ranging from 1 to 100 nanometers, synthesized using either *bottom-up* or *top-down* techniques (Khan *et al.,* 2017; Patra & Baek, 2014). Both processes play a significant role in modern industry, particularly nanotechnology. Thes*e* techniques are discussed next.

2.6.1 The *bottom-up* and *top-down* techniques for the synthesis of nanocatalysts

The *bottom-up* technique involves chemical reactions between atoms, ions, and molecules. In the *top-down* synthesis technique of nanoparticles, a solid is subjected to external stress, causing it to break down into smaller particles. This includes the mechanical crushing or breaking of bulk

materials into smaller pieces (Jaji *et al.*, 2020). The *bottom-up* technique uses molecular condensations or atomic transformations to synthesize nanoparticles from gas or liquid atoms. Controlled separation of atoms and molecules occurs when the atoms or molecules combine to form nanostructures (2-10 nm in size range).This technique is devided into liquid phase formation and gas phase syntheses (De Oliveira *et al.*, 2020), anfd the critical aspects of this process are nucleation and crystal growth (Hornak, 2021). This is because it has a better chance of producing nanoparticles with fewer defects and a more homogeneous chemical composition (Parashar *et al.*, 2020).

Recently, a reverse microemulsion technique has been used to prepare nanoscale metal oxides. The reverse microemulsion is a technique in which aqueous and oil phases (the phase is thermodynamically stable) are dispersed in an isotropic manner. It exhibits a dynamic structure of nano-sized water droplets that continuously deform, dissolve, and solidify (Azrini *et al.*, 2019). Depending on the water/surfactant ratio R_w, these aqueous droplets can be between 5 and 100 nm in size.

$$R_W = \frac{3V_{aq}[H_2O]}{\sigma[S]} \quad \text{.....Equation 2.1}$$

Where σ is the area per polar head of the surfactant, V_{aq} is the volume of the water molecule, and R_w is the radius of the water basin. The interaction of aqueous droplets containing the desired ions serve as a nanoscale reactor to precipitate nanoparticles (A. G. Niculescu *et al.*, 2021). The "oil" may be a mixture of the surfactants, while the microscopic drops of the aqueous phase (micelles) may contain soluble salts. When the surfactants in "oil," which regulate the micelles, mingle with

one another and the nanoparticles precipitate, a reaction occurs leading to the production of nanoparticles.

2.6.2. Synthesis of nanoparticles using bottom-up technique

The bottom-up approach builds larger structures or materials from smaller components, using reverse micelles for controlled and uniform nanoparticle synthesis at the molecular or nanoscale level. Reverse micelles are stabilized by surfactants in an organic phase and are nanometer-sized droplets in an aqueous phase. Specific reactions are performed in aqueous systems on the nanometer scale to produce materials with controlled size and shape. Figure 2.3 shows the schematic diagram of typical reverse micelles (RMs), which are arranged systems that coexist in water-in-oil (W/O) microemulsions.

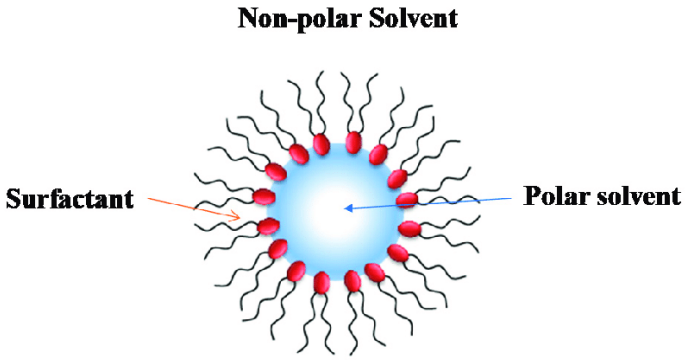

Figure 2.3: **Schematic representation of a typical reverse micelles (RMs) structure** (Dib *et al.*, 2021)

One of the criteria for regulating the size of nanomaterials during nanomaterial synthesis is the size of the inverse micelles. The more water there is, the larger the reverse micelles become, resulting in larger nanoparticles. This ability to adjust the size of the nanoparticles is the main advantage of this method, which is also cheap (Das *et al.*, 2021). Monodisperse droplets behave

as constrained, controllable nanoreactors. These droplets cause microemulsion droplets to spontaneously form well-separated domains. Additional advantages of this method include the exceptional ability to fine-tune the structural properties of the nanoparticles. The formation of a homogeneous product with the required size, shape, and morphology is preserved within the aqueous core (Sharma & Ganguli, 2014). The highly polar compounds that are insoluble in non-polar organic solvents, such as water, can be used to dissolve the polar core of RMs. These microscopic pools of water or solvent can speed up chemical reactions during the production of nanoparticles and polymers *(Dib et al.,* 2021). Adjusting parameters controlling the interfacial layer stiffness of micro-emulsion droplets and crystal growth kinetics in a constrained environment also makes the RMs approach highly adaptable (Arsene *et al.,* 2021). Modulating certain parameters can affect the interfacial film flexibility of microemulsion droplets. The nature of the continuous organic solvent, the inter-micellar exchange rate, the water-to-surfactant molar ratio (W_0), the structure of the surfactant and co-surfactant, and the packing parameter are among them (Mehebub *et al*., 2023)

2.6.3. Co-precipitation Method

The coprecipitation method is a *bottom-up* technique used to synthesize nanoparticles. This was accomplished via coprecipitation of aqueous solutions' sparingly soluble components, followed by thermal breakdown to produce oxides. Nucleation, growth, coarsening, and/or aggregation processes may co-occur during co-precipitation reactions (Bader *et al.*, 2014). The most important factors that influence the precipitation process include; particle size, pH, temperature, the surfactant or co-surfactant used, the electrolyte used, its concentration, and the molar ratio (Yi *et*

al., 2017). Figure 2.4 is a schematic diagram of a typical co-precipitation method for micro and nano-particle synthesis.

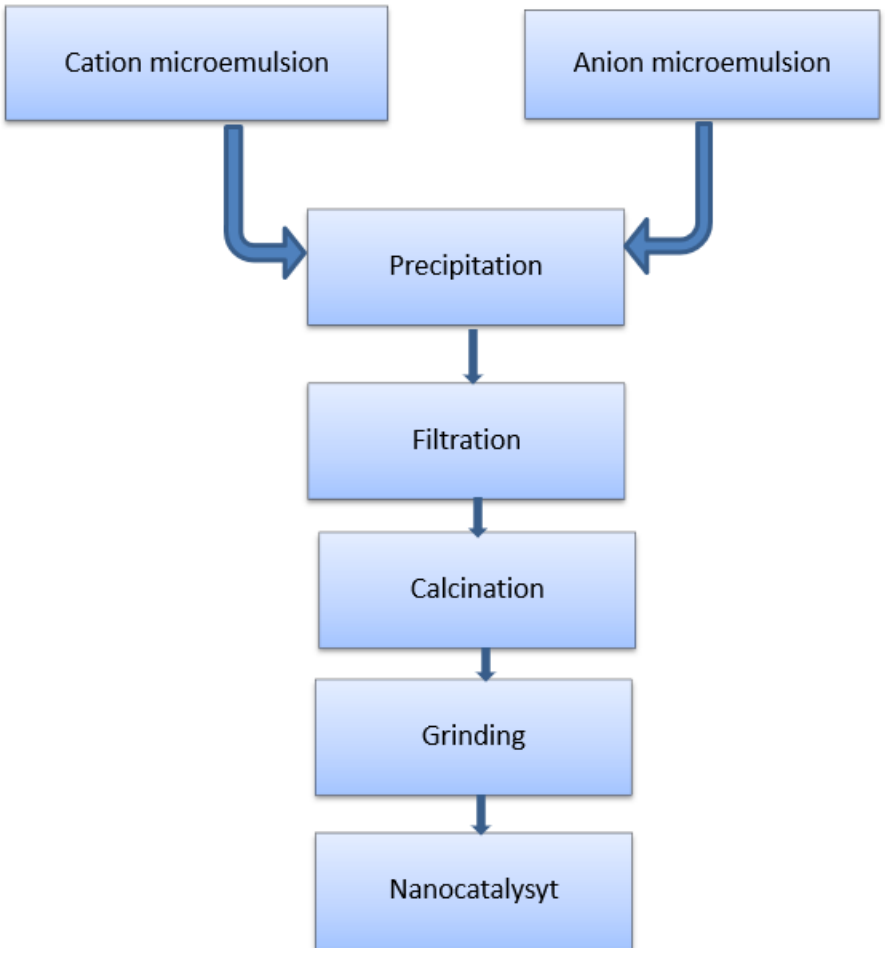

Figure 2.4: Typical co-precipitation method for micro and nano-particle synthesis

The co-precipitation method approach is useful in synthesizing metal oxides. First, it produces insoluble salts through nucleation and growth, and these particles build up through aggregation to form the nanoparticles (Legg *et al.*, 2016). Next, organic additives are necessary for the controlled nucleation and crystallization process (Olderay *et al.*, 2009). Finally, the precipitates are filtered and annealed to obtain the final mixed oxide product (Pareek *et al.*, 2017).

In reverse micelles, metal hydrolysis of metal alkoxides precipitates metal oxide nanoparticles such as silica, titania, zirconia, iron oxide, and complex oxides. A metal-ion-containing micro-emulsion producing hydroxide precipitates is combined with an alkaline micro-emulsion. Centrifugation and heating follow to eliminate water and/or enhance crystallinity (Qi, 2015).

The co-occurring processes of nucleation, growth, coarsening, and aggregation are included in the co-precipitation technique. A critical stage of precipitation is nucleation, which is the process through which the fundamental constituents of a new thermodynamic phase emerge

(Hu & McClements, 2015). Slow nucleation produces nuclei with a lower concentration and larger particles, while fast nucleation produces nanocrystals with a higher nucleation concentration and smaller size. To lower the surface energy of smaller particles during the developmental phase, larger particles absorb smaller ones in a process known as coarsening or Ostwald ripening (Polte, 2015).

Particle size and dispersion are significantly influenced by the recovery of nanoparticles generated from reverse micelles. High surfactant content makes this process challenging. Additional washing with ethanol, distilled water, or other solvents is necessary to obtain high-purity nanoparticles (Abid *et al.*, 2022). The advantages of co-precipitation over the micro-emulsion method include its simplicity and effectiveness. The main disadvantage is residual surfactants, which have adverse effects on properties and difficult scale-up procedures. This precipitate can be a major source of contamination and separating the analyte from the precipitate matrix can be complicated (Ali *et al.*, 2016). The following section focuses on the analytical techniques used to characterize nanocatalysts.

2.6.4. The analytical techniques for the analysis of nanoparticles

The study of size, shape, structure, temperature, and other physicochemical properties are necessary factors in the analysis of nanoparticles. Techniques such as; Thermogravimetric Analysis (TGA), Differential Thermal Analysis (DTA), Differential Scanning Calorimetry (DSC), X-ray Diffraction (XRD), X-ray Fluorescence (XRF), Fourier Transform Infrared (FTIR) Spectroscopy, Scanning Electron Microscopy (SEM), Energy Dispersive X-ray Analysis (EDX), and transmission electron microscopy (TEM), among others may be used.

2.6.4.1. Thermogravimetric analysis of materials

Thermogravimetric analysis (TGA) is a thermographic technique used to characterize materials by evaluating the chemical, physical, and structural changes in a material using temperature changes (Zainal *et al.*, 2020). In principle, temperature is a variable that affects most materials physical properties and may lead to structural transformations. However, this technique is limited to thermogravimetric and calorimetric effects. TGA can also predict the thermal stability of materials from room temperatures up to 1200°C (Emiola-sadiq *et al*., 2021).

The TGA data collected during a thermal process is used to plot a graph of mass against either temperature or time, giving a typical plot as given in Figure 2.5.

The thermal stability of the eggshells material varied with temperature. The first mass drop with a mass loss of 4% was observed between 200 and 400 °C. This loss of mass is due to the loss of water and organic matter from the eggshell. A decrease of 2.5% was then observed between 250 and 300 °C. Eggshell $CaCO_3$ was thermally stable up to 600 °C. The decomposition of the $CaCO_3$ took place between 600 and 800 °C with a total mass loss of 52% and the release of carbon dioxide (CO_2).

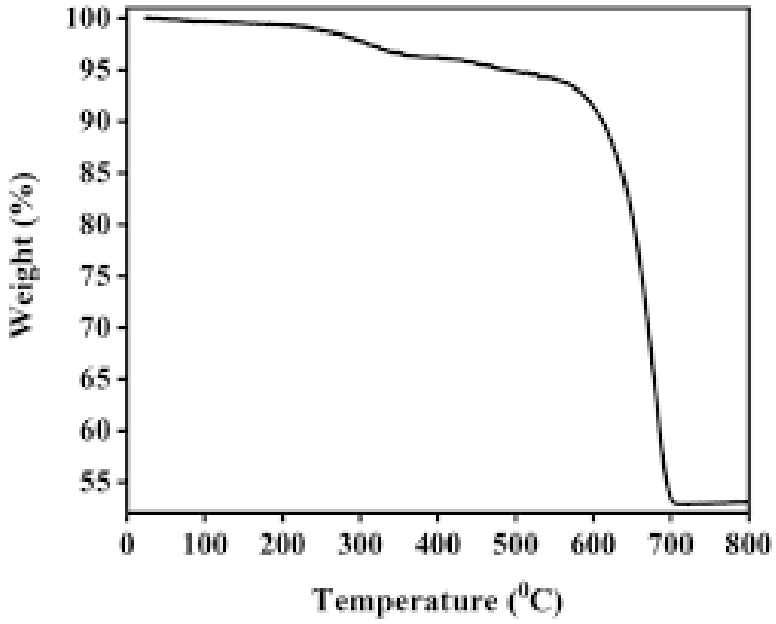

Figure 2.5. Thermogravimetric analysis of the eggshell powder (Araque, 2018) (Nath *et al*., 2021)

Da Silva *et al.,* (2019) observed two levels of decomposition during the TGA analysis of eggshells. This material showed a mass loss of 1.95% in the first stage between 30 to 400 °C, which was caused by the loss of combustibles such as water and organic matter. After that, it lost 4.2% of its mass from the decomposition of eggshell membrane which was full of organic material. With a mass loss of 42.88 %, the second stage's mass loss took place at 782.3°C. This resulted from the release of CO_2 by the breakdown of $CaCO_3$.

Kristl *et al.,* (2019) observed that the TGA analysis for eggshell powder samples was divided into three decomposition levels. First, a slight mass loss of between 1% and 1.15 percent is due to the loss of volatile components, primarily water, between ambient temperature and 350 °C. Once more, the second breakdown process occurred between 350 and 520 °C and resulted in a mass loss of between ~1 to 1.15 %. This resulted from the decomposition of organic residue that made up

the outer shell membrane. Finally, the average mass loss of 43 to 43.4 %, occurred between 600 and 850 °C. This was due to the thermal breakdown of $CaCO_3$ into CaO and CO_2.

The main advantage of TGA is that if the material is thermally stable within the expected temperature range, no subsequent mass change is observed (Díaz *et al.*, 2021). The mass loss of volatile elements, which is not proportional to the formation of degradation products, is the fundamental disadvantage of TGA processes. This limits its ability to provide accurate assessments of the degree of deterioration (Díaz *et al.*, 2021).

2.6.4.2. Differential thermogravimetric analysis (DTG)

The differential thermogravimetric curves are the first derivative of weight with respect to temperature or time. Both quantitative and qualitative data about the sample can be obtained from the DTG curve. DTG provides additional information about the intensity and temperature at which the mass changes occur. DTG is valuable for identifying multiple degradation or reaction events in a sample and can help distinguish overlapping processes that may be difficult to resolve with DTA or TG alone. In DTG analysis, a derivative curve for change in mass is plotted, giving $-\frac{dm}{dt}$. DTG curve helps to determine the temperature at which there is maximum weight loss or weight gain at temperatures called the inflection point. The temperature remains constant until a thermal event occurs, during melting, decomposition, or change in the crystalline structure of material. A typical DTG graph is given in Figure 2.6.

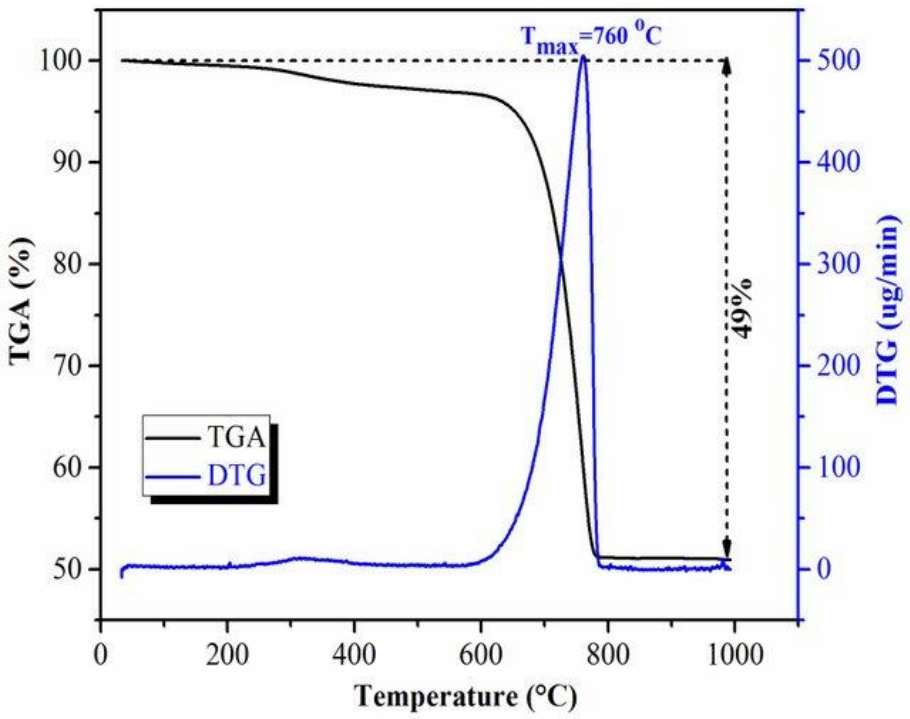

Figure 2.6: **DTG compared to TGA curve of waste eggshell** (Demir *et al.*, 2017)

DTG, a derivative of TGA, enhances the analysis of a material's thermal properties by providing a more detailed examination of specific thermal events. Therefore, the DTG peak temperature of 760 °C is usually used as a characteristic value to specify the decomposition temperature of $CaCO_3$ in the eggshells.

Demir *et al.*, (2017) observed that the weight of the eggshells decreased during the heating process. There was a noticeable weight loss from 600 to 800 °C as the temperature rose. At 760 °C, the $CaCO_3$ decomposed into CaO, releasing CO_2 molecules. As a result, the eggshells had a CaO content of ~ 49% (w/w).

2.6.4.3. Differential scanning calorimetry (DSC) analysis

Differential Scanning Calorimetry (DSC) is a thermoanalytical technique used to study the heat fluxes associated with thermal transitions in a material. This method calculates the difference between the heat required to raise a sample temperature and that of a reference.

A typical DSC graph is presented in Figure 2.7.

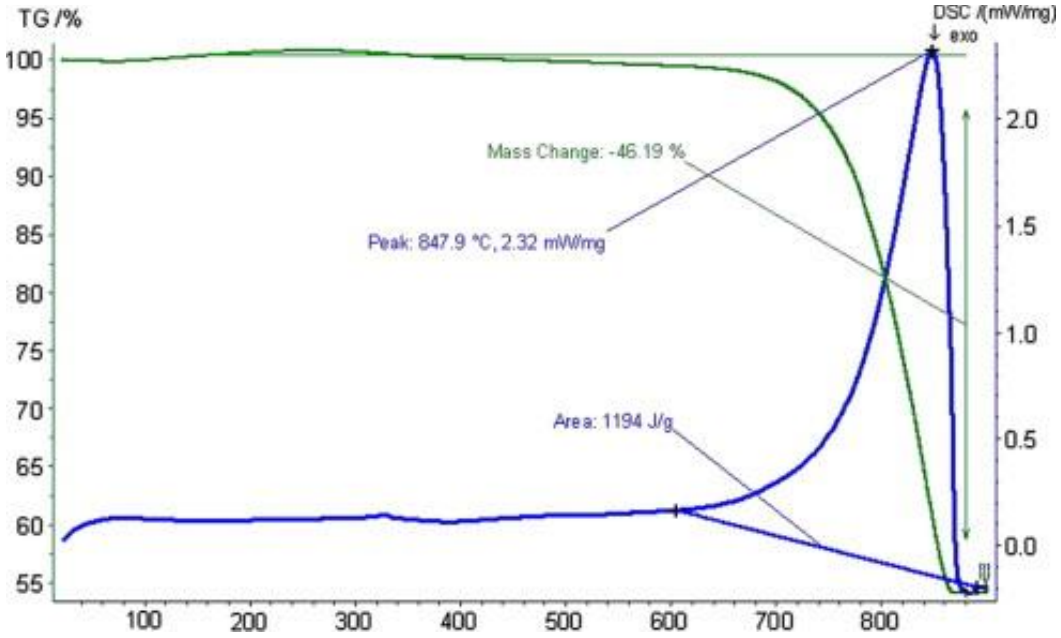

Figure 2.7: DSC-TGA curves of nanoeggshell powder (Mosaddegh, 2013)

DSC provides information about the thermal stability, phase transition, melting points, and crystallization temperatures. DSC is also used to determine the enthalpy changes and specific heat of a material. The heat flow signal is determined internally from the temperature difference between sample and reference material (Aniolek *et al.*, 2021). DSC provides quantitative and qualitative data on changes in a material's physical and chemical properties induced by endothermic and exothermic reactions (Jacob, 2019).

Mosaddegh *et al.*, (2013), observed exothermic peaks with $\Delta H_f° = 1194$ J/g in the DSC analysis of the eggshell nanocatalyst, which was caused by the evolution of carbon dioxide. The physisorbed H_2O evaporates from the material surface, resulting in a weight loss of less than 1.3% at 600 °C. At a weight loss of 46.2% and full calcination, which occurred between 600 and 847 °C, a phase change was caused by the breakdown of $CaCO_3$ to CO_2, and CaO was formed.

Bet-Moushoul *et al.* (2016) studied the decomposition and phase transition of CaO-based materials using DSC analysis. This was realized by only one noticeable step of weight loss of ~ 45–50 % between ~ 550–850 ºC. Since the samples of eggshells decomposed at ~ 700 ºC to form $CaCO_3$ to CaO.

The advantages of DSC include: DSC, when used with TG, allows simultaneous measurements of heat flow and mass changes, enabling comprehensive analysis of thermal events and mass changes. It offers detailed phase transition information, identifies polymorphic presence, quantifies enthalpy changes, and aids in calorimetric analysis, assessing thermal stability, and complementing TG data. The main disadvantage of DSC is the interpretation of results that are often tricky in the transitions temperature range for different materials since they often overlap. Therefore, experience is required to handle cases where the transition temperature overlap. In addition, DSC analysis involves sample preparation and requires appropriate reference material (Klancnik *et al*., 2010).

2.6.5. X-Ray Spectrometry

X-ray spectroscopy is an optical technique used to identify and quantify materials in the wavelengths of particles in the X-ray region of the electromagnetic spectrum (0.1-1 Å) (Susi,

2021). Figure 2.8 is a schematic diagrammatic explanation of how an electron is excited using incident high energy X -rays.

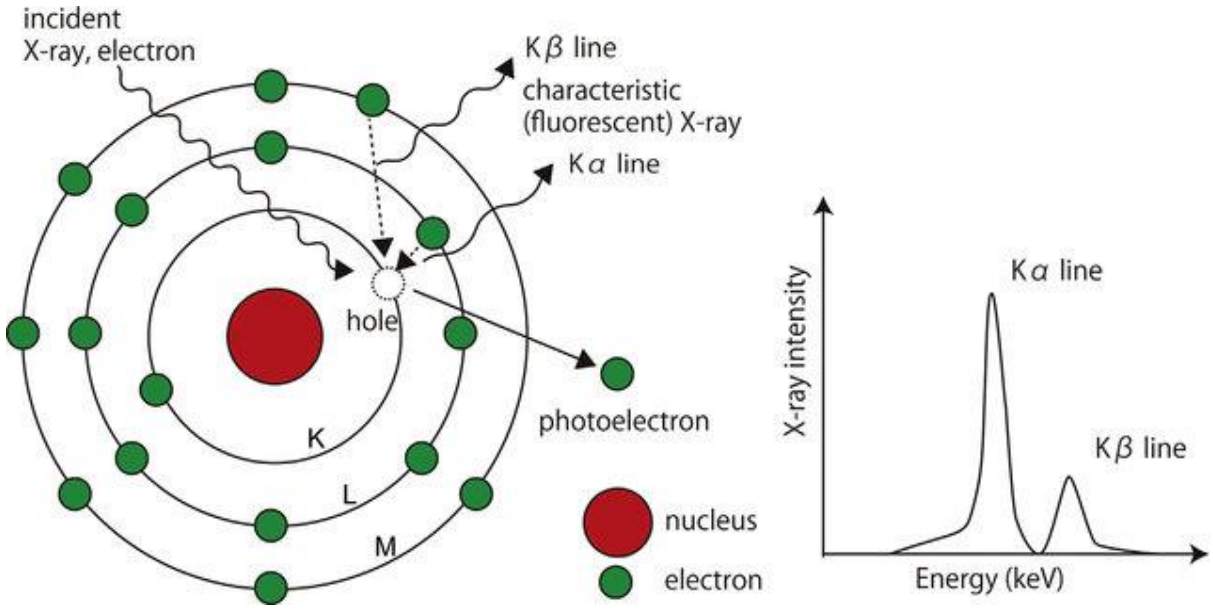

Figure 2.8: The mechanism of characteristic X-ray generation (Uo *et al.*, 2015)

X-rays are created when accelerated electrons collide with tungsten nuclei in the anode tube. An outer shell electron enters the open inner shell after the electron is discharged. It then emits a characteristic X-ray beam with an energy equal to the difference between the energy levels of the outer and inner envelopes.

These X-rays can be used to examine the smallest, most complicated structures that can be found in a wide range of materials (Uo *et al.*, 205).

The structural integrity, morphological, chemical, and elemental properties of a material can all be studied using X-ray techniques, which include analysis of X-ray emission, absorption, scattering, fluorescence, and diffraction properties (Fetisov, 2020). X-ray diffraction (XRD) and X-ray

fluorescence (XRF) spectrometry are the two most advantageous X-ray spectroscopy techniques (Igwebike-ossi, 2017).

2.6.5.1. X-ray Powder Diffraction

X-ray diffraction (XRD) is a non-destructive technique for studying the physical properties, chemical composition, and crystallographic structure of samples. It provides unique data for analysis, including crystal structure determination, phase identification, crystallinity and amorphous content, grain size and microstructure, strain and stress analysis, among others (Siddiqui *et al.*, 2015). Instead of using X-ray fluorescence (XRF) or other spectroscopic methods to identify elements, crystalline material phases, units of measurement, and particle size are determined using X-ray diffraction analysis (Zhao *et al.*, 2019).

In X-ray diffraction (XRD) analysis, samples are analyzed by exposing them to a collimated X-ray beam at a specific angle known as the Bragg angle. The Bragg angle is crucial in maximizing the constructive interference of X-rays diffracted by the crystal lattice of the sample. X-ray diffraction is used to study crystal structures and atomic spacing. Constructive interference between monochromatic X-rays and a crystalline sample is the basis of X-ray diffraction. X-rays are produced by a cathode ray tube, which is then focused and collimated to produce monochromatic radiation. XRD analysis uses collimated X-ray beam to create a diffraction pattern, influenced by the angle of diffraction 2θ, to understand the material's crystallographic properties. It shows the qualitative and quantitative analyses using an international computer database. The analysis involves qualitative methods like phase identification, crystal structure determination, polymorphism, amorphous content, and texture, while quantitative methods include crystallite size, strain, phase quantification, and stress and texture analysis.

Figure 2.9 shows Bragg's law of X-ray diffraction.

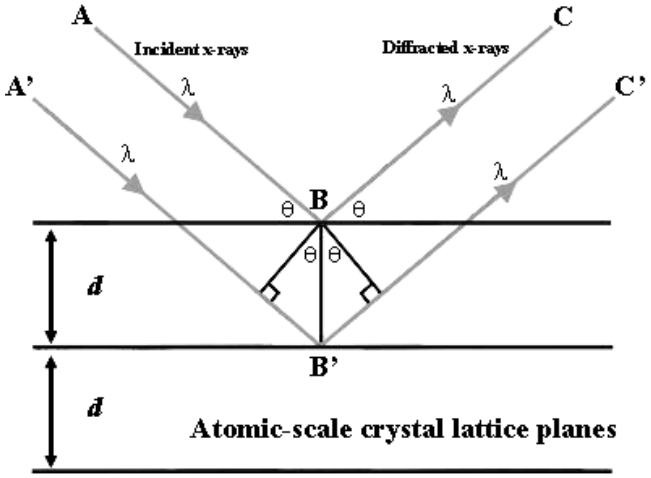

Figure 2.9: Bragg's law of X-ray diffraction (Sharmin, 2016)

Copper X-ray tubes are used for X-ray diffraction of the monochromatic X-ray radiations to analyze inorganic substances. These monochromatic X-rays radiations cause X-ray diffractions, leading to kα radiation used in X-ray instruments. They have energy with a wavelength of 1.5406 Å meanwhile, all other radiations are removed by a nickel filter (Fetisov, 2020). When conditions are right, the collimated X-ray beam interacts with the materials to produce constructive interference and a diffracted beam as represented in Equation 2.2.

$n\lambda = 2d\sin\theta$ …… Equation 2.2.

Where, λ is the wavelength of the incident X-rays, d is the distance between the planes, and θ is the diffraction angle, where n is an integer. This law compares the lattice spacing and diffraction angle of a crystalline structure to the wavelength of electromagnetic radiation. By scanning the material using various 2θ angles, diffracted X-rays are found, processed, and analyzed (Lavina *et al.*, 2014). In X-ray diffraction (XRD), the diffraction peaks are transformed into d-spacings. These d-spacing values are then compared against established reference patterns to identify the

corresponding element (Hansford *et al.*, 2017). The average particle size (D) of a substance can be determined using the Scherrer formula, Equation 2.3.

$$D = \frac{K\lambda}{FWHM\cos\theta}$$ …….. Equation 2.3

Where: K is the Scherrer constant, FWHM is the full width of the reflection peaks at half maximum with the same maximum intensity in the diffraction pattern, λ is the wavelength of the x-rays, and θ is their diffraction angle. The Scherrer constant (K) in the formula, which is predicted to be 0.94 for spherical solids, accounts for the shape of the particle (Valério & Morelhão, 2019).

According to Asri *et al.*, (2017) the composition of non-calcined eggshells consisted mainly of $CaCO_3$ with a concentration of ~ 94%. When the eggshell was calcined at 900 °C, $CaCO_3$ completely decomposed into CaO and CO_2 gas. The crystalline structure of the nanocatalyst and the presence of CaO were demonstrated by the narrow and highly intense peaks of the calcined catalyst.

Ayodeji *et al.*, (2018) observed that the incinerated eggshells' narrow and intense high peaks at 1000 °C show how the catalyst's crystalline structure mainly contained CaO as the active ingredient

One of the advantages of X-ray diffraction is that it is a fast and effective method for studying unidentified organic and inorganic compounds. In addition, it requires little sample preparation, it makes identification of unit cells easy, and XRD measuring devices are widely available (Kovalev *et al.*, 2017).

Disadvantages of XRD samples include the fact that samples should be homogeneous for better analysis and analysis cannot work without access to standard reference data. Pattern indexing can be challenging for non-isometric crystalline samples to identify unit cells (Kovalev *et al.*, 2017).

2.6.5.2. X-Ray Fluorescence Spectroscopy (XRF)

An X-ray spectrochemical analysis method called X-ray fluorescence analysis examines elements present in solid samples. Figure 2.10. shows how XRF spectroscopy works.

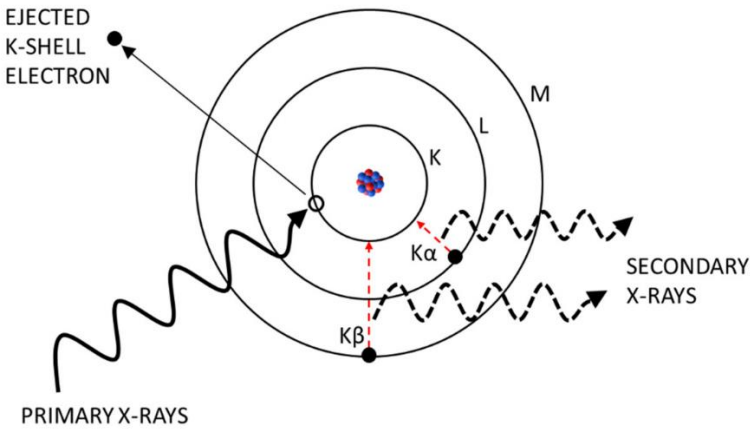

Figure 2.10. Physical mechanisms within an atom for X-ray-fluorescence (Horf *et al.*, 2021).

It is comparable to optical emission and atomic absorption spectrometry. Electrons in the inner orbitals in the sample are excited by incident X-rays, causing the ejection of electrons in the inner shell. For example, when an electron from the K shell is pushed out, either an electron from the L shell or an electron from the M shell fills the hole. As it happens, electron transitions generate the most pronounced emissions from L to K shells (K_α) and M to K shells (K_β) of the atom the elements (Duarte *et al.*, 2018)**.** Each element is unique, giving characteristic emission spectra, leading to qualitatively and quantitatively analysis of elements (Yao *et al.*, 2015). A semiconductor detector

examines the X-ray fluorescence emission of the sample. When analyzing the radiation, the detector distinguishes between photon yield and energy. Each photon entering the detector is counted and then sorted by energy (Schramm, 2016). Computer-based multichannel analyzers acquire, display spectra, and perform data analysis. The measured spectrum shows peaks characteristic of the chemical elements present in the sample (Rodrigues *et al.,* 2018).

Ahmad *et al.,* (2015) studied the XRF analysis of raw eggshells and incinerated eggshells. They observed that CaO was the major element in the eggshells after incineration.

XRF instrument has the following advantages: it is non-destructive and does not affect the quality of the analyte; it is a quick method of analysis. However, XRF instruments face limitations in analyzing higher elements such as beryllium (Chebakova *et al.,* 2021).

2.6.6. FTIR analysis of the synthesized eggshells nanocatalyst

FTIR spectroscopy uses the absorption of infra red light buy amterials to identify the type of chemical bonds and structure within a sample. This method can be used to characterize organic, polymeric, and occasionally inorganic materials (Baker *et al.,* 2015).

FTIR spectroscopy is a powerful technique for analyzing materials by measuring and interpreting vibrations associated with molecular bonds, providing insights into a sample's functional groups and structure. It records between 4000 and 400 cm^{-1} depending on the material (Munajad *et al.,* 2018).

Pornchai *et al.,* (2016) found a broad transmission band at around 2863 cm^{-1} in the FTIR spectra of uncalcined and calcium carbonate-treated eggshells associated with raw eggshells. This was caused by the oscillation of the OH stretch. At 2360 cm^{-1} there was a weak band caused by the C=O bonds caused by carbonate ions. There were prominent infrared bands at 710 cm^{-1}

representing a Ca-O bond and other infrared bands at 1398 cm $^{-1}$ and 872 cm $^{-1}$ representing C - O stretching and bending of CO_3^{-2} ions.

Figure 2.11 shows the FTIR spectra of calcined eggshells.

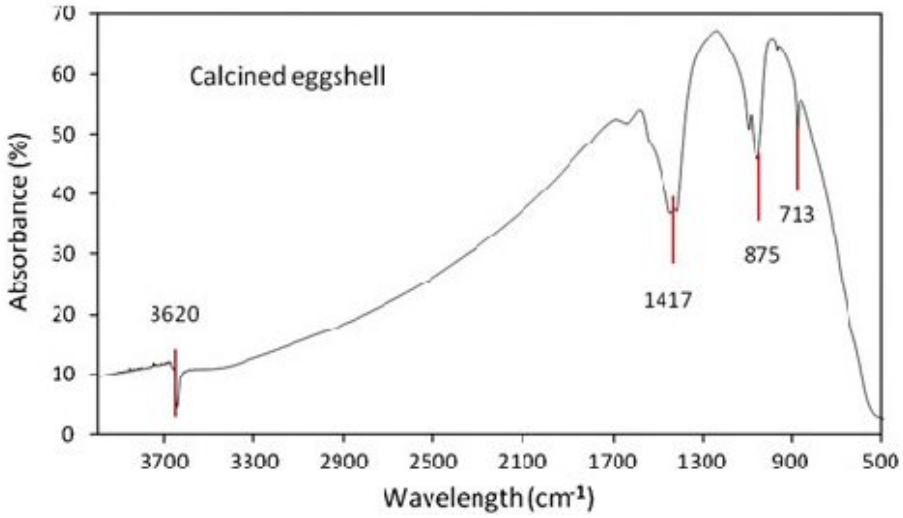

Figure 2.11: FTIR spectra of calcined eggshell (Carvalho *et al.*, 2011).

The advantages of FTIR spectroscopy include the following: it is a highly sensitive and rapid method. Comparing this spectroscopy to the dispersive instrument, it provides a better signal-to-noise ratio. FTIR spectroscopy can analyze gases, solids as well as liquids. FTIR requires no external calibration and provides accurate results. In addition, FTIR is a non-destructive method that can analyze both organic and inorganic substances (El Fels *et al.*, 2015). The disadvantage of FTIR instruments is that they only have a single beam, in contrast to dispersive instruments which often have two beams. While dispersive instruments often have two beams (El Fels *et al.*, 2015).

2.6.7. Electron microscopy

Electron microscopes are powerful tools useful in studying materials. They are versatile, exceptionally high spatial resolution and are valuable for many applications (Möckl & Moerner,

2020). Then major types of electron microscopes used in imaging incude; Transmission Electron Microscope (TEM) and Scanning Electron Microscope (SEM) (Ul-Hamid, 2018).

2.6.7.1. Scanning Electron Microscopy (SEM)

In SEM analysis, the electron beam is scanned across the surface of the sample in a grid pattern, and the signals produced by the interactions are detected and used to produce an image. The resulting SEM images provide detailed information about the topography, composition and morphology of the sample at high magnification (Venkateshaiah *et al.*, 2020).

Singh and Verma (2020) used SEM to study the morphology of CaO that was generated from chicken and duck eggshells following calcination at various temperatures of 800, 900, and 1000 °C. The results showed that the grains of CaO were asymmetrical and of varying sizes at different temperatures. At higher temperatures, the particles agglomerated.

The advantages of an SEM include its ability to give detailed topographical imaging, as well as versatile information from several detectors like X-ray and Electron Backscatter Diffraction (EBSD). SEM is user-friendly, digitally outputs data, and requires quick preparation, making it an attractive tool for research (Choudhary & Ka, 2017).

Disadvantages of a scanning electron microscope, on the other hand, include its high cost, size, and the need for an environment free from electromagnetic, magnetic, and vibrational disturbances. To control the temperature of the SEM machine, the operation also involves maintaining constant voltage, currents to electromagnetic coils, and cold-water circulation (Choudhary & ka, 2017).

2.6.7.2. Energy Dispersive X-ray (EDX) Spectroscopy

The Energy Dispersive X-ray spectroscopy is used for examining the elemental makeup of a material (Ellingham *et al.*, 2018). The Scanning Electron Microscope (SEM) or Transmission Electron Microscope (TEM) may incorporate the EDX spectroscope (Scimeca *et al.*, 2018) or a Transmission Electron Microscope (TEM).

2.6.7.3. EDX elemental analysis

Elemental mapping extracts elemental composition data for a cross-sectional area of a sample, while the EDX spectrum offers information on the elements and their quantities in a sample. Figure 2.12 illustrates an EDX spectrum.

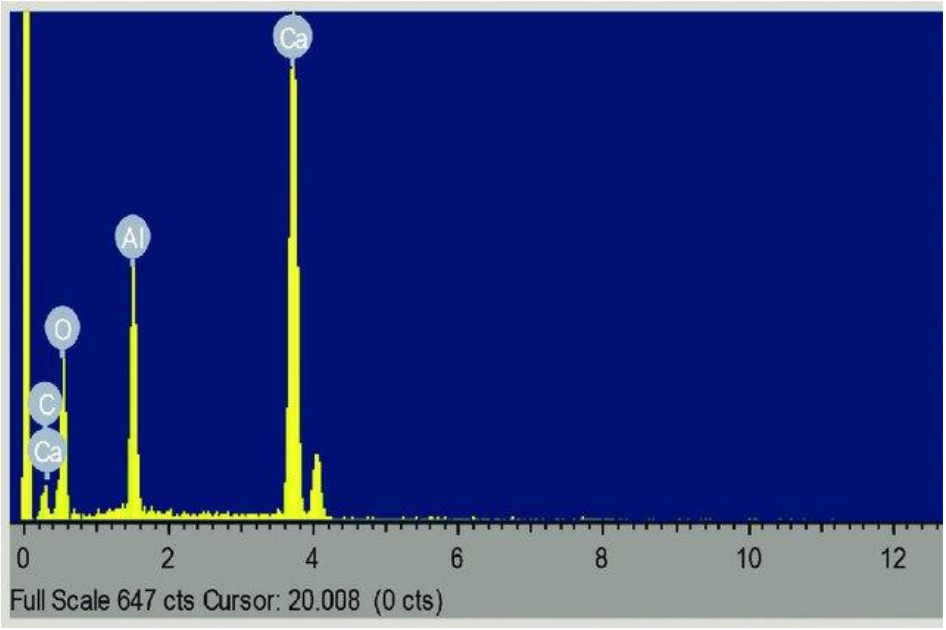

Figure 2.12. **EDX spectrum for 80% CaO/Al_2O_3 catalyst** (Rabiu *et al.*, 2018)

Peaks in the EDX spectrum correspond to the energies where the elements Ca, C, Al, and O are found. The concentration of an element in a substance correlates with the height of a spectral peak (Mourdikoudis *et al.*, 2018). Polat and Sayan (2020) studied ultrasound-assisted eggshell extract-

mediated polymorphic transformation of calcium carbonate. Using the EDX spectrum, they observed that mainly C, O, Na, Mg, Ca, and Si were detected on the surface of the eggshell sample. The EDX technology has benefits such as quick elemental analysis of tiny features. Additionally, it has a high count rate at low kV and beam current and can provide a two-dimensional elemental mapping and semi-quantitative analysis with standards (Mourdikoudis *et al.*, 2018). One of its key drawbacks is that EDX frequently involves destructive analysis. As a result, it features a low peak-to-background ratio and poor peak energy resolution.

2.6.7.4. Transmission Electron Microscopy (TEM)

TEM uses a broad beam of electrons to create photographs of the internal structure of a material. Details may include morphology, composition, and crystal structure (Fischer *et al.*, 2013), size, shape, and distribution of the particles within a material (Venkateshaiah *et al.*, 2020). The illuminating system, the objective lens, and the imaging system are the three main parts of the TEM instrument. The electron gun and condenser lenses make up the illumination system. Each TEM has an electron gun that generates electrons from the cathode and emits them to illuminate the sample at the anode. The potential difference of up to 50 keV accelerates the electrons along the column to the sample to create an electron beam. In the TEM system, these electrons are bundled into a narrow beam by electromagnetic electron lenses and directed onto the test object. Most of the electron beams pass through the sample. When the unscattered electrons hit a fluorescent screen at the base of the microscope, the image of the sample is created, which shows its individual components in varying degrees of blackening depending on their density. This image can be seen immediately or captured with a camera.

Mosaddegh *et al.,* (2013) examined the TEM image of 2-aminochromenes synthesized from eggshell nanopowders. They observed that the nanocrystals had high porosity and surface area with an average size of 50 nm.

Pandit & Fulekar (2017) studied the CaO nanocatalyst obtained from waste eggshells using TEM. They observed that the particles were spherical with an average particle size of around 75 nm, and this result was consistent with the results of the XRD study.

Gaurav *et al.,* (2021) studied the TEM image of a CaO nanocatalyst prepared from chicken eggshell waste. They found that the particles had a higher specific surface area, were cubic in shape, and had an average particle size of 43 nm.

TEM analysis offers high magnification, precise structural information, and surface properties, shape, size, and structure in various scientific, educational, and industrial settings with proper training (Anka, 2018).

The disadvantages of TEM spectroscopy include the large size and expensive cost of TEMs. Sample preparation is time-consuming and can lead to artefacts due to instrumentation, image conditions, and sample nature. It also only accepts electron transparent samples, and both its operation and analysis require special training. For TEMs, special caging, maintenance, and black-and-white images are also required (Anka, 2018).

2.6.8. Surface area, pore diameter and volume characteristics

The surface area, pore volume, and pore diameter of material are crucial characteristics that have a big impact on how well they function in different applications. Surface area is calculated by dividing the entire surface area of a material by its mass or volume. This feature is essential for a number of processes, such as catalysis, adsorption, and gas separations because it increases the

amount of surface area available for chemical reactions or molecular adsorption (Gorgolis & Galiotis, 2017).

The "pore diameter" of a substance refers to the size of its pores. The size of the pores can affect the ability the material to adsorb substances as well as the passage of molecules or ions through them. Larger molecules can pass through pores with a bigger diameter, whereas larger molecules cannot flow through pores with a smaller diameter (Cychosz & Thommes, 2018).

"Pore volume" refers to the total volume of holes or gaps in a substance. In applications like gas storage, a greater pore volume can provide more space for gas molecules to be stored (Cychosz & Thommes, 2018).

Surface area, pore diameter, and volume characteristics of a material are related and can influence one another. For instance, a substance with small pore widths may have a bigger surface area if it contains a large number of microscopic holes. Similarly to this, a substance with a higher pore volume may also have a higher surface area since there are more connected pores present. These qualities can be measured using a variety of techniques, including nitrogen physisorption, gas adsorption, and mercury porosimetry. The process of measuring the quantity of gas adsorbed as a function of pressure is known as nitrogen physisorption, which includes the adsorption of nitrogen gas onto the surface of a material. Using this method, measures the surface area, pore volume, pore size, and pore distribution of material. The BET technique is commonly used to examine the data from nitrogen physisorption, and it is predicated on the idea that the adsorbed gas forms a monolayer on the surface of the material. Physical adsorption and desorption isotherms for nitrogen at 77 K or argon at 87 K are widely used for material characterization (Cychosz & Thommes, 2018). In Brunauer-Emmett-Teller (BET) analysis, liquid nitrogen gas is recommended

because it is readily available in high purity and interacts strongly with most solid particles. Very low surface area materials can use argon or krypton instead (Gierszal *et al.*, 2013). A partial vacuum is created by gradually releasing known amounts of nitrogen gas into the pores of the sample to achieve relative pressures below atmospheric levels.

After the saturation point, no further adsorption may take place, regardless of the pressure increase. Pressure fluctuations during the adsorption process are tracked with pressure transducers that are incredibly precise and accurate. After the adsorption layers have developed, the gas is heated by the sample surface. The surface of the substance releases the adsorbed nitrogen and the volume is calculated (Giraldo *et al.*, 2019). The surface area is calculated according to the Brunauer-Emmett-Teller (BET) method, the pore diameter distribution according to the Barrett-Joiner-Halenda (BJH) hypothesis (Xiong *et al.*, 2016).

2.6.8.1. Brunauer-Emmett-Teller (BET) surface area analysis

The automated process known as BET analysis may determine the specific surface area of materials (Anovitz & Cole, 2015). The results obtained are represented by a BET isotherm plotting the amount of gas adsorbed versus the relative pressure. From the plot, the surface area of the catalyst sample can be determined from the isotherm data using BET Equation 2.4.

$$\frac{P}{(P_\circ - P)V} = \frac{1}{CV_m} + \frac{C-1}{CV_m}\left(\frac{P}{P_\circ}\right) \text{.....Equation 2.4}$$

Where V_m is the monolayer capacity, which is the volume of gas adsorbed at standard temperature and pressure (STP), C is constant, and V is the weight of nitrogen adsorbed at a given relative pressure $\left(\frac{P}{P_\circ}\right)$ (Hwang & Barron, 2011).

A plot of $\frac{1}{V\left[\left(\frac{P_0}{P}-1\right)\right]}$ against $\frac{P}{P_o}$ gives; The y intercept as, $\frac{1}{cV_{mono}}$, the slope is $\frac{(c-1)}{cV_{mono}}$, and

$C = \exp\left(\frac{q_1 - q_L}{RT}\right)$…….Equation 2.5.

BET plot presented in Figure 2.13 below.

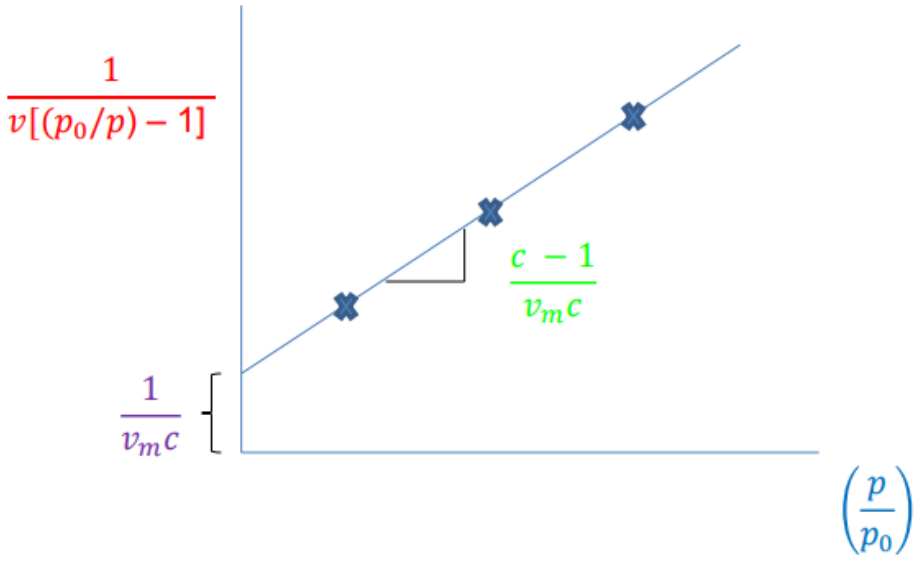

Figure 2.13: BET Surface Area Plot (Lundstedt, 2019)**.**

The value of C serves as a measure of how strongly the adsorbent and adsorbate interact. Where q_1 exactly is the heat of adsorption of the first monolayers and q_L the heat of liquefaction (condensation) of the adsorbates. The temperatures of physisorption vary depending on the values of C and q_L, heats of physisorption are < 10 kcal mol. Standard temperature and pressure (STP) is defined as 273 K and 760 mm Hg (Paz-Ferreiro *et al.*, 2013).

Peng *et al.*, (2018) examined eggshell waste as a basic catalyst for the production of biodiesel using BET. They found that the specific surface area of the catalyst was 0.7334 m^2/g.

2.6.8.2. Pore volume and average pore radius

The amount of vapor adsorbed at a relative pressure close to unity is used to calculate the total pore volume, assuming that the pores are filled with a liquid adsorbate ($\frac{P}{P_\circ} \approx 1$). This equation translates the volume of liquid nitrogen contained in the pores (V_{liq}) to the volume of nitrogen adsorbed (V_{ads}):

$$V_{liq} = \frac{P_a V_{ads} V_m}{RT} \quad \text{……Equation 2.6}$$

P_a is the atmospheric pressure, T is the atmospheric temperature, V_m is the molar volume of the liquid adsorbates (34.7 cm^3/mol for nitrogen) and R is the universal gas constant (Anovitz & Cole, 2015).

The average pore diameter is inferred from the pore volume because pores that would not fill below ($\frac{P}{P_\circ} \approx 1$) contribute insignificantly to the overall pore volume. For a cylindrical pore, for instance:

$$r_p = \frac{2V_{liq}}{S} \quad \text{……Eqaution 2.7}$$

Where; S – BET surface area (Anovitz & Cole, 2015)

Oulego *et al.,* (2020) studied the BET analysis of eggshell-supported catalysts. They found that the specific surface area (BET area) and pore volume of the calcined eggshell were 4 m^2/g and 0.059 cm^3/g, respectively.

Pandit & Fulekar, (2017) studied the synthesized waste eggshells nanoCaO and observed that it had a specific surface area of 16.4 m^2g^{-1}.

The BET adsorption isotherm may effectively explain the many adsorption isotherm types. This equation only works when the ratio $\frac{P}{P_{\circ}}$ lies between 0.05 - 0.35 (Mikšík *et al.*, 2020). Deviations from linearity begin to occur outside of this range. Furthermore, the gas adsorbate having liquid characteristics is a fundamental presumption of the BET isotherm. This is only accurate, though, when the critical temperature is high. But permanent gases with low critical temperatures include hydrogen, oxygen, and nitrogen, among others (Kim *et al.*, 2016).

2.6.8.3. Barrett-Joyner-Halenda (BJH) method

The BJH method is used to determine the pore diameter of materials. It is based on a study of the desorption branch of the isotherm derived from experiments on the physisorption of nitrogen or other gases. With this technique, the desorption isotherms at the boiling point of N_2 are compared with the distribution of pore volume and area. The gas phase and adsorbate equilibrium are calculated from the desorption layer thickness on the pore walls and the capillary evaporation in the inner capillary volume. This assumption treats each individual pore as an open, cylindrical structure that responds to changes in relative pressure (Mukhtar *et al.*, 2020).

2.6.8.4. Pore size

The BJH method assumes that the pores in the material are cylindrical and that the pore size distribution can be obtained from the desorption branch of the isotherm. The desorption branch is the part of the isotherm where the amount of gas desorbed from the material decreases as the pressure decreases. This is because the smaller pores in the material are filled first, and as the pressure decreases, the gas is desorbed from the larger pores.

Calculations the size of the mesopore diameter assumed of cylindrical pore geometry and the Kelvin Equation 2.8:

$$r_k = \frac{-2\gamma V_m}{RT \ln\left(\frac{P}{P_\circ}\right)} \quad \text{……Equation 2.8}$$

The Kelvin equation is used to calculate the pore diameter distribution (PSD) assuming cylindrical pores and adsorption isotherms. where P_0 is the vapor pressure of the same liquid at the surface of the material, r_k is the radius of the drop, Vm is the gas molar volume, γ is the surface tension, R is the gas constant, T is the temperature in Kelvin, and P relates to the vapor pressure of the curvature of the liquid-vapor interface (P)..

The term r_k refers to the radius at which condensation took place in multilayer adsorption. It depends on the statistical thickness of the adsorbed coating and the pore radius. Several thickness formulas, including the t-plot provided by the De Boer equation, can be used to determine the thickness of the adsorbed film. Thickness equations, such as the t-diagram, are used to determine the thickness of the adsorbed film. For nitrogen as adsorbate:

$$r_k\left(\overset{\circ}{A}\right) = \frac{4.15}{\log\left(\frac{P_\circ}{P}\right)} \quad \text{……..Equation 2.9}$$

$$r_p = r_k + t \quad \text{…….. Equation 2.10,}$$

Where $t = 3.15\left(\frac{V_{ads}}{V_m}\right)$ or from de Boer equation:

$$t\left(\overset{0}{A}\right) = \left[\frac{13.99}{\log\left(\frac{P_0}{P}\right) + 0.034}\right]^{\frac{1}{2}} \quad \text{……. Equation 2.11}$$

Where; r_p is the true pore radius and t is the thickness of the adsorbed layer. For a non-porous solid of the same composition as the material, V_m is the volume of nitrogen adsorbed upon completion of a monolayer and V_{ads} is the volume of nitrogen adsorbed at a given relative pressure.

Although the BJH method has been employed for conventional mesopore pore diameter distribution (PSD) analysis, narrow mesopores cannot be reliably identified using this method. The BJH technique underestimates pores with a width of less than 10 nm by ~ 20 - 30% (Landers *et al.*, 2013). To circumvent the limitations of the Kelvin equations, various microscopic models including molecular simulation (Monte Carlo simulation) and density functional theory (DFT) are used to accurately calculate the size of micropores and small mesopores (Medina-Rodriguez & Alvarado, 2021). The DFT model offers numerous approaches for different pore architectures and accounts for the interaction potentials for fluid-adsorbent and fluid-fluid interactions, resulting in a pore diameter distribution calculation that is more accurate and versatile than the Kevin equation (Landers *et al.*, 2013).

2.6.8.5. Pore size Distribution (PSD)

BJH pore size distribution is used to analyze the pore size distribution of porous materials. The BJH equation is used to obtain the pore size distribution from the desorption branch of a nitrogen physisorption isotherm. Since the BJH equation derived from the Kelvin equation assumes cylindrical pores and a narrow pore size distribution.

Figure 2.14 displays a typical curve for the distribution of pore sizes.

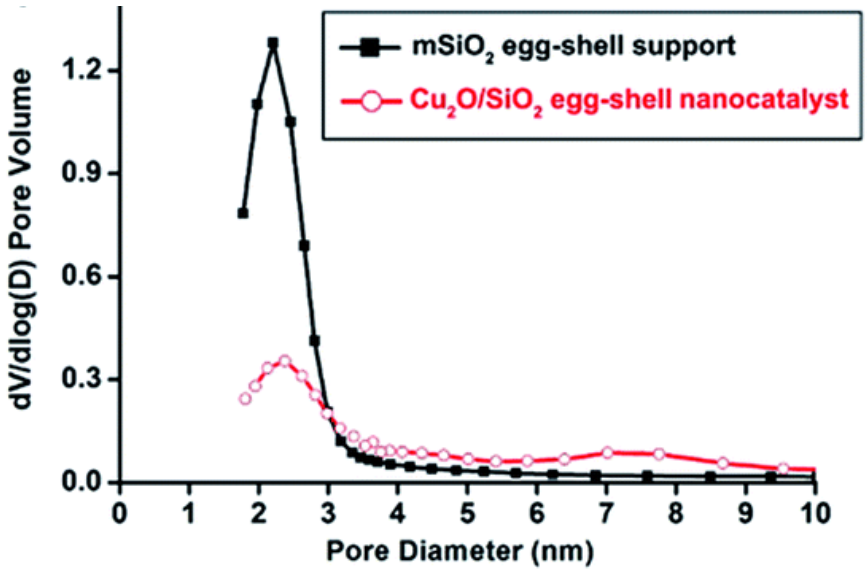

Figure 2.14: **dV/d(logD) representations of PSD for two samples of the $mSiO_2$ egg-shell support and the Cu_2O/SiO_2 egg-shell nanocatalyst** (Kim *et al.*, 2018)

The BJH equation 2.12 is:

$$\frac{dV}{dD} = V \times \left(\frac{1}{\rho}\right) \times \left(\frac{dP}{dD}\right) \times \left(\frac{1}{1+e^{\left(\frac{4\sigma V}{D\rho RT}\right)}}\right) \quad \text{..... Equation 2.12}$$

where; $\frac{dV}{dD}$ is the differential pore volume with respect to pore diameter, V is the cumulative pore volume, ρ is the density of nitrogen at the temperature of the measurement, $\frac{dP}{dD}$ is the differential pressure with respect to pore diameter, σ is the surface tension of the nitrogen, R is the gas constant and T is the absolute temperature

The BJH equation is used to determine the pore diameter distribution by integrating the differential pore volume with respect to the pore diameter. As a result, the differential pore volume is plotted as a function of the pore diameter. It is important to note that the BJH equation assumes that all pore sizes have the same surface tension of nitrogen and that the pores are cylindrical. Since not all materials conform to these hypotheses, caution should be exercised in interpreting the resulting distribution of pore sizes (Li *et al.,* 2019). Various methods are used to represent PSD data. However, the most popular ones are $\frac{dV}{dD}$ and $\frac{dV}{d\log D}$. $\frac{dV}{dD}$ is the derivative pore volume normalized to the pore-diameter interval) and $\frac{dV}{d\log D}$ is the derivative pore volume normalized to the natural logarithm of the pore-diameter interval.

Kim *et al.,* (2018) examined the Cu_2O/SiO_2 eggshell nanocatalyst's total pore volume and found that it was 0.19 cm^3 g^{-1}, or around 54% of the original $mSiO_2$ eggshell support, which was 0.35 cm^3 g^{-1}. Due to the occupied copper oxide nanoparticle in the silica pore, the pore volume of the Cu_2O/SiO_2 eggshell nanocatalyst has significantly decreased. The initial $mSiO_2$ eggshell support and Cu_2O/SiO_2 eggshell nanocatalyst both had pore sizes that ranged between 2 and 3 nm. This demonstrated the size of the implanted Cu_2O crystallite.

The advantages of the BET and BJH techniques include the simultaneous acquisition of surface area and pore diameter data of an analyte, and secondly, the fact that it is a non-destructive method (Zhang *et al.,* 2015).

On the other hand, the disadvantage of the BET and BJH techniques is that the closed pores are not accessible through the material surface. Therefore, the gas adsorption technique cannot be used for their assessment (Zhang *et al.*, 2015).

2.7. Optimization of the production of biodiesel using the synthesized nanocatalyst

Most researchers follow classical experimental methods when optimizing experiments by changing one parameter while leaving other factors unchanged. But statistically designed experiments are a powerful tool for improving the efficiency of experimental results (Jankovic *et al.*, 2021). Several statistical analysis design expert softwares are applied to maximize biodiesel production yield. These softwares include, Design Expert 11, Mini Tab, and Design-Expert Stat-Ease 6.0.8 among others. Using these sofwates help to decrease the number of experiments, speeding up and improving research (Kandar & Akil, 2016).

Optimizing the production of biodiesel can be achieved using the Design of Experiments (DOE). DOE is a statistical technique in which the input factors of a process or system are systematically varied to determine their effect on the output response. In the context of biodiesel production, the input factors can include the type and quantity of the starting material, the type of catalyst and catalyst loading, the reaction temperature and time, and the ratio of the reactants. Different designs of experiments (DOE) are available depending on the experiment's objectives and the current state of knowledge about the experimental environment. The DOEs fall into the following categories: Fractional & full factorial, Screening, and Response Surface (Dangat *et al.*, 2021; Kandar & Akil, 2016).

2.7.1. Response Surface Methodology (RSM)

Response Surface Methodology (RSM) using Central Composite Design (CCD) can be a useful tool to optimize biodiesel production. The type of feedstock, type and amount of catalyst, alcohol to oil molar ratio, reaction time, and reaction temperature are some of the variables that can affect the quality and production of biodiesel. RSM with CCD can be used to methodically study the effects of these variables and find the ideal conditions for biodiesel production. RSM minimizes the number of experiments required to analyze the interaction between parameters, it also reduces chemical consumption, and analytical works (Mäkelä, 2017).

RSM is the most advantageous technique in statistical analysis to optimize biodiesel because it is based on a linear function. Constructing a 3-D response surface and contour plot using experimental data allows this technique to look at the interactions between process factors (Adepoju *et al.*, 2018). With the fewest possible simulations, this experimental design methodology delivers inference while providing an effective means of quantifying uncertainty (Mourabet *et al.*, 2017). The Central Composite Design (CCD) and Box-Behnken design are two significant classes of RSM with distinct architectures. Therefore, selecting an experimental design is crucial before using RSM since it determines which experiment will be used in the study area (Sarrai *et al.*, 2016). The two favored RSM models are the first-order and second-order models these are explained using Equations 2.13 and 2.14;

$$Y = \beta_{\circ} \sum_{i=1}^{k} \beta_i X_i + \varepsilon. \text{ ……..Equation 2.13}$$

$$Y = \beta_{\circ} \sum_{i=1}^{k} \beta_i X_i + \sum_{i=1}^{k} \beta_{ii} X_i^2 + \sum_{i=1}^{k} \sum_{1 \neq j=1}^{k} \beta_{ij} X_i X_j . + \varepsilon \text{ …..Equation 2.14}$$

Where the symbols; Y denote the yield, $\beta_{\circ}$ is a constant, β_i is the slope factor, X_i is the linear effect factor, β_{ii} is the quadratic effect factor, X_j & β_{ij} are the interaction effect between the input components X_i and X_j and $\mathcal{E}$ is the residual factor. The first-order models are inadequate to represent authenticity due to functional relationships between independent variables.

The second-order model is the most commonly used RSM approximation polynomial model. The most common designs for the second-order model are the central composite, Doehlert, Box Behnken, and three-factorial (CCDs). Between these symmetric designs, there are differences in the experimental points used, the number of levels for the variables, and the number of runs and blocks (Chumuang & Punsuvon, 2017).

2.7.2. Central Composite Design

CCD is a type of response surface methodology (RSM) design commonly used to estimate the coefficients of a second-order polynomial model. CCD includes three types of design points, which include factorial points, axis points, and midpoints. The axial points are intermediate values spaced from the center, while the factorial points are a combination of the high and low levels of the input variables. The net error and the lack of model fit are usually estimated using the midpoints. CCD is essential for delivering data on the overall experimental error and the impact of the observed variables in a limited number of runs. However, level modifications might occasionally be complex because of star points and outside design (Ani *et al.*, 2019).

In general, three independent experimental runs that make up central composite designs often consist of multiple center points, 2^k or, (for greater values of k, 2^{k-f}), 2k axial points α away from

the center, and 2k points. Where; *k* is the number of independent variables and f is the number of factorial points.

Figure 2.15 illustrates the design for CCD with three factors and α star point.

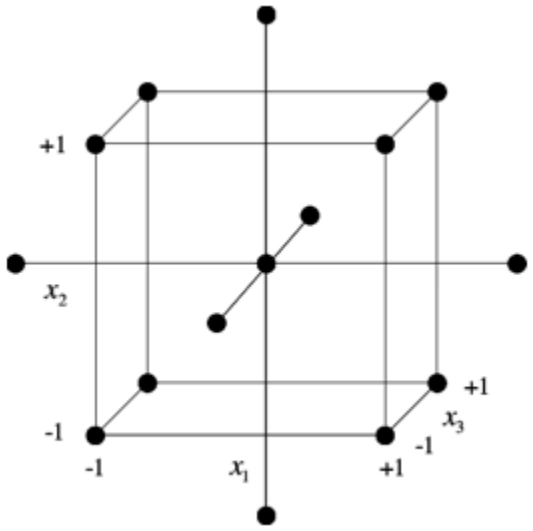

Figure 2.15: Graphical representation of a three-factor central composite design with

$\alpha = \sqrt[4]{nF}$ (Garroi *et al.*, 2008).

From $\alpha = \sqrt[4]{nF}$ = (Number of factorial runs)$^{1/4}$ = (2^k or 2^{k-f})^{¼}. If K (number of factors) =2. Then, (α) = (2^2)$^{1/4}$ = $2^{2/4}$ = $2^{1/2}$ = 1.414.

The midpoints define the experimental error and the reproducibility of the results. Any point evenly spaced from the design center has a constant model prediction variance, and the axial points are chosen to ensure rationality. The set of input variables and midpoints used determines the number of runs in a CCD. The second-order polynomial equation's resulting regression coefficient is very useful for the linear, interaction, and quadratic terms (Cortes *et al.*, 2018). The number of total experimental runs is calculated using Equation 2.15:

$N = 2^n + 2n + n_c$ ……..Equation 2.15

Where; N is the total number of experimental runs, n_c is the number of center points, 2n axial points, 2^n factorial runs and n is the number of independent variables (factors).

When n = 3, then $N = 2^3 + 2(3) + 6 = 8 + 6 + 6 = 20$

This showed that 20 experimental runs were needed for the modeling and optimization process, including 8 factorial runs, 6 axial runs, and 6 central runs (Bayuo *et al.,* 2020).

CCD is an advantageous design for RSM because it allows the estimation of the curvature of the response surfaces. The best input variables can then be identified to maximize or minimize the response variable. In addition, CCD is effective compared to other designs, including full factorial or fractional factorial designs, as it requires comparatively few experimental runs (Kasina *et al.*, 2020).

2.7.3. Production of biodiesel

Vegetable oils have been tested in the past in diesel engines. However, using lipids directly as fuel in diesel engines is not recommended. They adversely affect engine performance due to their large molecular mass, low volatility and high kinematic viscosity, causing further problems such as incomplete combustion, engine lockup and increased CO_2 emissions (Corsini *et al*., 2016; Zahan & Kano, 2018). Various methods such as transesterification, pyrolysis, microemulsions and dilution with petrodiesel can be used to produce biodiesel from vegetable oils (Bet-Moushoul *et al.*, 2016; Mishra & Goswami, 2018; Zahan & Kano, 2018).

Pyrolysis is the thermal decomposition of biomass from various sources and other waste products such as rubber tires in a vacuum to produce biodiesel, charcoal, and syngas (Callegari *et al.*, 2018). At temperatures above 500°C and atmospheric pressure, vegetable oil is converted into solid

charcoal, biodiesel, and gaseous products (Sarangi *et al.*, 2018). The conversion of lipids using thermal cracking is a promising biodiesel production technology. The process is very similar to the conventional petroleum refining process and the resulting bio-oil has properties similar to diesel fuel (Hoang *et al.*, 2013).

Thermal pyrolysis of vegetable oils has several benefits, including low processing costs, ease of use, minimal waste, and zero emissions (Gebremariam & Marchetti, 2017).

Disadvantages of pyrolysis include the equipment needed for the distillation to separate the different fractions. The equipment for thermal cracking and pyrolysis equipment is expensive, and the finished product contains sulfur, making it less environmentally friendly. In general, the elimination of oxygen during pyrolysis is an advantage in the production of biofuels such as biodiesel. As a result, biomass cannot undergo combustion to produce carbon dioxide and water because there is no oxygen. Instead, pyrolysis allows biomass to be broken down into liquid bio-oil, which can then be used to produce biodiesel (Gebremariam & Marchetti, 2017).

A microemulsion is an isotropic liquid mixture of oil, water, and surfactant that is thermodynamically stable. In fact, it is an optically isotropic equilibrium colloidal dispersion with liquid microstructure prepared from two immiscible liquids. To lower the high viscosity of vegetable oils, these immiscible liquids react with one or more ionic or nonionic amphiphiles in a mixture with a co-surfactant (Srivastava *et al.*, 2018). Though micro-emulsion reduces the viscosity of vegetable oils. However, issues including the buildup of a lot of carbon, incomplete combustion, and increased viscosity of lubricating lubricants could happen when the engine consumes fuels created by the microemulsion process over time (Ge *et al.*, 2017).

Dilution involves blending biodiesel with petrodiesel in varying proportions, reducing viscosity to produce a fuel that meets ASTM specifications. This makes it suitable for use in diesel engines (Mahmudul *et al.*, 2017). It can be beneficial to dilute biodiesel with petrodiesel in the production of biodiesel as it can save costs, improve emissions and promote sustainability. When considering using biodiesel-diesel mixtures, however, the disadvantages of this approach, such as reduced energy content and difficulties in storage stability, are considered (Negm *et al.*, 2017).

In general, transesterification is the most popular and economical process for making producing biodiesel on a large scale.

2.7.3.1. Transesterification reaction

A triglyceride from vegetable oil or fat, and an alcohol are mixed during the transesterification reaction in the presence of the right catalyst to create an ester (biodiesel) and glycerol combination (Gardy *et al.*, 2019; Silva *et al.*, 2011). The catalyst used in the transesterification of vegetable oils is either homogeneous, heterogeneous, or enzyme catalyst (Kayode & Hart, 2019). Homogeneous catalysts are used as soluble catalysts during the production of biodiesel. They include compounds such as sodium or potassium hydroxide or methoxide. They are widely used for industrial biodiesel production due to their high catalytic activity and low cost. However, homogeneous catalysts can also cause several side effects, including soap formation, and corrosion, and they require post-reaction neutralization and separation. Separating the homogeneous catalyst from the reaction mixture, despite the fact that the mixture is challenging, a homogeneous catalyst can speed up accelerate reactions more quickly faster than a heterogeneous one. The production of biodiesel by enzyme catalysis is a safe and promising substitute for the chemical process.

Enzymatic catalysts are biocatalysts that can reduce the energy demand in biodiesel production. This happens because the transesterification reaction takes place under moderate circumstances including low temperatures and pressures. High specificity and selectivity of enzymes can improve the quality of biodiesel and reduce the production of by-products. However, enzymatic catalysts can be expensive and may require additional measures such as immobilization to avoid their deactivation during the process. In comparison to acid-catalyzed transesterification, base-catalyzed transesterification is a faster (Talha & Sulaiman, 2016). An equation for the transesterification reaction is in Equation 2.16. below.

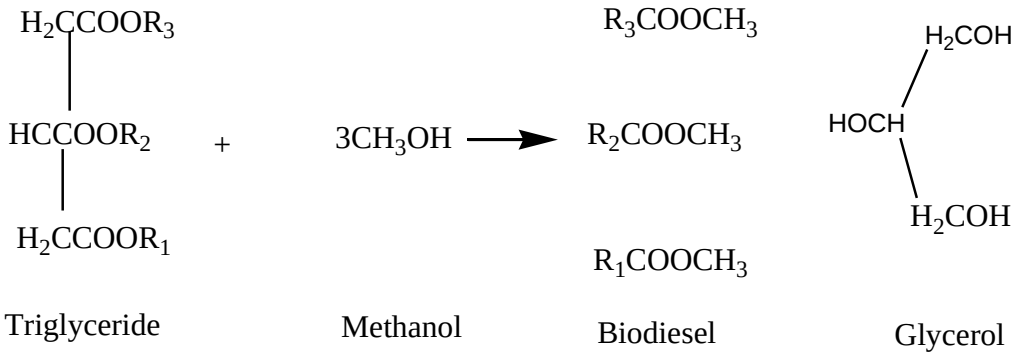

Equation 2.16.

The advantages of homogeneous catalysts include strong catalytic activity, which helps accelerate transesterification processes and increase biodiesel yield. They are a practical choice for producing industrial biodiesel because they are inexpensive and easily accessible. In general, they are easy to handle and store. In addition, they can be used in a straightforward, one-step transesterification reaction process that can reduce overall processing time and energy requirements. They also generate less waste and have high response selectivity (Nomanbhay & Ong, 2017). This method is useful in the large-scale production of biodiesel.

The disadvantage of a homogeneously catalyzed reaction is that it requires a feedstock that contains less water and free fatty acids (FFAs). Numerous separation and purification steps are required, which can have negative side effects, and a lot of NaOH is released into the wastewater (Zahan & Kano, 2018). Hence, researchers have recently focused on the use of heterogeneous catalysts in biodiesel production (Istadi *et al.*, 2015).

2.7.3.2. Preparation of biodiesel using waste derived heterogeneous catalyst

The heterogeneously catalyzed reaction is cheaper than homogeneously catalyzed reactions, because glycerol, a byproduct of transesterification, lowers production costs (Aransiola *et al.*, 2014), making biodiesel compete with petro-diesel fuels (Solomon *et al.,* 2018). The development of heterogeneous catalysts from low cost, waste, and naturally occurring materials for biodiesel production has been considered. This is because it offers a solution to the problems associated with homogeneous catalysts and enzymes (Yusuff *et al.*, 2017). In addition, the heterogeneous catalysts inhibit the formation of soaps and can be easily separated from the batch, and are easily reusable (Talha & Sulaiman, 2016). The presence of alkaline earth metal oxide in a heterogeneous catalyst also increases the strength of the basic sites (Jamil *et al.*, 2017). These sites have a significant positive impact on their catalytic performance.

Habte *et al.,* (2019) studied the thermal stability of nano-CaO derived from waste eggshell by sol-gel method using TGA. They found that CaO is a significant quantity in the synthesized nanomaterial, with a composition of ~ 86.93%.

Tahvildari *et al.,* (2015) studied CaO and MgO heterogenic nano-catalyst coupling in biodiesel production. They observed that using this catalyst, the ideal circumstances are; a methanol to oil ration of 1:7, taking 6 hours, and a catalyst loading of 1.5 % w/w. It produced is 94.37 % w/w

biodiesel. Besides, nano CaO was found to be a better catalyst since it provided a better efficacy, reaction duration, and repeatability.

Talha & Sulaiman, (2016) investigated the use of heterogeneous base catalysts in biodiesel production. They observed that heterogeneous catalysts are cost-effective due to their reusability, availability, ease of product separation, and longer lifetime.

Heterogeneous base catalysts suffer from a number of disadvantages, including the fact that they become poisoned quickly when exposed to the outside air. Because of this property, soap occurs when the FFA content of the oil exceeds 2% w/w and there is also a risk of contamination from the leaching of active catalyst sites (Diamantopoulos, 2015).

The use of heterogeneous nanocatalysts in transesterification can have several advantages over the use of homogeneous catalystsor enzymatic catalysts, including, cost-effectiveness, improved stability, recyclability, high activity and selectivity, and ease of separation, compatibility with different feedstocks, resulting in a more efficient and environmentally friendly process (Diamantopoulos, 2015).

2.7.3.3. Biodiesel blends

A biodiesel blend is a mixture of biodiesel and petrodiesel. Biodiesel is a renewable fuel made from biological sources such as vegetable oils, animal fats, or recycled cooking oils. The blend can vary in the percentage of biodiesel, which is usually represented as the B factor, where B100 is pure biodiesel and B0 is petrodiesel (Ofori-Boateng & Lee, 2011). Biodiesel blends such as B5, B10, B20, and B100 are commonly used. These include, pure biodiesel (B100), B20 (20% biodiesel with 80% petrodiesel), B10 (10% biodiesel with 90% petrodiesel) and B5 (5% biodiesel with 95% petrodiesel) are some of these blends (Keera *et al.*, 2018). Biodiesel blends are used in

diesel engines without requiring any changes to the engine itself. They are considered a more environmentally friendly alternative to petrodiesel because biodiesel is made from renewable resources and tends to emit fewer pollutants. Blending biodiesel with petrodiesel can be a strategy to balance cost, performance, and environmental considerations in the transportation sector. The Energy Policy Act of 1992 allows fleet use of the most popular biodiesel blend, B20 in USA (EPAct) (Aktas *et al*., 2010). Almost no engine or fuel system modifications are required for a diesel engine to run on B20 (Go--, 2016). The calorific value of petrodiesel is in the range of 42 to 45 MJ/kg. While that of biodiesel is in the range of 35 to 40 MJ/kg (Zulqarnain *et al.*, 2021). The blending of petrodiesel with biodiesel lowers the calorific value of petrodiesel fuels (Islam *et al*., 2014).

Mofijur *et al.*, (2015) studied the effect of biodiesel-diesel blending on the physicochemical properties of biodiesel produced from *Moringa oleifera*. They observed that as the proportion of biodiesel in the blends increased, the density (D), kinematic viscosity (KV), flash point (FP), cloud point (CP), pour point (PP), cold filter plugging point (CFPP) also increased, but the calorific value (CV) decreased.

2.7.4. Characterization of yellow oleander biodiesel

The yellow oleander biodiesel was analyzed and the results compared to ASTM D6751 international standard biodiesel specifications (Basumatary, 2014). The following properties were examined: specific gravity, kinematic viscosity at (40 °C) cSt, cetane number, flash point °C and pour point °C. Saponification number (mg/KOH/g), acid number (mg KOH/g), peroxide value (mEg O_2/kg), iodine value (gI_2/100 g) and calorific value (kJ/kg) were also examined.

Arun *et al.*, (2018) studied how well the biodiesel made from yellow oleander works in compression-ignition (CI) engines. They found that engine performance was affected by the high viscosity of the yellow oleander oil (34 cSt). This resulted in poor fuel atomization. After transesterification, the viscosity of yellow oleander oil dropped to 4.5 cSt, and as a result, fuel atomization increased. The viscosity of the biodiesel blends increased with the proportion of yellow oleander biodiesel in the diesel blend.

Ana & Udofia, (2015) characterized *Thevetia peruviana* oil and biodiesel and found that after transesterification the kinematic viscosity reduced from 21.50 cSt, (in the oil) to 4.70 cSt, (in the biodiesel) which was also within the ASTM D6751 limit of 1.9 - 6.0 cSt limit.

Bora *et al.* (2014) and Nasirudeen *et al.* (2019) studied the acid value of yellow oleander oil and observed 0.658 and 0.16 KOH/g, respectively. These values were found to be below the ASTM limit of 0.80 KOH/g.

Basumatary (2014) & Adepoju *et al.* (2018) studied the acid value of yellow oleander biodiesel and found that the AVs were 0.057 mg KOH/g and 0.508 mg KOH/g, respectively. These values were found to be within the ASTM D6751 limit of 0.80 mg KOH/g.

Adepoju *et al.* (2018) studied the iodine value of yellow oleander oil and yellow oleander biodiesel. They found the IV of 87.60 and 80.42 gI_2/ 100 g oil, respectively. All these values were below the ASTM D6751 maximum limit of 120 gI_2/ 100 g oil.

The temperature at which a fuel will ignite when exposed to flame is known as its flashpoint. Biodiesel is safer than fossil fuels since it has a higher flashpoint. Conversely, low flashpoints indicate methanol, an essential criterion when considering safety concerns for handling and storing fuel (Rupasianghe & Gunathilaka, 2018).

Adepoju *et al.* (2018) studied the higher heating value (HHV) and reported 45.335 MJ/kg HHV for yellow oleander biodiesel. These values were within the ASTM standard of 33 - 40 MJ/kg for biodiesel and would therefore give better engine performance in a diesel engine.

The advantages of biodiesel fuel include they are easy to use with no engine modification. They also exhibit strong power, performance, and are economical. Biodiesel became a valuable fuel due to its proven power output, and good performance. Biodiesel helps reduce CO_2 emissions, which reduces the impact of greenhouse gases, reduces pollution, and improves health. Petroleum oils are used less because of environmental emissions. Biodiesel is less hazardous and safer to store than petroleum, biodiesel is safer to handle (Saxena *et al.*, 2013).

Biodiesel fuel is expensive, requires energy, and can damage engine rubber seals and fuel filters, necessitating routine maintenance for clogging (Saxena *et al.*, 2013).

In general, research into the physicochemical properties of biodiesel is necessary to determine whether it is a viable and sustainable substitute for petrodiesel and to understand its impact on engine efficiency and the environment.

2.7.5. Engine Testing

Dynamometers are used to provide information about combustion, performance and emissions from internal combustion engines (ICEs). The dynamometer can provide useful insight into how well the engine is performing and how it can be tuned for greater combustion efficiency and reduced emissions by measuring engine power, torque, fuel consumption, and emissions generation in various operating situations (Vijayakumar & Kumar, 2019). The data obtained from the dynamometer are converted to a series of curves. Indicator diagrams are obtained electronically during the test using a pressure transducer, time sweep unit, cathode ray oscilloscope (CRO), and

camera (Tziourtzioumis & Stamatelos, 2017). Some of the parameters used in analyzing the engine performance of biodiesel is reviewed next.

2.7.5.1. Performance of diesel engine using yellow oleander biodiesel

The Internal combustion engine (ICE or IC engine) performance can be evaluated using various parameters. These parameters include brake power, brake thermal efficiency and brake-specific fuel consumption.

2.7.5.2. Torque

Torque is the amount of rotational force that an engine can generate at the crankshaft. This power is then transmitted to a vehicle's wheels through the transmission system. Torque is calculated from the engine arm connected to the weight scale using Equation 2.17;

$$\tau = f \times d \text{ …….. Equation 2.17}$$

Where; d is the distance of the engine arm from the center of the rotor to the load, f is the force applied to the load (N), and τ is the brake torque in Nm.

The torque formula helps estimate how much rotational force is generated by the force applied midway from the pivot point.

2.7.5.3. Brake power (BP)

Brake power is the amount of power output of a diesel engine. It gives an indication of engine performance in real operating conditions. First, BP is calculated as the difference between the indicator power and the engine power losses. Then, using a dynamometer, BP is calculated according to Equation 2.18, it is expressed in kilowatts (kW).

$$BP = IP - FP = 2\pi\tau\frac{N}{60}10^{-3}(kW) \text{ …….Equation 2.18}$$

Where IP is indicator power, FP is power loses, τ is the engine torque, N is the angular speed in rpm. (Raheman *et al.*, 2013)

Jagadevkumar and Pravin (2020) studied the performance of heterotrophic chlorella protothecoides microalgae biodiesel and its blends with petrodiesel in a diesel engine. They found that the HCP-B100 had a 2.89% reduction in brake power at full engine load (100%) and a 2.42% reduction in braking effort at part load (i.e. 80%) compared to the D-100. At full load (100% load) HCP-B20 showed a decrease of 1.75%, and at half load (80% load) a decrease of 1.24%. Other blends have BPs that range between HCP-B20 and D100. HCP-B100 had a higher viscosity than petroleum diesel, although it had a lower calorific value. Since biodiesel has a lower calorific value than petroleum diesel, it also has lower engine power, which lowers the BP. Finally, increased viscosity and density result in suboptimal atomization and fuel spray characteristics, which lowers BP.

2.7.5.4. Brake Thermal Efficiency (BTE)

Brake thermal efficiency measures the efficiency with which an engine converts the chemical energy of a fuel into mechanical energy. BTE is a measure of how much energy an internal combustion engine produces while burning fuel (Hadi *et al.*, 2020). The energy in the fuel is also referred to as the lower heating value. BTE is calculated using Equation 2.20.

$$\text{BTE (\%)} = \eta_{th} = \frac{BP}{m_f (LHV)} \quad \text{……..Equation 2.20}$$

Where BP is the brake power, m_f is the mass flow rate of fuel

A high BTE indicates that the engine is converting the energy in the fuel into mechanical energy more efficiently. The brake thermal efficiency of biodiesel is lower than that of pure diesel due to the lower calorific value and specific weight (Wu *et al.,* 2020).

Raheman *et al.,* (2013) studied the performance of a diesel engine with biodiesel and high-speed diesel (HSD) blends at different loads. They observed that at 20% engine load, the BTE values for HSD, B10, and B20 were 16.72 %, 16.50 %, and 15.80 %, respectively. Under maximum load, these increase to 30.89 %, 30.50 %, and 29.99 %. The BTE increased as the engine load increased, primarily because a lower percentage of power was wasted as the engine load increased. The mean BTE with B10 and B20 was 21.87 % and 21.46 %, respectively, compared to 22.27% with HSD. They also found that the BTE decreased as the biodiesel fraction in the fuel blends increased due to the decrease in the calorific value of the fuel blend. Compared to 22.27 % for HSD, the mean BTE for B10 and B20 was 21.87 % and 21.46 %, respectively. They also found that as the amount of biodiesel in gasoline blends increased, BTE decreased as the caloric content of the fuel blend decreased.

2.7.5.5. Brake Specific Fuel Consumption (BSFC)

Brake Specific Fuel Consumption (BSFC) is the amount of fuel the engine uses to produce one unit of braking power (BP). BSFC determines how efficiently an internal combustion engine burns fuel to produce rotary power (at the shaft or crankshaft), measured in kg/kWk. BSFC is calculated using Equation 2.21;

$$BSFC = \frac{M \times 3600}{t \times BP} \quad \text{.....Equation 2.21}$$

Where BP is Brake power (kW), M is mass of fuel in kgs, and t is time used to consume mass of fuel in seconds.

Lower BSFC values indicate better fuel economy because the engine can produce more power with the same amount of fuel. On the other hand, high BSFC numbers indicate that the engine is less efficient as it uses more fuel to produce the same amount of power.

Rahemann *et al.,* (2013) studied the effects of biodiesel and high-speed diesel (HSD) blends on the performance of a diesel engine under different loads. They observed that BSFC generally increased as the amount of biodiesel in the fuel blends with HSD increased. B10 and B20 were found to have mean BSFC values of 287.29 and 298.67 g/kWh, respectively, which were 2.44% and 5.63% higher than those with HSD. The lowest BSFC among the tested gasoline blends was 10% and increased as the proportion of biodiesel in the blends increased. All tested fuels also showed a significant drop in BSFC with increasing engine load due to the significantly lower heat losses at higher loads. Compared to 506.76, 519.52, and 550.37 g/kWh at 20% engine load, the mean BSFCs for HSD, B10, and B20 at full load were determined to be 274.29, 281.05, and 290.00 g/kWh, respectively. The fact that the percentage increase in fuel required to run the engine was less than the percentage increase in braking power may be the cause of the drop in BSFC with an increase in engine load. Higher engine loads resulted in relatively lower heat losses.

2.7.5.6. Engine emission and combustion analysis

Combustion analysis of biodiesel in a diesel engine can reveal important details about the combustion process and the pollutants emitted while the engine is running. This type of analysis allows the performance and emissions characteristics of biodiesel to be compared to petroleum diesel. An exhaust gas analysis can be used to carry out this, in which the exhaust gases produced

during engine operation are examined for the levels of various pollutants such as nitrogen oxides (NOx), particulate matter (PM), carbon monoxide (CO), and hydrocarbons (HC) (Suresh *et al.*, 2018). Inhaling these gases and particles can lead to a number of illnesses, including skin cancer, lung cancer, respiratory issues, and poisoning. Many researchers are looking into technologies that can reduce these emissions from diesel engines. It has been suggested that this could be done successfully by using sustainable and alternative fuels such as alcohols, natural gas, biodiesel and dimethyl ether.

Combustion analysis of biodiesel in a diesel engine includes the in-cylinder pressure analysis, in which the pressure in the engine's combustion chamber is measured during the combustion process to determine characteristics such as combustion timing and peak pressure. Fuel injection analysis, which analyzes the rate and timing of fuel injection into the engine's combustion chamber to determine how effectively the fuel is incinerated. Heat release analysis, in which the amount of heat released during the combustion process is analyzed to determine combustion efficiency and emissions produced. Analyzing the pressure in the engine's combustion chamber while the engine is running to pinpoint details such as peak pressure and timing of the combustion process is called in-cylinder pressure analysis. Fuel combustion efficiency is evaluated using fuel injection analysis, which examines the rate and timing of fuel injection into the engine's combustion chamber. Heat release analysis is the technique of calculating how much heat is released during combustion to calculate combustion efficiency and emissions. The combustion and emission behavior of biodiesel is comparable to that of petrodiesel. Therefore, no modifications are required to use this fuel in diesel engines. In addition, biodiesel has a higher cetane number, no aromatics, and 10-

11% more oxygen than gasoline. The properties of biodiesel fuels make it possible to reduce these pollutants (R. Niculescu *et al*., 2019).

Abed *et al.,* (2019) studied how CO, HC, and smoke emissions for the B10 and B20 biodiesel blends produced from used cooking oil, algae, palm, and jatropha changed with engine load. It was found that for all fuels evaluated, CO, HC, CO_2, and smoke emissions decreased at part load before increasing again at full load. When using biodiesel and its mixtures, the CO, HC, and CO_2 emissions were significantly reduced. Smoke emissions decrease with engine load increase due to biodiesel's superior combustion and higher NO_x emissions compared to diesel fuel, including B10 and B20 blends.

Yadav *et al.,* (2017) studied the emission characteristics of biodiesel fueled with yellow oleander oil in an indica diesel engine. They found that emissions of CO, UHC, and smoke opacity all decreased dramatically. As engine load increases, combustion temperature rises, leading to increased formation of nitrogen oxides, specifically NO_x and NO_2. They also concluded that existing C.I. engines could easily be converted to use yellow oleander oil biodiesel blends as an alternative fuel without requiring major hardware modifications.

This type of research can help scientists and engineers better understand the combustion characteristics, pollution levels, and overall effectiveness of biodiesel when used in diesel engines. Using this knowledge will improve fuel economy, reduce pollutant emissions and increase engine performance.

2.7.6. The life cycle analysis (LCA)

Life Cycle Analysis (LCA), is a method of determining the environmental impact of all phases of a product's life, including the extraction of raw materials, their processing, manufacture,

distribution, use, maintenance and repair, and eventual disposal or recycling. By creating a list of relevant energy and material inputs and environmental releases, assessing the potential impacts associated with those inputs and releases, and interpreting the results to support decision-making, LCAs can help avoid a narrow view of environmental concerns (Siregar *et al.*, 2020).

The phases of a life cycle cost analysis of a material are summarized in Figure 2.16.

Figure 2.16: Life cycle analysis of a biobased material

The goal and scope of the LCA analysis are determined during the goal and scope definition phase. It includes the aim of the study, the limitations of the system, and the functional unit to be evaluated. During the life cycle inventory analysis step, all inputs and outputs related to the product are identified and evaluated. It considers the resources and energy used, the waste and emissions generated, and the need for transport and disposal (Razon *et al.*, 2019). In the life cycle assessment phase, the inputs and outputs identified in the life cycle inventory analysis are evaluated for

possible ecological and social impacts. Among other things, the effects on ecosystems, human health, and the scarcity of resources are evaluated.

Finally, the interpretation phase is about understanding the results of the LCA analysis and concisely summarizing the results. This includes identifying key cost drivers, environmental impacts, and any areas that may need improvement or further research (Razon *et al.*, 2019).

2.7.6.1. The life cycle cost analysis (LCCA) of yellow oleander biodiesel production

The Life Cycle Cost Analysis (LCCA) is a technique for assessing the total cost of biodiesel production and use over the entire life cycle. It considers all phases from raw material production to end use. The costs of all inputs and outputs used in the production of biodiesel are considered by the LCCA, including prices for production, processing, transportation, distribution, and use of raw materials. At the end of the biodiesel lifecycle, it also considers the cost of disposal or recycling. The price of producing and using biodiesel was also compared to that of petrodiesel. This can provide important information on the competitiveness and economic viability of biodiesel as an alternative to conventional petrodiesel (Liu *et al.*, 2021).

LCCA offers a comprehensive economic analysis of biodiesel production and consumption, guiding sustainable business practices and policy development, considering all costs throughout the product's life cycle.

2.7.6.2. Energy balance of yellow oleander biodiesel production

The life cycle analysis (LCA) of the energy balance of biodiesel is an important method for evaluating the environmental impact of biodiesel production. The ratio of energy intake to energy production (biodiesel energy) is referred to as the energy balance of biodiesel. (energy required for growing and harvesting raw materials, transporting raw materials to the processing plant,

processing raw materials into biodiesel, and transporting biodiesel to end users). The life cycle assessment (LCA) of biodiesel accounts for the energy input required to produce the feedstock, transport the feedstock to the processing facility, process the feedstock into biodiesel, transport the biodiesel to the end user, and the energy input required for disposal or recycling of used biodiesel is required (Wahyono *et al.*, 2019).

The Biodiesel Energy Balance LCA results assess the environmental sustainability of biodiesel production, with a positive energy balance indicating more sustainable production compared to negative energy balance.. There is noliterature available on life cycle analysis of yellow oleander biodiesel.

CHAPTER THREE

3.0 METHODOLOGY

This chapter details the collection, preparation, and analysis of waste eggshells and yellow oleander seeds in a laboratory, outlining the research protocol and statistical tests used.

3.1. Materials and chemicals

3.1.1. Chemicals

The following chemicals were commercially available and used as purchased. Manufactured by Merck Germany: Sodium hydroxide pellets (99%), Acetic acid (99.5%), 2,2,4-Trimethylpentane (Iso-octane, for synthesis), and Chloroform (99%). Manufactured by Sigma Aldrich (UK): methanol (99.8%), hydrochloric acid (96.5%), Sodium Thiosulphate (*ReagentPlus*®, 99%), Nitric Acid (ACS reagent, 70 %), Cetryl methyl ammonium Bromide (CTAB)(Molecular Biology Grade, 99%, Calbiochem®), potassium hydroxide pellets (ACS reagent, ≥ 85%), Methanol (99.5%), n-Hexane (95% HPLC grade), Phenolphthalein (98%), Iodine (99.8%, Pharma Grade), Petroleum ether (95%), and n- Butanol - (98%, ACS/HPLC). Potassium iodide (≥ 99.0% ACS reagent). Manufactured by others: Dimethylformamide (DMF) (ACS grade, BDH), Potassium Hydroxide (KOH) pellets (ACS reagent, ≥ 85%), Ethanol, 99%, and anhydrous Sodium Carbonate (Na_2CO_3) (99%, Promark Chemicals). All chemicals used in the study were analytical grade and were sourced from commercial suppliers in Nairobi including Travotech Agencies Limited and Kobian Kenya Limited. In addition, distilled water was obtaend from The Technical University of Nairobi, School of Chemistry and Material Science Laboratory.

3.1.2. Equipment and apparatus

The equipment used during the experimentations includes a pestle and mortar, digital weight balance, and oven for handling the kernels. The Soxhlet extractor, vacuum distiller, and water bath condenser were used in extracting the yellow oleander oil.

The eggshells were incinerated in a muffle furnace. A magnetic stirrer and a reflux separatory funnel were placed in a 500 cm^3 three-necked round bottom glass reactor for the transesterification reaction. This was done to improve the efficiency of mixing the oil and alcohol. A hotplate, Bunsen burner, various Erlenmeyer and Erlenmeyer flasks, beakers, hotplate-MSH-20D, graduated cylinder, burette, and micropipettes were among the additional tools needed to produce the biodiesel. The following instruments were used to analyze the incinerated eggshells and oil samples; XRD, XRF, FTIR, GC-MS, TG/TGA, SEM and TEM. Fuel properties were analyzed using PetroOxy instruments to determine oxidation stability. Flash point cup device (DM 93) for determining the flash point of the fuel and density bottle for determining the density of the fuel. To measure the cloud and pour points of fuel, use a cloud and cloud point instrument. The viscosity of the fuel was assessed using a viscometer, a bomb calorimeter used to determine the calorific value of fuels. Fuel engine performance was evaluated using a computer-controlled, direct-injection, single-cylinder, four-stroke engine.

3.1.3. Materials

Yellow oleander seeds were purchased from the West Gem area of Siaya County. The chicken egg shells were collected from hotels, homes, and cafeterias. Sampling took place over four months between January and April 2015. The dried seeds were sent to the Technical University of Kenya laboratory in Nairobi, Kenya, for oil extraction.

3.1.4. Cleaning of apparatus

The glassware used in the study was immersed in 2 M nitric acid for 24 hours, cleaned, and then rinsed three times with distilled water. The rinsed glassware was dried in an oven at 110 °C for one hour, allowed to cool, and then stored in a clean locker at room temperature..

3.1.5. Pre-treatment preparations and oil extraction

This pre-treatment and oil extraction process can vary depending on the type of raw materials and the desired quality of the oil. However, these basic steps provide a general overview of the process. Seed pretreatment has been reported to increase oil yield, oil oxidative stability, bioactive chemical recovery, and the creation of novel functional compounds (Kaseke *et al.*, 2021)**.**

3.1.5.1. Gravimetric analysis of yellow oleander seeds

In West Gem, Siaya County, ripe yellow oleander seeds were hand-picked, dried, parked, and taken to the Technical University of of Kenya Laboratory. A JT601N electronic scale was used to determine the average mass of the seeds. The nuclear envelope protecting the seeds inside was removed and discarded. The seeds were first sun-dried for at least two weeks, weighed, and ground into a powder using a manual grinder.

3.1.5.2. Moisture content of yellow oleander seeds (AOCS- Ac 2-41)

Oil extraction can be significantly affected by the amount of moisture present. In order to optimize oil extraction, potency, and quality, the moisture content of the seed must be properly regulated (Nde & Foncha, 2020). The yellow oleander seeds were sun-dried for 15 days to constant weight, then the fruit kernels were deshelled. In order to reduce the water content, 25 g of kernels were dried at 105 ± 5°C to constant weight for 3 hours. The moisture content of the seed samples was calculated using Equation 3.1.

$$\% \text{ Moisture content} = \frac{w_2 - w_3}{w_2 - w_1} \times 100 \ldots\ldots \text{Equation 3.1.}$$

where, W_1 = weight of crucible, gm, W_2 = weight of crucible + sample, gm, W_3 = weight of crucible + sample after heating, gm.

3.1.5.3. Yellow oleander oil extraction

The fruit was separated from the chaff by sorting and crushing, to a fine powder with a pestle and mortar prior to oil extraction. The Soxhlet extractor was filled with 250 cm^3 petroleum ether, and 25g of finely ground yellow oleander seed was placed in Whatman No. 1 filter paper in a Soxhlet extraction thimble. The extraction was performed using a heating mantle maintained at 80°C for three hours. After extraction, vacuum distillation was used to separate the oil and petroleum ether mixture in a vacuum still with a rotary still heated to 80°C (the boiling point of petroleum ether). Finally, the pure yellow oleander oil was weighed and its mass was noted. The oil content of yellow oleander seeds was calculated using Equation 3.2;

$$\textit{Yellow oleander oil } (\%) = \frac{\textit{Weight } (gms) \textit{ of oil extracted}}{\textit{Weight } (gms) \textit{ of powdered dry seed used}} \times 100 \quad \ldots\ldots \text{Equation 3.2}$$

3.1.5.4. The kinetics of oil extraction

Oil extraction kinetics refers to the study of the rate at which oil is extracted from various feedstocks. Understanding the kinetics of oil extraction is crucial in order to optimize the extraction process and achieve the best possible oil yield and quality (Owolabi *et al.*, 2018).

The second-order pseudo model is preferred for studying vegetable oil extraction from seeds because of its realistic representation of the process. The oil extraction rate is assumed to be proportional to the active sites and solute concentration. Experimental data often agree better with

the model, indicating that its assumptions and equations are consistent with actual behavior. The pseudo-second-order model also provides insights into the oil extraction mechanisms and provides rate constants for seed-solvent chemical interactions (Lim *et al*., 2020). It is predictive and consistent with chemisorption processes, suggesting that chemical interactions rather than physical adsorption play a role in vegetable oil extraction. It is applicable to various extraction techniques including solid-liquid extraction and supercritical fluid extraction. Consequently, this study used a pseudo-second-order model to study the kinetics of oil extraction from yellow oleander seeds. The second-order mechanism model, which offers better agreement with experimental data and can be used to predict oil production rates under different conditions, is often preferred over other kinetic models. This formula assumes that the amount of oil remaining in the material squares the rate of oil production. Equation 3.3 explains how quickly the oil in the meal dissolves in solution;

$$\frac{dC_t}{dt} = k(C_s - C_t)^2 \quad \text{..... Equation 3.3}$$

Where:

k is the second-order extraction rate constant

C_s is the concentration of oil at saturation (g/ml)

C_t is the concentration of oil in the solution at any time ($t/\min$). The integrated rate for a second-order extraction was obtained by considering the boundary condition t = 0 to t and $C_t = 0$ to C_t. This is expressed in Equation 3.4;

$$C_t = \frac{C_s^2 kt}{(1 + C_s kt)} \quad \text{..... Equation 3.4}$$

Linear form of the Equation 3.4 becomes Equation 3.5;

$$\frac{C_t}{t} = \frac{C_s^2 k}{(1 + C_s kt)}$$ …….. Equation 3.5;

When $t \to 0$, the LHS of Equation 2.4.3 is the initial extraction rate, E_i, this forms Equation 3.6 and Equation 3.7;

$E_i = kC_s^2$ …… Equation 3.6.

$$\Rightarrow \frac{C_t}{t} = \frac{kC_s^2}{1} + \frac{kC_s^2}{C_s kt} \Rightarrow \frac{C_t}{t} = \frac{E_i}{1} + \frac{C_s}{t}$$ …….. Equation 3.7

Rearranging Equation 3.7, gives the Equation 3.8;

$$\frac{t}{C_t} = \frac{1}{kC_s^s} + \frac{t}{C_s}$$ …….Equation 3.8

This can be rewritten as Equation 3.9

$$\frac{t}{C_t} = \frac{1}{E_i} + \frac{t}{C_s}$$ …….. Equation 3.9.

By plotting a graph of $\frac{t}{C_t}$ versus t, it yields the initial extraction rate, E_i, the extraction capacity, C_s the second order extraction constant, and *k*, can be calculated experimentally (Santos *et al.*, 2015).

3.1.5.5. The thermodynamics of oil extraction

Oil extraction thermodynamics is the energy change that takes place during the extraction of oil feedstocks. Fluctuations in enthalpy (heat) and entropy (disorder) are two examples of these energy changes that are critical to the effectiveness and quality of the oil extraction process (Fallis, 2013). Temperature, pressure, solvent type, and moisture content are just a few of the variables that can

affect the thermodynamics of oil production. The extraction of the oil using petroleum ether as solvent was estimated uder constant temperature and pressure using Equation 3.10.

$\Delta G = \Delta H - T\Delta S$ …… Equation 3.10.

Gibbs energy change (ΔG) is measured in kJ/mol, enthalpy change (ΔH) is measured in kJ/mol, and entropy change (ΔS) is measured in kJ/mol.

The thermodynamics of yellow oleander oil extraction were based on the change in Gibbs free energy can also be determined using the Equation 3.11 below.

$\Delta G = RT \ln k$……. Equation 3.11

Where; $k = \frac{Y_T}{Y_U}$ ……Equation 3.12

Where Y_T the percentage of yellow oleander oil extracted at temperature, T and, Y_U is the percentage of the unextracted yellow oleander oil.

Where k is the equilibrium constant, R is the Universal gas constant (8.314 kJ/K mol), and T is Kelvin's temperature (Mohd *et al.,* 2017). Rearranging gives Equation 3.13

$$\ln k = -\frac{\Delta G}{RT} = \left(\frac{\Delta H}{R}\right)\left(\frac{1}{T}\right) + \frac{\Delta S}{R}$$ ……Equation 3.13

Plotting a graph of $\ln k$ against $\frac{1}{T}$ givers a straight line giving $\frac{\Delta H}{R}$ as the gradient and $\frac{\Delta S}{R}$ as the y – intercept (Mohd *et al.,* 2017). These values are used to determine the changes in enthalpy, Gibbs free energy, and entropy, establishing if the extraction process is spontaneous or non-spontaneous.

3.1.5.6. Activation energy

The activation energy Ea and temperature required for a given reaction are two factors that have a significant impact on the reaction rate. The magnitude of the activation energy for oil extraction from raw materials depends on the moisture content in the seed, the equipment used, and the processing conditions. This is summarized by the Arrhenius Equation 3.14;

$k = Ae^{\frac{-E_a}{RT}}$ ……..Equation 3.14

Where;

k is the rate constant of the reaction

A is the Arrhenius factor (of constant or coefficient)

e = exponential constant = 2.718

E_a is the activation energy of the reaction

T is the temperature of the reaction mixture in the absolute scale (in K) i.e. (°C +273)

R (universal gas constant) = $8.314\ JK^{-1}mol^{-1}$ (Piskulich *et al*., 2019)

E_a is the source of the activation energies because it is related to the activation energy of the reactions. A slower reaction is implied by a high activation energy. The statistical probability that the transition state occurs correctly is correlated with the constant A (El Seoud *et al.*, 2016). When this probability is high, then the reaction is fast. The values of A and E_a are determined experimentally by measuring the rate constant at several temperatures and working on the data in a standard way (Piskulich *et al*., 2019).

Rewriting the Arrhenius equation in natural logarithmic form gives Equation 3.15:

Arrhenius equation,

$$\ln k = \left(\frac{-E_a}{R}\right)\left(\frac{1}{T}\right) + \ln A \text{ …….Equation 3.15}$$

Plotting a graph of $\ln k$ *vs* $\frac{1}{T}$ gave a straight-line graph, and the gradient of the straight line was used to calculate the activation energy of etxraction.

3.2. Preparation of the synthesized nanocatalyst

The nanocatalyst was synthesized using bottom-up coprecipitation technology. In this technique, coprecipitation is a versatile and straightforward method to prepare nanocatalysts with controlled particle size and morphology (Arbab Ali *et al*., 2021). Waste shells from chicken eggs were collected, then washed and the adherent membranes were removed from the shells manually. The eggshells were thoroughly cleaned with distilled water, dried at 105°C for one hour, ground into a powder, and then incinerated in a muffle furnace at 900°C for three hours. The powdered eggshell and 0.1 M aqua regia were then combined to prepare an eggshell solution. Solutions A and B, the two different microemulsions, were prepared to produce an eggshell nanocatalyst. 25 cm^3 microemulsion A was prepared using 2.5 cm^3 of 0.1 M aqueous eggshell solution, 3.5 cm^3 n-butanol as co-surfactant, 15 cm^3 isooctane as non-polar solvent and 4.20 g cetyltrimethylammonium bromide (CTAB) as surfactant. 2.5 cm^3 0.1 M aqueous ammonium carbonate solution, 3.5 cm^3 n-butanol, 15 cm^3 isooctane, and 4.20 g CTAB were combined to form 25 cm^3 microemulsion B. The microemulsions (A and B) were mixed separately for 30 minutes. A white precipitate formed after microemulsions (A and B) were uniformly mixed for 12 hours using a magnetic stirrer at 700 rpm. This precipitate was separated from the microemulsions by centrifugation. The precipitate was cleaned with a 1:1 combination of methanol and chloroform,

allowed to dry at ambient temperature for 12 hours, and then calcined at 900°C for three hours. As a reference, an eggshell nanocatalyst was prepared by burning eggshells at 900 °C for 3 hours.

3.2.1. Characterization of the synthesized nanocatalyst

The synthesized nanocatalyst was characterized using various analytical techniques including TGA/DTG, XRF, FTIR, BET/BJH, XRD, TEM, SEM, and EDX.

3.2.1.1. Thermal analysis of materials

The thermogravimetric analysis (TGA) involves tracking changes in sample mass brought on by controlled rate heating in a controlled environment. The thermograms are expressed in terms of weight loss percentage with temperature (Loganathan *et al.,* 2017).

DTG is a derivative technique commonly used in conjunction with TGA to provide additional information about the thermal behavior of a sample. It requires the derivation of the TGA data, which could highlight other aspects of the data that may not be immediately apparent from the TGA curve alone. The rate of change in weight loss of the samples is plotted in DTG as a function of time or temperature. This can reveal details on the kinetics of thermal degradation, including the samples' rate of degradation, peak temperature, and onset temperature (Charmas *et al.*, 2019).

Differential scanning calorimetry (DSC), on the other hand, measures the difference in heat flow between the sample and the reference material. During the entire analysis, the temperature difference between the reference and sample cells is monitored and kept at zero. The amount of additional heat released or absorbed is equal to the energy difference needed to raise the temperature of the sample to that of the reference material (Charmas *et al.*, 2019). The DSC data is be explained by Equation 3.16;

$$\frac{dH}{dt} = mC_p \frac{dT}{dt}$$ ……..Equation 3.16

Where; $\frac{dH}{dt}$ denotes the DSC heat flow signal, *m* (gm) denotes the sample mass, C_p denotes the material specific heat capacity, and $\frac{dT}{dt}$ denotes the heating rate of the material (Mansfield, 2015).

The results are plotted as heat flux density in watts per square meter (W/m^2) with temperature.

3.2.1.2. X-ray fluorescence (XRF) analysis of materials

X-ray fluorescence (XRF) (Philips, model PW 2400) was used to determine the elemental composition of the nanocatalyst samples with a tube current of 1000 A and a detection lifetime of 30 s.

The percent chemical composition of elements in the sample was determined using the XRF diffraction pattern. Samples are excited by the X-ray tube either directly or indirectly via a filter. A filter was used to shield part of the stimulating radiation to prevent overstimulation of the detector.

3.2.1.3. Fourier Transform Infrared Spectroscopy (FTIR) analysis of the synthesized nanocatalyst

FTIR spectroscopy is used to analyze the chemical composition and moleculatr structures of materials. Functional groups were found in the nanocatalyst samples using an FTIR-600 spectrophotometer with a resolution of 4 cm^{-1} and at a wavenumber of 4000–250 cm^{-1}. Dried samples of the prepared nanocatalysts were combined with KBr to produce pellets.

3.2.1.4. XRD analysis of materials

XRD analysis is used to determine the crystalline structures of materials. Crystal structure and particle size of the synthesized nanocatalyst were determed using XRD Spectroscopy. X-ray powder diffraction was carried out on a Rigaku (MiniFlex II, England) diffractometer using CuK_α radiation (λ = 1.54060 Å) at 40 kV and 40 mA. Samples of the nanocatalysts were collected over a 2θ range of 0 to 85° and scanned at a rate of 1 °C per minute. The typical XRD powder patterns of calcium oxide and calcium carbonate from JCPDS data were compared to the XRD powder patterns of synthesized nanocatalysts at different temperatures. The crystalline phases were identified by XRD spectroscopy and the observed peak positions were compared to the International Center for Diffraction Data Standard (JCPDS).

The mean particle size was calculated using the Scherrer equation presented in Equation 3.17;

$$L = \frac{k\lambda}{\beta\, Cos\theta} \text{ ……..Equation 3.17}$$

Where L represents the crystallite size, K denotes the shape factor (K = 0.94), and λ represents the wavelength of the X-rays (λ = 1.5406 Å for Cu K_α radiation). β represents the full width at half maximum in radians, and θ is the Bragg angle.

3.2.1.5. Analysis of surface area and pore diameter of the materials

A Micromeritics TriStar 3000 surface area and porosity analyzer were used to calculate the catalyst surface area using the BET method (Brunauer, Emmett, and Teller) using the low-temperature N_2 adsorption method. To remove impurities and moisture adsorbed on the catalyst surface and pores, samples were degassed at 120 °C for 12 hours while continuously pumped with N_2 gas prior to

analysis. The surface area of the nanocatalyst was calculated using the Brunauer-Emmett-Teller (BET) equation presented in Equation 3.18;

$$\frac{1}{X\left(\left(\frac{P_0}{P}\right)-1\right)} = \frac{1}{X_m C} + \frac{C-1}{X_m C}\left(\frac{P}{P_0}\right) \text{ ……..Equation 3.18}$$

Where; X is the weight of nitrogen adsorbed at the relative pressure $\left(\frac{P}{P_\circ}\right)$, X_m is monolayer capacity, the volume of gas adsorbed at standard temperature and pressure (STP), and C is constant at STP. A graph plotted of $\frac{1}{X\left(\left(\frac{P_0}{P}\right)-1\right)}$ against $\frac{P}{P_\circ}$ lies between 0.05 - 0.35 gives a straight line with a gradient $\frac{C-1}{X_m C}$ and y intercept $\frac{1}{X_m C}$.

The Barret-Joyner-Halenda (BJH) equation was used in this study to determine mean pore diameter and volume (Bardestani, Patience, and Kaliaguine 2019; Buasri *et al.*, 2014). The multilayer thickness is added to the BJH equation to determine the pore radius (t). The meniscus radius was calculated using the Kelvin equation presented in Equation 3.19;

$$\ln\frac{P}{P_0} = \frac{2\gamma V_m}{rRT} \text{ ……..Equation 3.19}$$

where $\left(\frac{P}{P_\circ}\right)$ is the equilibrium relative pressure with a meniscus, γ is the surface tension of the liquid adsorbates, V_m is the molar volume of the liquids, and R is the universal gas constant; T is the temperature and r_k is the average radius of curvature of the meniscus generated in the mesopore.

BJH determines the change in the adsorbed layer thickness based on the relative pressure drop in the desorption branch (Bardestani *et al.*, 2019).

The micropore volume and micropore surface area of the prepared nanocatalysts were calculated using the t-plot method and the Harkins and Jura thickness Equation 3.20.

$$t = \sqrt{\frac{13.99}{0.034 - \log_{10}\frac{P}{P_0}}} \quad \text{.....Equation 3.20}$$

Where P and P_0 are the absolute vapor pressure and saturation vapor pressure, respectively, and t is the film thickness (Å) of nitrogen adsorbed on the sample surface.

Kevin's equation was used to determine the pore radius and the thickness of the adsorbed multilayer t for cylindrical pores. This is presented in Equation 3.21.

$$R_p = r_k + t \quad \text{.....Equation 3.21}$$

Where; R_p is the pore radius and t the statistical thickness of adsorbed. Values for t can be derived from standard isotherms.

The average pore diameter = $2.R_p$ .....Equation 3.22

Using the information on nitrogen adsorption, the Brunnaer-Emmett-Teller surface area (BETs, m^2/g) and total pore volume (Vm, cm^3/g) were determined at STP using BET theory. Based on knowledge of the differential pore volume to the desorption isotherms, the Barrett-Joyner-Halenda (BJH) equation determines the pore size.

3.2.1.6. Scanning electron microscope (SEM) images of materials

Camscan-MX 2000 (England) scanning electron microscope (SEM), was used to study the microstructures of the nanocatalysts. The SEM had energy dispersive spectrometer (EDS) detector for chemical composition analysis.

Accelerated electrons in an SEM have high kinetic energy, they lose energy through a variety of signals when they come into contact with the solid sample. Secondary electrons (SE), backscattered electrons (BSE) and diffracted backscattered electrons (EBSD) are generated by these signals. While BSE is used to show differences in the composition of multiphase samples, SE shows the morphology and topography of samples. Mineral crystallography and orientation are determined using EBSD.

3.2.1.7. Energy dispersive spectrometer (EDS) elemental analysis of materials

A scanning electron microscope (SEM) equipped with an energy dispersive spectrometer (EDS), the Camscan-MX 2000 (England), was used for the investigation of the elemental composition. In addition, the electron-probe interaction releases powerful X-rays for elemental analysis. When incident electrons collide with electrons in specific orbitals of atoms in the sample, X-rays are produced (Oleshko, 2014).

3.2.1.8. Transmission electron microscopy (TEM) images of materials

The particle size of the synthesized nanocatalyst was analyzed using TEM spectroscopy. TEM, HR-TEM-JEOL 2100F microscope (JEOL, USA) operating at 80 kV was used for imaging. The catalyst nanoparticle suspension was placed on a copper grid (Ted Pella, CA). The transmission electron microscope equipped with Selected Area Electron Diffraction (SAED) and were used to

confirm the particle size and determine the nanosphere structures. To prepare the TEM, the samples were first degassed at 300 °C for 4 hours before analysis.

3.3. Optimization of synthesized eggshell nanocatalyst for transesterification of yellow oleander oil

To study the impact of different transesterification process variables on percent biodiesel conversion, the Response Surface Methodology (RSM) of Experiments and Central Composite Design (CCD) was used to optimize the biodiesel manufacturing process from yellow oleander oil. These are the steps to optimize yellow oleander biodiesel production using the design of experiments (DOE). The aim is to define the goal and decide what output reaction, such as yield, purity, or conversion efficiency you want to maximize. Input factor selection involves selecting the input elements that are most likely to have an impact on the response of the output. Often 4 to 6 criteria are chosen. To identify the input factor range, the range of values for each input factor subject to the test must be specified. This range should include high and low values that may affect the output response. Designing the experiments, using software or another tool for DOE. The program generates a series of trials that cover all possible combinations of the input factor values within the specified ranges. Conducting the experiments involves conducting the tests according to the planned plan and documenting the results for each experiment. When analyzing the data to evaluate the relevance of each input element and its interactions with other factors in the output response, experimental data must be analyzed using statistical techniques such as analysis of variance (ANOVA). To optimize the process, the analysis results must be used to determine the ideal set of input elements that produce the intended output response. Change the process variables

accordingly. To validate the results, further testing must be performed to verify the improved method and ensure that the expected output response is realized.

The RSM-CCD experimental design requires a 5-level-3-factor level, which is –α, -1, 0, 1, α three factors each at two-level. There are three independent variables: the temperature of the reaction (A), reaction time (B) and catalyst concentration (C). The factorial part of the design, gives us a rotatable design. In contrast, the axial point is defined as $\alpha = 1.68$, whereas, $k = 3$ in this research - the range and levels of individual variables of 3k design. From Equation 2.13;

When $n = 3$, then $N = 2^3 + 2(3) + 6 = 8 + 6 + 6 = 20$

20 trial runs were conducted to optimize the biodiesel production technique of the yellow oleander with Central Composite Design. A regression analysis of the experimental data was performed using Design Expert software version 11 (STAT-EASE Inc., Minneapolis, USA) to fit the equations. The quality of the generated model was instead determined by the value of the correlation coefficient (R^2), and analysis of variance (ANOVA) was used to determine the statistical significance of the equations developed.

3.4. Transeterification of the yellow oleander oil

The nanocatalyst was first activated by adding 3.68 % (w:w) of the synthesized eggshell-derived nanocatalyst to methanol. The mixtures were stirred and heated to 65 °C at 650 rpm for 3 hours to form calcium methoxide. The transesterification reaction was then carried out at 60 °C and 750 rpm in a 250 cm^3 three-necked flask fitted with a reflux condenser, thermometer, and magnetic stirrer heating. 40 cm^3 of calcium methoxide was added to the flask after 100 cm^3 of yellow oleander oil. The optimized experimental conditions included; Temperatures from 30 to 70 °C, 0.3 to 1.5% catalyst loading, and reaction times from 10 to 60 minutes. The reaction product was

separated by layering the top (biodiesel) and bottom (glycerol) layers of the biodiesel samples in a separatory funnel overnight. The nanocatalyst was then separated from the biodiesel layer by centrifugation. The biodiesel produced (a clear amber-yellow liquid) was dried using 1g of anhydrous Na_2SO_4 at 100 ºC to eliminate any residual moisture and excess methanol. Finally, the dried biodiesel was weighed, and the yield was calculated using Equation 3.23:

$$Biodiesel\ \ yield\ (\%) = \frac{mass\ of\ \ biodiesel\ (g)}{mass\ of\ \ yellow\ oleander\ oil\ (g)} \times 100 \quad \text{.....Equation 3.23}$$

3.4.1. Catalyst reusability studies

Catalyst reusability testing is an important step in evaluating a catalyst's performance and effectiveness in a catalytic reaction. The aim of the test is to determine if the catalyst can be applied more than once without degrading activity, selectivity, or stability.

After the transesterification process, the nanocatalyst from the combination of glycerol and nanocatalyst was collected under a vacuum using a Buchner funnel. The residue, after frequent stirring, was then rinsed with hot methanol to remove any remaining unreacted oil. The recovered nanocatalyst was dried in an oven at 105°C before being used for transesterification.

3.5. Biodiesel blends

Fuels made from mixtures of petrodiesel and biodiesel fuels are referred to as biodiesel blends. Different biodiesel blends were made by blending different amounts of biodiesel with petroleum diesel fuel. The B5, B10, B20, and B100 biodiesel blends are the most popular. Table 3.1 presents a summary of biodiesel/petrodiesel blends.

Diesel and biodiesel test blends (B5, B10, B15, B20, B30, and B100) were prepared on a v/v% basis and used in a diesel engine to evaluate engine performance. In a 1-liter volumetric flask,

required volumes of diesel and biodiesel were added and mixed to obtain the different blends. A total of 50 cm^3 (5%) pure yellow oleander biodiesel or petrodiesel was measured and thoroughly mixed with 950 cm^3 (95%) petrodiesel to make a 1 liter B5 blend.

Table 3.1: Various biodiesel/petrodiesel blends

Blend	**B0**	**B5**	**B10**	**B15**	**B20**	**B30**	**B100**
Petrodiesel cm^3)	100	95	90	85	80	70	0
Biodiesel(cm^3)	0	5	10	15	20	30	100

The B10 blend consisted of 900 cm^3 (90%) petrodiesel and 100 cm^3 (10%) undiluted yellow oleander biodiesel. The B20 blend was produced by combining 800 cm^3 (80%) fossil diesel and 200 cm^3 (20%) virgin yellow oleander biodiesel (Goudilyan, 2015).

3.6. Physicochemical properties of oil, biodiesel and blends.

The study used the American Society for Testing and Materials (ASTM D-6751), the American Oil Chemists Society (AOCS) Cd 8-53, and the International Organization for Standardization (ISO) to evaluate the quality of yellow oleander oil and biodiesel. The analysis included the following spectroscopic and physicochemical fuel properties include: FTIR, GC-MS, cetane number, specific gravity, kinematic viscosity, saponification value, acid value, peroxide value, iodine value, flashpoint, and pour point, among others. The standards used for the tests included: ASTM D 1962, D 664, D 1563, D 127, D 445, D 613, D 93, D 287, D 287, D 97 AOAC 993.20 and AOCS 1d – 92.

3.6.1. FTIR analysis of nanocatalyst, yellow oleander oil and biodiesel

The FTIR spectrometer was used to analyze the functional groups in the synthesized nanocatalyst, yellow oleander biodiesel, and the oil. This study used the FTIR-600 spectrophotometer with a NaCl cell. The FTIR spectrometer used in this experiment is presented in Figure 3.1.

Figure 3.1: FTIR-600 Spectrophotometer

A sensitive pyroelectric deuterated L-alanine-doped triglycine sulfate (DLaTGS) detector was also used in the spectrophotometer. This improved the signal-to-noise ratio and cut the analysis time in half. Wet KBr pellets and liquid films from the oil sample were analyzed in KBr cells to generate FTIR spectra.

3.6.2. GC-MS analysis of yellow oleander oil

Gas chromatograph-mass spectrometry was used to examine the acid profiles of the yellow oleander oil composition (GC-MS QP2010SE SYSTEM, Shimadzu Corporation, Japan). The 30m x 0.32mm x 0.25m (DB-WAX, Carbowax 20M) GC capillary column was used. The oil sample

size was 2 µl, the carrier gas was helium, and the inlet temperature was 250 °C. Figure 3.2 is an image of the GC-MS used in this study.

Figure 3.2: Gas chromatography-mass spectrometry (GC-MS)

3.6.3. Determination of saponification values (SV)

The saponification value was determined using the titrimetric method using the Equation 3.24.

$$SV = \frac{v_0 - v_1 \times C \times 56.1}{m} \quad \text{……Equation 3.24.}$$

where V_0 is the volume in cm^3 of the standard HCl solution used for the blank, V_1 is the volume in cm^3 of the standard HCl solution used for the sample, C is the concentration of the standard HCl solution (0.5 N) and m is the mass in grams of the test portion (2g), KOH has an equivalent weight of 56.1**.**

3.6.4. Determination of Acid values (AV)

The acid value was determined using the titration of free fatty acids in the oil against KOH. Equation 3.25 was used to calculate the AV;

$$AV = \frac{56.1 \times v \times M}{x} \quad \text{.....Equation 3.25}$$

Where M is the exact concentration in the KOH solution used (0.1N); v is the volume in cm^3 of the standard volume of KOH solution used; and x is the mass in grams of the test portion (1 g).

3.6.5. Determination of Peroxide values (PV)

The peroxide value was determined according to AOCS Official Method Cd 8-53(2003) (Fallis, 2013). The analysis used Equation 3.26 to determine the peroxide value.

$$PV = \frac{10 \times (v_1 - v_2)}{x} \quad \text{.....Equation 3.26}$$

Where: V_1 volume of 0.01 N $Na_2S_2O_3$ to determine the volume of the test sample in cm^3, V_2 volume of 0.01 N $Na_2S_2O_3$ of the blank solution determined in cm^3, and x is mass of the tested portion in g (5 g).

3.6.6. Determination of Iodine value (IV) (AOAC 993.20)

The average degree of unsaturation of a lipid is measured by the iodine number; the higher the iodine number, the more C=C double bonds are present in the lipid. By definition, the iodine valueis expressed as grams of iodine consumed per 100g of fat. Lubrizol test method was used to determine the iodine value (Negash *et al*., 2019).

In a 250 cm^3 Erlenmeyer flask, 20 cm^3 of carbon tetrachloride (CCl_4) was added to 0.24 g of yellow oleander oil. Another 20 cm^3 of carbon tetrachloride was added to two other flasks that served as blanks. Into each of these flasks, a 25 cm^3 pipette of Wij's reagent was added. These flasks were

corked, swirled to mix the contents, and stored at 28 °C in a dark place for 30 minutes. The sample solution was then mixed with 100 cm^3 filtered water and 10 cm^3 30 % potassium iodide (KI) and the solution was immediately titrated with standard 0.1M sodium thiosulfate ($Na_2S_2O_3$) until the yellow color became colorless. The titration was repeated, this time dropwise with vigorous swirling, until the blue starch-iodine color became colorless. One cm^3 of 1% starch indicator solution was added. The blanks were also titrated in the same way. The iodine value was calculated using Equation 3.27:

$$IV = \frac{(B-T)\times 0.01269\times 100}{W} \quad \text{.....Equation 3.27}$$

Where 0.01269 is the calculated mass of iodine per cm^3 of $Na_2S_2O_3$ solution, T is the volume of the sodium thiosulfate standard solution taken, B is the volume of the blank titre of the standardized sodium thiosulfate solution, W is the mass of the oil sample used in grams.

3.6.7. Determination of specific gravity (ASTMD 287)

The specific gravity of oil was calculated as the ratio between the density of oil and that of water (specific gravity has no units). Equation 3.28 is used to calculate specific gravity.

$$\text{Specific density} = \frac{Density\ of\ oil}{Density\ of\ water} = \frac{\rho_{oil}}{\rho_{water}} = \frac{mass\ of\ oil}{mass\ of\ water} \quad \text{..... Equation 3.28.}$$

3.6.8. Kinematic viscosity (ASTM D 445)

The kinematic viscosity of samples was measured by using Redwood Viscometer based on the IS: 1448 [P: 25] 1976 standard. The time of gravity flow in seconds of a fluid volume (50 cm^3) at 38 °C was obtained. The kinematic viscosity was computed using Equations 3.29 and 3.30.

$v_k = 0.26t - \frac{179}{t}$ Equation 3.29, When 34 < t < 100, and $v_k = 0.26t - \frac{50}{t}$ …Equation 3.30, when t > 100

Where, ν_k = Kinematic viscosity in centistokes and t = Time for flow of 50 cm^3 sample in second.

3.6.9. Cetane Number (ASTM D 613)

The cetane number was calculated from the aniline point (Apt.) by mixing 10 cm^3 aniline and 10 cm^3 biodiesel sample in a U-tube glass with a thermometer and stirrer. This substance was heated with an infrared lamp and constantly stirred with a motor. When the mixture was homogenized, the aniline points were recorded.

3.6.10. Flash point (ASTM D93)

The flash points of the fuels were determined using the PenskMartens closed-cup tester. The Pensky Martens test cup was filled to the brim with the oil sample and then sealed. The temperature was then raised to 40°C, which is approximately 20°C below the expected flash point. Before the test flames were applied to the sample, they were lit and adjusted to a diameter of 4mm. The temperature of the sample was recorded after it was agitated for around 5 minutes. The test fuels were heated and mixed continuously. A flame was passed over the fuel through an opening. The temperature of the sample was recorded after it was agitated for around 5 minutes. A standard test flame was introduced into the vapor space at intervals of around 1°C increases, while the sample was constantly heated at a steady rate until a flame that flashed the air vapor combination occurred. Once the vapor reached the flash point temperature, it caught fire and produced a visible flash. The flash point was determined as determined by the air pressure of the sample fuel and the temperature at which the flame was seen.

The corrected Flash point was calculated using Equation 3.31;

Corrected Flash Point (°C) = C + 0.25 (101.3 – P) ……..……. Equation 3.31

Where; C is the observed flash point (°C) and P is the Barometric Pressure (kPa)

3.6.11. Calorific value (CV) (ASTM D 4809)

A bomb calorimeter was used to determine the calorific value of fuel. In this study, a fully automated SDAC6000 bomb calorimeter was used to calculate the calorific value of yellow biodiesel. The calorific value of the fuel was calculated using Equation 3.32.

$$Q = 10.38 \frac{kJ}{kg\ ^{\circ}C} \times \Delta T(^{\circ}C) \ldots\ldots\ldots\ldots \text{Equation 3.32}$$

Where Q represents the calorific value (kJ/kg), ΔT represents the temperature rise of the surrounding water (°C) and the precision of ΔT in this device is ± 0.0005

3.6.12. Specific gravity (SG), American Petroleum Institute (API), and Diesel Index (DI) (ASTM D2015)

This experiment was carried out at room temperature, a dry and empty bottle with a specific gravity of 25 cm³ was weighed before and after filling with distilled water. After draining the bottled water, it was dried in an oven at 100°C for 30 minutes. After the gasoline sample was filled to the mark, the bottle was weighed again.

To determine the diesel index, a mixture of the sample fuel and an equal amount of aniline is heated. The aniline and petrol are then completely dissolved. Aniline can separate from the gasoline after the mixture has cooled. At this temperature, aniline separates from gasoline**.**

The properties of the fuel samples were calculated from the recorded weights based on Cetane Number (CN), API (American Petroleum Institute), and Diesel Index (DI) from the American

Society of Testing and Materials (ASTM) 2015. They were calculated using equations 3.34 to 3.35.

$$API = \frac{141.5}{S.G.} - 131.5 \ldots\ldots\ldots \text{ Equation 3.33,}$$

$$DI = \frac{aniline\ point\ (^{\circ}F) \times\ ^{\circ}API\ gravity\ (60^{\circ}F)}{100} \ldots\ldots \text{ Equation 3.34}$$

$$CN = DI \times 0.72 + 10 \ldots\ldots\ldots\ldots \text{ Equation 3.35}$$

Where, S.G. = specific gravity of the fuel.

The energy content of fuel decreases with increasing API gravity. A fuel with a higher specific gravity contains more energy because specific gravity is the inverse of API gravity. As the specific weight increases, the power output increases. The Biodiesel API limits for biodiesel range from 30 to 45 and specific gravities are in the range of from 0.879 to 0.802.

A high API G indicates that the paraffin fuel has good ignition quality and a low C/H ratio. A high API G indicates an aromatic asphalt fuel with poor combustion characteristics, while API < G 10 indicates difficult or impossible separation of water and solids.

Light crudes: > 38, medium crudes, 38 > API > 29, heavy crudes: 29 > API > 8.5, and very heavy crudes: API < 8.5

3.7. Engine performance analysis

In this study, the performance characteristics of a test engine fueled with petroleum diesel-yellow oleander blends and computer-controlled single-cylinder, four-stroke, liquid-cooled diesel fuel was examined. Various components of the experimental setup for engine performance are presented in Figure 3.3.

The performance of compression ignition (CI) engines is influenced by a number of variables. These variables include the viscosity, calorific value, flash point, pour point, density and cetane number of the fuel, as well as the injection pressure, the combustion time, the fuel-air mixture, the temperature of the air entering the combustion chamber and the ignition delay. To evaluate engine performance metrics such as torque, brake specific fuel consumption (BSFC), braking thermal efficiency (BTE), mechanical efficiency (ME) and volumetric efficiency, the CI engine was run on yellow oleander biodiesel and blends of petrodiesel with yellow oleander biodiesel.

Figure 3.3: IC Diesel engine test set-up

The results were compared to petrodiesel fuel based on the properties of yellow oleander biodiesel and its blends. The internal combustion engine (IC) system included a flexible coupling connecting a four-stroke diesel engine to a hydraulic dynamometer brake. To feed the load at various operating conditions, the motor used an eddy current type dynamometer.

The diesel engine was placed on a shared concrete bed and the frame structure was decoupled from the concrete using a vibration-damping fastening method. The engine is designed to allow modulation of the compression ratio (CR) even when the engine is running. An attached micrometer was used to measure cylinder movement. Piezo sensors were mounted on the cylinder head and fuel injector to control combustion pressure and fuel flow. It was initially run on diesel fuel and at full load for the first 20 minutes to verify that the exhaust and exiting cooling water temperatures were constant and that the variable compression ratio (VCR) engine was able to reach a steady state. As a result, data collection could begin as the combustion process in the cylinder stabilized. After that, the engine ran for five minutes before gradually idling again. Before starting the experiment to monitor the emissions, a flue gas analyzer was also switched on briefly to stabilize the system.

After the engine was started under no load, 25%, 50%, 75%, and 100% load conditions at 2-minute intervals, all data was collected under steady-state conditions. The disel engine was started with a fuel and allowed to warm up without load for about 10 minutes. Only diesel fuel was used for the tests, which were carried out at various engine speeds of 500, 750, 1000, 1250, and 1500 rpm. This data represented the engine braking forces at CRs 16:1, 17:1, and 18:1. The other experimental parameters including engine speed, IT, and IP were maintained at 1500 rpm, 23° bTDC, and 210 bar throughout, as such values were assumed to be typical of the VCR engine used. After the diesel tests, yellow oleander biodiesel blends (B5, B10, B15, B20, B30, and B100) were rated at CRs of 16:1, 17:1, and 18:1, with 17:1 serving as the reference CR. The data was taken at the test speed and engine load after the engine had settled for four minutes. The results were calculated using ICEngineSoft Version 9.0 software.

3.7.1. Engine specifications

After the thermal stabilization of the engines, all tests were carried out. The list of engine specifications is in Table 3.2.

All the fuel samples were tested with the 4-stroke engine under the above conditions. Before data collection, the engine was run for at least three minutes in each load scenario. Three replicates of the experiment were performed.

Table 3.2: Engine specifications

Spefification	**Value**
Engine type	Compression-ignition, water-cooled, vertical, 4-stroke, single cylinder, constant speed, DM-10 engine version
Rated power	3.5 kW at 1500 rpm
Bore/stroke	110 (mm)
Swept Volume (cc)	661.452
Compression ratio	17.5:1
Cylinder Bore (mm)	87.5
Connecting Rod Length (mm)	234
Start of fuel injection	26° bTDC
Nozzle opening pressure	200– 205 bar
BMEP at1500 rpm	6.34 bar

Emission values were recorded in triplicate for each setting, and their average was used as a benchmark. Engine performance was evaluated using the following metrics: brake efficiency (BTE), brake specific fuel consumption (BSFC), brake power (BP), exhaust gas temperature,

cylinder pressure (pc), pressure rise rate , net heat release rate , and emissions of carbon monoxide (CO), carbon dioxide (CO_2), unincinerated hydrocarbons (HC) and nitrogen oxides (NO_x) with exhaust gas opacity. During the combustion analysis of yellow oleander biodiesel and its blends, the cylinder pressure was detected with a Kistler 6058A piezoelectric sensor and the signal was acquired with a high-speed data acquisition system. The pressure sensor was installed in the first cylinder head using a glow plug adapter. The charge signal from the pressure sensors was amplified using charge amplifiers from Kistler. The encoder angle was changed using a Leine & Linde incremental encoder to provide a resolution of 0.125 crank angles (CA). Cylinder pressure readings were taken for each test and the average was calculated over 100 consecutive cycles.

An MRU DELTA 1600-V gas analyzer was used to measure the exhaust gas concentration after the exhaust gases were sampled from the exhaust line using a purpose-built device that diverted the exhaust gas to a sampling line without increasing the back pressure. Carbon monoxide (CO), carbon dioxide (CO_2), hydrocarbons (HC), and nitrogen monoxide are the measured gases (NO_x). The Kistler 601A piezoelectric pressure transducer was used to measure in-cylinder pressure from 0 to 250 bar with an accuracy of 1.12% and a sensitivity of 16.5 pc/bar. The Nexus charge amplifier type 2692-A-0S4 was coupled to the pressure sensor. A model LM12-3004NA proximity switch was used to measure the piston top dead center (TDC). The average cylinder pressure was observed over 125 engine cycles. The NI-USB-6210 data acquisition board collected the sensor data via the LABVIEW software connected to the PC.

3.8. Life energy cycle analysis of yellow oleander biodiesel

The study examines the life cycle cost analysis of yellow oleander biodiesel by calculating the total costs of production, investment, operation, and transportation. It estimates the net cost per liter assuming 300 working days per year and a production capacity of 10,000 tons per year.

3.8.1. Life Cycle Analysis methodology

According to the LCA methodology (ISO 14040, 2006, ISO 14044, 2006), allocations for production costs and life cycle resource (or energy) consumption are distributed proportionally (Cristóbal, 2016). Yellow oleander biodiesel and glycerol are the main products in biodiesel production. The study divided resource (energy) consumption and production costs using economic allocation. The resource consumption and energy loads were shared in this way, using the market prices of the by-products as parameters. Most importantly, energy use and economic allocation help determine the most economically viable method of using biodiesel and also educate decision-makers on the financial implications of proposed policies.

3.8.2. System boundaries

In this study, the following life cycle stages and sub-processes are examined: (i) cultivation of the yellow oleander; (ii) extraction of the oil from the yellow oleander; and (iii) generation of the biodiesel by trans-esterification reactions.

The system boundaries for the generation of yellow oleander biodiesel are presented in Figure 3.4

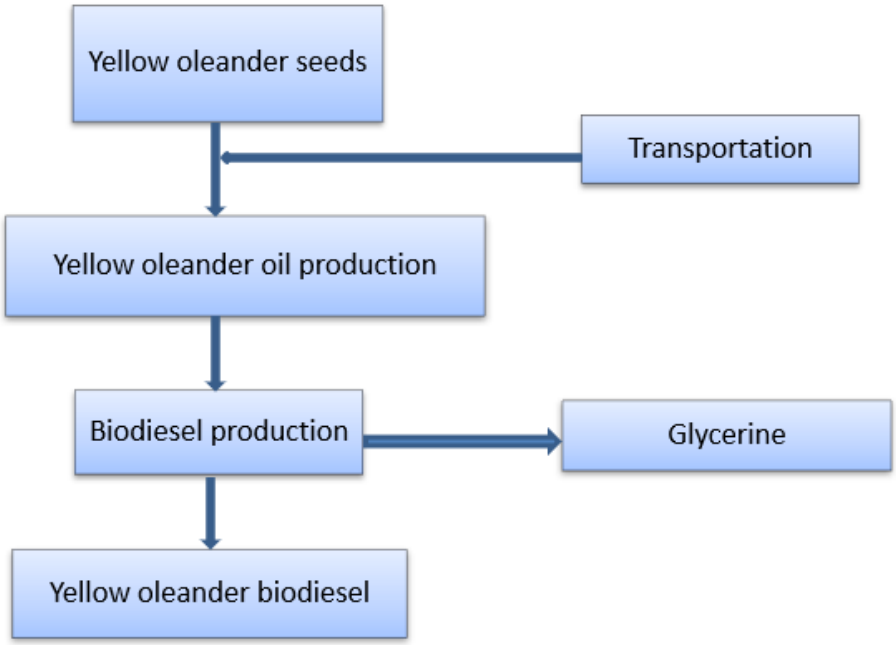

Figure 3.4: System boundary of yellow oleander biodiesel production

This analysis considers the yellow oleander plantation stage and the transit of yellow oleander seeds to biodiesel plants at the system boundary. First, the yellow oleander fruits were harvested and peeled to extract the seed from the skin. After drying, the seeds were pressed to make oil from them and filtered to remove contaminants.

3.8.3. Data Collection

The latest market prices and test results as well as research reports, technical notes, expert reports, and other sources were used to compile the data. Without specific information about the facts, assumptions must be made on the basis of comparable facts (Ong *et al.*, 2012). In addition, the most important data and the effects of deviations from real values must be identified using a sensitivity analysis. Analysis of the Yellow Oleander biodiesel plant was primarily based on the production capacity of the plant. A typical production capacity of 10,000 tons was assumed.

3.8.4. Life cost analysis

Capital and operating costs, such as those for the processing plant, services, catalyst, raw material, and product storage, and buildings, affect the price of biodiesel. The manufacturing process uses oil and alcohol as raw materials, mainly ethanol, and methanol. The by-product glycerin can be used to reduce costs or as an additional source of income in the production of biodiesel. the production of biodiesel and glycerine from vegetable oil and methanol as well as their yield and quality (Ben-iwo *et al.*, 2016).

3.8.4.1. Assumptions for life cost analysis

In the LCA, the following assumptions are made,

a) The Yellow Oleander Biodiesel Production Plant produces 10,000 tons of biodiesel annually on a 6,000-hectare farm. One hectare of yellow oleander yields about 3500 kg of dried plant material and 1750 litres of oil. This means that the facility will produce 1,0500,000 litres of yellow oleander oil annually as yellow oleander trees are planted at a density of 3,000 yellow oleander plants per hectare.
b) The soil quality and rainfall of the plantations are average. It also takes 5 to 10 years for the yellow oleander plant to reach full maturity, at which point full seed production can be expected.
c) No pesticides, insecticides, or herbicides were used on the crops.

3.8.4.2. Phases of yellow oleander biodiesel life cycle

The LCA of the yellow oleander system included

a) Cultivation phase: This stage involves growing seedlings in polybags at a nursery, transporting them to the planting site, digging pits, filling pits with nearby farmyard

manure, planting the seedlings, providing life-saving irrigation for the first two years of summer, and harvesting fruit for oil production after five to ten years. It is also about energy input and output and the associated emissions.

b) Oil extraction phase: Seed transport to the oil extraction facility, energy input and output, and released emissions are included in this phase.

c) Esterification phase: This phase includes the process of converting oil into biodiesel, the chemicals used, and the energy input, output, and associated emissions.

d) Combustion/usage phase: In this phase, biodiesel is incinerated in an engine, generating energy and emitting emissions (Lokesh *et al.*, 2015).

3.8.4.3. Estimation of the cost of biodiesel production

The sum of all running costs of a biodiesel production plant forms the total production costs. These include, but are not limited to, labor, maintenance, insurance, facility overheads, contingencies and general expenses including those related to administration, sales, and marketing. It also includes costs related to the recovery of the capital investment (Karmee *et al.*, 2015).

The manufacturing costs of an integrated strategy for yellow oleander biodiesel are evaluated using key figures in the cost-of-living analysis. The Total Capital Investment (TCI) is determined by Equation 3.41, which is the sum of the following three terms:

Total Capital Investment (TCI) = Fixed Capital Investment (FCI) + Working Capital (WC)

FCI = Direct Costs (DC) + Indirect Costs (IC) ……..…Equation 3.41

Or Total Capital Investment (TCI) = Direct Costs (DC) + Indirect Costs (IC) + Working Capital (WC) ……..…Equation 3.42.

Working Capital (WC) Include; raw materials, stock, and among others. About 10 - 20% of TCI (Zuorro *et al.*, 2020).

Fixed Capital Investment (FCI), which refers to the amount of money required to pay for the equipment, pipelines, electrical installations, land, civil works, legal fees, and control systems; Working Capital Investment (WCI), which refers to the amount of money required to cover operating costs before product sales begin; and start-up costs (SUC), which include personnel costs.

3.8.4.4. Profitability Analysis

The profitability of the proposed yellow oleander biodiesel production plant was evaluated using ROI. Equation 3.43 represent the investment criterion used to include return on investment (ROI), gross income (GI), and net profit (NP).

$$ROI = \frac{NP}{TCI} \times 100 \quad \text{.....Equation 3.43}$$

Where TCI stands for Total Capital Investment, ROI for Return on Investment, NP for Net Profit (Oyegoke & Geoffrey, 2022).

3.8.5. Energy balance calculation

Energy balances deal with the reduction of nonrenewable fossil fuels in the production chain when compared to biodiesel. The energy balance of yellow oleander biodiesel was evaluated using the net energy yield ratio (NER). The net energy yield ratio (NER) was computed using

Equation 3.44:

$$NET = \frac{Energy\ content\ in\ biodiesel\ (MJ/L)}{Energy\ content\ \ fossil\ \ fuel\ (MJ/L)} \quad \text{.....Equation 3.44}$$

The energy output was obtained from the module used in this study. The values of NER is categorized as either energy gain if the value was greater than 1 or energy loss if it is less than 1.

3.8.5.1. System inputs for energy balance

Following are seven criteria that can be used to categorize energy consumption/inputs from the plant nursery to the transesterification process to obtain yellow oleander biodiesel:

a) Plant nursery: It takes energy to prepare the soil, fill soil bags with soil, water the soil bags, use manpower and machinery, and provide security and care for up to a month. Irrigation, fertilizer, machinery for plowing, and labor for all tree nursery activities are the four main types of energy use (Singh, 2018). For Ferguson tractor models from the MF 1200 series, the average fuel consumption per hectare of work was 23.58 L ha^{-1}.

b) Plantation: Up to a year's worth of energy-related factors, including land type, preparation of the land, irrigation, care, and safety, are examined. The nursery uses four different forms of energy inputs, including personnel for all activities, irrigation, machinery for plows, and manures. The yellow oleander tree is a perennial plant, it continues to grow.

c) Development: Growing the plants for up to three years with restricted rigorous labor input during the growth period of up to two years.

d) Seed Collection: Since manual labor is used for seed collection, drying and de-husking, no mechanical inputs are considered.

e) Transfer of Seeds: When transporting seeds from the field to the biodiesel plant with a tractor vehicle with an internal combustion engine, the energy consumption is considered.

f) Oil Extraction: For the energy calculation, an oil expeller with a capacity of 1 ton of seed per hour is chosen.

g) Transesterification: The energy in alcohol utilized in the transesterification process is not considered here because glycerine is created as a by-product in an amount corresponding to the alcohol during the chemical reaction. The sum of the energy inputs of all sub-processes determines the total energy requirement for the life cycle of biodiesel.

h) The amount of NPK fertilizer needed is equal to the amount of seedcake used to maintain balanced fertilizer usage during planting.

i) This analysis does not consider the energy expended on material preparation or the equipment required to grow the yellow oleander plant.

j) The energy released during the combustion of the cake to create useful heat or power is not considered.

3.8.6. Mathematical modelling

The mathematical models of Yadav and Singh (2010) were applied. The life energy cycle was evaluated using formulas for different plant growth phases and the conversion of biomass into biodiesel.

3.8.6.1. Plant nursery

For a month, the energy expenditure for soil preparation, filling the soil bags, watering the soil bags, labor, maintenance and safety are considered (Yadav & Singh, 2010).

3.8.6.2. Ploughing

The first step is to prepare the ground for a nursery, and the energy used by a tractor for ploughing is given by Equation 3.45.

$$E_{N1} = v_f \times \rho \times CV \times k \quad \text{.....Equation 3.45}$$

Where; E_{N1} is energy input in ploughing for nursery (MJ), ρ is the power consumed in oil extraction (kWh/ton of seed), CV = calorific value of diesel fuel (MJ/kg) and k = 1.0, for normal soil (Yadav & Singh, 2010).

3.8.6.3. Irrigation

Using a water pump of 1 kWh that can move 1000 kg of water in 1 hour while assuming standard water availability, nursery plants require 0.5 kilograms of water per plant during the rainy season. Therefore, the energy consumed during irrigation is calculated using Equation 3.46.

$$E_{N2} = 3600 \times R_p \times t \times d \times r \quad \text{.....Equation 3.46}$$

Where; R_p is rating of water pump (kWh), t denotes the time taken in hours, d represents the normal depth up to 80 m and r = 2.5 (Yadav & Singh, 2010).

3.8.6.4. Manpower

According to Laureen Sherwood's book "Fundamentals of Physiology: A Human Perspective," a human worker uses 1 MJ/h of energy for normal labor, 0.84 MJ/h for moderate work, and 1.2 MJ/h for heavy activity. Therefore, Equation 3.47 determines how much energy is expended by labor based on the above estimates.

$$E_{N4} = E \times \left[\left(l_1 \times t_1 \right) + \left(l_2 \times t_2 \right) + \left(l_3 \times t_3 \right) + l_4 + l_5 \right] \times k \quad \text{..... Equation 3.47}$$

Where, E stands for the usual rate of 1 (MJ/h) and E for the energy expenditure rate (MJ/h). $l_1 = 1.0$ is the determining factor for the labor employed to plow the field. $l_2 = 1.2$ is a consideration for the labor employed when producing soil using manure. $l_1 = 1.0$ is the determining factor for the labor utilized to fill soil bags. $l_4 = 1.0$ is the labor-type factor for watering the plants, and irrigation

and $l_5 = 1.0$ is the labor-type factor utilized for one month for care and safety. The sum of the energies in equations 3.45, 3.46 and 3.47 is the total energy supplied to the nursery. Equation 3.47 illustrates the calculation.

$E_N = E_{N1} + E_{N2} + E_{N3} + E_{N4}$ ……. Equation 3.48

Where; E_N is the energy input in nursery (MJ), E_{N1} is the energy input in ploughing for nursery (MJ), E_{N2} is the energy input in irrigation for nursery (MJ), E_{N3} is the energy input in manures for nursery (MJ) $(E_{N3} = 0)$ and E_{N4} is the energy spent in manpower for nursery (MJ) (Strategy, 1975).

3.8.6.5. Plantation

Factors such as soil type, soil preparation, irrigation, maintenance, and safety are analyzed for energy use in planting and maintenance for up to 1 year. The calculations are identical to those of a nursery, but instead a plantation covers a unit area (i.e., 1 ha). As a result, the total energy can be determined using Equation 3.49.

$E_p = E_{P1} + E_{P2} + E_{P3} + E_{P4}$ ……. Equation 3.49

Where; E_p denotes the energy input in plantation and management for 1 year (MJ), E_{P1} represents the energy input in land preparation (MJ), E_{P2} is the energy input in irrigation (MJ), E_{P3} denotes the energy input in manures (MJ) and E_{P4} denotes the energy spent in manpower (MJ) (Yadav & Singh, 2010).

3.8.6.6. Growth

Care and safety are taken care of from the first year of a plant's existence until the third year. Therefore, the input for two years of expansion is manpower. Thereafter, no additional energy supplies are required. Although the tree receives enough rainfall and biomass to support its growth, some water sprays are applied annually. In the first two years of the plantation's life, up to three years, two hours of work per day are required for maintenance and safety. The total energy required for safety and care, as well as water sprays, is based on 2.5 times greater water consumption than in plantations. The energy for growth was calculated using Equation 3.50.

$$E_G = E \times t \times 2.5 \times E_{P2} \quad \text{..... Equation 3.50}$$

Where; E_G represents the energy input in growth for second and third years (MJ) (Yadav & Singh, 2010).

3.8.6.7. Seed collection

The collection n of kernels, drying, de-husking, and seed drying were done manually. During the harvest season, kernels are gathered twice and left for at least 4 days to dry in the sun. This was followed by physically dehusking the seed kernels (Yadav & Singh, 2010).

Finally, drying of the seed is done for 2 days. Equation 3.51 was used to determine how much energy was needed for seed harvesting in total.

$$E_{SC} = E \times (t_1 + t_2 + t_3 + t_4) \times k \quad \text{.....Equation 3.51}$$

Where; E_{SC} is energy for seed collection, and t_1 , t_2 , t_3 and t_4 time in hours for respective work.

a) t_1 is the time required for the kernel collection, one collects 40 trees every day and the second collection takes 75% of the first;

b) t_2 is the time taken for drying of seed kernels (h) (four workers for 4 days);

c) t_3 is the time it takes to hull the seeds (h); Assuming a worker can peel 50 kg per day and get a seed yield of 24 kg per tree, it would take 75 days in total;

d) t_4 is the seed drying time (h) (five workers for two days) (Yadav & Singh, 2010).

Where, t_1 is the time in hours required to collect the seeds, assuming that a worker collects 40 trees per day and that the second collection is 75% of the first, t_2 is the time in hours required to dry the fruit. Four workers are required for four days, t_3 is the time in hours required to de-husk the seeds from the fruit and t_4 is the time in hours required for seed drying. Four workers are required for two days.

3.8.6.8. Transportation of seeds

The amount of energy used to transport seed from the field to the biodiesel plant using a combustion engine-powered tractor was examined. The seeds are moved to the biodiesel production facility, located 2-4 km away, after drying. Transesterification and oil extraction take place at the same location. A tractor is used to transfer seeds to the factory; this process requires 30 minutes and uses 2 liters of diesel. It takes two people four hours to load and unload the truck. The study used Equation 3.52 to estimate the energy needed to transport seeds.

$E_{TP} = v_f \times \rho \times CV + E \times t$ ……..Equation 3.52

Where; E_{TP} is the energy input for the transportation of seeds (MJ) and v_f is the volume of diesel fuel consumed per hectare in litres (Yadav & Singh, 2010).

3.8.6.9. Oil extraction

A 1 ton/hr oil extraction device extracts the yellow oleander oil seed. Equation 3.53 gives the energy required for the extraction.

$$E_{OE} = (P \times M + E \times t) \times y \quad \text{.....Equation 3.53}$$

Where E_{OE} is the energy input for oil extraction (MJ), *t* is the man-hour time taken in oil extraction., P is the power consumption in oil extraction (kWh/ton of seed), and M is the total mass of oil in ton (Yadav & Singh, 2010).

3.8.6.10. Transesterification

The yellow oleander biodiesel production plant, with a capacity of 100,000 tons per year and a conversion efficiency of 92%, consumes 36 kWh of energy for each ton of oil produced. Equation 6.0 calculates the energy necessary for the transesterification process. It is assumed that two men are needed for every 2 working hours. Equation 3.54 gives the energy required for the transesterification process.

$$E_T = P \times M + E \times t \quad \text{.....Equation 3.54}$$

Where *t* is the transesterification process's man-hour. This does not consider the energy that alcohol contains that is used in the transesterification process assuming that glycerine is created as a byproduct of the chemical reaction in an equivalent quantity (slightly less than the mass of alcohol). The processes as mentioned above will determine the overall amount of energy needed to produce biodiesel.

Total energy demand/input in the life cycle of the biodiesel production can be calculated using some of the above equations and given by Equation 3.55;

$$E_{INPUT} = E_N + E_P + E_G + E_{SC} + E_{TP} + E_{OE} + E_T \text{ ……..Equation 3.55}$$

This is the total energy requirement by the system under consideration (Yadav & Singh, 2010).

3.8.6.11. System Outputs

The yellow oleander biodiesel contains the energy given by Equation 3.56.

$$E = CV_{YOBD} \times T \times 1000 \text{ ……Equation 3.56}$$

Where CV_{EED} is the calorific value of the yellow oleander biodiesel in MJ/Kg and T is the quantity of biodiesel in tons.

Putting into consideration the brake efficiency of the C.I engine, the output energy can be calculated using the Equation 3.57.

$$E_{output} = 0.20 \times E^{'} \text{ ……..Equation 3.57}$$

Where; $E^{'}$ energy contained in biodiesel produced from 1 ha land crop and E_{output} = total energy output (MJ) (Singh, 2018).

3.8.6.12. Net Energy Ratio

The relationship between energy input into a system needed to release useable energy and the usable energy itself is expressed by the term "net energy ratio" (Stamenkovi *et al.*, 2012). This gives the fuel's capacity for regeneration and the percentage of energy required for its conversion into usable fuel. Equation 3.58 is used to calculate the Energy Ratio (R).

$$R = \frac{E_{output}}{E_{input}} \text{ ……..Equation 3.58 (Singh, 2018).}$$

CHAPTER FOUR

4.0. RESULTS AND DISCUSSION

In this chapter, the results of a study on the use of yellow oleander seeds (*Thevetia peruviana*) as feedstock for biodiesel synthesis are presented. The study explores the thermodynamic and kinetic aspects of oil production, focusing on the physicochemical properties of yellow oleander oil, eggshell-derived nanoparticles, and biodiesel. This study also included the physicochemical properties, engine performance, combustion and emission properties, and life cycle analysis of the yellow oleander biodiesel prepared.

4.1. Extraction of yellow oleander oil

4.1.1. Pre-treatment

The determined average dry matter content of the yellow oleander seeds was 1.75 ± 0.07%. This is within the maximum moisture content in biodiesel allowed by ASTM biodiesel standards (D 2709) of 0.05% (Jonas *et al.*, 2020). Removing moisture from seeds by drying is a critical step in oilseed pretreatment. This is because the moisture content is one of the factors that determine the lifespan of a seed, as well as the quantity and quality of oil extracted (Yusuf & Widyanie, 2019). Mold, germs, heat, and insects quickly damage seeds with high moisture levels. The moisture content of the oil hydrolyzes the triglycerides and produces free fatty acids (FFA), making it unusable for biodiesel production (Enrica *et al*., 2020).

4.2. Optimization of the extraction of yellow oleander oil

Optimizing seed oil extraction is critical for economic, environmental, and industrial reasons as it maximizes oil yield and contributes to greater profitability in the oil production industry. Increasing oil production maximizes resource efficiency and makes production sustainable. It

minimizes waste and maximizes the utility of biomass, resulting in cost reductions in energy, solvent consumption, and operational costs (Nde & Foncha, 2020).

The conventional solvent extraction (CSE) process involves oil seed cleaning and conditioning, oil extraction, and miscella separation. Efficient extraction depends on the solvent's ability to dissolve oil, and the quality of crude oil and meal depends on solvent type, reaction temperature, and seed pretreatment (Nde & Foncha, 2020)**.**

4.2.1. Effect of solid/solvent ratio

The result obtained for the effect of the volume of solvent on the oil yield is in Figure 4.1 and Table 4.1 in the appendix.

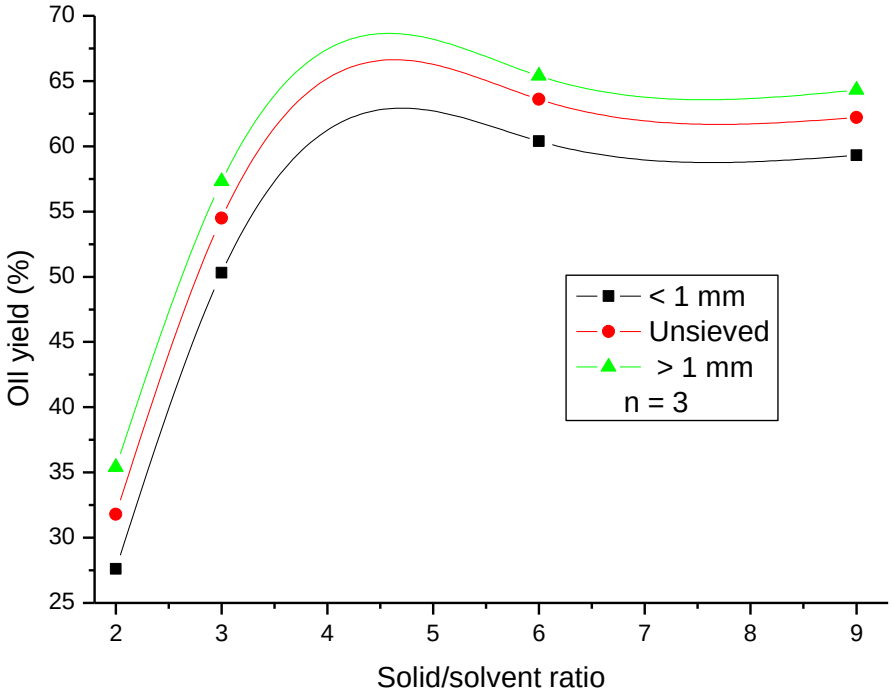

Figure 4.1: Effect of solid/solvent ratio

The extraction of oil increased gradually for all particle sizes, varying from < 1 mm, unseived, to > 1 mm, due to agglomeration and reduced contact surface between meal and solvent. The optimal yield was, 62.9, 66.4, and 69.0 % at a solid/solvent ratio of 1:4.5. The solid-to-solvent ratio in oil extraction improves solvent availability, mass transfer, and efficiency, but ratios that are too high can reduce oil concentration. Smaller particle sizes increase the solvent surface area, exposing more matrix, facilitating faster diffusion and oil mass transfer, and allowing solvent penetration into less accessible areas (Panchal, 2014).

Elkhaleefa & Shigidi (2015) studied the optimization of sesame oil extraction. They examined different ratios from 1:1 to 8:1. They observed a maximum extraction yield of 37% oil at a ratio of 6:1, and further increasing the amount of solvent had no effect on extracting more oil.

4.2.2. Effect of particle size and temperature

The study examined the impact of meal particle size and temperature on the optimal extraction conditions for yellow oleander oil, as depicted in Figure 4.2.and Table 4.2 in the Appendix.

The optimal yield for all sizes was at 345 K. The amount of yellow oleander oil produced increased from 63.3, 67.7 to 69.3 %. The larger meal size of > 1 mm had the highest yield, followed by the unsifted particles and the particles of l < 1 mm had the lowest oil yield. There was an increase in oil yield at higher temperatures and smaller particle sizes primarily due to improved solubility, larger surface area, and shorter diffusion path length. These factors strengthen the interaction between the solvent and the oil and led to more efficient extraction processes (Efthymiopoulos *et al*., 2018). Oil yield decreased at high temperatures because high temperatures can cause the degradation of heat-sensitive components in the oil and extremely small particle sizes can pose practical challenges and increase processing costs (Baig *et al*., 2022).

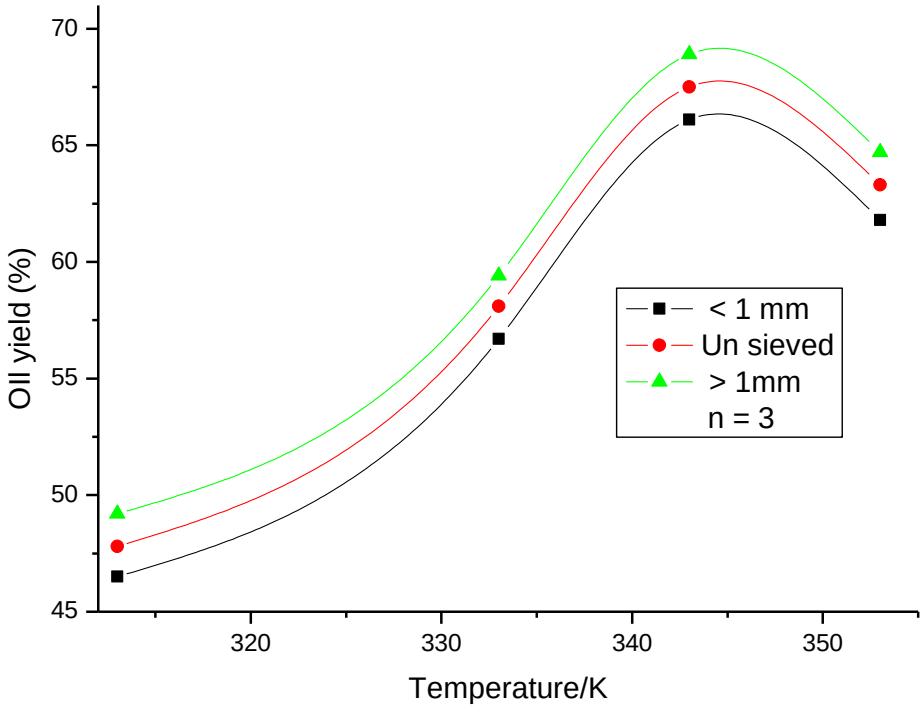

Figure 4.2: Effect of particle size and temperature on yield

Ntalikwa, (2021) studied the optimization of jatropha oil extraction for biodiesel production. He found that oil yield decreased with larger meal particle size due to larger specific surface area, which facilitated the diffusivity of the solvent and resulted in lower oil extraction yield. High temperatures ruptured the cell wall, creating a cavity and migration space for the contents of the oil-containing cells. High temperatures increase the rate of diffusion of the oil while reducing its viscosity (Nde & Foncha, 2020).

4.2.3. Effect of particle size and time

The effect of particle size and extraction time on yellow oleander seed oil yield is as shown in Figure 4.3 and Table 4.3 in the appendix.

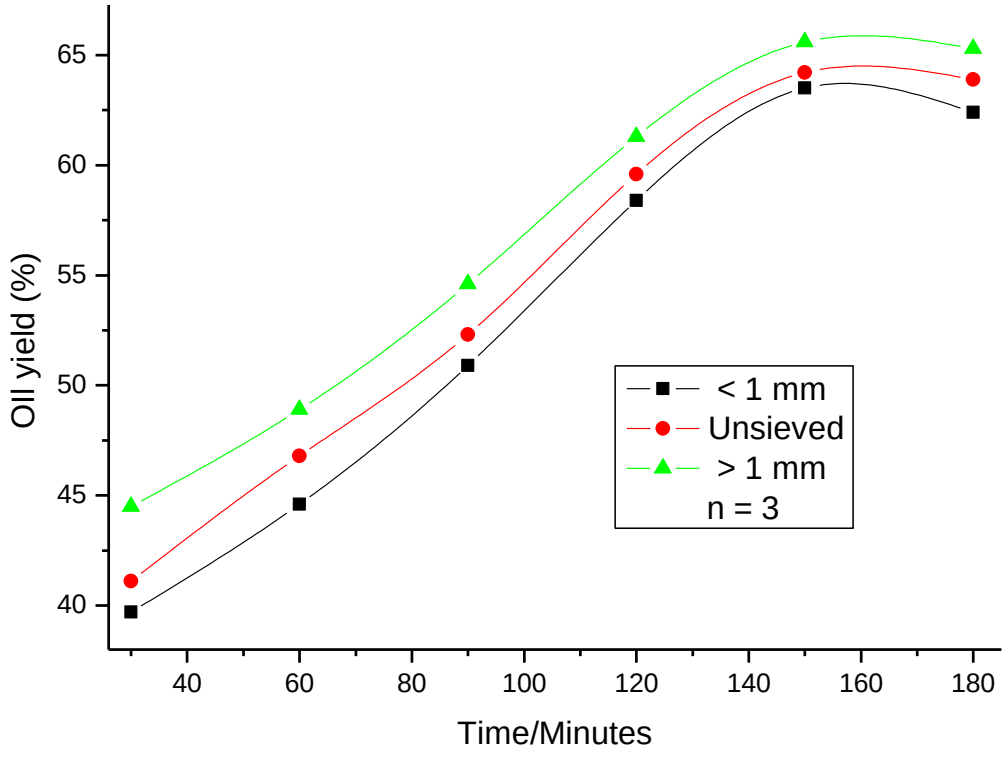

Figure 4.3: Effect of particle size and time on yield

The optimum percentage of oil extracted was obtained at 163 minutes at 66.1% for > 1mm, 159 minutes at 64.6 %, for unsieved and 154 minutes at 63.6 % for < 1 mm. The < 1 mm meal gave the lowest yield due to the low surface area. Longer extraction times allow the solvent to diffuse into solid materials, especially complex matrices with embedded oils. This allows for balance and maximum oil extraction through slow oil release kinetics. Reducing the particle size increases the surface area, exposes more matrix to the solvent, and reduces the length of the diffusion path, allowing for faster solvent diffusion and oil mass transfer (Pattnaik *et al*., 2021). Panchal (2014) studied optimization of oil extraction and characterization from Linn (*Tamarindus indica*) seed oil. He found that the amount of oil extracted by ethanol did not change after 6 hours. The

maximum yield of extracted oil was reached after 6 hours at 8%. He also observed that oil yield increased with increasing reaction time. For a 6-hour reaction, the oil yield increased by 5% compared to the 4-hour reaction sample. In terms of reaction time, the oil yield of 8 hours is the same as the reaction sample of 6 hours. Therefore, 6 hours was chosen as the optimal time for the extraction of *Tamarindus indica* seed oil.

4.3. Kinetics of extraction of yellow oleander oil

The kinetics of oil extraction from the flour is a crucial aspect for understanding and optimizing the efficiency of oil extraction processes. This involves investigating the speed at which oil is released from the flour into the solvent during the extraction process. Diffusion models are used to analyze the kinetics of oil extraction from the meal and predict the influence of various factors and conditions over time (Sangeetha *et al*., 2023). As the solvent penetrates the solid matrix and dissolves the oil, the rate of increase in oil concentration is proportional to the square of the concentration of oil remaining in the meal (Motlagh *et al*., 2022). Using the linear form of the pseudo second order kinetics equation;

$$\frac{t}{C_t} = \frac{1}{kC_s^2} + \frac{t}{C_s} \quad \text{……..Equation 4.1}$$

Where; C_t is the concentration at any given time, C_s is the equilibrium concentration, and k is the extraction rate constant.

The extraction kinetics were analyzed using a second order model shown in Figure 4.4 and Table 4.4 in the Appendix.

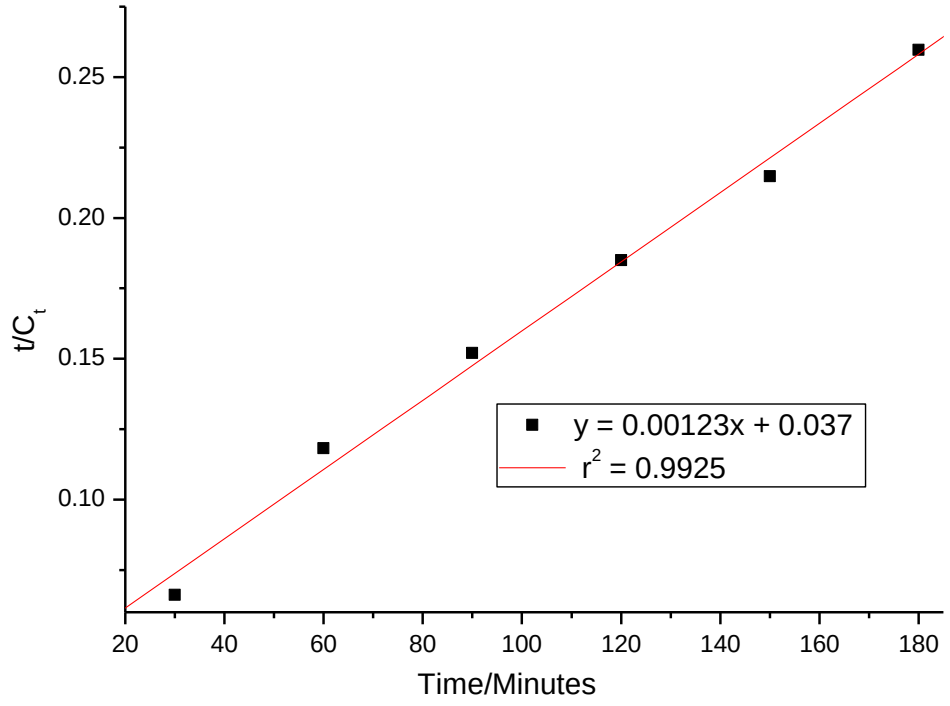

Figure 4.4: Second-order extraction kinetics of yellow oleander oil as determined using a plot of $\frac{t}{C_t}$ against time

The regression coefficient r^2 was 0.9925, confirming that this a graph of second-order kinetics model.

From the linear graph, $0.037 = \frac{1}{kC_s^2} \Rightarrow k = \frac{1}{0.037 \times C_s^2}$ …….Equation 4.2

Solvent extraction capacity, C_s was determined using the gradient as follows;

$\frac{1}{C_s} = 0.00123 \Rightarrow C_s = \frac{1}{0.00123} = 813.0\ g/L$,

The slope $\frac{1}{C_s} = 0.00123$ indicates a slower rate.

From the linear graph, $0.037 = \frac{1}{kC_s^2} \Rightarrow k = \frac{1}{0.037 \times C_s^2}$ …….Equation 4.2

The initial extraction capacity E_i , $E_i = kC_s^2$,was determined from the y-intercept:

$$\frac{1}{E_i} = 0.037 \quad \Rightarrow E_i = \frac{1}{0.037} = 27.03 \text{ g/l.}$$

The initial extraction rate (Ei) was 27.03 $gL^{-1}min^{-1}$; the extraction capacity (Cs), was 813.0 gL^{-1}.

The rate constant (k) were determined using Equation 4.2.

$$k = \frac{1}{0.037 \times (813)^2} = \frac{1}{24,455.85} = 4.09 \times 10^{-5} L/g \text{ min}$$

This means very low sensitivity to changes in oil concentration for the extraction process. The rate constant k is influenced by factors like temperature, pressure, particle size, and solvent properties, which can change the value of k and the overall extraction rate.

Jaber *et al.*,(2015) examined kinetic and thermodynamic studies on the extraction of yellow oleander oil. It was found that a pseudo-second-order kinetic model fit the kinetic process of yellow oleander oil extraction, as Y_e calculated ≈ Y_e experimental and volumetric mass transfer rate coefficient K was ≈ 0.04 h^{-1} at all extraction temperatures.

Agu *et al.*, (2021) studied modeling the kinetic of solvent extraction of *Irvingia gabonensis* seed oil. It was found that the initial extraction rate C_i of the pseudo-second-order models was 5.15 g L^{-1} min^{-1}. However, the oil yield predicted by the extraction capacity of the second-order pseudo-models, Cs, at the same temperature and particle size was 68.52 g L^{-1}. This showed that the second-order model was appropriate for *Irvingia gabonensis* seed oil production, and this could also be applied for the extraction of yellow oleander oil.

4.3.1. The activation energy of extraction

The activation energy of extraction was calculated from the slope of the line using the linear version of the Arrhenius equations. A graph of $\ln k_2$ against $\frac{1}{T}$ is presented in Figure 4.5 and Table 4.5 in the Appendix.

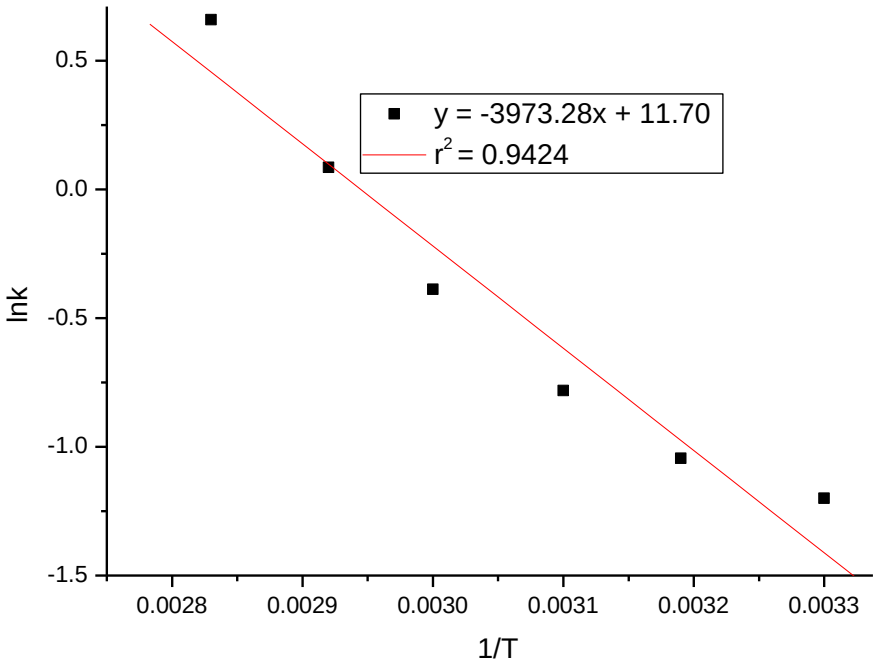

Figure 4.5: A plot of $\ln k_2$ versus 1/T

From the graph the activation energy (E_a) was determined using the slope of the curve as follows;

$\frac{-E_a}{R} = -3973.28, \Rightarrow -E_a$ = -3973.28 × R = -3973.28 × 8.314; $\Rightarrow$

$-E_a$ = -33 033.84 J/mol or E_a = + 33.033 kJ/mol.

The pre-exponential component A, was also determined as follows;

Ln A = 11.70, A = $\ln^{-1}11.70$ = 1.21 x10^5 min^{-1} = 2009.53 /sec.

From the plot the r^2 = 0.9424 indicating the linearity and suitability of the kinetic model in describing the extraction of yellow oleander oil. The calculated activation energy (Ea) and pre-exponential (A) factors are +33.033 kJ/mol and +2009.53 S^{-1}, respectively.

The activation energy and the prepotential constant indicate that the extraction of yellow oleander oil is an endothermic process with moderate activation energy. The high pre-exponential constant implies a significant frequency of molecular collisions and contributes to the overall temperature sensitivity of the extraction process.

Ahmad *et al.*, (2014) studied the kinetics of *Chlorella sp*. oil extraction. They found that the activation energy Ea and the Arrhenius constant A were calculated to be 38.893 kJ/mol and 2684 S^{-1}, respectively. The activation energy and pre-exponential constant for yellow oleander was 2.60% lower than the values for *Chlorella sp*. Oil.

4.3.2. Thermodynamics of yellow oleander oil extraction

The Gibbs model offers a robust method for examining the thermodynamics of oil production, focusing on changes in Gibbs free energy, enthalpy, and entropy. The thermodynamic parameters ΔH, ΔS, and ΔG, were studied using the Vant-Hoff equation. The linear form of the equation were used to solve the thermodynamic parameters of the extraction. Figure 4.5 above was also used in studying the Gibbs free energy equation.

From the linear equation, the ΔH, ΔG, and ΔS values were determined as follows.

$\frac{-\Delta H}{R}$ =-3973.28, $-\Delta H = -3973.28 \times R = -3973.28 = -33033.85\ J/mole$

or 33.03 kJ/mole = $33.03\frac{kJ}{mole} \times \frac{1}{863} \times \frac{1000}{1\,kg} = 38.27\ kJ/kg$

(The calculated relative molecular mass of yellow oleander oil was 863 kg/mole)

The results are summarized in Table 4.6 below.

Table 4.6: The thermodynamics of yellow oleander oil extraction using Van't Hoff Equation

T/K	ΔH kJ/mole	ΔS kJ/kg/K	TΔS kJ/mole	ΔG kJ/mole
303			29.48	8.79
313			30.45	7.82
323			31.43	6.84
333	+38.27	+0.0973	32.40	5.87
343			33.37	4.90
353			34.35	3.92

The positive enthalpy change, $\Delta H = +\ 38.27$ kJ/mol indicates that the extraction process is endothermic and external energy is required. However, the entropy of extraction was determined from the y-intercept as follows.

$$\frac{\Delta S}{R} = 11.70, \Rightarrow \Delta S = 11.70 \times 8.314 = 97.27 J / mole / K$$

The entropy (ΔS) for the extraction of yellow oleander oil was determined to be + 97.27 J/mol/K. This means that the extraction of yellow oleander oil occurs spontaneously.

The thermodynamic parameters for yellow oleander oil extraction: enthalpy (ΔH), entropy (ΔS) and Gibbs free energy (ΔG) were calculated according to each absolute temperature. The extraction of yellow oleander oil is an endothermic process, as shown by the positive value of the

enthalpy change (ΔH = +38.27 kJ/kg), meaning that energy has been absorbed into the seed to release the oil. Furthermore, the positive entropy (ΔS = +97.30 J/mol/K) suggested that the extraction process was irreversible, and the disorder of the liquid molecules increased during the process. This is presented in Figure 4.6.

As the extraction temperature increased from 303 to 353 K, the Gibbs free energy decreased from 8.79 to 3.93 kJ/mol. T higher temperature, the −TΔS term becomes more influential in the Gibbs-Helmholtz equation. If the sum of ΔH and -TΔS results in a negative ΔG, the extraction becomes more spontaneous. This is because the increase in temperature contributes to a higher probability of overcoming energy barriers and allowing the extraction to proceed spontaneously.

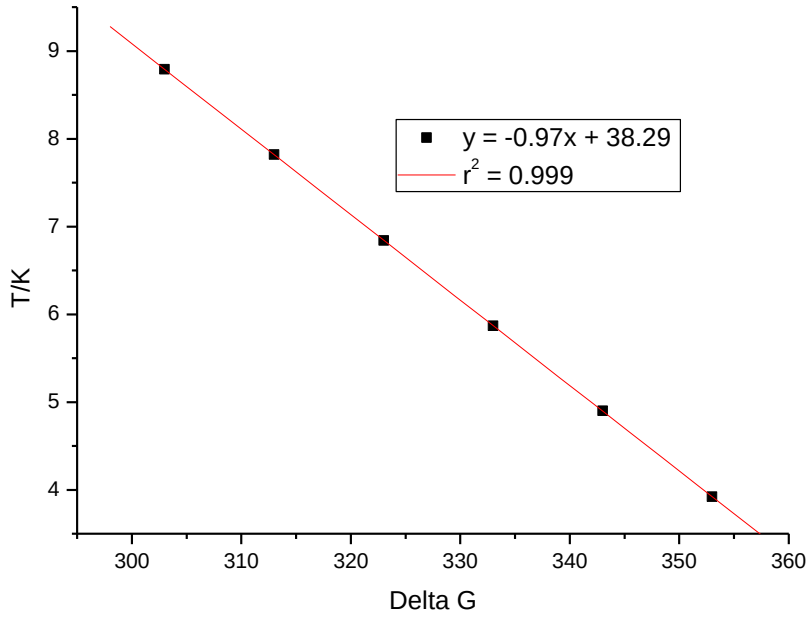

Figure 4.6: A plot of T against ΔG

Jabar *et al.,* (2015) Jaber *et al*., (2015) studied the thermodynamics of extraction of yellow oleander oil. They found that the correlation coefficient of the extraction process r^2 was 0.9912. The

enthalpy and entropy values of extraction of yellow oleander oil were found to be 29.20 and 91.84 $Jmol^{-1}$ respectively.

4.4. Characterization of the nanocatalyst

4.4.1. TGA for incinerated eggshells and the synthesized eggshells nanocatalyst.

Thermogravimetric analysis (TGA), differential gravimetric thermogravimetry (DGT), and differential scanning calorimetry (DSC) are analytical techniques for studying the thermal properties of materials. Figure 4.7 gives TGA results of both the incinerated chicken eggshells and the synthesized eggshell nanocatalyst.

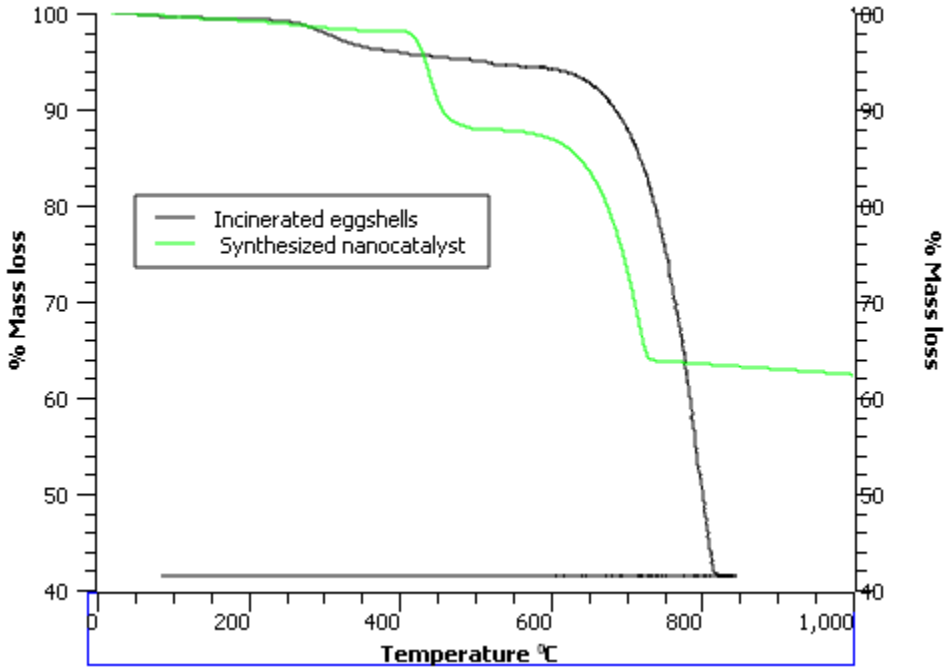

Figure 4.7: The TGA spectrogram for both incinerated chicken eggshells and the synthesized nanocatalyst

TGA, DGT, and DSC analyses are valuable techniques for studying the thermal properties of nanocatalysts. They provide essential information about catalyst stability, decomposition, and

reaction kinetics and contribute to the development and optimization of efficient nanocatalytic systems.

The first weight loss of the prepared nanocatalyst was observed between 25 and 105 °C. This weight loss of 4% was observed as a result of dehydration of the adsorbed water molecules. Another mass loss occurred above 105 °C, indicating thermal decomposition of CTAB molecules used in the synthesis of the nanocatalyst. The second phase is the dehydration of $Ca(OH)_2$, which took place between 390 °C and 450 °C and resulted in a weight loss of 11%. The final 22% weight loss, which occurred above 650°C resulted in the decomposition of $CaCO_3$ with the release of CO_2. The decomposition process for the waste eggshells and the synthesized nanocatalyst took place in a temperature range of 601 to 770 °C and 550 to 700 °C, respectively. As a result, weight losses of $\Delta m = 41.7\%$ and 42.0% were registered.

The calcium carbonate usually decomposes at temperatures above 600 °C with the release of CO_2. However, a small weight loss $\Delta m \sim 2\%$ for water vapor was observed between 726 and 900 °C, where the water vapor trapped in the CaO was finally released.

Ahmad *et al.*, (2015) obtained similar results when studying the thermal decomposition of waste eggshells to form calcium oxide catalysts, saw two significant weight losses. In the initial phase, weight losses were minimal and occurred below 64°C. These were attributed to the loss of organic chemicals used in the synthesis and water molecules adsorbed on the surface of the synthesized nanocatalyst. At 843°C there was a significant weight loss of 42.2 wt% in the second stage. This resulted from the thermal decomposition of the $CaCO_3$ phases and conversion to the CaO phase. Above this temperature, the sample weight does not change. A temperature of 900°C is

recommended as the most suitable calcination temperature to ensure complete conversion of $CaCO_3$ to CaO (Kristl *et al*., 2019).

4.4.2. TG/DTA for the synthesized nanocatalyst

The synthesized nanocatalyst's thermal stability was studied using the differential thermal gravimetric analysis (DTG) measurement. Figure 4.8 shows the results of the analysis.

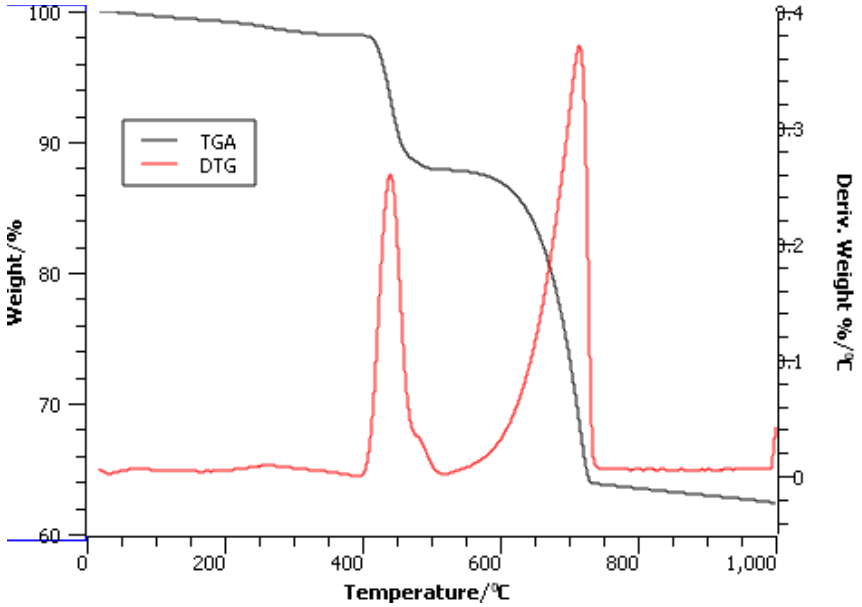

Figure 4.8: The TG/DTG spectrogram of synthesised eggshells nanocatalyst

As the decomposition temperature increased to about 200°C, a small weight loss of ~2.55% occurred due to moisture loss. The second weight loss of ~10.07% w/w was due to the decomposition of CTAB. In the temperature range from ~ 512 °C to ~ 1000 °C, there was a significant weight loss of ~ 25.12%, which was due to a phase transformation from calcium carbonate ($CaCO_3$) to calcium oxide (CaO) with an associated loss of CO_2. The rapid weight loss and endothermic peaks at between ~401°C to ~ 512°C, and from ~600°C to ~750°C. These were due to phase the decomposition of $Ca(OH)_2$ and thermal decomposition of $CaCO_3$.

Differential thermogravimetric (DTG) analysis of burnt eggshells and the nanocatalysts revealed a series of curves indicating the decomposition behavior of these materials. The synthesized nanocatalyst underwent three stages of thermal degradation between room temperature and 400 °C, 400 °C and 700 °C, and between 700 and 900 °C, compared to the incinerated eggshells. These stages were attributed to decomposition of CTAB molecules, decomposition of $CaCO_3$ to CO_2 and water vapor loss of CaO. Furthermore, two large peaks at 420 °C and 700 °C caused by the degradation of $Ca(OH)_2$ and $CaCO_3$ were visible on the DTG curve of the synthesized CaO nanocatalyst

(Fayyazi *et al*., 2018) studied the characterized CaO catalyst from chicken eggshells using TGA/DTG. They observed that a calcination temperature above 800 °C is sufficient to completely decompose chicken egg shells into CaO, resulting in a weight loss of 37.2%. From the weight loss below 400 °C on the DTG curve, the physically absorbed water and organic compounds were removed from the eggshell sample by heating above 400 °C. TGA analysis on fresh eggshells revealed small peaks at 450–500 °C, indicating minimal presence of $Ca(OH)_2$, indicating weight loss.

4.4.3. TGA/DSC for the synthesized nanocatalyst

DSC was used to detect the phase transformation of the synthesized eggshell nanoparticles upon heating. Figure 4.9 shows the differential scanning calorimetry (DSC) results for the synthesized eggshell.

The diagram shows the presence of three endothermic peaks. The first is caused by both moisture loss and the decomposition of CTAB at temperatures of ~117.3°C, resulting in a total weight loss of 1.73%. The second weight loss occurred between ~408.2 and 509 °C, this was due to the thermal

decomposition of $Ca(OH)_2$. This endothermic process is also associated with the transformation of the aragonite to the calcite phase. The mass loss between 600 °C and 867 °C is 47.2%, which is an exothermic process associated with the decomposition of calcium carbonate in CaO with the release of CO_2.

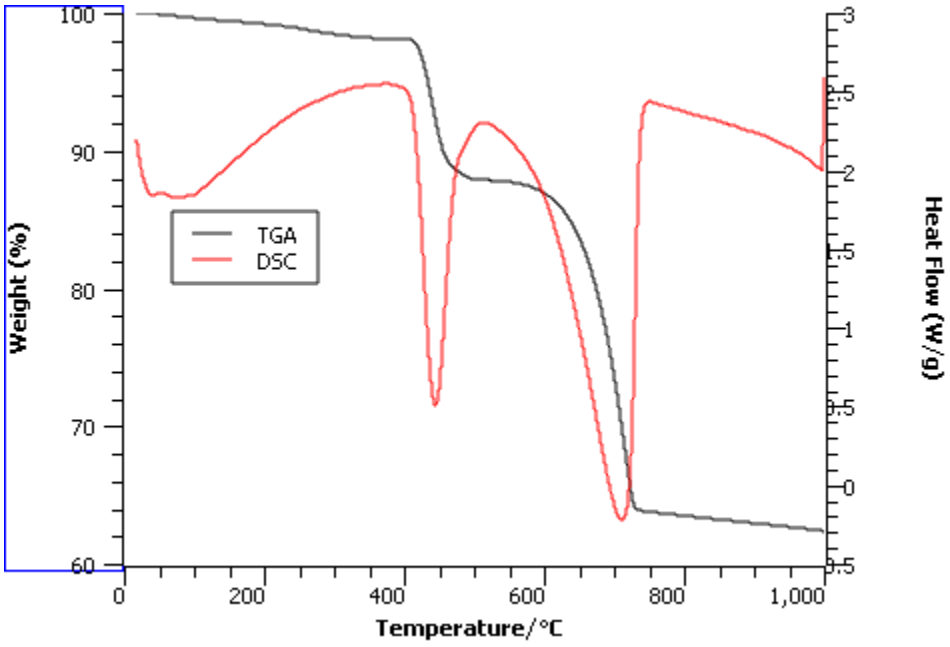

Figure 4.9: The DSC spectrogram for synthesized eggshells nanocatalyst

Praikaew *et al*., (2018) studied the TGA/DSC of dimethyl carbonate synthesized from eggshells using CaO. They observed from the DSC curve that there was an endothermic peak above 800 °C, which confirmed the decomposition of $CaCO_3$ to form CaO.

4.4.4. XRF Spectroscopy

The X-ray fluorescence analyzed the chemical composition of incinerated eggshells and the synthesized nanocatalyst. The summarized results are in Table 4.7.

The calcium oxide content in the synthesized eggshell catalyst calcined at 900°C for 3 hours is 95.52 ± 2.04 % by weight and the rest of the elements and compounds were only 4.48 % by weight. This proves that the chemical composition of the synthetic eggshells changes from calcium carbonate ($CaCO_3$) to calcium oxide when heated. The other main components of the synthesized eggshell nanocatalyst were P_2O_5-2.10 ± 0.09%, Al_2O_3-1.64 ± 2.57 %, and MgO-0.087 ± 0.02%, respectively. The composition of CaO in the incinerated eggshells was 1.73% lower at 90.457. It also contained MgO - 4.38 ± 0.18, P_2O_5 - 2.99 ± 0.12 and Al_2O_3 - 1.66 ± 1.07, respectively.

Table 4.7: The chemical composition of the incinerated eggshells and the synthesized eggshells nanocatalyst

	Percentage of each element in XRF	
Element/ Compound	**Incinerated eggshells**	**Synthesized nanocatalyst**
CaO	90.46	95.52
P_2O_5	2.99	2.10
Al_2O_3	1.66	1.64
MgO	4.38	0.087
Fe	0.35	0.23

Rohim *et al.,* (2014) performed the XRF analysis of calcium oxide catalyst from waste eggshells. After incinerating the eggshells, the CaO content increased to 98.56 % as a result of the conversion of $CaCO_3$ to CaO, with CaO being the most abundant ingredient. Other elements present in eggshell nanocatalysts include; MgO (0.69%), Al_2O_3 (0.1%), SrO (0.051%), and CuO (0.027%). These results differed as follows: CaO was 3.04% lower, MgO - 0.603% higher, and Al_2O_3 - 1.54%

lower than the content in the synthesized nanocatalyst in this study. CaO remains the major componrent of the incinerated eggshells nanocatalyst (Rohim *et al*., 2014).

4.4.5. FTIR analysis of incinerated eggshells and synthesized nanocatalyst

Figure 4.10 shows the FTIR spectra for incinerated eggshells.

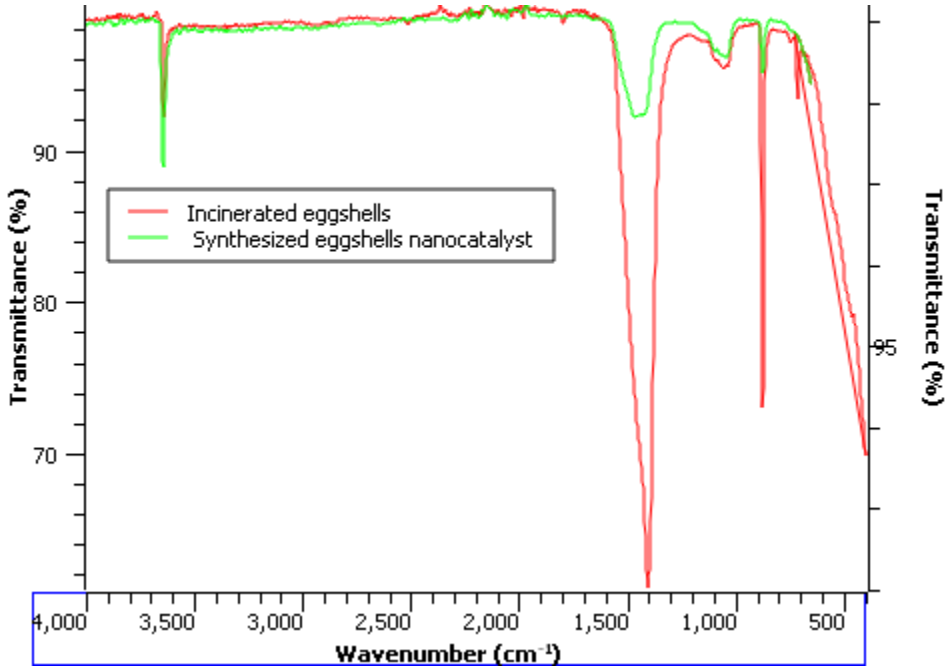

Figure 4.10: The FTIR spectrogram of incinerated eggshells and synthesized catalyst

The spectra showed clear and intense peaks at 1024, 703.9, 697, and 497 cm^{-1} corresponding to the C-O stretching and bending modes of the carbonate vibrational modes. The OH stretching mode associated with water molecules adsorbed to CaO was indicated by the peaks at 1400 and 3649 cm^{-1}.

Mmusi *et al.,* (2021) also studied the FTIR spectrum of CaO NPs and CaO derived from chicken eggshells. They observed that the spectrum of chicken eggshell had a sharp peak at 3614.37 cm^{-1}

caused by the presence of hydroxyl (OH). Another band was observed at 1083.86 cm $^{-1}$ and this was caused by the presence of $CaCO_3$ (Mmusi *et al*., 2021).

Hwidi *et al.,* (2018) also analyzed the FTIR spectrum of the limestone sample and found prominent calcite bands at 1,419, 874.08, and 712.20 cm^{-1}. The peaks of the spectra at 1799 and 2513.04 cm^{-1} provide further evidence for the presence of calcite. By identifying its primary absorption bands, these data indicate that the limestone examined is composed primarily of calcium in the form of calcite. The asymmetric stretching, out-of-plane bending, and in-plane bending of CO_3^{2-} were assigned to the reference bands seen at 1419, 874.08, and 712.20 cm^{-1}, respectively (Hwidi *et al.*, 2018). The study confirms the complete conversion of $CaCO_3$ in eggshells to CaO in nanocatalysts, also observed in the references.

4.4.6. XRD phase Spectroscopy

XRD analysis was aimed at determining the chemical composition, physical properties and crystal structure of the nanocatalysts, as presented in Figure 4.11. below.

The spectrum of the incinerated eggshell calcined at 900 °C had peaks at 2θ = 32.19°, 37.63°, 37.97°; 53.68°, and 67.15°. These correspond to the Miller indices (hkl) at (310), (200), (200), and (222) crystal planes, respectively. The lattice parameters derived align with the standard values in JCPDS 77-9574, which are applicable to a calcite-CaO powder sample. The XRD patterns of the eggshell nano-CaO and the main peak of the calcite phase (2θ = 29.4) were almost identical, suggesting that the $CaCO_3$ phase decomposed to form the CaO phase.

Pan *et al.*, (2018) studied the XRD spectrum of incinerated eggshells. They found that the spectrum for incinerated eggshells consisted of 2θ = 32.3°, 37.5°, 54.0°, 64.3°, and 67.6°, which corresponded to the spectrum of calcium oxide (CaO).

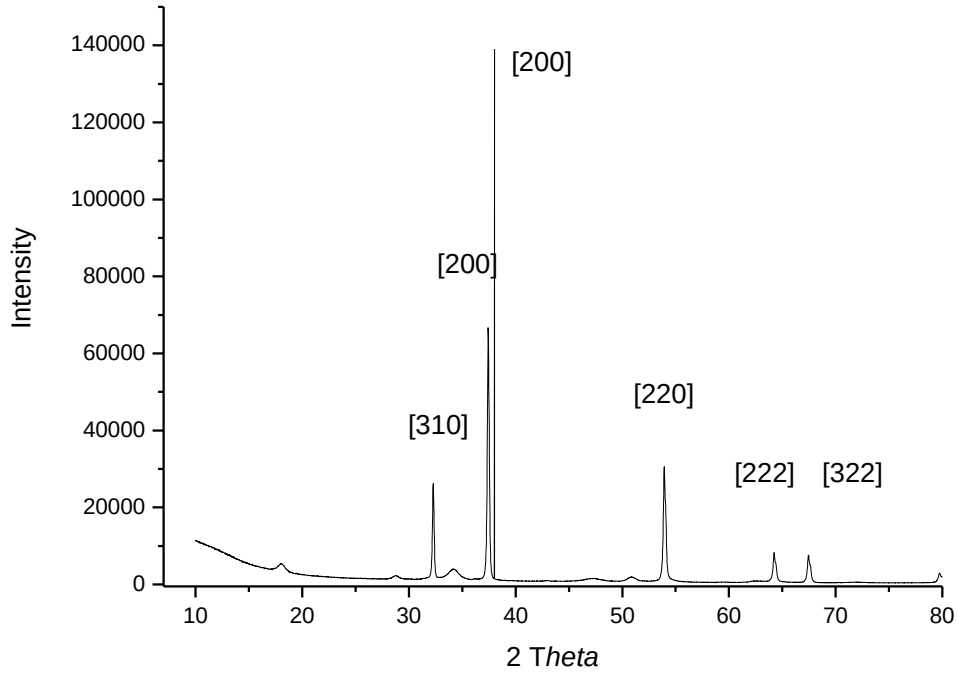

Figure 4.11: XRD Spectra for the synthesized nanocatalyst

Ayodeji *et al.* (2018) also studied the XRD spectrum of calcined eggshell catalysts used for biodiesel production. They also observed peak properties of calcium oxide at 2θ = 29.0°, 32.5°, 47.5°, and 54.0°. The result confirms that the calcium carbonate present in the incinerated eggshells and the synthesized nanocatalyst was completely converted into calcium oxide during the synthesis (Pan *et al*., 2018).

4.4.7. Crystal structure and particle size determination by XRD

The crystal structure of the nanocatalyst was calculated using Miller indices of the lattice plane, results are summarized in Tables 4.8 and 4.9.

XRD investigation revealed that the products are CaO nanoparticles with a lattice constant a = 4.788 ± 0.0204 with nano-sized particles; the d-spacing values in parentheses indicate

corresponding Miller indices. The crystallite size was measured using the Scherrer equation and it was found that the average size (D) of the synthesized CaO nanoparticles was 13.86 ± 0.987 nm.

Table 4.8. Crystal structure analysis of the synthesized nanocatalyst

2θ	$Sin^2\theta$	**d**	$h^2+k^2+l^2$	**Index**	$\frac{Sin^2\theta}{h^2+k^2+l^2}$	**a (Å)**
32.166	0.0767	2.7809	3	111	0.0256	4.8166
37.514	0.1034	2.7657	4	200	0.0259	4.7904
54.008	0.2062	1.6963	8	220	0.0258	4.7979
64.662	0.2860	1.6889	11	311	0.0260	4.7771
67.623	0.3097	1.6953	12	222	0.0258	4.7949
						4.788 ± 0.0204

X-ray diffraction studies show that the synthesized eggshell-derived nanocatalysts were pure face-centered cubic crystals with h, k, l, all odd, or all even cubic (111, 220, and 311) CaO nanoparticles. The study confirmed the presence of CaO (d = 2.7809; 2.7657; 1.6963; 1.6889 and 1.6953) formed as a result of incineration. The crystal structures are in good agreement with the data reported in JCPDS Powder Diffraction Data.

The characterization of the crystal structure of the nanocatalyst prepared from incinerated eggshells is given in Table 4.9

Ayodeji *et al.,* (2018) studied eggshell catalysts used in biodiesel production. They observed that the primary peaks for the calcined eggshell catalyst were measured at 21.4°, 32.5°, 47.5°, and 54.0° which is characteristic of calcium oxide (Ayodeji *et al.,* 2018).

Table 4.9: Crystal structure analysis of the incinerated eggshells nanocatalyst

2θ	$Sin^2\theta$	**d**	$h^2+k^2+l^2$	**Index**	$\frac{Sin^2\theta}{h^2+k^2+l^2}$	**a (Å)**
18.003	0.0245	4.9220	3	111	0.008164	8.5252
23.014	0.0398	3.8612	5	201	0.00796	8.6338
28.724	0.0615	3.1060	8	220	0.007688	8.7852
29.373	0.0643	3.0386	8	220	0.008033	8.5946
29.423	0.0652	3.0162	8	220	0.008153	8.5310
34.08	0.0858	2.6289	11	311	0.007804	8.7194
						8.6164 ± 0.1014

These results confirm the presence of CaO in the incinerated eggshells and the synthesized nanocatalyst.

XRD analysis of the incinerated eggshell nanocatalyst revealed a particle size of 23.1 ± 2.53 nm. They also showed d-spacings of; 4.9220, 3.8612, 3.1060, 3.0386, 3.0162, and 2.6289; corresponding to Miller indices hkl of; 111, 201, 220, 220, 220, and 311, respectively. This was a characteristic reflection of rhomboidal calcite for aragonite and vaterite.

Habte *et al.,* (2020) analyzed the XRD patterns of the chicken eggshell and observed a calcite phase consistent with the rhombohedral calcite. JCPDS PDF Card No. 70-4068 and Space Group no. 225 confirmed this (Habte *et al.*, 2020).

4.4.8. Brunauer-Emmett-Teller (BET) and Barrett-Joyner- Halenda (BJH) Analyses

The surface area, pore volume, and average pore diameter data for incinerated eggshells and the prepared nanocatalyst were determined usin BET and BJH analyses. The results are summarized in Table 4.10 below

Table 4.10: Report of pore structure parameters of the samples

	SAMPLES:	
PARAMETERS:	**Incinerated eggshells**	**Synthesized catalyst**
Surface area ($m^2 g^{-1}$)		
BET surface area	4.44 ± 0.38	5.54 ± 0.48
Pore volume ($cm^3 g^{-1}$)		
Single Point Desorption Total Pore Volume	0.019 ± 0.01	0.017 ± 0.02
Pore diameter (nm)		
Desorption Average Pore Diameter (4V/A by BET)	15.69 ± 0.63	10.04 ± 0.98

BET is a useful tool for measuring surface area, pore volume, and average pore diameter. The incinerated eggshells and the synthesized nanocatalyst had specific areas of 4.44 ± 0.38 $m^2 g^{-1}$ and 5.54 ± 0.48 $m^2 g^{-1}$ The synthesized nanocatalyst has a higher specific surface area than incinerated eggshells, indicating a more extensive surface for transesterification. In the BJH analysis the average pore diameter and pore volume of 15.69 ± 0.63 nm and 10.04 ± 0.98 nm and 0.019 ± 0.01 $cm^3 g^{-1}$ and 0.017 ± 0.02 $cm^3 g^{-1}$, respectively. The average pore diameter values indicate that the pores in incinerated eggshells are larger than those in the synthesized nanocatalyst. Pore volume

values indicate void spaces available for various processes, with incinerated eggshells and synthesized nanocatalyst having similar pore volumes.

The reported average pore diameters of the nanocatalyst range from 2 to 50 nm and represent the mesopore material. Research has proven that metal oxide mesoporous materials are potential catalysts because they are porous structures with uniform mesopores and the surface area to volume ratio and surface area of the materials are high (Qiu *et al.,* 2019).

These large surface areas could increase the number of reactive sites, increase reaction efficiency, and lead to improved catalytic performance (Elías *et al.,* 2016).This confirms the presence of micropores in the incinerated eggshell samples.

Oulego *et al.,* (2020) studied the BET analysis of eggshell-supported catalysts. They observed that the specific surface area (BET area) and pore volume of the calcined eggshell were 4 m^2 g^{-1} and 0.059 cm^3 g^{-1}, respectively. These results are similar to those reported in this study.

4.4.9 BJH Adsorption Cumulative Pore Volume (Larger)

Figure 4.12 gives the pore volume distributions of incinerated eggshells and synthesized eggshells nanocatalyst.

Pore volume and size distributions of incinerated eggshells and the synthesized nanocatalyst were analyzed using the BJH method for the N_2 adsorption branch isotherms. The surface areas for incinerated eggshell and the synthesized nanocatalyst were 4.30 ± 0.57 m^2g^{-1} and 6.07 ± 0.17 m^2g^{-1}, respectively. The synthesized nanocatalysts exhibited a higher specific surface area compared to incinerated eggshells, likely due to nanoscale features and structural changes during the synthesis process.

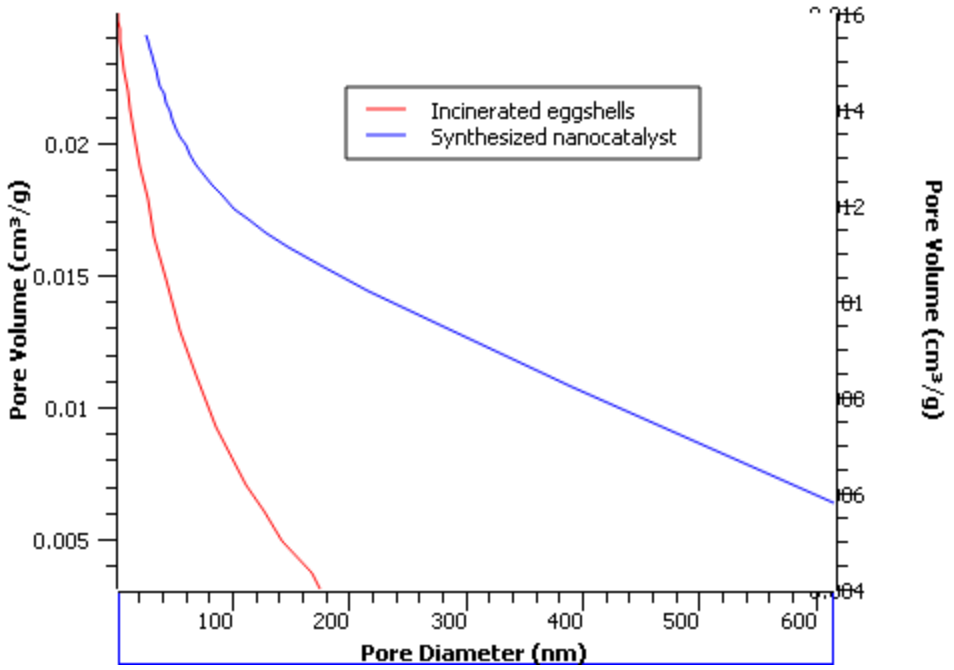

Figure 4.12: BJH desoprtion cumulative pore volume

The porosities according to the pore volume were 0.0082 ± 0.01 cm^3g^{-1} and 0.018 ± 0.0 cm^3g^{-1} (single point at $P/P_0 = 0.99$) at a pore diameter of 100 nm. The synthesized nanocatalyst has higher porosity at pore diameter of 100 nm compared to incinerated eggshells. This suggests that synthesized nanocatalysts have a greater capacity to adsorb gases or other substances at this specific pore size. Furthermore, they were classified as a mixture of microporous, mesoporous and megaporous materials by the International Union of Pure and Applied Chemistry (IUPAC) because their pore diameters ranged from 2 to 50 nm.

Febriansyar *et al*., (2022) study examined the impact of $CaCO_3$ impregnation on the surface area, pores size, and activity of HY Zeolite in the catalytic cracking of palm oil for biofuels. They found that $CaCO_3$ significantly increased Organic Liquid Product and coke production by 79.09% and

2.39%, respectively, as confirmed by BJH analysis and $CaCO_3$ aggregates covering the catalyst surface (Febriansyar *et al*., 2022).

4.5. SEM Spectroscopy

The morphology of powdered CaO prepared from waste eggshells was examined using a scanning electron microscope. Results are in Figure 4.13.

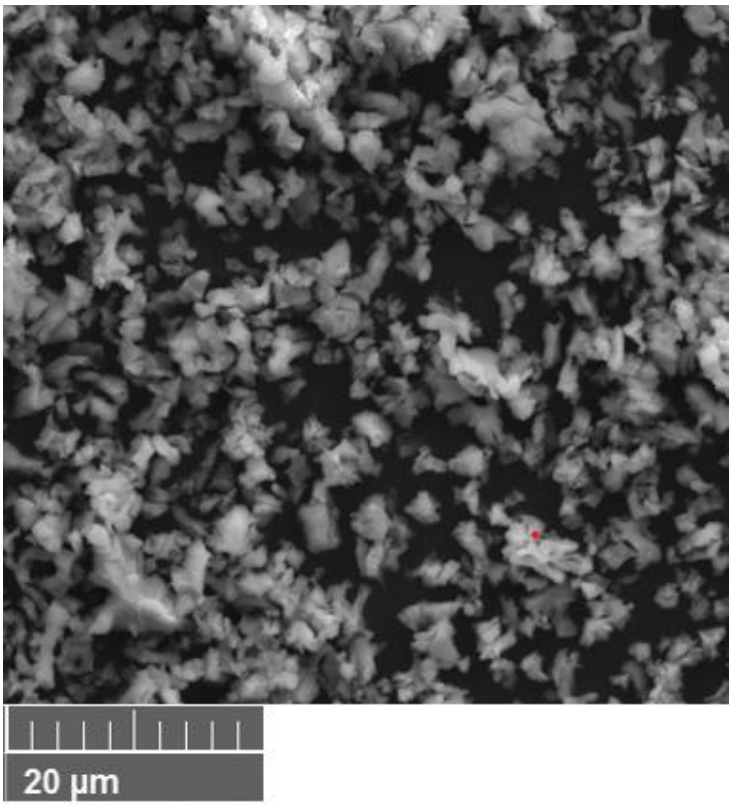

Figure 4.13: SEM images of incinerated eggshells

The image shows how the nanocatalyst particles from incinerated eggshells are roughly flaky and agglomerate. The flaky nature of the particles may expose a larger surface area, potentially affecting the reactivity of CaO. Agglomeration affects nanoparticle interaction with reagents, revealing their polycrystalline nature through clusters of tiny particles. Pandit and Fulekar (2017)

studied SEM images of eggshell waste as a heterogeneous nanocatalyst for biodiesel production. They observed that the images of the nanocatalyst were spherical.

Mmusi *et al.*, (2015) studied the SEM images of chicken egg shell-derived CaO in the production of biodiesel from *Schinziophyton rautanenii*. The images revealed that the CaO particles were granular and amorphous. This is because large amounts of CO_2 gas were evolved during the production of CaO nanoparticles by calcination at 800 °C. The $CaCO_3$ present in eggshells is broken down into CO_2 and CaO, resulting in the formation of nanoparticles.

Similar results were obtained in this research. SEM images of synthesized eggshell nanocatalyst at different scales of 500 μm and HRSEM at 50 000 × are in Figures 4.14. A, and B.

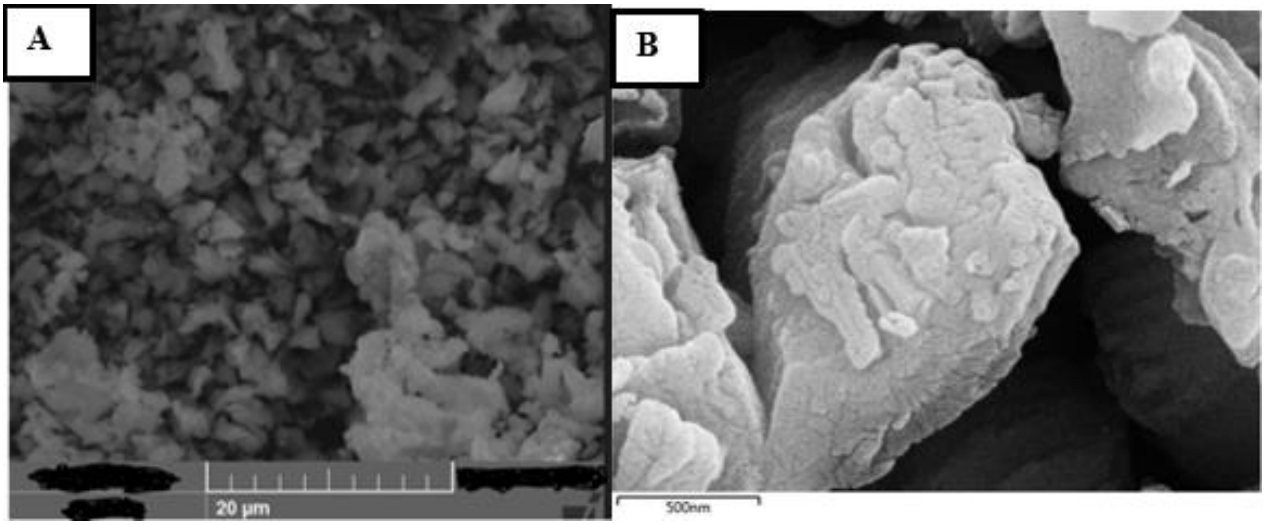

Figure 4.14: SEM Image of synthesized eggshells nanoparticles (a) A - SEM (b) B - SEM image under high magnification (50000 ×)

The SEM images of the synthesized nanocatalyst show that the catalyst possesses highly agglomerated particles, irregular in shape, and the particles exhibited an interconnected morphology. Incineration increases the surface area, making it a potentially better nanocatalyst.

Van der Waals forces of attraction accompany these high surface areas and are therefore responsible for agglomeration (Balaganesh *et al.*, 2018; Wu *et al.*, 2013).

Singh and Verma (2021) studied the morphology of calcium oxide catalysts prepared from eggshells for biodiesel production. The images showed that the CaO granules were irregular in shape and size. This was because the samples were exposed to different temperatures. The granules agglomerated and assumed a porous character at higher temperatures.

4.5.1. EDX Spectroscopy

The EDX spectrum was used to determine the elemental composition of the incinerated eggshells and the synthesized nanocatalyst. Results The results are shown in Figure 4.15 A & B below.

EDX analysis shows calcium peaks at 3.8 keV, indicating a higher concentration of calcium in burnt eggshells, while an oxygen peak at 0.4 keV indicates the presence of oxygen. The elemental composition of the sample is also enhanced by the less intense peaks of Ca at 0.3 keV, 4 keV, and 0.6 keV of the oxygen atoms.

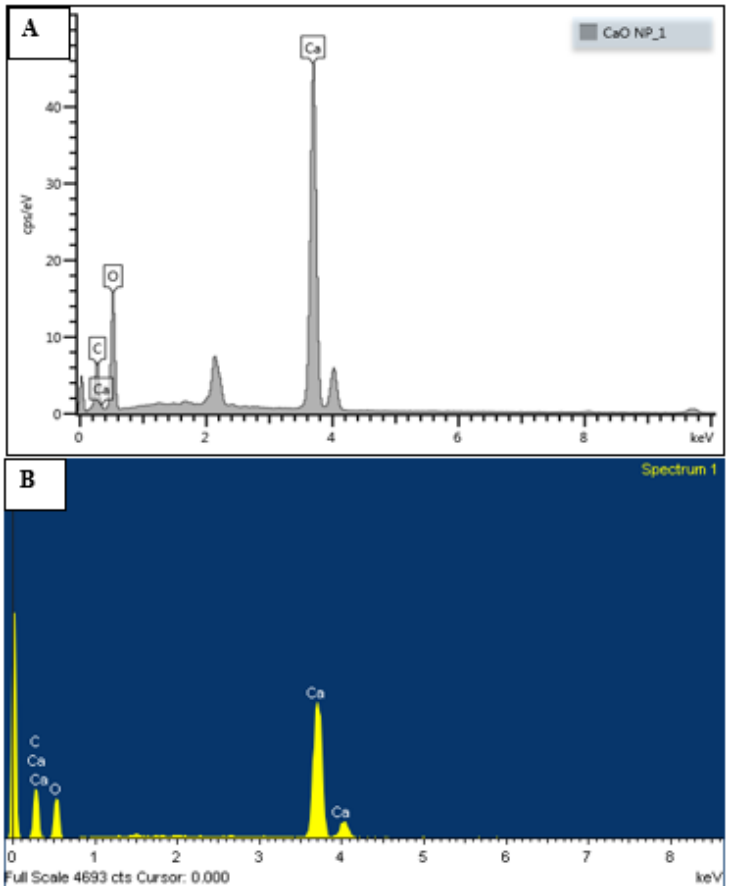

Figure 4.15: (A)- EDX spectrum of incinerated eggshells. (B)- EDX spectrum of synthesized nanocatalyst

The elemental analysis of the chemically produced eggshells nanocatalyst is presented in Table 4.11 (n = 6).

Incinerated eggshells, with a high calcium content (51.99%), are likely composed of calcium carbonate, a common component in eggshells, with oxygen accounting for 32.23%. The synthesized nanocatalyst, with a weight percentage of 44.78% and an atomic percentage of 49.72%, dominates at the atomic level, while oxygen has a weight percentage of 30.31%. The sample's carbon presence is likely due to the use of carbon-based capping agents and the use of carbon-coated adhesive on the SEM Aluminium Tab.

Table 4.11: The EDX elemental analysis of the synthesized eggshells nanocatalyst

	Incinetrated eggshells		Synthesized nanocatalyst	
Element	Av. weight %	Av. atomic %	Av. weight %	Av. atomic %
C	15.78 ± 1.19 %,	24.48 ± 0.11	21.07 ± 1.20	32.56 ± 0.02
Ca	51.99 ± 0.10	60.54 ± 0.13	44.78 ± 0.10	49.72± 0.14
O	32.23 ± 0.14	14.98 ± 0.16	, 30.31 ± 0.25	13.43± 0.21

Mmusi *et al.,* (2015) studied the EDX spectrum of CaO obtained from chicken eggshells for biodiesel synthesis. The spectrum confirmed that CaO was formed in high concentration. The calculated percent atomic compositions for calcium (Ca), oxygen (O), carbon (C), and magnesium (Mg) were 28.15, 64.40, 16.24, and 0.01%, respectively. Confirming that the eggshell ash contained CaO.

4.5.2. TEM Spectroscopy

The CaO particle size distribution of the incinerated eggshells were observed by TEM. The results are presented in Figures 4.16. (A to B) & 4.17 (A to B).

The images confirmed that CaO particles from incinerated eggshells is primarily coagulated rods with a diameter of approximately 7-40 nm.

Pandit and Fulekar (2017), studied the TEM images of waste eggshells for use as a heterogeneous nanocatalyst for biodiesel production. The TEM images revealed a spherical shape of the CaO nanocatalyst with an average size of ~75 nm, and these results were consistent with those determined by XRD analysis.

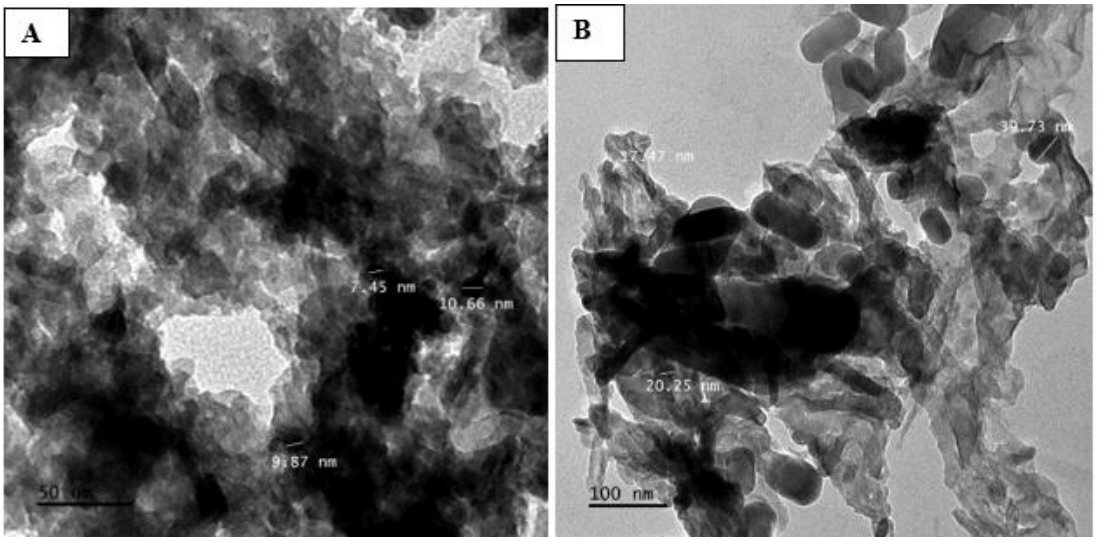

Figure 4.16. (A-B): TEM images of incinerated eggshells

The effect of the bottom-up technique on the synthesis of synthesized eggshell nanocatalysts was also observed using TEM images. These are presented in Figure 4.17. (A to B).

TEM images revealed that the synthesized eggshell nanocatalyst exhibited regular spherical mixtures with needle-shaped agglomerates crystals. These particle sizes ranged from ~13 to 48 nm.

Venkatesh *et al.,* (2018) obtained similar results when examining the TEM image of a CaO nanocatalyst for the production of *Butea monosperma* biodiesel. They observed NP agglomerates with a size of ~10 to 15 nm and showed NP as a cone-like structure. Mesoporous materials, with their large surface areas and well-defined pore structures, are excellent catalysts for various chemical processes.

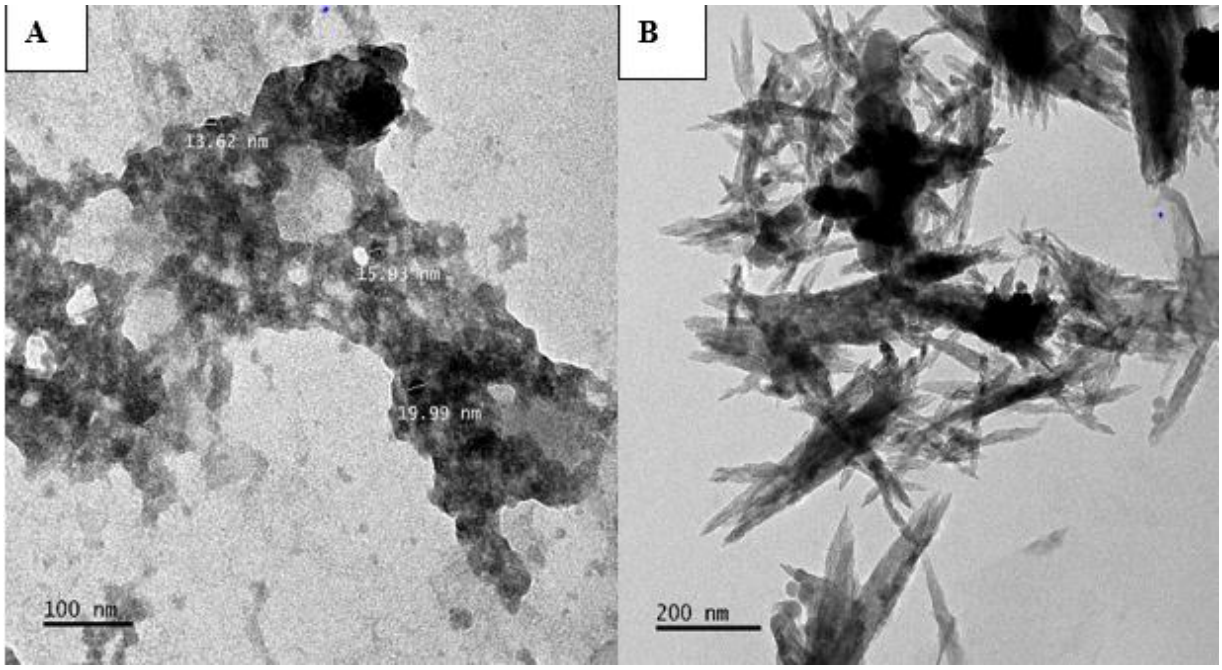

Figure 4.17 (A-B): TEM Images of synthesized nanocatalyst

Mesoporous materials are the ideal choice for use as catalyst supports because of their high surface area and large pore volume. Additionally, the pore shape of these materials can help control reaction selectivity by preferentially adsorbing certain reactants or products (Lan & Zhao, 2022).

4.6. Optimization of the production of the yellow oleander biodiesel

When optimizing using Response Surface Methodology (RSM) with Central Composite Design (CCD) using Design Expert softwares. The data often relates to the factors you are studying and their impact on the response variable. Results obtained include, but are not limited to, factor levels, experimental analyses, response data, predicted responses, residuals, statistical parameters, contour and surface plots, optimal conditions, and sensitivity analyses. Design-Expert 13 software was used to generate data for optimal conversion and yield of yellow oleander biodiesel.

Details of the independent variables used in the study are given in Table 4.12 below.

Table 4.12: Experimental design for yellow oleander biodiesel production

Variables	$-\alpha$	**-1**	**0**	**+1**	$+\alpha$
Time (Min)	6.36	20	40	60	73.64
Temp /°C	43.18	30	50	70	76.82
Catalyst (%)	0.318	1	2	3	3.68

The ideal experimental conditions were chosen considering three independent variables: reaction time (A), reaction temperature (B), and catalyst concentration (C), The model consists of six-axis points, six midpoints, and sixteen factorial points. The response surface regression technique and the second order polynomial formula were both used to examine this data using Equation 4.3.

$$y = b_{\circ} + \sum_{i=1}^{n} b_i x_i + \sum_{i=1}^{n} b_{ii} x_i^2 + \sum_{i=1}^{k-1} \sum_{j=2}^{k} b_{ij} x_i x_j + c$$ ……Equation 4.3 (Onukwuli *et al.*, 2017)

Where the response variable of interest is Y, b_0, b_i, b_{ii} and b_{ij} are the biodiesel yield, intercept, linear coefficient, interaction effects, the quadratic and coefficients, while c stands for the system error and n, the number of independent parameters (n = 3), respectively (Tan *et al.*, 2018).

4.6.1. Full central composite design with experimental response value

The table contains results for the experimental runs and provides information about the specific experimental runs, including the combination of factor levels used in each run. The response data is also included. This is the most critical data that could be related to the performance or outcome of the optimization process. The summary of the full composite design with experimental response values is presented as an experimental matrix in Table 4.13.

Table 4.13: Experimental matrix for the production of yellow oleander biodiesel by CCD of Design Expert software

Std	Run number	Factor 1 A: Time/Minutes	Factor 2 B: Temperature/$^{\circ}C$	Factor 3 *C*: Catalyst %	Actual oil yield R_1 Experimental (%)	RSM predicted oil yield R_2 Predictions (%)
9	1	6.36	60	2	94.2	93.7
19	2	40	60	2	93.5	92.6
1	3	20	50	1	92.4	91.9
5	4	20	50	3	91.4	90.8
16	5	40	60	2	90.7	89.9
3	6	20	70	1	89.4	88.8
15	7	40	60	2	88.3	88.3
7	8	20	70	3	87.6	87.8
17	9	40	60	2	86.5	87.4
20	10	40	60	2	85.6	86.9
6	11	60	50	3	84.5	86.3
2	12	60	50	1	83.3	84.9
13	13	40	60	0.318	82.9	84.2
10	14	73.64	60	2	81.5	83.2
8	15	60	70	3	80.7	82.1
18	16	40	60	2	94.2	93.7
4	17	60	70	1	93.5	92.6
14	18	40	60	3.68	92.4	91.9
11	19	40	43.18	2	94.2	93.7
12	20	40	76.82	2	93.5	92.6

R1 = Actual oil yield (%), R2 = RSM predicted oil yield (%)In terms of actual factors;

In this case, this indicates the yield of yellow oleander biodiesel. The predicted responses occur in RSM optimization, where the software generates predictive models based on the experimental

data. Finally, the predicted response data, which are the expected results based on the model, is also provided. Design 13 software was used to calculate the effects and interactions of each parameter with other parameters. To create a rotatable center composite design, three more centers were added to the total factorial design (CCD) data. Eight factorial points, six stars, and six midpoints were used in each of the 20 tests.

The following second-order polynomial equation from Equations 4.4 and 4.5 which are used to get the predicted yeilds.

a) In terms of coded factors;

   Biodiesel yield (Y %) = + 86.28 + (0.339 × A) + (1.71 × B) + (0.445 × C) – (1.31 × AB) + (0.563 ×AC) + (0.513 × BC) + (1.67 × A^2) + (0.005 × B^2) + (2.21 × C^2) ……Equation 4.4.

b) Biodiesel yield (Y %) = +82.80 + (0.021 ×Time) + (0.325×Temperature) – (12.61×Catalyst loading) – (0.0066 × Time × Temperature) + (0.028 ×Time × Catalyst loading) + (0.0513 × Temperature × Catalyst loading) + (0.0042 × $Time^2$) + (0.00005 × $Temperature^2$) + (2.21 ×$Catalyst\ loading^2$) ……Equation 4.5.

The model shows the predicted yield of yellow oleander biodiesel (Y) as a function of time (A). reaction temperature (B), and catalyst loading (C).

The factors that represent time, reaction temperature, and catalyst loading are A, B, and C. AB, AC, and BC are the terms that show how the factors interact. When a factor and its combinations are positive, it means that these factors work together in a beneficial way. A negative sign indicates the presence of antagonistic interactions and they negatively affect the course of a reaction (Aina *et al*., 2023). From the model equation 4.2.6; A, B, and C and the quadratic terms AC, BC, A^2, B^2,

and C^2 showed a linear effect of increasing the YOBD yield. However, the AB square term had a negative impact on YOBD production.

4.6.2. ANOVA analysis of the module

The response surface design for yellow oleander biodiesel yield was analyzed using analysis of variance (ANOVA). Table 4.14 shows the results for ANOVA analysis of the module.

Table 4.14: ANOVA for biodiesel model

Source (R2)	Sum of Squares	df	Mean Square	F-value	p-value	
Model	165.58	9	18.40	3.09	0.0466	significant
A-Time	1.58	1	1.58	0.2651	0.6178	
B-Temperature	39.98	1	39.98	6.72	0.0268	
C-Catalyst loading	2.70	1	2.70	0.4539	0.5157	
AB	13.78	1	13.78	2.32	0.1590	
AC	2.53	1	2.53	0.4255	0.5289	
BC	2.10	1	2.10	0.3532	0.5655	
A^2	40.03	1	40.03	6.73	0.0268	
B^2	0.0004	1	0.0004	0.0001	0.9940	
C^2	70.69	1	70.69	11.88	0.0063	
Residual	59.49	10	5.95			
Lack of Fit	13.03	5	2.61	0.2806	0.9053	not significant
Pure Error	46.45	5	9.29			
Cor Total	225.07	19				

A 95% confidence level is implied by the factors included in the model, which have an F-value of 3.09 and a p-value of 0.0466. For the model terms, p-values less than 0.05 indicated that the specific model terms were statistically significant.

The key model terms emerging from the ANOVA results show that the variables with a significant impact on the FAME yield reaction are reaction time (A), temperature (B), and catalyst loading (C), and the interaction terms between the primary factors (AC and BC) were also discovered. The significant quadratic terms were reaction time (A^2), temperature (B^2), and catalyst loading (C^2), while the significant linear terms were reaction time (A) and temperature (A^2). The lack of test of fit, which had a p-value of 0.9053 and is not significant (p-value 0.05 is not significant), showed that the model adequately fitted the experimental data. The model's predictions are consistent with the observed data, and any discrepancies may be due to random variability rather than a lack of fit. In summary, the ANOVA results indicate that the RSM model is statistically significant overall, and certain factors (B, A^2, C^2) have individual significance. The lack of fit is not statistically significant, suggesting that the model provides a good fit to the data

Arun *et al.*, (2017) studied the optimization of biodiesel production from yellow oleander using the ANOVA test in RSM. They observed that the model's probability value (p-value) and Fisher's test (F-value) were 0.0183 and 3.1, respectively, indicating the significance of the model at the 95% confidence level ($p < 0.05$). Also, the statistical significance test of all linear, interaction, and quadratic terms of the polynomial model equation by ANOVA at a 95% confidence level ($p < 0.05$) showed that all terms were significant. These results are comparable to those of this study, and the fact that the p-value for the models used in these studies was also less than 0.05 indicated that they were statistically significant.

4.6.3. Pareto of effects of factors that affect biodiesel production.

The Pareto chart was utilized to assess the impact of linear, interaction, and quadratic model equations on yellow oleander biodiesel yield, aiding in resource allocation, cost reduction, and waste reduction (Ashad *et al*., 2023). Pareto analysis optimizes biodiesel production by identifying critical factors, reducing production interruptions, quality issues, and compliance issues, enabling producers to adapt to market demands and environmental regulations (Almeida *et al*., 2022). The results of the Pareto effects are indicated in Figure 4.18 below.

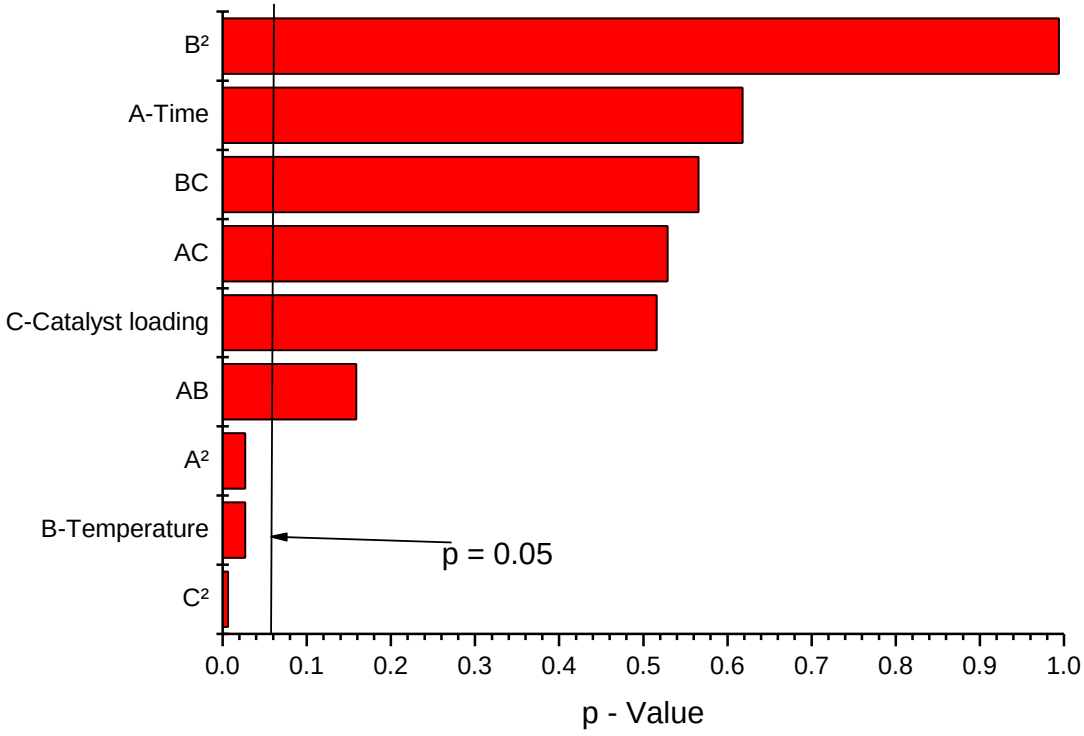

Figure 4.18: Pareto of effects

All model terms except B, A^2, and C^2 had a positive and significant impact on the yield of yellow oleander biodiesel. The model term with the most positive significance involved interactions between temperature, followed by reaction time and catalyst loading, and interactions between

catalyst loading had the least positive significance. The F-values of 3.09 and p-value of 0.0466 from the ANOVA analysis all agree with the observations from the Pareto chart.

Betiku and Ajala, (2014). studied the use of the Pareto diagram in RSM to optimize the production of biodiesel from yellow oleander. They observed that each bar representing a model term was above the reference line (p=0.05), indicating that each model term was significant. With the exception of time (Q) and catalyst loading (CL) over time, all model terms had a positive, significant impact on the production of yellow oleander biodiesel. Similar results were obtained in this study as time (minutes) and catalyst loading (%) had a positive impact on the production of biodiesel from yellow oleander (Betiku & Ajala, 2014).

4.6.4. Response surface estimation

The study utilized Design 13 software to generate 3D graphs, analyzing two variables while keeping one constant to determine the optimal yield of yellow oleander biodiesel.

4.6.4.1. Interaction Effect of time and temperature of the reaction (Experimental values)

The surface plot of temperature versus time and biodiesel yield obtained when individual experimental data were plotted are presented in Figure 4.19.

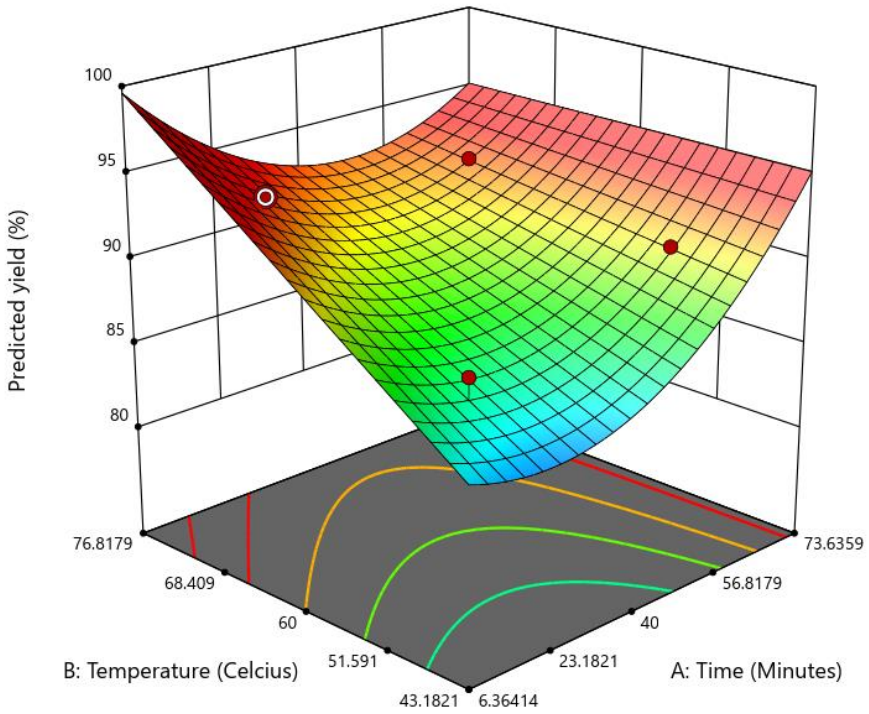

Figure 4.19: Interaction effect of time and temperature of the reaction

The study achieved a 93.7% yellow oleander biodiesel yield with a 40-minute extraction time, 2% constant catalyst loading, and 70°C temperature

Arun *et al.*, (2017) studied the optimization of yellow oleander biodiesel using RSM. They observed that as the reaction temperature increased from 40 °C to 70 °C, the biodiesel yield also increased from 74% to 77%.

4.6.4.2. Interaction effect of catalyst loading and time of the reaction

The surface plot of catalyst loading versus time and biodiesel yield obtained when individual experimental data were plotted are presented in Figure 4.20.

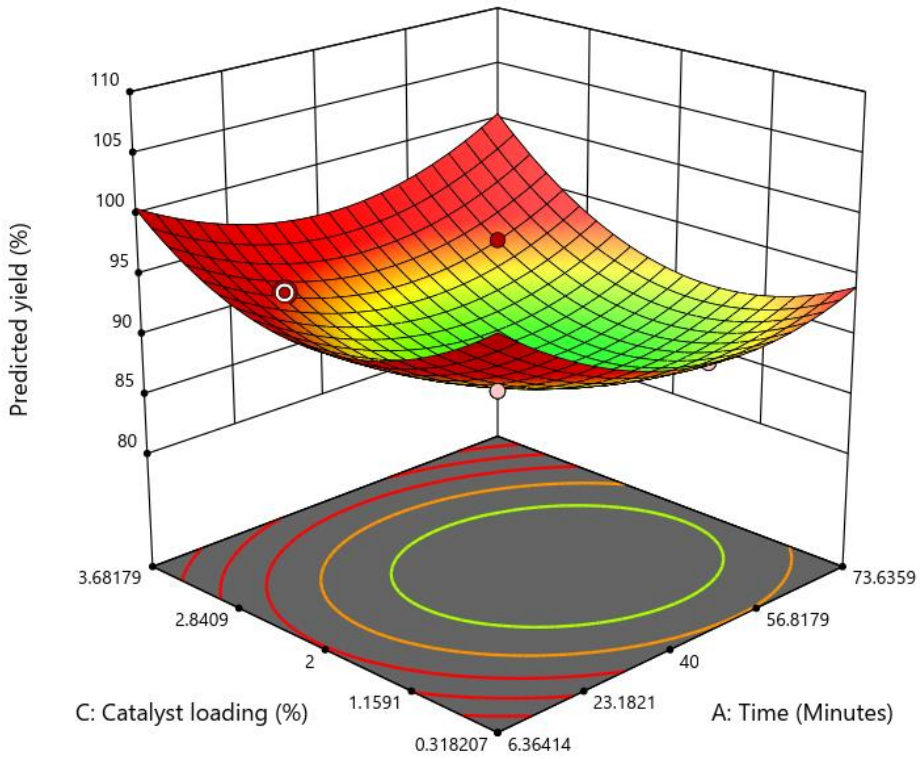

Figure 4.20: Interaction effect of catalyst loading and time of the reaction

The study achieved a biodiesel yield of 93.7% with an extraction time of 40 minutes, a constant temperature of 60°C, and a 2% wt catalyst loading.

Arun *et al*., (2017) used RSM to optimize the production of yellow oleander biodiesel. They observed that increasing the catalyst loading from 1.2 to 2.8% also increased the biodiesel yield from 69% to 79%.The reaction time increased from 45 to 75 minutes. This study also found that catalyst loading and time significantly increased the yield of yellow oleander biodiesel, as it positively influenced reaction kinetics, selectivity, yield, and overall process efficiency.

4.6.4.3. Interaction Effect of catalyst loading and temperature of the reaction

The surface plot of catalyst loading versus temperature and yellow oleander biodiesel yield

obtained when individual experimental data were plotted are presented in Figure 4.21.

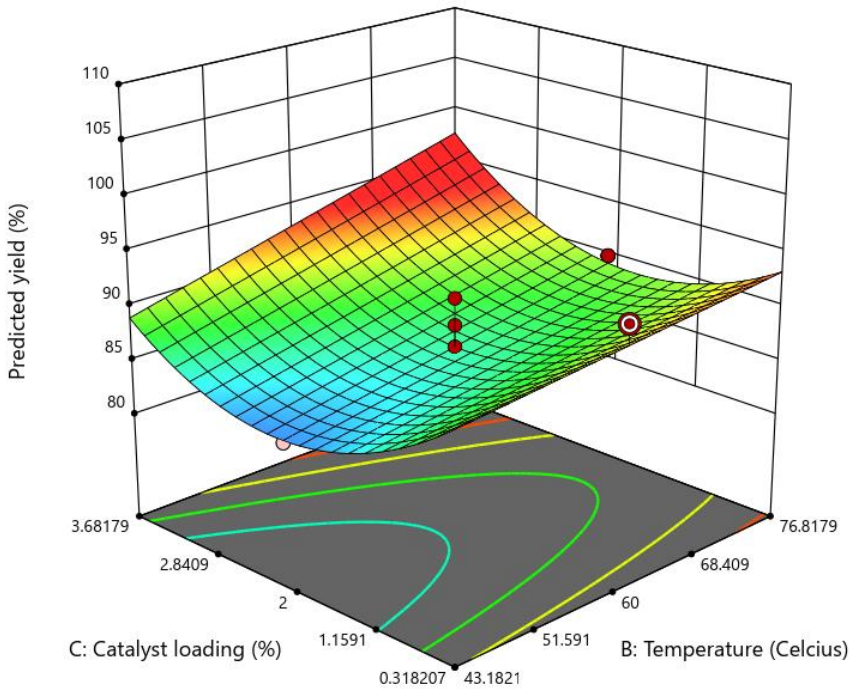

Figure 4.21: Interaction Effect of catalyst loading and temperature of the reaction

At a constant reaction time of 70 minutes, in the optimization of biodiesel from yellow oleander, the interaction time varied from 43.18 to 76.82 °C and the catalyst loading from 0.318 to 3.68 wt % and the yield varied from 82.1 to 93.7%. A time of 40 minutes, a temperature of 60 °C and a catalyst loading of 3.68% by weight (w/w%) proved to be the best conditions for the production of biodiesel, which led to a yield of 93.7%.

Arun *et al.*, (2017) used RSM to optimize the biodiesel produced from yellow oleander. They found that increasing the reaction temperature from 400 °C to 700 °C also increased the biodiesel yield from 75% to 82%. In contrast, no significant difference in biodiesel yield was observed when

the catalyst loading was varied. Similarly, catalyst loading and temperature positively contributed to increasing the yield of yellow oleander biodiesel in this study.

4.6.4.4. Effect of the reusability of nanocatalyst on the biodiesel yield

Reusability of catalysts in biodiesel production enhances efficiency, reduces costs, and minimizes replacement frequency, contributing to the process's economic viability and sustainability. Figure 4.22 and Table 4.15 in the Appendix, shows the results for the test on the reusability the nanocatalysts.

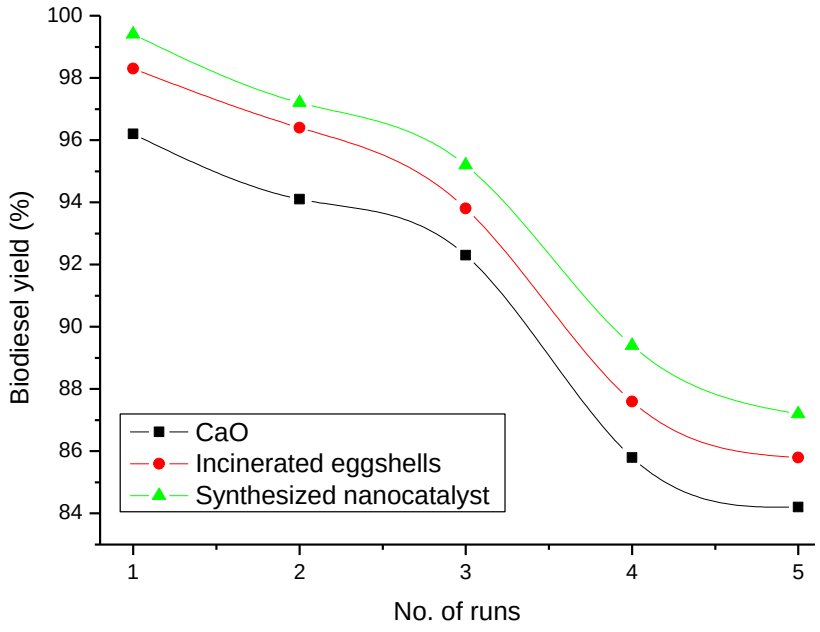

Figure 4.22: Effect of the reusability of nanocatalysts on the biodiesel yield

The research demonstrates that nanocatalysts, including synthesized nanocatalysts, incinerated eggshells, and CaO nanocatalysts, can be recycled and reused up to five times, achieving the highest biodiesel yield. The synthesized nanocatalyst showed the following yields; 99.4, 97.2, 95.2, 89.4, and 87.2 % respectively. From the literature, the structural changes of the nanocatalyst

during the production of biodiesel is given as the reason for its reduced catalytic activity (Pandit & Fulekar, 2017).

Yue *et al.*, (2018) studied the optimization of CaO catalysts from chicken eggshells for the production of biodiesel. They observed that the biodiesel yield did not decrease significantly in the first four cycles. The biodiesel yield dropped slightly to less than 80% during the fifth and sixth cycles. The slight decrease in catalyst activity was caused by the formation of inert $CaCO_3$ and less active $Ca(OH)_2$ on the catalyst surface during catalyst recovery and drying. Compared to this study, where the catalytic stability remained around 80 % even after the fifth extraction, the synthesized nanocatalyst turned out to be the better catalyst.

4.7. Analysis of the yellow oleander oil and yellow oleander biodiesel

Gas chromatography-mass spectrometry was used to determine the chemical composition of yellow oleander oil (YOO). It is a useful analytical technique to determine the acid profile of feedstocks used to produce biodiesel. FTIR spectroscopy was used to study the functional groups present in both yellow oleander oil and yellow oleander biodiesel (YOBD).

4.7.1. GC/MS Analysis

GC-MS analysis of yellow oleander oil for biodiesel production is a crucial step to ensure the quality and suitability of the feedstock. It provides valuable information about the composition, impurities, and properties of the oil, which is essential for the efficient and consistent production of high-quality biodiesel. The results for the fatty acid profile of yellow oleander oil as determined by GC/Ms results are in Figure 4.23 below and Table 4.16 below.

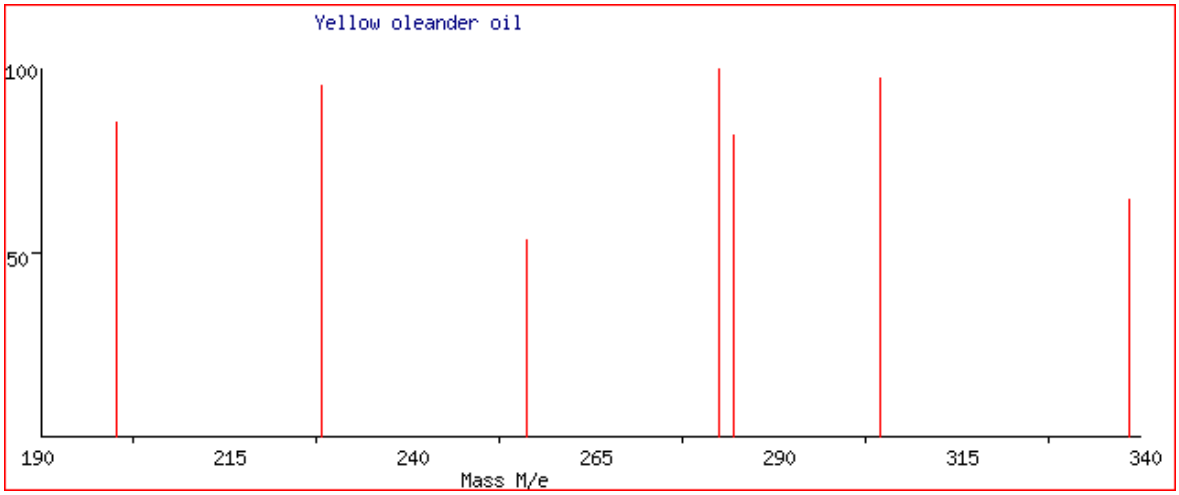

Figure 4.23: Yellow oleander oil GCMS spectrum

Table 4.16 displays the GC-MS analysis of yellow oleander oil, revealing a diverse fatty acid composition, crucial for evaluating the oil's functional properties.

Oleic acid had the highest percent acidity in yellow oleander seed oil (17.31%), followed by arachidonic acid (16.86%) and myristic acid (16.52%). Palmitic acid had the lowest acidity at 9.24%. Unsaturated oils are potentially unstable and may go rancid on storage. The unsaturated acids present in the yellow oleander oil included arachidonic acid [C20:4], erucic acid [C22:1] and oleic acid [C18:1] for a total of 45.26% (De Menezes *et al.*, 2022).

Table 4.16: Acid profile for yellow oleander oil

Fatty Acid Profile		**This study**	**(Arun *et al.*, 2017)**	(**Adepoju** *et al.*, 2018)	**RMM**
Propeties		**Oil Content (%)**			
Saturated acids					
Arachidic acid	[C20:0]	-	-	-	312.00
Stearic acid	[C18:0]	14.18 ± 1.54	3.86	7.02	284.50
Palimitic acid	[C16:0]	9.24 ± 1.43	26.4	9.52	256.43
Myristic acid	[C14:0]	16.52 ± 5.16	-	-	228.38
Lauric acid	[C12:0]	14.79 ± 2.41	-	-	200.32
Monounsaturated acids					
Erucic acid	[C22:1]	11.09 ± 1.71	-	-	338.60
Oleic acid	[C18:1]	17.31 ± 3.11	39.4	32.32	282.50
Polyunsaturated acids					
Arachidonic acid	[C20:4]	16.86 ± 2.34	-	-	304.50
Linolenic acid	[C18:3]	-	-	12.32	278.43
Linoleic acid	[C18:2]	-	27.03	37.91	280.40
Total unsaturation		45.26	66.43	70.73	

The values are means ± se, n = 4

Therefore, yellow oleander oil has an unstable composition that becomes rancid during storage. Bora *et al*.(2014) studied the acid profile of yellow oleander oil using the GCMS spectrum. They found that the percentage composition of fatty acid content was as follows: saturated acid; Palmitic acid (16:0) had 23.28, compared to 9.24% in this study. Stearic acid (18:0) had 10.71% compared to 14.18% in this study. Study: Arachidic Acid (20.0) had 2.41%, there was none in this study. Monounsaturated acids include Oleic acid (18:1) had 43.72% compared to 17.31%, which also had the highest acidity in this study. They also found that the polyunsaturated (linoleic acid (18:2)

had 19.85% was not present in this study. This study also contained erucic acid (18:1) had 24.83%. They also found that the unsaturation level was 61.47% compared to 45.26% determined in this study.

Adepoju *et al.,* (2018) obtained comparable results when analyzing the acid profile of yellow oleander oil using GC/MS. They also noted the high unsaturation level of 70.73% in yellow oleander oil. These confirm that yellow oleander oil has a high content of unsaturated acids and would go rancid on storage.

4.7.2. FTIR Spectrum for yellow oleander oil and biodiesel

FTIR analysis is crucial for assessing yellow oleander oil and biodiesel composition, functional groups, and reaction progress, ensuring feedstock quality and advancing biodiesel production processes. The FTIR spectra of methyl ester and yellow oleander oil are in Figure 4.24 and Table 4.17 below.

As shown by the absorption peak at 3423 cm^{-1}, highly stretchable alcohol groups were present. The presence of stretches and strong intensity in both the 2940 and 2827 cm^{-1} peaks indicates the presence of alkane compounds. This shows the presence of a high-intensity extensional vibration methyl ester (O-CH_3) peak is present as indicated by the peaks at 1647 cm^{-1}. This was accompanied by an intensity bending of the alkane compounds present, indicated by the peak at 1465 cm^{-1}. Finally, the alkene was fully detected with bending vibration and strong intensity was fully detected at the peaks at 1027 and 729.5 cm^{-1}, respectively.

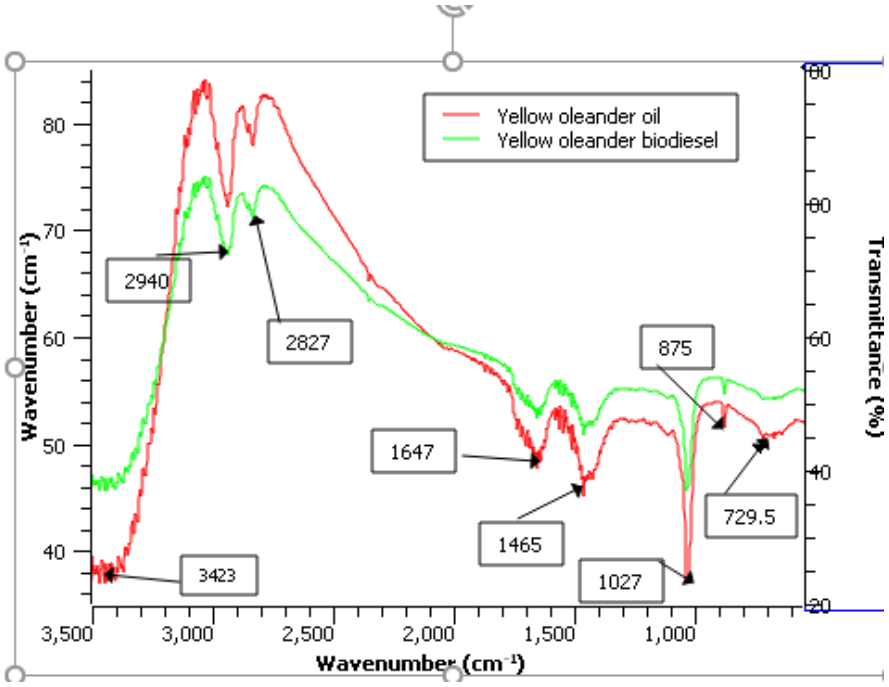

Figure 4.24: FTIR spectrum for yellow oleander oil and biodiesel

The FTIR spectrum analysis identifies specific functional groups in the sample, aiding in the identification of molecular components and their concentrations. These are summarized inn Table 4.17 below.

Table 4.17: FTIR peak locations for biodiesel and yellow oleander oil (cm^{-1})

Wavenumber (cm^{-1})	Assignment	Absorption intensity
	The region where hydrogen is stretched	
3423	Triglyceride stretching vibration caused by -OH	Strong
2940	Aliphatic groups with the $-CH_2$ and $-CH_3$ suffixes vibrate both symmetrically and asymmetrically.	Strong
	Stretch zone for double bonds	
1647	ester carbonyl functional group of the oil or biodiesel	Middle
1465	Olefins' stretching vibration at -C=C	Middle
	Deformation and bending zones for other bonds	Middle
	CH_2 group bending vibrations	Middle
	Biodiesel fingerprint region	
1027	The ester group's C–O stretching vibration	Middle
729.5	The out-of-plane vibration of disubstituted olefins and CH_2 rocking vibration	Weak

Bora *et al*., (2014) evaluated alkyd resins in yellow oleander oil using the FTIR spectrum. They found that peaks occur at 3456 cm^{-1} due to the O-H stretching vibration and aliphatic C-H stretching vibration at 2858-2924 cm^{-1}. Peaks for the C=O stretching vibration of the triglyceride ester appear at 1747 cm^{-1}, while the C=C stretching vibration occurred at 1639 cm^{-1} and C-H

bending occurred at 1458 cm^{-1}. Furthermore, the peaks at 1161 cm^{-1} are due to the C-O-C stretching vibration of the ester, and the peak for methylene vibration appeared at 721 cm^{-1}.

The results of this study agree with the observations of Bora etal., (2014).

4.7.3. Physical and chemical analysis of the yellow oleander oil and yellow oleander biodiesel using the ASTM D6751 specifications

Physical and chemical analysis of yellow oleander oil and yellow oleander biodiesel in accordance with ASTM D6751 specifications is critical to ensuring quality assurance, environmental stewardship, engine protection, regulatory compliance and market acceptance. These results are presented in Table 4.18.

Table 4.18: Physical and chemical characteristics of yellow oleander oil and biodiesel

Property	YOO	YOBD	ASTM	Method
Saponification value (mg/KOH/g)	197.33±3.96	129.24± 6.38	Varied	D 94
Acid value (mg KOH/g)	2.24±0.23	0.205 ± 0.14	0.8 max	D 664
Peroxide value (mEg O_2/Kg)	1.88± 0.04	2.2± 0.42	10-20 max	D-1563
Iodine value gI_2/100 g	80.77± 0.76	70.8± 2.74	120 max	D 2078

These factors include iodine value(degree of unsaturation), peroxide number (formation of primary oxidation products), moisture content, specific gravity (purity), and acid number (formation of free fatty acids due to rancidity). The physicochemical analysis of yellow oleander oil and yellow oleander biodiesel using the specifications of ASTM D6751.

4.7.3.1. Saponification value

The average molecular weight of the oil is determined by the saponification number (SV), which is expressed in milligrams of potassium hydroxide per gram of oil (mg KOH g^{-1}). The saponification number of the yellow oleander oils and biodiesel were 197.33 ± 3.96, and 129.24 ± 6.38 mg/KOH/g, respectively.

Adepoju *et al.,* (2018) obtained the same results studying the saponification numbers of yellow oleander oil. They recorded 157.50 mg KOH/g and 126.65 mg KOH/g for yellow oleander oil and biodiesel, respectively. These values decreased by 20.27% for the oil and by 2% for the yellow oleander biodiesel. No literature is available on the saponification value of yellow oleander biodiesel.

4.7.3.2. Acid value

Both vegetable oil acid values (AV) are essential parameters when considering the oil quality because lower AV implies better quality oil. This parameter measures the presence of both corrosive free acids and oxidation products (Access, 2018).

The acid values for yellow oleander oil and biodiesel were 0.224 ± 0.23 and 0.205 ± 0.14 mg/KOH/g, respectively. Since these values are below the ASTM standard of 0.8 mg/KOH/g, the yellow oleander biodiesel does not lead to operational problems such as corrosion and pump clogging from corrosion and deposits. Betiku and Ajala (2014) obtained similar results when studying the acidity of yellow oleander biodiesel. They found an acid value of 0.46 mg KOH/g oil, which was close to the value in this study, which was also within ASTM standards for biodiesel.

4.7.3.3. Peroxide value

In this research, the peroxide values for yellow oleander oil and biodiesel were 1.88 ± 0.04 and 2.2 ± 0.42 meq O_2/kg, which were lower than 10 meg O_2/kg established by Codex Alimentarius International Standard (FAO, 1981). Hence, both yellow oleander oil and biodiesel were fresh. Adepoju *et al*., (2018) found that yellow oleander oil had a low peroxide value of 23.8 meq. O_2/kg. This study found that the extracted yellow oleander oil had a lower peroxide value, was stable at room temperature, and had high oxidation resistance.

4.7.3.4. Iodine value

Iodine values for yellow oleander oil and biodiesel were 80.77 ± 0.76 and 70.8 ± 2.74 gI_2/100 g. The degree of unsaturation has a significant impact on the fuel's tendency to oxidize. ASTM D6751 requires that biodiesel used as a diesel fuel have an iodine value of less than 120g I_2/100g sample. Yellow oleander oil contained 45.62% unsaturated fatty acid, namely; erucic acid [C22:1], arachidonic acid [C20:4], oleic acid [C18:1], and palmitoleic acid [C16:1]. Yellow oleander oil and biodiesel contain moderate levels of iodine, which generally make them resistant to oxidation, have a long shelf life, and can be stored for long periods without becoming rancid (Bora *et al*., 2014). Adepoju *et al.*, (2018) came to similar conclusions when examining the iodine values of yellow oleander oil and biodiesel. They found iodine levels of 97.60 and 73.20 g I_2/100g, respectively, which were below the ASTM D6751 standard of 120 g I_2/100g. This oil could still go rancid due to high unsaturation.

The fuel properties of petrodiesel, yellow oleander biodiesel, and their blends have significant implications for energy sustainability, environmental impact, engine performance, and regulatory compliance. Careful consideration of these characteristics is essential to making informed fuel

selection decisions and optimizing fuel consumption in various applications. The fuel properties of petrodiesel, yellow oleander biodiesel and blends are considered in Table 4.19 below.

Table 4.19: Fuel properties of yellow oleander oil, biodiesel and blends

	B0	B5	B10	B15	B20	B30	B100	ASTM
Specific gravity	0.83	0.8315	0.833	0.835	0.836	0.839	0.86	0.86-0.90
KV @ (40 °C) cSt	3.3	3.345	3.39	3.435	3.48	3.57	4.2	1.9 - 6.0
Cetane number	46.6	50.34	54.07	57.81	61.54	69.01	121.3	47 min.
Flash point °C	57.5	63.03	68.55	74.08	79.6	90.65	168	> 93
CV kJ/kg	45.5	45.32	45.14	44.96	44.78	44.42	41.9	>35.00
API	41.06	43.88	43.28	42.68	42.08	40.89	33.03	36.95
DI	50.83	56.03	61.21	66.41	71.58	81.96	154.58	331.0

4.7.3.5. Specific gravity

In this study, the specific gravities of petrodiesel and yellow oleander biodiesel/petrodiesel blends (B5, B10, B15, B20, B30, and B100) were 0.83, 0.832, 0.833, 0.835, 0.836, 0.839, and 0.86, respectively. The specific gravity of the blends increased as the volume of biodiesel in the blends increased. These were within the acceptable ASTM D6751 range of 0.86 to 0.90. There is no literature on the specific gravity of yellow oleander biodiesel/petrodiesel blends. Montero *et al.,* (2017) studied the quality assessment of biodiesel blends. They found that biodiesel-specific gravity increased linearly as the concentration of biodiesel in the fuel blend increased. As a result, the specific gravity for petrodiesel was 0.838 and that for B100 was 0.888.

4.7.3.6. Kinematic viscosity

The kinematic viscosity of petrodiesel (B0), and yellow oleander biodieselpetrodiesel blends (B5, B10, B15, B20, B30, and B100) were; 3.3, 3.345, 3.39, 3.44, 3.48, 3.57, and 4.2 $mm^2 s^{-1}$. Accordingly, the kinematic viscosity values also increased with increasing biodiesel content of the mixtures, which led to improved lubricity. These were within the limit of ASTM D6751 standard of 1.9 - 6.0 $mm^2 s^{-1}$ though much higher than petro-diesel, confirming that yellow oleander biodiesel and blends can be used in a diesel engine. There is no literature on the kinematic viscosity of yellow oleander biodiesel/petrodiesel blends. Guo *et al*., (2016) investigated the physicochemical properties of biodiesel/biodiesel blended fuels. The kinematic viscosities of biodiesel and diesel were measured to be 6.53 mm^2/s and 4.27 mm^2/s, with the blended fuels lying between these two values. Similar to this study they found that the kinematic viscosity of biodiesel-diesel fuel blends increased with the volume fraction of biodiesel.

4.7.3.7. Cetane number

The cetane numbers of petrodiesel (B0), and yellow oleander biodiesel (B5, B10, B15, B20, B30, and B100) were 71.60, 71.17, 70.73, 70.29, 69.86, 68.99, and 121.3, respectively. Cetane number (CN) increased with increasing biodiesel content in the blends and values exceeded the ASTM standard of 47 minutes. This confirmed that yellow oleander biodiesel and blends had good ignition and combustion fuel properties. Momin & Deka (2015) studied the cetane number of fellow oleander biodiesel blends. They got results similar to this study, the cetane number of the blends in B5, B10, B15, B20 and B100 increased from 48.5, 49.0, 49.2, 49.9 to 61.5.

Guo *et al*. (2016) investigated the fuel properties of biodiesel/biodiesel blended fuels. The study found that the He cetane number of biodiesel and diesel was 70.6 and 49.5, respectively, while that

of the blended fuels was between the two values. As the proportion of biodiesel in the mixtures increased, these cetane numbers gradually increased. Therefore, the addition of biodiesel should help reduce diesel engine detonation

4.7.3.8. Flash point

The flash points for petrodiesel (B0), petrodiesel/yellow oleander biodiesel blends (B5, B10, B15, B20, B30, and B100) were; 57.5, 63.03, 68.55, 74.08, 79.6, 90.65 and 168 °C, respectively. The flash points of the biodiesel blends increased with the increasing biodiesel content of the blends. All blends except B100 had flash point values below the ASTM value of 93 (Momin & Deka, 2015). These results showed that the yellow oleander biodiesel and its blends can be used in a diesel engine.

Momin & Deka (2015) analyzed the flash point of yellow oleander biodiesel and petrodiesel blends. They were observed to increase the flash point of the blends in B0, B5, B10, B15, B20, and B100 from 43.0, 45.0, 46.0, 46.0, and 47.0 to 175.0.

4.7.3.9. Calorific value

The calorific values of petrodiesel (B0), yellow oleander biodiesel (B5, B10, B15, B20, B30, and B100) were; 45.5, 45.32, 45.14, 44.96, 44.78, 44.42 and 41.9 kJ/kg, respectively. Due to its oxygen content, biodiesel has lower calorific values compared to petrodiesel and is completely incinerated in an internal combustion engine. It was observed that the calorific value (CV) decreased as the proportion of biodiesel in the blends increased. The calorific values of biodiesel and yellow oleander blends were above the ASTM minimum level of 35 kJ/kg and close to the calorific values of petrodiesel. There is no literature on the calorific value of yellow oleander blends. Adepoju *et*

al., (2018) came to similar conclusions when studying the calorific value of yellow oleander biodiesel. They observed that the calorific value of yellow oleander biodiesel was 45.34 kJ/kg.

4.7.3.10. American Petroleum Index (API)

The API index of petrodiesel (B0) and yellow oleander biodiesel blends (B5, B10, B15, B20, B30, and B100) were 41.06, 43.88, 43.28, 42.68, 42.08, 40, 89 and 33.03 respectively. For all blends except B100, these values were within the ASTM limit of greater than 36.95.

Adepoju *et al*., (2018) found that an API value of 23.48 for yellow oleander biodiesel was lower than the ASTM value and that the oil to biodiesel value decreased by 10.71%. As expected, these values are still below those of petrodiesel.

4.7.3.11. Diesel Index (DI)

The diesel index of petrodiesel (B0), and yellow oleander biodiesel (B5, B10, B15, B20, B30, and B100) were 85.56, 84.95, 84.35, 83.74, 83.14, 81.93, and 154.58, respectively. These values were below the ASTM limit of 331. It was found that the diesel index (DI) increased with increasing petrodiesel content in the blends. There is no literature on the DI value of yellow oleander blends. Adepoju *et al.,* (2018) obtained similar results studying the diesel index of yellow oleander biodiesel. They observed a diesel index of 50.40 for the biodiesel, which is 67.40 % lower than that obtained in this research.

All samples of the yellow oleander biodiesel blend met ASTM specific gravity and kinematic viscosity standards, with the exception of B100, which is slightly above the ASTM standard with very insignificant values of 0.86 and 4.2 mm^2/s. Therefore, yellow oleander biodiesel oil and blends could be a better choice for use in internal combustion engines to improve the quality of atomization, combustion, fuel droplets, and air-fuel mixing. The calorific values of biodiesel and

yellow oleander blends were all within the ASTM standard, although slightly lower than petrodiesel; Similarly, the flash point of biodiesel made from yellow oleander and its blends was higher than that of petrodiesel, but within the ASTM range. This makes the yellow oleander biodiesel and blends safe to handle during storage. They do not ignite easily when exposed to a flame and are therefore recommended for use in internal combustion engines. All cetane numbers are higher than petrodiesel and meet ASTM standards. This means that yellow oleander biodiesel and its blends have the shortest possible start-up time when combusted in a 4-stroke engine. All yellow oleander biodiesel and petrodiesel blends have fuel properties that meet ASTM standards. Yellow oleander can therefore be a potential feedstock for biodiesel production to meet partial energy needs in an environmentally friendly way if introduced in Kenya

4.7.4. Performance, combustion, and emission characteristics

The following properties are examined; Performance, combustion and emissions characteristics were also studied. The effects of the following biodiesel blends (B5, B10, B15, B20, B30, and B100) on indirect injection engines operating at 1500 rpm under various loads.

4.7.4.1. Four Stroke Engine Performance characteristics

The performance characteristics of a yellow oleander biodiesel four-stroke engine are diverse and include power, combustion efficiency, emissions, and exhaust gas temperature, among others. Careful consideration of these characteristics is critical to optimizing engine performance and ensuring the long-term sustainability of biodiesel use.

4.7.4.2. Variation of brake thermal efficiency with load

The Brake thermal efficiency (BTE) represents the ratio of the useful work output to the heat input into an engine and is a measure of how effectively an engine converts the energy in the fuel into

useful work. BTE also indicates the crankshaft power of the engine from the total power generated during combustion. a specific fuel. The variation of brake thermal efficiency with load is given in Figure 4.25.

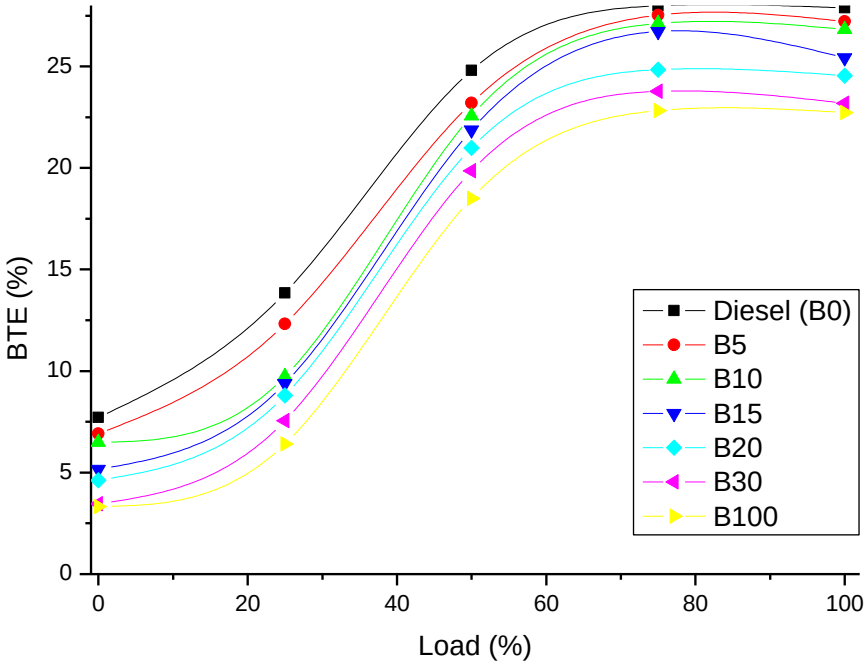

Figure 4.25: Variation of brake thermal efficiency with load

The engine BTE of blends of petrodiesel and yellow oleander biodiesel increased from 7.77% to 28.06% with increasing engine load. This is because thermal energy is released when the engine is subjected to increased loads, which in turn promotes a better combustion process and thus increases the BTE. It was also found that the BTE values of yellow oleander biodiesel blends were lower than that of petrodiesel, and that increasing the proportion of yellow oleander biodiesel in the blend reduced the BTE. The reduction in BTE of biodiesel blends is due to: the high viscosity and density of biodiesel causing poor atomization during combustion, the lower calorific value of yellow oleander biodiesel resulting in reduced engine braking performance and increased fuel consumption (Mohan *et al.*, 2021).

The BTE of biodiesel blends B5, B10, B15, B20, B30, and B100 decreased by 0.46, 0.86, 1.25, 3.14, 4.2, and 5.15%, respectively, compared to petrodiesel.

Arun *et al.,* (2018) obtained similar results by analyzing the performance of yellow oleander biodiesel in compression ignition engines. They found that, in general, BTE decreased with increasing biodiesel content in the blends and BTE increased with increasing engine load. This was due to an increase in fuel consumption, which increases BTE. Among the test fuels, the BTE values of all biodiesel-diesel blends were lower than diesel at all load conditions, which is due to diesel's high calorific value, which results in high energy released during combustion. The BTE curves of the YOME diesel blend B30 showed a lower BTE of 28.11% than B100 of 27.31%, while the BTE of petrodiesel was 31.68%.

4.7.4.3. Brake Specific Fuel Consumption

Brake-specific fuel consumption (BSFC) of yellow oleander biodiesel measures the fuel consumption required by an engine to generate electricity and provides insight into its efficiency. The brake-specific fuel consumption results from the fuel consumption divided by the power delivered. A lower BSFC indicates better fuel conversion.

The variation of BSFC with engine load can be seen in Figure 4.26.

As the load increased, the BSFC decreased, with B100 recording the highest BSFC. The figure shows that the BSFC of biodiesel blends of yellow oleander and petrodiesel decreased with increasing engine load.

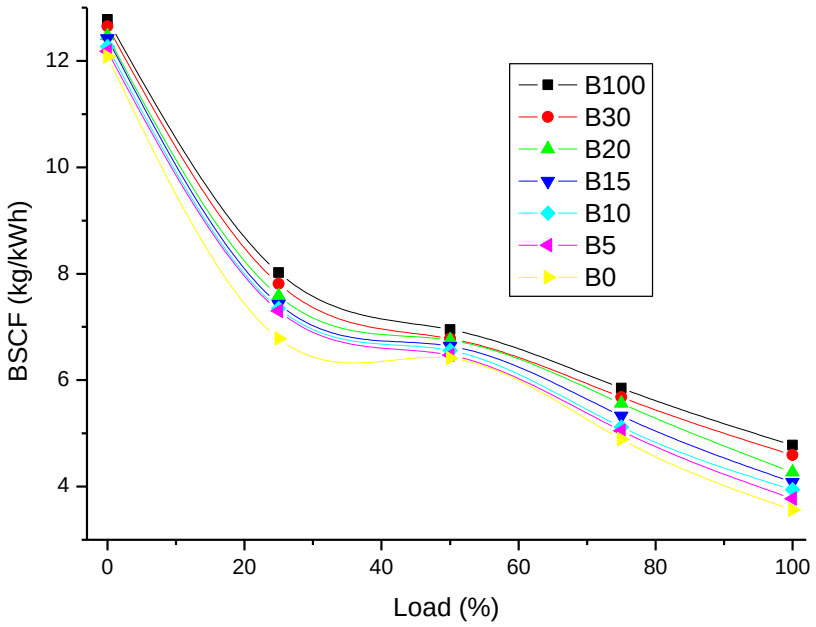

Figure 4.26: Variations of brake specific fuel consumption and engine load

This was due to the improved fuel combustion process as the engine load increased. It was also observed that the BSFC of yellow oleander biodiesel was higher than that of petrodiesel, and the BSFC increased more as the proportion of yellow oleander biodiesel in the blend increased. The reason for the increase was the lower calorific value of yellow oleander biodiesel compared to petrodiesel, which requires more fuel for the same output. The BSFC of B5, B10, B15, B20, and B100 increased by 0.1, 0.19, 0.3, 0.39, 0.57, and 0.70 % compared to petrodiesel respectively.

Arun et al., (2018) obtained similar results analysing engine performance of yellow oleander biodiesel in compression ignition (CI) engines. They found that the BSFC of all test blends of yellow oleander decreased with increasing engine load. This was because yellow oleander biodiesel has a lower calorific value (37.56 MJ/kg) and energy density compared to petroleum diesel. This means that more fuel is required for the same engine performance. All test fuels had a

BSFC of 0.3 kg kW/h, petrodiesel had a BSFC of 0.28 kg/kW/h. In the study, B30 showed less BSFC than B100, while the BSFC of pure diesel was lower than B100.

4.7.4.4. Emission characteristics

Yellow oleander biodiesel, like other biodiesel fuels, has certain emission characteristics when used in engines. These properties are influenced by the properties of the biodiesel and can bring both benefits and potential challenges. The emission characteristics of yellow oleander biodiesel may vary depending on the specific blend, engine type, engine design, operating conditions, and the presence of emission control technologies (Abdul Hakim Shaah *et al*., 2021). Conducting emissions testing and considering local regulations and guidelines is essential when using biodiesel fuels to ensure regulatory compliance and optimal environmental performance

4.7.4.5. Carbon dioxide (CO_2) emissions

Burning fossil fuels and biodiesel releases carbon dioxide, which is an uncontrolled emission. Combustion of fossil fuels Combustion of fossil fuels releases accumulated carbon dioxide into the atmosphere, which degrades the atmosphere and harms both the environment and human health. However, the crops used for biodiesel production can quickly absorb the CO_2 released during combustion. This maintains the atmospheric CO_2 balance.

Figure 4.27 shows variation of carbon dioxide of petrodiesel (B0), yellow oleander biodiesel (B100), biodiesel blends (B5, B10, B15, B20, and B30).

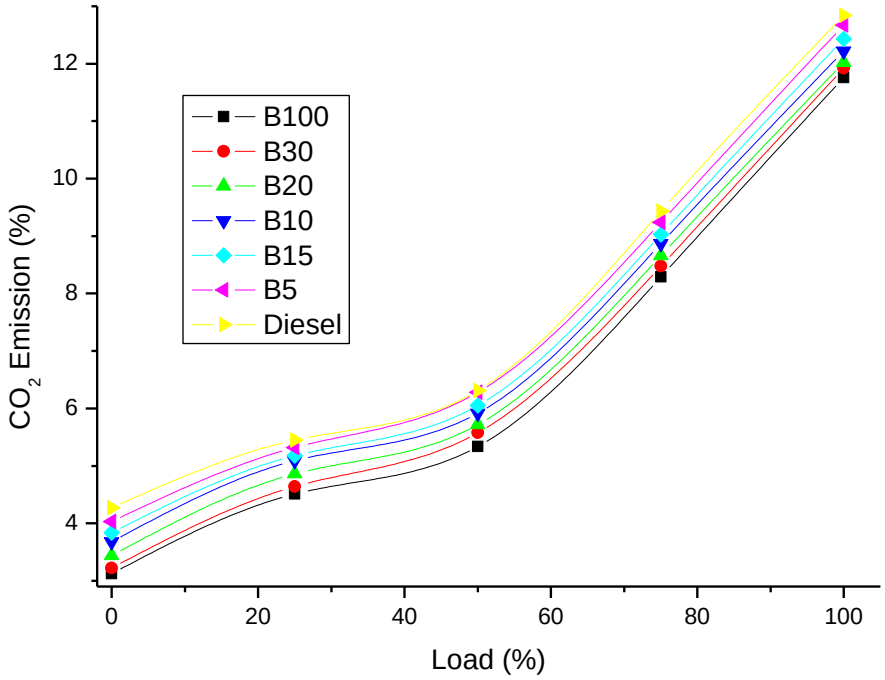

Figure 4.27: Variations of CO_2 with engine load

For all fuel modes, CO_2 emissions increased with load up to a maximum load level of 100%. The maximum charge for CO_2 emissions when using petrodiesel was 12.9%, while the minimum charge for CO_2 emissions when using all biodiesel fuel blends was 3.1%. It was also observed that as the proportion of biodiesel in the biodiesel blends increased, so did CO_2 emissions. For B 100 there were lower carbon dioxide levels due to better fuel atomization and complete fuel combustion. Arun *et al.*, (2018) obtained similar results by analyzing the CO_2 emissions of yellow oleander biodiesel in compression ignition (CI) engines. In their study, they found that petrodiesel had the highest CO_2 emissions compared to the yellow oleander biodiesel fuel blends studied. At 100% load, the CO_2 emissions of petrodiesel (B0) and yellow oleander (B100) biodiesel are 9.4% and 8.7%, respectively.

4.8.2.1. Emission of CO

CO emissions result from the incomplete combustion of fuel in internal combustion engines due to a lack of oxygen. The CO emission is controlled by the fuel/air equivalence ratio and is very high for a rich mixture when the excess air ratio is below 1.0.

Figure 4.28 shows the variation of CO of petrodiesel, yellow oleander biodiesel (B100) and blends of B5, B10, B15, B20, and B30, respectively.

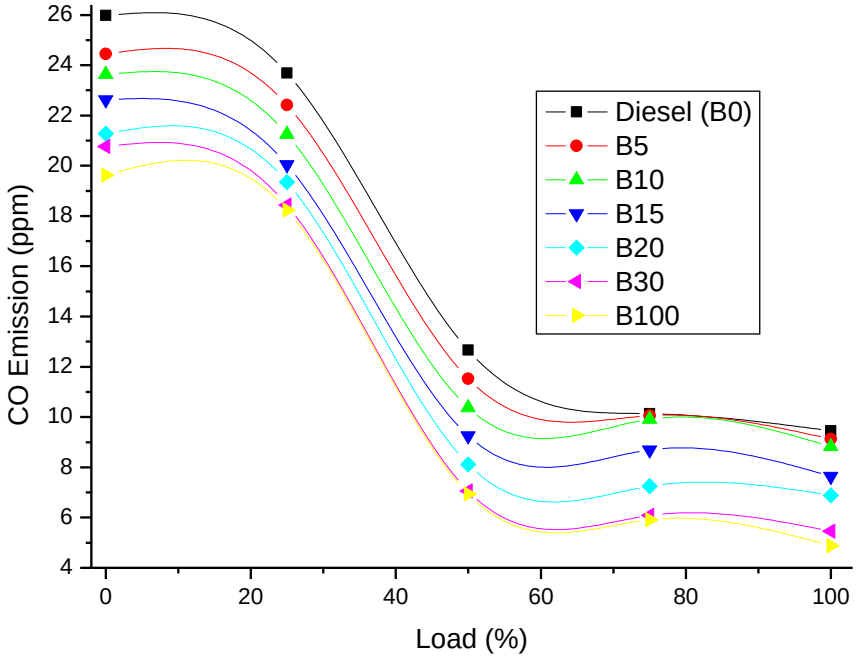

Figure 4.28: Variation of CO emission with Load

The variation of CO emission for petrodiesel (B0), different yellow oleander biodiesel blends (B5, B10, B15, B20, B30, and B100) fuel versus various engine loads is shown. It was observed that when the engine load (%) increased, the CO emissions gradually decreased for petrodiesel, and all yeloow oleander biodiesel blends. Petrodiesel (B0) had the highest CO emissions of; 25.98, 23.69, 12.66, 10.14 and 9.45 ppm, respectively over all loads of 0, 25, 50, 75 and 100%. Pure yellow oleander biodiesel (B100) had the lowest CO emissions across all loads, 19.62, 18.24, 6.93, 5.92,

and 4.88 ppm. Recording a reduction in CO emissions of 24.48, 29.79, 73.32, 77.21, and 81.22%. The reason behind this decrease is when the engine load increases, the air temperature inside the cylinder increases. This helps to improve fuel combustion, leading to a complete combustion process and thus reducing CO emissions.

Arun *et al.,* (2018) obtained similar results by analyzing the CO emissions of yellow oleander biodiesel in compression ignition (CI) engines. They observed that the CO emission decreased with the concentration of yellow oleander biodiesel–diesel blends as a fuel in a diesel engine. Among all test fuels, B10, B20, and B30 blends indicated decreased CO emissions. The CO of yellow oleander biodiesel at 100% load was found to be 8 ppm.

4.7.4.6. Emission of NO_x

Engine NOx emissions depend on cylinder temperature. NOx is formed by the reaction between nitrogen and oxygen molecules at high temperatures during the combustion process of petrodiesel and biodiesel fuels.

Figure 4.29 shows the NOx emissions for all the yellow oleander blends and petrodiesel fuel.

The NOx emissions of all biodiesel blends are lower than those of petrodiesel under all load conditions. All biodiesel blends showed a complete reduction in NOx emissions. Under full load conditions, the NOx emissions of the biodiesel blends B100, B30, B20, B15, B10, B.5 and petrodiesel are 1378, 1392, 1409, 1425, 1439, 1463 and 1480 ppm, respectively. The reduced NOx emissions are due to the higher cetane number of the yellow oleander oil. Higher cetane number fuels have shorter premixed combustion time due to shorter ignition delay. Accordingly, lower temperatures and a slower NOx production rate are predicted along with a slower rise in combustion pressure.

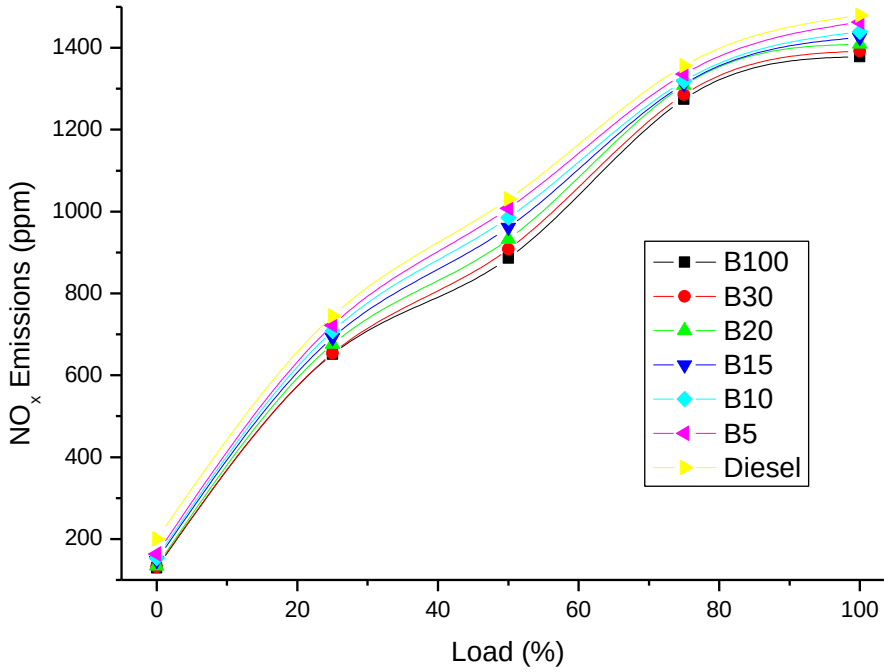

Figure 4.29: Variation of NO_x emission with Load

The NOx emissions were found to increase with engine load and fuel blend. The higher oxygen content in biodiesel blends and the degree of unsaturation of the fuel mixtures increased the formation of HC radicals, which led to the formation of NOx (Yadav *et al.*, 2019).

Arun *et al.*, (2018) obtained similar results when analyzing the NOx emissions of yellow oleander biodiesel in diesel engines. They found that as the load increased, fuel consumption also increased, causing air (nitrogen) to flow into the cylinder. All biodiesel blends showed high NOx emissions at all load conditions compared to mineral oil diesel. Of all the test fuels, B10, B20, and B30 blends showed increased NOx emissions. Yellow oleander Biodiesel NOx emission at 100 % load was 1737 ppm.

4.7.4.7. Combustion characteristics

Factors such as crank angle diagram, peak pressure, rate of pressure rise, ignition delay and combustion duration are often used to describe an engine's combustion behavior. The above fuel economy analysis information is critical to understanding engine performance and emissions. In addition, combustion characteristics can sometimes be used to compare alternative fuels under the same operating conditions or to explain the effect of engine operating conditions on engine performance. This was done to evaluate the combustion properties of B100, B30, B20, B15 and B5 and to compare them with the combustion behavior of petroleum diesel.

4.7.4.8. The variation in combustion pressure

The ability of a fuel to combine with air and burn efficiently is characterized by cylinder pressure. High peak pressure and fastest pressure rise are correlated with high fuel consumption through premixed combustion (Wu *et al.*, 2020).

The relationship between instantaneous heat release rate (HRR) and crank angle for biodiesel blends (B5, B10, B15, B20, B30, and B100) based on petrodiesel at full load is presented in Figure 4.30.

The results show that the peak cylinder pressure of all fuel samples B0, B5, B10, B15, B20, B30, and B100 ranged from -5.06° to 2.24° after top ofdead centre (aTDC) and 74.44, 74.38, 74.22, 74, 09, 74.04, 73.88 and 73.84 bar respectively. The peak pressure increase showed similar patterns for all fuels. The highest cylinder pressure (74.44 bar) was measured due to its high calorific value for petrodiesel fuel. The next highest pressure was achieved for the B5 fuel blend at 14.38 bar, which is very close to that of petrodiesel fuel.

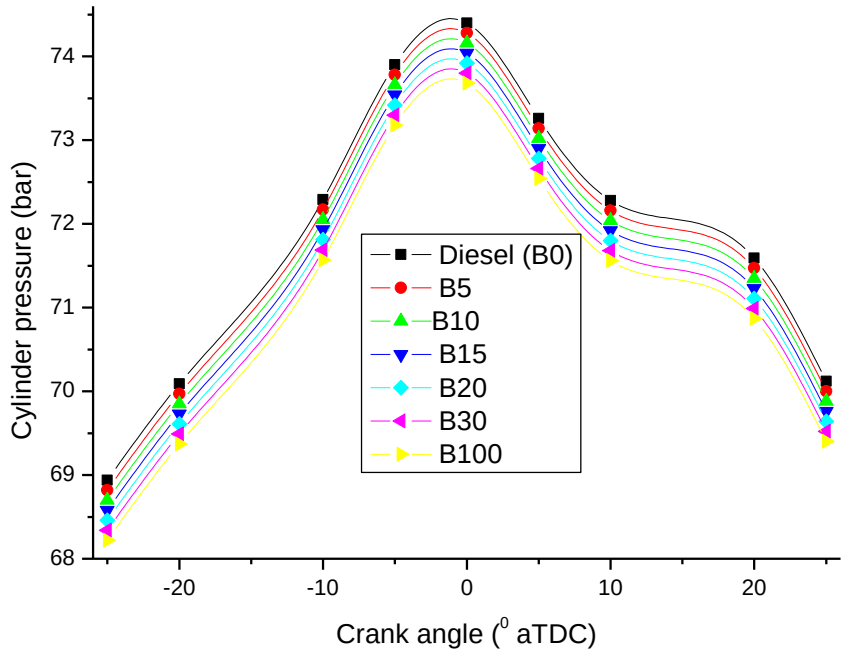

Figure 4.30: Variation of cylinder pressure with crank angle at 100% load

Among all fuel samples, the lowest in-cylinder pressure was measured for B100, which could be due to its lower volatility and higher viscosity, resulting in a lower air-fuel mixture in the premixed combustion zone compared to petrol. Lower cylinder pressure was previously reported for biodiesel combustion compared to petrodiesel fuel. Compared to the peak pressure of petrodiesel, biodiesel blends had lower peak cylinder pressures. This is because biodiesel-based diesel fuels have a shorter lag time (Hou *et al.*, 2022). Arun *et al.*, (2018) obtained similar results for studying the combustion parameters for yellow oleander biodiesel in a compression ignition (CI) engine. They observed that the pressure increases for biodiesel-diesel fuels from 5° bTDC to 10° bTDC is less than for petrodiesel. This is due to the higher cetane number and lower calorific value compared to petroleum diesel. The maximum cylinder pressure for B30 test fuels was high at 71.076 bar (8). B30, which is 0.93% lower than diesel, was identified as the test fuel with the

highest peak cylinder pressure. B100 had the lowest peak cylinder pressure, which was 7.42% lower than the peak cylinder pressure for petrodiesel.

4.7.4.9. Heat release rate

The heat release rate of yellow oleander biodiesel is a crucial parameter in understanding combustion characteristics, typically obtained through experimental testing or engine simulation. Its shape and magnitude can vary based on engine type, operating conditions, and blend used. In a diesel engine, heat is released in two stages during combustion. The premixed combustion stage (PC) is the first stage; after the start of the injection, the ignition delay creates an air-fuel-rich mixture in which the pressure is increased (Lodi *et al.*, 2020). HRR also provides comprehensive start of combustion (SOC) information that occurred 12-13 before the top dead center (bTDC) for all fuels tested. As the piston approaches the top dead center, the fuel vaporizes due to the high pressure and temperature. Due to the ignition delay causing a negative heat release, the heat release becomes positive momentarily as ignition begins. At the beginning of combustion, the fuel-rich mixture burns quickly and uncontrolled combustion occurs, in which the heat release is maximum (Dhahad *et al.*, 2014).

The heat release rate (HRR) of diesel, yellow oleander biodiesel (B100), (B5, B10, B15, B20, and B30) biodiesel blends are presented in Figure 4.31.

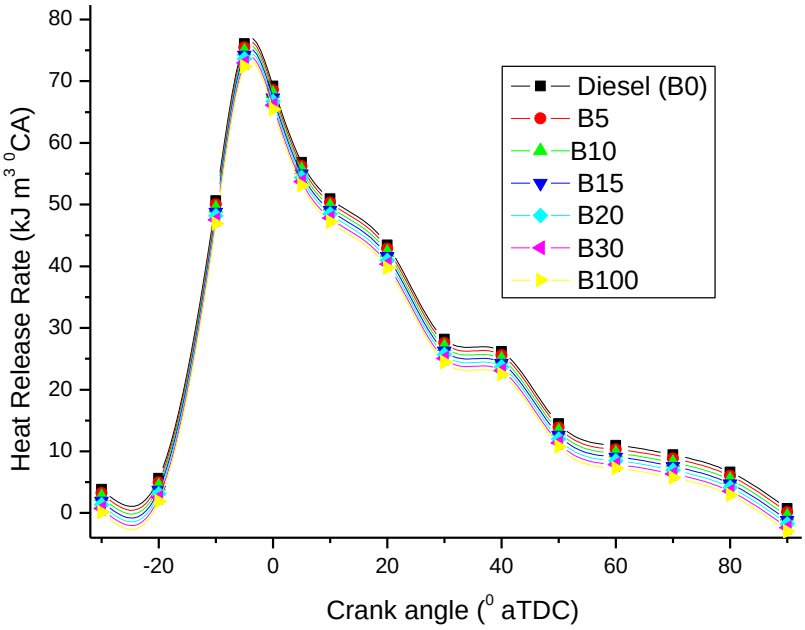

Figure 4.31: Variation of heat release rate with crank angle at 100% load.

The HRR of petrodiesel was comparable to B5, B10, B15, B20, B30 and B100 yellow oleander biodiesel blends. The B5 yellow oleander biodiesel blend achieved the highest HHR due to better atomization due to low viscosity. The results show that the fuel blends of B5, B10, B15, B20, B30 and B100 reduced the HHR in the fuel compared to the HHR (76.87 kJ/m^3) of petrodiesel. Values decreased by 2.07, 1.88, 2.67, 3.43, 8.24, 5.04 and 5.85b%, respectively, due to the increase in oxygen content in the mixtures.

Arun *et al.,* (2018) obtained similar results analyzing the HHR of yellow oleander biodiesel in a 4 - stroke diesel engine. Diesel (69.87 kJ m^{-3} °CA) had the highest HRR, followed by B30 (64.01 kJ m^{-3} °CA), B20 (56.30 kJ m^{-3} °CA) B10 (54.02 kJ m^{-3} °CA), B40 (51.44 kJ m^{-3} °CA) and B100 (47.24 kJ m^{-3} °CA). The diesel's longer ignition delay causes more fuel to accumulate in the cylinder; Unlike biodiesel blends, lower density and lower viscosity diesels improve fuel mixing and atomization and produce a higher HRR.

Engine operating conditions have a major impact on engine performance, combustion and emission characteristics. Petrodiesel and yellow oleander blends have been shown to work more effectively at higher loads than at lower loads. The B5 blend attained higher peak HRR than the other yellow oleander fuel blends, due to the better atomization and calorific value. Engine performance is enhanced by the high density, oxygen concentration and viscosity of oleander yellow biodiesel. As a result, all tested blends B5, B10, B15, B20, B30 and B100 showed better performance and emission properties compared to petroleum diesel. Petrodiesel exhibited better combustion abilities than the biodiesel blends while maintaining higher calorific values

4.7.5. Economic analysis of yellow oleander biodiesel production plant in Kenya

A biodiesel production cost (BPC) breakdown study was conducted for a large-scale biodiesel production plant with an installed operating capacity of 100,000 tons per year. This study evaluated the economics of such a pilot project in Kenya.

4.7.5.1. Estimation of specific investment costs (SIC)

The capital required to install the process equipment is represented in this study by the capital investment cost (CIC). Costs covered include the cost of site preparation, plumbing, instrumentation, insulation, foundations and ancillary facilities. The capital required for the land acquisition, contract fees, contingent liabilities and all plant components not directly related to the operation of the process are also included in CIC (Tsagkari *et al.*, 2016). These components include field service and supervision costs, home office costs, engineering costs and other supervision costs. Four process regions can be distinguished for the most important pieces of equipment required for the construction of a biodiesel production plant. Some examples are process plants with a working supply capacity (storage tanks), transesterification plants, purification plants and glycerin recovery plants. They create four different cost centers that represent the total cost of

equipment (TEC) (Pasha *et al.*, 2021). The TEC has been calculated in the next section using trusted and up to date cost information based on Kenyan market prices for biodiesel processing plants

4.7.5.2. The total equipment cost (TEC)

Some assumptions were made for the technical-economic analysis of the production of biodiesel from yellow oleander. The prices of the raw materials biodiesel and glycerol are estimated (US$ = 146.25). The breakdown of the total equipment costs is given in Table 4.14 below.

From Table 4.20, the purchase cost of equipment is KES 54,260,800.00 (US$ 375,034.21). Taking that the quipment work for 15 years and taking 6% interest rate, (PMI, 2008).

4.7.5.3. Purchase cost of equipment (PCE)

The Purchase Cost of Equipment (PCE) is the total cost of acquiring necessary equipment and machinery for a biodiesel production plant, a significant part of the Fixed Capital Investment.

Apparatus and equipment cost for 15 years =

$$54,260,800\left(1+\frac{6\times 15}{100}\right)=KES\,103,095,520.00\,(US\$\,740,926.63)$$

PCE = KES 103,095,520.00 or US$ 704,926.63.

4.7.5.4. Physical Plant Cost (PPC)

The Physical Plant Cost (PPC) is the financial allocation for construction, maintenance, and operation of physical facilities, including building construction, utility costs, maintenance, repairs, groundskeeping, and security. PPC = 3.4 × PCE (El-Galad *et al.*, 2015)

From the above data, PPC = 3.4 × 103,095,520.00 = KES 350,524,768.00 or US$ 2,396,750.54.

Table 4.20: Total equipment cost (TEC)

Item	Unit Price (KES ,000)	Quantity	Estimated cost, KES ('000)
Grinders (Ball or vertical roll mills, 10 ton/hr capacity, 46kW) -Chaina	11,000.00	2.0	22,000.00
Oil storage tanks (200 m3)- Chaina	900.00	10.0	9,000.00
Mechanical Screw Press, 1000 tons capacity; (Mohit International - India: HCT35)	36.00	10.00	360.00
Biodiesel Reactor (V R Process Engineering Consultants Private Limited- India: 380-400 V); 250 tons/day capacity)	2,400.00	2.00	4,800.00
Above ground oil storage tankers (Bomaque Steel Fabricators – Nairobi)	550.00	1.00	550.00
Above ground biodiesel oil storage tankers (Bomaque Steel Fabricators – Nairobi)	550.00	1.00	550.00
Above ground glycerol storage tankers (Bomaque Steel Fabricators – Nairobi)	550.00	1.00	550.00
Tractor (Tractors – Kenya); Massey Fergusson MF 2600 series	1,600.80	1.00	1,600.80
Irrigation pump (Diesel engine) biashara.co.ke; 20hp (14.7kw)	90.00	1.00	90.00
Motor Vehicle, Pickup truck (Toyota Vigo)	5,000.00	1.00	5,000.00
Mitsun Automatic Filter Press (Mutsin Engineering – India); Capacity 500 tons/day	475.00	2.00	950.00
2 Megapixels 8 cameras kit dome and or bullet cameras (CCTV solutions Nairobi)	60.00	2.00	120.00
Stainless Steel Liquid Mixing Tank - 10 000 lts (B & M Water Tower Industries LLP -India)	7,000.00	1.00	7,000.00
Computer and computer accessories -Total (Bright source Investments Kenya)	1,690.00	Various	1,690.00
Total equipment cost (TEC)			54,260.80

4.7.5.8. Auxiliary Plant Cost (APC)

Auxiliary Plant Cost (APC) refers to additional costs that are not directly related to the core production process, such as; Equipment, systems, and facilities for a biodiesel production facility that is critical to its successful and compliant operation. APC includes expenses for equipment, systems, and facilities to support biodiesel production, which vary depending on plant size and complexity. Budgeting for these additional costs is critical to successful operation. APC = 0.45 × PPC (El-Galad *et al.*, 2015)

From the above data APC = 0.45 × 350,524,768.00 = KES 157,736,145.60 or US$ 1,078,5822.91

4.7.5.9. Fixed capital investment (FCI)

Fixed capital investment (FCI), in the context of a biodiesel production facility, refers to the total amount of capital or financial resources required to construct the facility and its infrastructure, including any fixed or non-operating assets required for its operation. FCI covers the initial investment costs associated with the construction and commissioning of the system. These costs typically do not include operating costs or working capital. FCI = PPC + APC (El-Galad *et al.*, 2015)

From the above data, FCI = KES 508,260,913.60 or US$ 3,475,288.28

4.7.6. Total capital investment (TCI)

The total capital investment is the sum of the fixed capital investment and the working capital investment, i.e., TCI= FCI + Working Capital Investment (WCI) (Zuorro *et al.*, 2020). Calculated costs are presented in Table 4.21 below.

Table 4.21: The total capital investment (TCI)

Type	Cost/KES
Fixed capital investment (FCI)	508,260,913.60
Working capital investment (WCI) = 0.25 × FCI	127,065,228.40
Total capital investment (TCI) = FCI + WCI	635,326,142.00 (US$ 4,344,110.35)

The total capital investment (TCI) for the large-scale biodiesel production plant was estimated at KES 635,326,142.00 (US$ 4,344,110.35). This value is the sum of Fixed Investments (FCI) and Working Capital Investments (WCI) valued independently. The purchase of apparatus and equipment costed about 16.23 %, fixed capital investment about 80.00% and working capital 20.00 % of the total capital investment. In this project, a significant portion of the investment goes into fixed capital, indicating that the project requires significant infrastructure and long-term assets.

In addition, working capital is provided to ensure that the project has the necessary funds to cover ongoing operating costs. The purchase of machinery and equipment represents a smaller but still necessary portion of the overall investment, which may apply to specific tools and resources required for project activities.

4.7.7. The annual cost of electricity for the production of biodiesel

The electricity costs for the various production stages are determined from 1 kWh electricity price = 21.99 KES (KPLC 2022 Tarr (1).Pdf, n.d.), the specific heat of water = 4.18 kJ/kg/K, the specific heat of yellow oleander oil = 1.67 kJ/kg / K (Oseni *et al.*, 2014), and heat loss due to radiation and convection is 10 %.

4.7.7.1. The cost of electricity in mixing methanol and the synthesized nanocatalyst

The cost of electricity used in stirring methanol and synthesized eggshells catalyst when the motor's power was 45 kW. The duration used for thorough stirring was 30 minutes, and the annual cost of electricity used in stirring for 300 working days.

$$300 \times 45 \times \frac{30}{60} \times 21.99 = KES\ 148{,}432.50 (US\$\ 1{,}014.92)$$

The cost of running the mixing machine four times is KES 148,432.50 (US$ 1,014.92)

4.7.7.2. The cost of electricity used in heating during transesterification

The cost of electricity used in heating oil from 20°C to 60°C during transesterification was derived from the amount of heat energy required for the reaction by the Equation 4.6;

$$Q = \frac{mC_p \Delta T}{efficiency} \quad \text{……Equation 4.6}$$

$$Q = \frac{mC_p \Delta T}{efficiency}. = \frac{102{,}040{,}816.30 \times 1.67 \times 40}{0.9} = 7{,}573{,}696{,}145.00\ kJ / annum$$

Where; Q = heat required (kJ), m = mass consumed in the production of 100,000,000 kg of biodiesel, Cp = specific heat (kJ/kg C), = temperature difference (C) and efficiency = 0.9 (van Gelderen *et al.*, 2017)

$$= \frac{7,573,696,145}{3,600} = 2,103,804.49\ kWh$$

$$2,103,804.49 \times 21.99 = KES 46,262,660.62\ (US\$\ 316,325.88)$$

The cost of using electricity for heating during transesterification is 46,262,660.62 (US$ 316,325.88) per annum.

4.7.7.3. The cost of electricity used in stirring during the heating process

Assume power of the motor was 45 kW, and the duration used for thorough stirring was 2 hour/day for 300 working days in a year. The annual cost of electricity cost for this process is

$$300 \times 45 \times 2 \times 21.99 = KES\ 573,730\ (US\$\ 4,059.69)$$

4.7.7.4. The cost of electricity used in drying the biodiesel

The cost of electricity used in heating 100 000 000 kg biodiesel from 20°C to 110°C to remove residual methanol. The heat energy used in the heating process was;

102,040,816.3 ×2 ×70 = 14,285,714,286.00/0.9 = 15,873,015,873.00kJ= 4,409,171.08 kWh

$$Q = \frac{mC_p \Delta T}{efficiency} = \frac{102,040,816.30 \times 2.0 \times 70}{0.9} = \frac{14,285,714,286}{0.9} = 15,873,015,873\ kJ$$

$$= \frac{15,873,015,873}{3,600} = 4,409,171.08\ kWh$$

The annual cost of electricity cost for this process was;

$$4,409,171.08 \times 21.99 = KES\ 96,957,671.96\ (US\$662,958.44)$$

4.7.8. The annual cost of electricity used in biodiesel production

The annual cost of electricity used in the production of biodiesel is 148,432.50 + 46,262,660.62 + 593,730.00 + 96,957,671.96 = 143,665,630.08 (US$ 984,358.94)

4.7.8.1. Total production cost of biodiesel (TPC)

The total production cost of biodiesel also called the total manufacturing cost (TMC), is the cost of running a biodiesel plant in one year. They cover a wide range of costs, including labor costs, raw materials, building rent, and other costs incurred during the course of production. Production costs include all direct and indirect costs, including material, labor, production costs, factory costs, and office and administration costs. The following formula is used to determine this cost.

Total manufacturing cost (TMC) = Direct cost of production + Indirect cost of production

4.7.8.2. Direct cost of production (DCP)

The direct costs of biodiesel production represent the costs directly associated with converting raw materials into biodiesel. These include costs associated with manufacturing and processing, such as raw materials, maintenance, quality control, labor costs, and energy, which are typically variable and tied to the production process. The DCP varies depending on factors such as volume, technology, location, and raw material costs. Accurate accounting and cost tracking are critical to managing these costs and optimizing production processes.

The breakdown of the total production costs of a biodiesel production plant with an installed operating capacity of 100,000 tons/year is given in Tables 4.22, and 4.23.

The operating labor costs was estimated at 12,480,000.00 KES (US $ 85,333.33) per annum, assuming one operator worked 49 weeks per year and three 8-hour shifts per day were required for a continuous plant (El-Galad *et al.*, 2015).

The production of biodiesel often requires chemicals and catalysts such as methanol or ethanol, as well as catalysts such as sodium hydroxide or potassium hydroxide. These chemicals are used in the transesterification process to convert feedstock into biodiesel. Energy costs include electricity and heat required for various phases of the manufacturing process such as mixing, heating, and separating.

Table 4.22: Estimated operating labour cost

Item	Unit Price (KES)/Month	Quantity	Estimated cost, KES ('000)
Managers	200,000.00	2.00	400.00
Engineer	150,000.00	1.00	150.00
Chemist	80,000.00	1.00	80.00
Technologists	80,000.00	3.00	240.00
Secretary	50,000.00	1.00	50.00
Messenger	30,000.00	1.00	30.00
Labourers	90,000.00	1.00	90.00
Operating labour (OL)			1,040.00

Biodiesel production facilities require regular maintenance to keep equipment and machinery in optimal operating condition. Maintenance costs are part of the direct production costs. Utilities include water, gas, and other resources needed for the production process. If raw materials or finished biodiesel need to be transported to and from the production site, transportation costs are included. Biodiesel production requires quality control and testing to ensure the end product meets industry standards (Poddar *et al.*, 2015). There is no data on the direct production costs of biodiesel from yellow oleander.

Table 4.23. Calcuating biodiesel production cost (BPC)

Category	Factor	Unit cost (KES)'000	Total Unit cost (KES)'000
Seedlings/kg	230,000,000.00	0.025	5,750,000.00
Methanol (1:3 stoichiometric ratio with oil)	13,575,417.56	0.4	5,430,167.02
Electricity (Administration)	0.1 × TEC	54,260.80	5426.08
Electricity (manufacturing Section: 4.8.4.4)		143,665.63	143,665.63
Shipping & packaging	0.02 × Raw materials	10,150,000.00	203,000.00
Plant overheads	0.5 × (OL + M &O)	47,532.48	23,766.24
Property insurance cost	5% PCE	103,096	5,154.78
Maintenance labour	0.01 × FCI	508,260.91	5,082.61
Maintenance and operational cost (M & O)	0.1 × PPC	350,524.77	35,052.48
Other fixed operating costs	0.1 × FCI	508,260.91	50,826.09
Rent	0.02 × PCE	103,095.52	2,061.91
Royalties	0.01 × FCI	508,260.91	5,082.61
Supervision	0.2 × Labour	12,480	2,496.00
Operating supplies	0.15 × Maintenance	5,082.61	762.39
Laboratory charges	0.15 × Labor	12,480	6,240.00
Direct production cost (DPC)			10,638,616.81
Indirect production cost (IPC)	0.25 × DPC	10,638,616.81	2,660,478.83
Biodiesel production cost (BPC)	DPC + IPC		13,299,095.64

4.7.8.3. Indirect Production Cost (IPC)

The indirect production costs of a biodiesel production facility include payments that are required to run the business but are not related to the production process itself, such as: Costs of office supplies, furniture,

and administrative and support tasks such as accounting, staff, and salaries, property taxes, utilities including water, electricity, and gas, and rent or lease payments.

The calculation of the annual biodiesel production costs is shown in the Table 4.17 above.

The total cost of biodiesel production (TCP) was KES 14,674,865,741.00 (US $ 100,340,962.30), with the direct (DCP) and indirect costs of biodiesel production (ICP) accounting for 80 % and 20 %, respectively. This means that a large part of the costs incurred in the biodiesel production process are directly related to the conversion of the raw materials into biodiesel. The remaining 20% typically includes indirect costs such as administrative costs, financing, rent, utilities, insurance, marketing, sales, research and development costs and profit margins (El-Galad *et al.*, 2015). The relative cost distribution can vary depending on factors such as raw material source, raw material price, scale of production, energy efficiency, and efficiency of the production process. Several tactics can be used to reduce indirect production costs, including a larger production facility, which could benefit from economies of scale by reducing overhead. Better manufacturing technology could also reduce the costs associated with research and development (Pasha *et al.*, 2021).

In this study, raw material and labor costs accounted for 76.19 % and 0.085 % of annual production costs, respectively. Raw material costs account for a significant portion of the total annual production costs. Biodiesel production processes are often highly automated and optimized for efficiency. Automated processes reduce the need for large labor forces, resulting in lower labor costs relative to overall production costs. Although biodiesel production may require skilled technicians and engineers to operate and maintain equipment, the amount of manual labor is relatively low compared to some other industries. Qualified personnel can keep the factory running smoothly with minimal labor. Large biodiesel plants can also benefit from economies of scale, meaning they produce biodiesel in large quantities, which can help reduce labor costs per unit of oil. Maheshwari *et al.*, (2022) obtained similar results when reviewing recent trends in

biodiesel production. They found that the biggest challenge in producing commercial biodiesel is the high cost of pure vegetable oils. It accounts for between 70% and 95% of the total production cost of biodiesel.

4.7.9. Annual cost of production of yellow oleander biodiesel

A biodiesel production unit can determine total production costs and make informed decisions about pricing, cost-saving strategies, and other financial planning by summarizing all direct and indirect costs. The volume of yellow oleander biodiesel produced can be calculated using the following equation (Density of biodiesel = 0.86 kg/L)

In one year, the following volume of biodiesel is produced = $\frac{100,000,000\ kg}{0.86\ kg/L} = 116,279,069.77\ L$

With 93.7 % efficiency, the volume of biodiesel produced will be 106, 477,272.70 Litres.

4.7.9.1. Income generated from the sale of glycerine (a by-product)

According to the literature, 10% of the converted vegetable oil corresponds to the amount of glycerin produced (Papanikolaou *et al.*, 2017). In this study, the amount of glycerin produced in one year was ~ 10,647,727.27 liters. The annual income generated per year (@ KES 250 (US$ 1.70) per litre (Acacia *et al.*, 2022) from glycerine sales is KES 2,661,931,817.00 or (US$ 18,170,183.05)

Annual production cost = 13,299,095,642.46 – 2,661,931,817.00 = KES 10,637,163,825.46 (US$ 72,608,626.79).

This income reduced the cost of production by 20.02 %. By the mid-20th century, more than 1,500 uses foglycerine had been observed, although traditionally the substances were mainly used in the soap industry (Nanda *et al.*, 2018).

This volume can assist in calculating the annual production using Equation 4.7.

$$\text{Production cost}/kg = \frac{Annual\ cost\ of\ production\ (KES)}{Annual\ production\ rate} \quad \text{……Equation 4.7}$$

$$\Pr oduction \cos t / kg = \frac{10,637,163,825.46}{106,\ 477,272.70} = KES\ 99.90\ (US\$\ 0.68) / L$$

The net cost of biodiesel production from yellow oleander has been estimated at 99.90 (US$ 0.67)/L. No literature is available on the production costs of biodiesel from yellow oleander.

4.7.9.2. Income from yellow oleander biodiesel

Selling Price = Cost Price + (% Profit Margin × Cost Price)

= 99.90 + (0.2×99.90) = 99.90 + 19.98 = 119.88

The selling price of yellow oleander biodiesel was estimated at KES 119.88 (US$ 0.82)/L.

4.7.9.3. The price of the biodiesel blends

The estimated diesel blendstock price was based on average reported blends each year, the price of biodiesel and proportion of the blended fuel.

The price of diesel blends can be solved using the Equation 4.8.

$$P_{composite} = (\%BD) \times P_{BD} + (1 - \%BD) \times P_{diesel} \text{ .....……Equation 4.8}$$

Where; $P_{composite}$ is the composite price/litre of blended diesel, P_{BD} is the price/litre of pure biodiesel (BD), P_{diesel} is the price/litre of ptrodiesel; and % BD is the specified biodiesel blending (Alonzo & Alonzo, 2016). Using the current market price of petrodiesel fuel in Kenya at KES 203.47/L.

The market price for B5 = (0.05×119.88) + (0.95×203.47) = 193.49.

The calculated composite prices of blended diesel are represented in Figure 4.32 below.

The price of petrodiesel (B0), and all the yellow oleander biodiesel blends (B0, B5, B10, B15, B20, B30, and B100) were 203.47, 193.29, 195.11, 190.93, 186.75, 178.39, and 119.88/L, respectively. The price of biodiesel blend B20 is KES 186.75/L, which is 8.22 % lower than the petrodiesel market price in Kenya. Biodiesel blend prices fell as the biodiesel content of the blend increased. B5 is the most expensive blend, priced at 193.49 KES (US$ 1.32)/L.

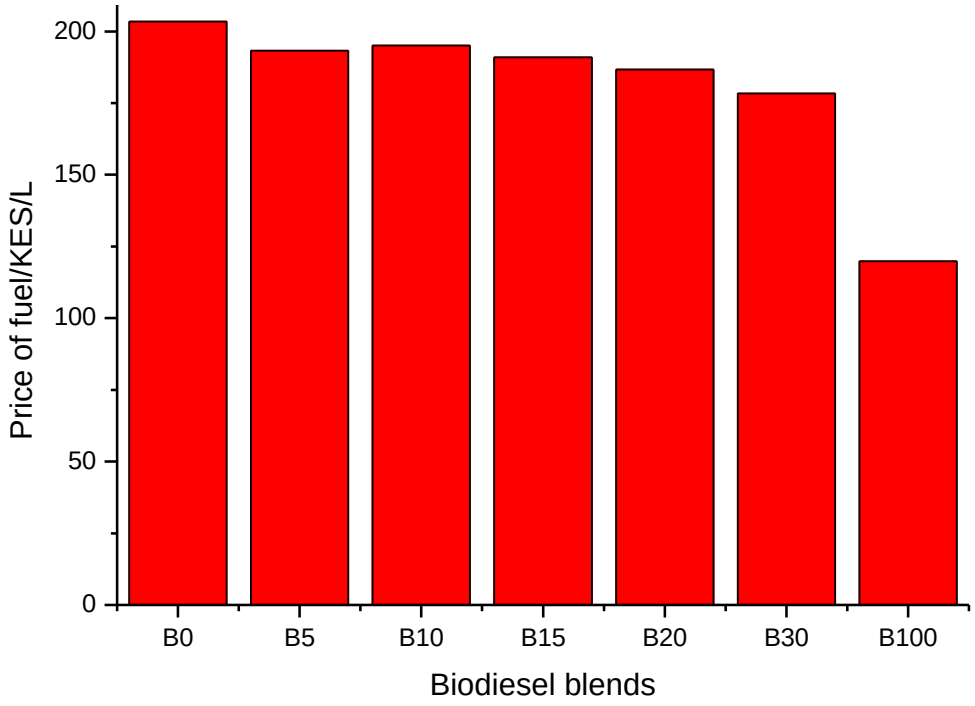

Figure 4.32: Selling price of biodiesel blends

B20 is the most popular biodiesel blend because it is compatible with existing diesel engines and infrastructure. It can be used in most diesel engines without modification, making it a practical choice for blending with conventional diesel fuel. It is a standard blend; it strikes the right balance of cost and emissions, cold-weather performance, and materials compatibility (Zahan & Kano, 2018). There is no literature on the selling price of biodiesel blends.

4.7.9.4. Return of investment for yellow oleander biodiesel production

Return on Investment (ROI) is a financial metric used to measure the profitability of an investment compared to its cost. When calculating the ROI, the net return on the investment is divided by the price of the investment and the result is expressed as a percentage.

SP = the selling price of B20 fuel is KES 186.75.

Net profit = Total revenue – Total cost of production Equation 4.8

Total revenue = Price/L × Volume of biodiesel sold Equation 4.9

= 184.77 × 106,477,272.70 = KES 19,884,630,677.00 (US$ 135731267.40)

Net profit = 19,884,630,677.00– 13,299,095,642.46 = 6,585,535,034.27 (US$ 43,513,379.07)

$$ROI = \frac{NP}{TCI} \times 100$$ ……..Equation 4.10

Where; TCI = Total capital Investment = KES 635,326,142.00 (US$ 44,952,457.57)

$$ROI = \frac{6,585,535,034.27}{635,362,142} \times 100 = 1,036.50\ \%$$

The ROI for biodiesel production from yellow oleander was 1,036.50 %, which represents a high return on investment. This means that the production of yellow oleander biodiesel is a profitable business and offers significant financial benefits compared to capital investments. This is a positive sign for the financial viability of biodiesel production. No data is available to examine the return on investment for yellow oleander biodiesel.

4.8. Energy Analysis

Energy balance is the ratio between the amount of energy used by a system and the amount of energy it uses or loses over a period of time. It is essentially the ratio between the energy input and output of the system. It actually accounts for the total amount of energy used in the production of biodiesel compared to the amount of energy contained in the fuel produced (Renewable & Agency, 2017).

4.8.1. Ploughing

The energy used in plowing is determined by the method used and can be human, animal or mechanical energy. In this study study, a tractor was used and the energy consumed was determined using the equation;

$$E_{N1} = v_f \times \rho \times CV \times k .....Equation \quad 4.3.6.$$ (A. Yadav & Singh, 2010)

Where; k = 1.0 for normal soil, ρ = 55L/hectare/year;

E_{N1} = 55 L × 804 kg/L × 43.20 kJ/kg × 1.0 = 1,910,304.00 MJ

Where; E_{N1}: is energy input used in ploughing the plants in the nursery. vf: is the volume of diesel in liters fuel consumed in 1 hectare. ρ : is the specific gravity of the diesel fuel. CV: is the soil resistance coefficient (N/m^2) which is a measure of how much force is required to plow the soil. k: represents the shape factor of the plow, which considers the width and depth of the plow and its interaction with the soil. k is the soil constant (k = 1, normal soil).

4.8.2. Irrigation

The energy expenditure for irrigation is given by;

$$E_{N2} = 3600 \times R_p \times t \times d \times t = 3600 \times 1\,kWh \times (8 \times 300) \times 1 \times 2.5 = 21{,}600{,}000\ MJ$$

Where;

E_{N2} is the energy input used in irrigating the plants in the nursery. R_p is the 1 kWh which pumps 1000 kg of water in 1 hour and considering normal depth of water is available, r = 2.5 (Yadav & Singh, 2010).

4.8.3. Manpower

The manpower spent is calculated as follows;

$$E_{N4} = E \times \left[l_1 \times t_1 + l_2 \times t_2 + l_3 \times t_3 + l_4 \times t_4 + l_5 \times t_5 \right] \times k\ =$$

Where;

- EN_4: represents the energy required (MJ) to plow a given length of soil with a given plow under given conditions is represented by this variable.

- l_1, l_2, l_3, l_4, l_5: represent the length of soil plowed by the plow in each pass, typically measured in meters.
- t_1, t_2, t_3, t_4, and t_5: represent the time it takes to plow each section of soil, typically measured in seconds

$1.0 \times [1 \times (8 \times 300) + (1.2 \times 8 \times 300) + 1 \times (1 \times 8 \times 300) + (1 \times 8 \times 7 \times 4)] \times 1.2 = 9{,}484.80 MJ$

$E_N = E_{N1} + E_{N2} + E_{N3} + E_{N4}$ $E_N = E_{N1} + E_{N2} + E_{N3} + E_{N4}$ (A. Yadav & Singh, 2010)

Where;

E_N is energy input (MJ) in the nursery, E_{N3} is the energy input (MJ) in placing manure in the nursery. $E_{N3} = 0$

l_1 =1.0, the factor for the type of labor used in ploughing the field.

l_2 = 1.2, the factor for the type of labor used in mixing the soil with manure.

l_3 =1.0, the factor for the type of labor used for filling bags with soil.

l_4 =1.0, the factor for the type of labor used for irrigating the plants.

l_5 = 1.0, the factor for the type of labor used for care and safety for a period of one month.

For normal soil;

E_N = 1,910,304.00 + 21,600,000.00 +0 + 9,484.80= 23,519,788.80 MJ

4.8.4. Plantation

The total energy used in plantation may be calculated using the following equation;

$E_P = E_{P1} + E_{P2} + E_{P3} + E_{P4}$ (Yadav & Singh, 2010).

Where; $E_{P1} = 1{,}910{,}340.00\ MJ$, $E_{P2} = 21{,}600{,}000.00\ MJ$, $E_{P3} = 0\ MJ$, and $E_{P4} = 9{,}484.80\ MJ$

For normal soil;

E_p = 1,910,304.00 + 21,600,000.00 +0 + 9,484.80= 23,519,788.80 MJ

Where; E_P in the energy (MJ) input used in plantation and management of the plants for a period of 1 year. E_{P1} is the energy input in land preparation (MJ), E_{P2} is the energy input in irrigation (MJ), E_{P3} is the energy input in placing manures (MJ), E_{P4} is the energy input in manpower used (MJ)

4.8.5. Growth

The total energy for nurturing and water sprays is given by $E_G = E \times t + 2.5 \times E_{P2}$ = (1 × 12 × 365 × 2) + 2.5 × 21,600,000.00 = 54,008,760.00 MJ.

Where;

E is the energy expenditure rate in MJ/h. The normal rate is 1 MJ/h. E_G is the energy input during growth for the second and third years, and t is the time taken for the growth of the plant ~ 2 years.

4.8.6. Seed collection

The energy used in seed collection is calculated as; $E_{SC} = E \times (t_1 + t_2 + t_3 + t_4) \times k$ (A. Yadav & Singh, 2010)

For normal soil;

E_{SC} = 1.96 × [(15×8×20) + (6 × 4 × 300) + (15 × 8 × 300) + (4×2×52) × 1.0 = 156,047.36 MJ

Where; E_{SC} is the energy input for seed collection (MJ). t_1 is the time in hours taken for pod collection (Assuming one man collects from 40 trees per day and the second collection is 75 % of the first one), t_2 is the time in hours required to dry the fruit. Four workers are required for four

days, t_3 is the time in hours required to de-husk the seeds from the fruit and t_4 is the time in hours required for seed drying. Four workers are required for two days (Yadav & Singh, 2010).

4.8.7. Transport of seeds

Seeds were transported using a tractor, which consumed 2 l of diesel and takes half an hour. The energy used can be calculated using the equation;

E_{TP} = $v_f \times \rho \times$ CV + $E \times$ t = 4 litres × 300 × 804 kg/l × 43.200MJ/kg + 1.0 × 2 ×4 × 300 = 10,422,240.00 MJ.

Where; E_{TP} is the energy (MJ) input used in transporting the fruits (Yadav & Singh, 2010) .

4.8.8. Oil extraction

Oil extraction from the yellow oleander seed uses an extraction unit a capacity of 1 ton/h (A. Yadav & Singh, 2010).

The energy consumed in oil extraction is given by E_{OE} = (P ×M + E × t) × y = [(55 kWh×100,000) + (1.0 × [(8 ×300)] × 1.0 = 5,502,400.00 MJ.

Where; E_{OE} is the energy input used for oil extraction (kJ), P = 55 kWh of seeds input and M is the total mass of the oil in tons (Yadav & Singh, 2010).

4.8.9. Transesterification

The energy expenditure in transesterification process is given by;

E_T = P ×M + E × t = 36 ×100,000 + 1.0 × (2 ×300) = 3,600,600.00 MJ

Where;

- E: is the total energy expenditure (kJ) involved in the transesterification process is represented by this variable.

- P: is the power (kWh) required to drive the transesterification reaction.
- M: The mass (in kg) of the reactants in the reaction is represented by this variable.
- t: is the time (in seconds) required to complete the transesterification process

E_T is the energy input for transesterification in kJ, and P = 36 kWh tons of oil (Yadav & Singh, 2010).

4.9. Total Energy Demand/Input

Total energy demand/input in the life cycle of the biodiesel production can be calculated using the equation; $E_{input} = E_N + E_P + E_G + E_{SC} + E_{TP} + E_{OE} + E_T$ (Yadav & Singh, 2010).

E_{input} = the total energy input used for transesterification reaction in kJ.

For normal soil;

E_{input} = 23,519,788.80 + 23,519,788.80 + 54,008,760.00 + 156,047.36 + 10,422,240.00 + 5,502,400.00 + 3,600,600.00 = 120,729,624.96 MJ or $= \frac{120,729,624.96}{113,363,364} = 1.06\ MJ/L$

4.9.1. Energy Output

The energy contained in the biodiesel produced from 10 000 tons of oil is given by;

$E' = CV_{BD} \times T \times 1000$ (Yadav & Singh, 2010); Where CV_{BD} is the calorific value of the yellow oleander (MJ/kg) and T is the quantity of the biodiesel in tons.

E' = 41.90 × 100,000 × 1000 = 4,190,000,000 MJ. Taking into consideration the thermal efficiency of a C.I engine as 20 % (Yadav & Singh, 2010)., the remaining energy can be calculated as;

E_{output} = 0.20 × E = 0.20 × 4,190,000,000 = 838,000,000 MJ

4.9.2. Net Energy Ratio

The ratio of the available energy of the final product (yellow oleander biodiesel) to the energy consumed during the conversion process is called the net energy ratio. This can be obtained using the equation; Net energy ratio $= \frac{838,000,000}{113,363,364} = 6.94\ MJ / L$

The net energy ratio for yellow oleander biodiesel is 6.94, which means that for every unit of energy invested in growing, harvesting and processing the biodiesel, 6.94 units of energy are obtained as the end product. This indicates that the yellow oleander biodiesel production process is energy efficient and can be used as a viable energy source. Energy sources with a high net energy ratio are generally considered to be more efficient, economically feasible, and environmentally benign than energy sources with a low net energy ratio. Although this research found that biodiesel production from yellow oleander is energy efficient. No data are available on the energy balance of yellow oleander biodiesel.

5.0 CONCLUSION AND RECOMMENTATION

Yellow oleander oil extraction from feedstock yielded an impressive 65.14 ± 0.66%, indicating a robust and efficient process for oil recovery from oleander seeds. The extracted yellow oleander oil's physicochemical properties meet ASTM specifications, ensuring its quality and suitability for various applications, including biodiesel production.

The nanocatalyst, primarily composed of 95% CaO, is a suitable catalyst for biodiesel production due to its diverse and complex matrix, including Aragonite, Vaterite, and Calcite. The nanocatalyst, ranging from 10 to 50 nm in size, enhances catalysis efficiency by increasing surface area and facilitating better interaction with reactants. The eggshell-derived nanocatalyst, with its high CaO content, polycrystalline structure, nano-size, and large surface area, is well-suited for biodiesel production due to its enhanced catalytic efficiency.

The Response Surface Methodology (RSM) with Central Composite Design (CCD) has proven to be an effective tool for optimizing yellow oleander biodiesel production. The obtained results, under the optimized conditions of temperature (60 ℃), reaction time (40 min), and catalyst loading (3.68% w:w), yielded an impressive biodiesel production efficiency with a % biodiesel yield of 93.7%.

The fuel properties of B20 derived from yellow oleander biodiesel blends showcase characteristics that align with established standards and closely resemble those of petrodiesel. This suggests the potential for the utilization of yellow oleander biodiesel blends as a viable and ASTM-compliant alternative in conventional diesel engines, contributing to environmentally sustainable fuel option.

The initial findings indicate that B20, containing Yellow Oleander Biodiesel, holds promise as a fuel option for diesel engines. Further research and testing are recommended to validate these findings and address potential challenges that may arise under various engine operating conditions. The energy balance of yellow oleander biodiesel, calculated at 6.94, signifies a positive and substantial net energy gain in the production process. This finding holds significant implications for the environmental sustainability and potential benefits of yellow oleander biodiesel when compared to traditional petrodiese.

Further research can contribute to the advancement of environmentally friendly solvent use in vegetable oil extraction, promoting sustainable and responsible practices in the industry.

Further feasibility studies are to be conducted to assess the technical, economic, and environmental feasibility of the industrial production of yellow oleander biodiesel.

More studies need to be done to determine the optimal size range for nanocatalysts in yellow oleander biodiesel production and to evaluate their influence on reaction kinetics, yield, and process efficiency.

Further studies to explore the different synthesis methods and conditions required to achieve different nanocatalyst sizes. This it to be done by adjusting precursor concentrations, reaction times, temperatures, and other relevant parameters.

REFERENCES

Abdul Hakim Shaah, M., Hossain, M. S., Salem Allafi, F. A., Alsaedi, A., Ismail, N., Ab Kadir, M. O., & Ahmad, M. I. (2021). A review on non-edible oil as a potential feedstock for biodiesel: physicochemical properties and production technologies. *RSC Advances*, *11*(40), 25018–25037. https://doi.org/10.1039/d1ra04311k

Abeydeera, L. H. U. W., Mesthrige, J. W., & Samarasinghalage, T. I. (2019). Global research on carbon emissions: A scientometric review. *Sustainability (Switzerland)*, *11*(14), 1–25. https://doi.org/10.3390/su11143972

Abid, N., Khan, A. M., Shujait, S., Chaudhary, K., Ikram, M., Imran, M., Haider, J., Khan, M., Khan, Q., & Maqbool, M. (2022). Synthesis of nanomaterials using various top-down and bottom-up approaches, influencing factors, advantages, and disadvantages: A review. *Advances in Colloid and Interface Science*, *300*(January 2022), 102597. https://doi.org/10.1016/j.cis.2021.102597

Acacia, G., N-acetyl-l-cysteine, S., & Symbols, H. (2022). *LOBA Chemie Price List 2021-2022 with1st Amendment LOBA Chemie Price List 2021-2022 with1st Amendment*. 1–353.

Access, O. (2018). A Review of Selected Non-Edible Biomass Sources as Feedstock for Biodiesel Production. *Long-Haul Travel Motivation by International Tourist to Penang*, *i*(tourism), 13.

Acevedo, J. C., Hernández, J. A., Valdés, C. F., & Khanal, S. K. (2015). Analysis of operating costs for producing biodiesel from palm oil at pilot-scale in Colombia. In *Bioresource Technology* (Vol. 188). Elsevier Ltd. https://doi.org/10.1016/j.biortech.2015.01.071

Adaileh, W. M., & Alqdah, K. S. (2012). Performance of diesel engine fuelled by a biodiesel extracted from a waste cocking oil. *Energy Procedia*, *18*(December 2012), 1317–1334. https://doi.org/10.1016/j.egypro.2012.05.149

Adepoju, T. F., Olatunbosun, B. E., Olatunji, O. M., & Ibeh, M. A. (2018). Brette Pearl Spar Mable (BPSM): a potential recoverable catalyst as a renewable source of biodiesel from Thevetia peruviana seed oil for the benefit of sustainable development in West Africa. *Energy, Sustainability and Society*, *8*(1), 1–17. https://doi.org/10.1186/s13705-018-0164-1

Adepoju, T. F., Rasheed, B., Olatunji, O. M., Ibeh, M. A., Ademiluyi, F. T., & Olatunbosun, B. E. (2018). Modeling and optimization of lucky nut biodiesel production from lucky nut seed by pearl spar catalysed transesterification. *Heliyon*, *4*(9), e00798. https://doi.org/10.1016/j.heliyon.2018.e00798

Aina, N., Mohd, I., & Zawawi, R. M. (2023). *RSC Advances Optimization of a lipase / reduced graphene oxide / metal – organic framework electrode using a central*. 13493–13504. https://doi.org/10.1039/D3RA01060K

Aktas, D. F., Lee, J. S., Little, B. J., Ray, R. I., Davidova, I. A., Lyles, C. N., & Suflita, J. M.

(2010). *Anaerobic Metabolism of Biodiesel and Its Impact on Metal Corrosion*. *49*(12), 176–181. https://doi.org/10.1021/ef100084j

Al-Mashhadani, H., & Fernando, S. (2017). Properties, performance, and applications of biofuel blends: A review. *AIMS Energy*, *5*(4), 735–767. https://doi.org/10.3934/energy.2017.4.735

Alhindawi, R., Nahleh, Y. A., Kumar, A., & Shiwakoti, N. (2020). Projection of greenhouse gas emissions for the road transport sector based on multivariate regression and the double exponential smoothing model. *Sustainability (Switzerland)*, *12*(21), 1–18. https://doi.org/10.3390/su12219152

Ali, Arbab, Shah, T., Ullah, R., Zhou, P., & Guo, M. (2021). *Review on Recent Progress in Magnetic Nanoparticles : Synthesis , Characterization , and Diverse Applications*. *9*(July), 1–25. https://doi.org/10.3389/fchem.2021.629054

Ali, Attarad, Zafar, H., Zia, M., ul Haq, I., Phull, A. R., Ali, J. S., & Hussain, A. (2016). Synthesis, characterization, applications, and challenges of iron oxide nanoparticles. *Nanotechnology, Science and Applications*, *9*, 49–67. https://doi.org/10.2147/NSA.S99986

Almeida, C., Oliveira, G. G., Pereira, T., & Ferreira, D. S. (2022). *Biodiesel and Bioplastic Production from Waste-Cooking-Oil Transesterification : An Environmentally Friendly Approach*. 1–16.

Alonzo, R. P., & Alonzo, R. P. (2016). *An Economic and Environmental Analysis of the Impact of Higher- Blended Biodiesel on the Philippine Economy By*. *8293*, 0–8.

Alves, J. L. F., da Silva, J. C. G., da Silva Filho, V. F., Alves, R. F., de Araujo Galdino, W. V., & De Sena, R. F. (2019). Kinetics and thermodynamics parameters evaluation of pyrolysis of invasive aquatic macrophytes to determine their bioenergy potentials. *Biomass and Bioenergy*, *121*(September 2018), 28–40. https://doi.org/10.1016/j.biombioe.2018.12.015

Amin, A. (2019). Review of diesel production from renewable resources: Catalysis, process kinetics and technologies. *Ain Shams Engineering Journal*, *10*(4), 821–839. https://doi.org/10.1016/j.asej.2019.08.001

Ani, J. U., Okoro, U. C., Aneke, L. E., Onukwuli, O. D., Obi, I. O., Akpomie, K. G., & Ofomatah, A. C. (2019). Application of response surface methodology for optimization of dissolved solids adsorption by activated coal. *Applied Water Science*, *9*(3), 1–11. https://doi.org/10.1007/s13201-019-0943-7

Aniolek, M., Smith, T., & Czerwinski, F. (2021). Combining differential scanning calorimetry and cooling- heating curve thermal analysis to study the melting and solidification behavior of al-ce binary alloys. *Metals*, *11*(2), 1–17. https://doi.org/10.3390/met11020372

anka, P. (2018). Uses of Transmission Electron Microscope in Microscopy and its Advantages and Disadvantages. *International Journal of Current Microbiology and Applied Sciences*, *7*(05), 743–747. https://doi.org/10.20546/ijcmas.2018.705.090

Anovitz, L. M., & Cole, D. R. (2015). Characterization and Analysis of Porosity and Pore Structures. *Reviews in Mineralogy and Geochemistry*, *80*(1), 61–164. https://doi.org/10.2138/rmg.2015.80.04

Aransiola, E. F., Ojumu, T. V., Oyekola, O. O., Madzimbamuto, T. F., & Ikhu-Omoregbe, D. I. O. (2014). A review of current technology for biodiesel production: State of the art. *Biomass and Bioenergy*, *61*(January 2019), 276–297. https://doi.org/10.1016/j.biombioe.2013.11.014

Araque, L. M. (2018). *Biodegradation of Poly (3-hydroxybutyrate) / Eggshellsystems*. *May*. https://doi.org/10.1590/1980-5373-mr-2017-0792

Aro, E. M. (2016). From first generation biofuels to advanced solar biofuels. *Ambio*, *45*(1), 24–31. https://doi.org/10.1007/s13280-015-0730-0

Arsene, M. L., Răut, I., Călin, M., Jecu, M. L., Doni, M., & Gurban, A. M. (2021). Versatility of reverse micelles: From biomimetic models to nano (bio)sensor design. *Processes*, *9*(2), 1–43. https://doi.org/10.3390/pr9020345

Ashad, M., Nasim, G., Khan, O., Parvez, M., & Kumar, B. (2023). Green Technologies and Sustainability Optimizing ultrasonic reactor operating variables using intelligent soft computing models for increased biodiesel production. *Green Technologies and Sustainability*, *1*(3), 100033. https://doi.org/10.1016/j.grets.2023.100033

Ashraful, A. M., Masjuki, H. H., Kalam, M. A., Rizwanul Fattah, I. M., Imtenan, S., Shahir, S. A., & Mobarak, H. M. (2014). Production and comparison of fuel properties, engine performance, and emission characteristics of biodiesel from various non-edible vegetable oils: A review. *Energy Conversion and Management*, *80*, 202–228. https://doi.org/10.1016/j.enconman.2014.01.037

Atabani, A. E., Silitonga, A. S., Ong, H. C., Mahlia, T. M. I., Masjuki, H. H., Badruddin, I. A., & Fayaz, H. (2013). Non-edible vegetable oils: A critical evaluation of oil extraction, fatty acid compositions, biodiesel production, characteristics, engine performance and emissions production. *Renewable and Sustainable Energy Reviews*, *18*, 211–245. https://doi.org/10.1016/j.rser.2012.10.013

Ayodeji, A. A., Ojewumi, M. E., Rasheed, B., & Ayodele, J. M. (2018). Data on CaO and eggshell catalysts used for biodiesel production. *Data in Brief*, *19*, 1466–1473. https://doi.org/10.1016/j.dib.2018.06.028

Azad, A. K., Rasul, M. G., Khan, M. M. K., Sharma, S. C., Mofijur, M., & Bhuiya, M. M. K. (2016). Prospects, feedstocks and challenges of biodiesel production from beauty leaf oil and castor oil: A nonedible oil sources in Australia. *Renewable and Sustainable Energy Reviews*, *61*, 302–318. https://doi.org/10.1016/j.rser.2016.04.013

Azmir.J, Zaidul.I.S.M, Rahman.M.M, Sharif.K.M, Mohamed. A, F. Sahena, Jahurul.M.H.A, Ghafoor. K, Norulaini. N.A.N, & M, O. A. K. (2013). Techniques for extraction of

bioactive compounds from plant materials: A review. *Journal of Food Engineering*, *117*, 426–436.

Azrini, N., Azmi, N., Elgharbawy, A. A. M., Motlagh, S. R., & Samsudin, N. (2019). Nanoemulsions: Factory for Food, Pharmaceutical and Cosmetics. *Processes*, *7*(617), 1–34.

Bader, N., Benkhayal, A. A., & Zimmermann, B. (2014). Co-precipitation as a sample preparation technique for trace element analysis: An overview. *International Journal of Chemical Sciences*, *12*(2), 519–525.

Baig, A., Zubair, M., Sumrra, S. H., Nazar, M. F., Zafar, M. N., Jabeen, K., Hassan, M. B., & Rashid, U. (2022). Heating effect on quality characteristics of mixed canola cooking oils. *BMC Chemistry*, 1–11. https://doi.org/10.1186/s13065-022-00796-z

Baker, M. J., Trevisan, J., Bassan, P., Bhargava, R., & Butler, H. J. (2015). *HHS Public Access*. *9*(8), 1771–1791. https://doi.org/10.1038/nprot.2014.110.Using

Balaganesh, A. S., Sengodan, R., Ranjithkumar, R., & Chandarshekar, B. (2018). Synthesis and Characterization of Porous Calcium Oxide Nanoparticles (CaO NPS). *International Journal of Innovative Technology and Exploring Engineering (IJITEE)*, *2*, 2278–3075. https://doi.org/10.7324/RJC.2018.1111934

Bardestani, R., Patience, G. S., & Kaliaguine, S. (2019). Experimental methods in chemical engineering: specific surface area and pore size distribution measurements—BET, BJH, and DFT. *Canadian Journal of Chemical Engineering*, *97*(11), 2781–2791. https://doi.org/10.1002/cjce.23632

Basumatary, S. (2014). Yellow oleander (Thevetia peruviana) seed oil biodiesel as an alternative and renewable fuel for diesel engines: A review. *International Journal of ChemTech Research*, *7*(6), 2823–2840.

Bauer, N., Calvin, K., Emmerling, J., Fricko, O., Fujimori, S., Hilaire, J., Eom, J., Krey, V., Kriegler, E., Mouratiadou, I., Sytze de Boer, H., van den Berg, M., Carrara, S., Daioglou, V., Drouet, L., Edmonds, J. E., Gernaat, D., Havlik, P., Johnson, N., … van Vuuren, D. P. (2017). Shared Socio-Economic Pathways of the Energy Sector – Quantifying the Narratives. *Global Environmental Change*, *42*, 316–330. https://doi.org/10.1016/j.gloenvcha.2016.07.006

Baumeister, C., & Kilian, L. (2016). Forty years of oil price fluctuations: Why the price of oil may still surprise us. *Journal of Economic Perspectives*, *30*(1), 139–160. https://doi.org/10.1257/jep.30.1.139

Bayuo, J., Abdullai, M., Kenneth, A., & Pelig, B. (2020). Optimization using central composite design (CCD) of response surface methodology (RSM) for biosorption of hexavalent chromium from aqueous media. *Applied Water Science*. https://doi.org/10.1007/s13201-020-01213-3

Behera, S., Singh, R., Arora, R., Sharma, N. K., Shukla, M., & Kumar, S. (2015). Scope of Algae

as Third Generation Biofuels. *Frontiers in Bioengineering and Biotechnology*, *2*(February), 1–13. https://doi.org/10.3389/fbioe.2014.00090

Ben-iwo, J., Manovic, V., & Longhurst, P. (2016). Biomass resources and biofuels potential for the production of transportation fuels in Nigeria. *Renewable and Sustainable Energy Reviews*, *63*, 172–192. https://doi.org/10.1016/j.rser.2016.05.050

Bet-Moushoul, E., Farhadi, K., Mansourpanah, Y., Nikbakht, A. M., Molaei, R., & Forough, M. (2016). Application of CaO-based/Au nanoparticles as heterogeneous nanocatalysts in biodiesel production. *Fuel*, *164*(October), 119–127. https://doi.org/10.1016/j.fuel.2015.09.067

Betiku, E., & Ajala, S. O. (2014). Bora *et al*., (2014) catalyst: A case of artificial neural network vs. response surface methodology. *Industrial Crops and Products*, *53*(February), 314–322. https://doi.org/10.1016/j.indcrop.2013.12.046

Bhargavi, G., Nageswara Rao, P., & Renganathan, S. (2018). Review on the Extraction Methods of Crude oil from all Generation Biofuels in last few Decades. *IOP Conference Series: Materials Science and Engineering*, *330*(1). https://doi.org/10.1088/1757-899X/330/1/012024

Bharti, P., Singh, B., & Dey, R. K. (2019). Process optimization of biodiesel production catalyzed by CaO nanocatalyst using response surface methodology. *Journal of Nanostructure in Chemistry*, *9*(4), 269–280. https://doi.org/10.1007/s40097-019-00317-w

Bora, M. M., Gogoi, P., Deka, D. C., & Kakati, D. K. (2014). Synthesis and characterization of yellow oleander (Thevetia peruviana) seed oil-based alkyd resin. *Industrial Crops and Products*, *52*, 721–728. https://doi.org/10.1016/j.indcrop.2013.11.012

Buasri, A., Worawanitchaphong, P., Trongyong, S., & Loryuenyong, V. (2014). Utilization of Scallop Waste Shell for Biodiesel Production from Palm Oil – Optimization Using Taguchi Method. *APCBEE Procedia*, *8*(Caas 2013), 216–221. https://doi.org/10.1016/j.apcbee.2014.03.030

Bušić, A., Kundas, S., Morzak, G., Belskaya, H., Mardetko, N., Šantek, M. I., Komes, D., Novak, S., & Šantek, B. (2018). Recent trends in biodiesel and biogas production. *Food Technology and Biotechnology*, *56*(2), 152–173. https://doi.org/10.17113/ftb.56.02.18.5547

Çakaloğlu, B., Özyurt, V. H., & Ötleş, S. (2018). Cold press in oil extraction. A review. *Ukrainian Food Journal*, *7*(4), 640–654. https://doi.org/10.24263/2304-974x-2018-7-4-9

Carvalho, J., Araujo, J., & Castro, F. (2011). Alternative low-cost adsorbent for wived from eggshell waste: An overvater and wastewater decontamination deriew. *Waste and Biomass Valorization*, *2*(2), 157–167. https://doi.org/10.1007/s12649-010-9058-y

Chai, J., & Jin, Y. (2020). The dynamic impacts of oil price on China's natural gas consumption under the change of global oil market patterns: An analysis from the perspective of total consumption and structure. *Energies*, *13*(4). https://doi.org/10.3390/en13040867

Changmai, B., Vanlalveni, C., Ingle, A. P., Bhagat, R., & Rokhum, L. (2020). Widely used catalysts in biodiesel production: A review. *RSC Advances*, *10*(68), 41625–41679. https://doi.org/10.1039/d0ra07931f

Charmas, B., Kucio, K., Sydorchuk, V., Khalameida, S., Zięzio, M., & Nowicka, A. (2019). Characterization of multimodal silicas using tg/dtg/dta, q-tg, and dsc methods. *Colloids and Interfaces*, *3*(1). https://doi.org/10.3390/colloids3010006

Che Mat, S., Idroas, M. Y., Hamid, M. F., & Zainal, Z. A. (2018). Performance and emissions of straight vegetable oils and its blends as a fuel in diesel engine: A review. *Renewable and Sustainable Energy Reviews*, *82*(July), 808–823. https://doi.org/10.1016/j.rser.2017.09.080

Chebakova, K. A., Dzidziguri, E. L., Sidorova, E. N., Vasiliev, A. A., Ozherelkov, D. Y., Pelevin, I. A., Gromov, A. A., & Nalivaiko, A. Y. (2021). *X-ray Fluorescence Spectroscopy Features of Micro- and Nanoscale Copper and Nickel Particle Compositions*. 1–15.

Chen, Y., Zou, C., Mastalerz, M., Hu, S., Gasaway, C., & Tao, X. (2015). Applications of micro-fourier transform infrared spectroscopy (FTIR) in the geological sciences—A Review. *International Journal of Molecular Sciences*, *16*(12), 30223–30250. https://doi.org/10.3390/ijms161226227

Choudhary, O. P., & ka, P. (2017). Scanning Electron Microscope: Advantages and Disadvantages in Imaging Components. *International Journal of Current Microbiology and Applied Sciences*, *6*(5), 1877–1882. https://doi.org/10.20546/ijcmas.2017.605.207

Chumuang, N., & Punsuvon, V. (2017). Response Surface Methodology for Biodiesel Production Using Calcium Methoxide Catalyst Assisted with Tetrahydrofuran as Cosolvent. *Journal of Chemistry*, *2017*. https://doi.org/10.1155/2017/4190818

Corsini, A., Di Antonio, R., Di Nucci, G., Marchegiani, A., Rispoli, F., & Venturini, P. (2016). Performance Analysis of a Common-rail Diesel Engine Fuelled with Different Blends of Waste Cooking oil and Gasoil. *Energy Procedia*, *101*, 606–613. https://doi.org/10.1016/j.egypro.2016.11.077

Cortes, L. A., Simpson, J. R., & Parker, P. A. (2018). Response surface split-plot designs: A literature review. *Quality and Reliability Engineering International*, *34*(7), 1374–1389. https://doi.org/10.1002/qre.2350

Cristóbal, J. (2016). *Life cycle assessment for the impact assessment of policies Environmental impact of different areas of EU consumption: food, mobility, housing, household goods View project Environmental Footprint Pilot-survey for weighting environmental impact categories in the LCA context View project Serenella Sala European Commission*. https://doi.org/10.2788/318544

Cychosz, K. A., & Thommes, M. (2018). Progress in the Physisorption Characterization of Nanoporous Gas Storage Materials. In *Engineering* (Vol. 4, Issue 4, pp. 559–566). https://doi.org/10.1016/j.eng.2018.06.001

Da Silva Castro, L., Barañano, A. G., Pinheiro, C. J. G., Menini, L., & Pinheiro, P. F. (2019). Biodiesel production from cotton oil using heterogeneous CaO catalysts from eggshells prepared at different calcination temperatures. *Green Processing and Synthesis*, *8*(1), 235–244. https://doi.org/10.1515/gps-2018-0076

Dangat, S., Patel, D., & Kuchekar, A. (2021). Design Space by Design of Experiments. *Journal of Pharmaceutical Research International*, *September*, 7–18. https://doi.org/10.9734/jpri/2021/v33i44a32584

Danlami, J. M., Arsad, A., Zaini, M. A. A., & Sulaiman, H. (2014). A comparative study of various oil extraction techniques from plants. *Reviews in Chemical Engineering*, *30*(6), 605–626. https://doi.org/10.1515/revce-2013-0038

Das, A., Yadav, N., Manchala, S., Bungla, M., & Ganguli, A. K. (2021). Mechanistic Investigations of Growth of Anisotropic Nanostructures in Reverse Micelles. *ACS Omega*, *6*(2), 1007–1029. https://doi.org/10.1021/acsomega.0c04033

Datta, A., & Mandal, B. K. (2014). Use of Jatropha Biodiesel as a Future Sustainable Fuel. *Energy Technology & Policy*, *1*(1), 8–14. https://doi.org/10.1080/23317000.2014.930723

de ALMEIDA, D. T., Viana, T. V., Costa, M. M., Silva, C. de S., & Feitosa, S. (2019). Effects of different storage conditions on the oxidative stability of crude and refined palm oil, olein and stearin (Elaeis guineensis). *Food Science and Technology*, *39*(June), 211–217. https://doi.org/10.1590/fst.43317

de Castro Vasconcellos, P., da Rocha, G. O., Caramão, E. B., Machado, M. E., & Krause, L. C. (2015). Chromatographic Techniques for Organic Analytes. *Comprehensive Analytical Chemistry*, *70*(November 2017), 267–309. https://doi.org/10.1016/bs.coac.2015.09.009

De Menezes, L. C., De Sousa, E. R., Da Silva, G. S., Marques, A. L. B., Viegas, H. D. C., & Dos Santos, M. J. C. (2022). Investigations on Storage and Oxidative Stability of Biodiesel from Different Feedstocks Using the Rancimat Method, Infrared Spectroscopy, and Chemometry. *ACS Omega*, *7*(35), 30746–30755. https://doi.org/10.1021/acsomega.2c01348

Deka, D. C., & Basumatary, S. (2011). High quality biodiesel from yellow oleander (Thevetia peruviana) seed oil. *Biomass and Bioenergy*, *35*(5), 1797–1803. https://doi.org/10.1016/j.biombioe.2011.01.007

Demir, D., Ceylan, S., Öfkeli, F., Şen, D., & Bölgen Karagülle, N. (2017). Eggshell Derived Nanohydroxyapatite Reinforced Chitosan Cryogel Biocomposites for Tissue Engineering Applications. *Jotcsb*, *1*(October), 77–88.

Demirbas, A., Bafail, A., Ahmad, W., & Sheikh, M. (2016). Biodiesel production from non-edible plant oils. *Energy Exploration and Exploitation*, *34*(2), 290–318. https://doi.org/10.1177/0144598716630166

Dhahad, H. A., Abdulhadi, M. A., Alfayyadh, E. M., & Megaritis, T. (2014). An investigation of the relation between combustion phase and emissions of ULSD & RME biodiesel with a

common-rail HSDI diesel engine. *ASME 2014 12th Biennial Conference on Engineering Systems Design and Analysis, ESDA 2014*, *1*(July). https://doi.org/10.1115/ESDA2014-20067

Diaby, M., Amza, T., Onivogui, G., Omar, K. A., & Zou, X. Q. (2017). *Physicochemical properties of refined and unrefined oils of gingerbread plum (Neocarya macrophylla) kernels from Guinea and Niger*. *March*.

Diamantopoulos, N. (2015). Comprehensive Review on the Biodiesel Production using Solid Acid Heterogeneous Catalysts. *Journal of Thermodynamics & Catalysis*, *06*(01). https://doi.org/10.4172/2157-7544.1000143

Díaz, M. J., Ruiz-Montoya, M., Palma, A., & de-Paz, M. V. (2021). Thermogravimetry applicability in compost and composting research: A review. *Applied Sciences (Switzerland)*, *11*(4), 1–15. https://doi.org/10.3390/app11041692

Dib, N., Lépori, C. M. O., Correa, N. M., Silber, J. J., Falcone, R. D., & García-Río, L. (2021). Biocompatible solvents and ionic liquid-based surfactants as sustainable components to formulate environmentally friendly organized systems. *Polymers*, *13*(9). https://doi.org/10.3390/polym13091378

Dong, T., Knoshaug, E. P., Pienkos, P. T., & Laurens, L. M. L. (2016). Lipid recovery from wet oleaginous microbial biomass for biofuel production: A critical review. *Applied Energy*, *177*, 879–895. https://doi.org/10.1016/j.apenergy.2016.06.002

Duarte, J., Moreira, S., & Pombo, J. (2018). *Implementation of a methodology for elemental analysis of sediments based on a handheld X-ray fluorescence analyzer*. *1755*(June).

Dutta, K., Daverey, A., & Lin, J. G. (2014). Evolution retrospective for alternative fuels: First to fourth generation. *Renewable Energy*, *69*, 114–122. https://doi.org/10.1016/j.renene.2014.02.044

Edomah, N. (2018). Economics of Energy Supply. *Reference Module in Earth Systems and Environmental Sciences*, *June*. https://doi.org/10.1016/b978-0-12-409548-9.11713-0

Efthymiopoulos, I., Hellier, P., Ladommatos, N., Russo-Profili, A., Eveleigh, A., Aliev, A., Kay, A., & Mills-Lamptey, B. (2018). Influence of solvent selection and extraction temperature on yield and composition of lipids extracted from spent coffee grounds. *Industrial Crops and Products*, *119*(September), 49–56. https://doi.org/10.1016/j.indcrop.2018.04.008

El-Galad, M. I., El-Khatib, K. M., & Zaher, F. A. (2015). *Economic feasibility study of biodiesel production by direct esterification of fatty acids from the oil and soap industrial sector*. https://doi.org/10.1016/j.ejpe.2015.06.002

El-Hamidi, M., & Zaher, F. A. (2018). Production of vegetable oils in the world and in Egypt: an overview. *Bulletin of the National Research Centre*, *42*(1). https://doi.org/10.1186/s42269-018-0019-0

El Fels, L., Zamama, M., & Hafidi, M. (2015). Advantages and Limitations of Using FTIR Spectroscopy for Assessing the Maturity of Sewage Sludge and Olive Oil Waste Co-composts. *Biodegradation and Bioremediation of Polluted Systems - New Advances and Technologies*. https://doi.org/10.5772/60943

El Seoud, O. A., Baader, W. J., & Bastos, E. L. (2016). Practical Chemical Kinetics in Solution. In *Encyclopedia of Physical Organic Chemistry, 5 Volume Set*. https://doi.org/10.1002/9781118468586.epoc1012

Elías, V. R., Ferrero, G. O., Oliveira, R. G., & Eimer, G. A. (2016). Improved stability in SBA-15 mesoporous materials as catalysts for photo-degradation processes. *Microporous and Mesoporous Materials*, *236*, 218–227. https://doi.org/10.1016/j.micromeso.2016.09.001

Ellingham, S. T. D., Thompson, T. J. U., & Islam, M. (2018). Scanning Electron Microscopy–Energy-Dispersive X-Ray (SEM/EDX): A Rapid Diagnostic Tool to Aid the Identification of Burnt Bone and Contested Cremains. *Journal of Forensic Sciences*, *63*(2), 504–510. https://doi.org/10.1111/1556-4029.13541

Emiola-sadiq, T., Zhang, L., & Dalai, A. K. (2021). *Thermal and Kinetic Studies on Biomass Degradation via Thermogravimetric Analysis : A Combination of Model-Fitting and Model-Free Approach*. https://doi.org/10.1021/acsomega.1c02937

Energy, U. S. (2017). US Energy Information Administration, International Energy Outlook 2017 Overview. *International Energy Outlook*, *IEO2017*(2017), 143. https://doi.org/www.eia.gov/forecasts/ieo/pdf/0484(2016).pdf

Enrica, M., Pietro, D., & Mannu, A. (2020). *NMR Determination of Free Fatty Acids in Vegetable Oils*.

Esfarjani, F., Khoshtinat, K., Zargaraan, A., Mohammadi-Nasrabadi, F., Salmani, Y., Saghafi, Z., Hosseini, H., & Bahmaei, M. (2019). Evaluating the rancidity and quality of discarded oils in fast food restaurants. *Food Science and Nutrition*, *7*(7), 2302–2311. https://doi.org/10.1002/fsn3.1072

Faghihzadeh, F., Anaya, N. M., Schifman, L. A., & Oyanedel-Craver, V. (2016). Fourier transform infrared spectroscopy to assess molecular-level changes in microorganisms exposed to nanoparticles. *Nanotechnology for Environmental Engineering*, *1*(1), 1–16. https://doi.org/10.1007/s41204-016-0001-8

Fallis, A. . (2013). Extraction and Characterization of Vegetable Oils. *Journal of Chemical Information and Modeling*, *53*(9), 1689–1699. https://doi.org/10.1017/CBO9781107415324.004

Faruque, M. O., Razzak, S. A., & Hossain, M. M. (2020). Application of heterogeneous catalysts for biodiesel production from microalgal oil—a review. *Catalysts*, *10*(9), 1–25. https://doi.org/10.3390/catal10091025

Febriansyar, R. A., Riyanto, T., & Istadi, I. (2022). *Analysis of CaCO 3 Impregnation on HY*

Zeolite Surface Area , Pore Size , and Activity in the Catalytic Cracking of Palm Oil to Biofuels. *43*(1), 78–86. https://doi.org/10.14710/teknik.v43i1.44579

Fetisov, G. V. (2020). X-ray diffraction methods for structural diagnostics of materials: progress and achievements. *Uspekhi Fizicheskih Nauk*, *190*(01), 2–36. https://doi.org/10.3367/ufnr.2018.10.038435

Fischer, E. R., Hansen, B. T., Nair, V., Hoyt, F. H., & Dorward, D. W. (2013). *Nihms-375012*. https://doi.org/10.1002/9780471729259.mc02b02s25.Scanning

Folayan, A. J., Anawe, P. A. L., Aladejare, A. E., & Ayeni, A. O. (2019). Experimental investigation of the effect of fatty acids configuration, chain length, branching and degree of unsaturation on biodiesel fuel properties obtained from lauric oils, high-oleic and high-linoleic vegetable oil biomass. *Energy Reports*, *5*(July), 793–806. https://doi.org/10.1016/j.egyr.2019.06.013

Fregolente, P. B. L., Wolf Maciel, M. R., & Oliveira, L. S. (2015). Removal of water content from biodiesel and diesel fuel using hydrogel adsorbents. *Brazilian Journal of Chemical Engineering*, *32*(4), 895–901. https://doi.org/10.1590/0104-6632.20150324s20140142

Gardy, J., Rehan, M., Hassanpour, A., Lai, X., & Nizami, A. S. (2019). Advances in nano-catalysts based biodiesel production from non-food feedstocks. *Journal of Environmental Management*, *249*(July), 109316. https://doi.org/10.1016/j.jenvman.2019.109316

Garroi, J., Goos, P., & Kenneth, S. (2008). *A variable-neighbourhood search*. *November 2006*. https://doi.org/10.1016/j.jspi.2008.05.014

Gaurav, P. K. P. J. R., & Sharmac, S. D. U. S. (2018). *A Review on Production of Biodiesel by Transesterification using Heterogeneous Nanocatalyst*. *January*.

Ge, J., Yoon, S., & Choi, N. (2017). Using Canola Oil Biodiesel as an Alternative Fuel in Diesel Engines: A Review. *Applied Sciences*, *7*(9), 881. https://doi.org/10.3390/app7090881

Gebremariam, S. N., & Marchetti, J. M. (2017). *Biodiesel production technologies : review* (Vol. 5, Issue May). https://doi.org/10.3934/energy.2017.3.425

George, K. M., Ruthenburg, T. C., Smith, J., Yu, L., Zhang, Q., Anastasio, C., & Dillner, A. M. (2015). FT-IR quantification of the carbonyl functional group in aqueous-phase secondary organic aerosol from phenols. *Atmospheric Environment*, *100*, 230–237. https://doi.org/10.1016/j.atmosenv.2014.11.011

Gershon, O., Ezenwa, N. E., & Osabohien, R. (2019). Implications of oil price shocks on net oil-importing African countries. *Heliyon*, *5*(8), e02208. https://doi.org/10.1016/j.heliyon.2019.e02208

Gezici, O., Demir, I., Demircan, A., Ünlü, N., & Karaarslan, M. (2012). Subtractive-FTIR spectroscopy to characterize organic matter in lignite samples from different depths. *Spectrochimica Acta - Part A: Molecular and Biomolecular Spectroscopy*, *96*, 63–69.

https://doi.org/10.1016/j.saa.2012.05.004

Giakoumis, E. G., & Sarakatsanis, C. K. (2019). A comparative assessment of biodiesel cetane number predictive correlations based on fatty acid composition. *Energies*, *12*(3), 1–30. https://doi.org/10.3390/en12030422

Gielen, D., Boshell, F., Saygin, D., Bazilian, M. D., Wagner, N., & Gorini, R. (2019). The role of renewable energy in the global energy transformation. *Energy Strategy Reviews*, *24*(June 2018), 38–50. https://doi.org/10.1016/j.esr.2019.01.006

Gierszal, K., Kruk, M., & Jaroniec, M. (2013). Estimating pore-size distributions of moderately hydrophobic mesoporous solids. *Adsorption Science and Technology*, *31*(2–3), 153–164. https://doi.org/10.1260/0263-6174.31.2-3.153

Giraldo, L., Rodriguez-Estupiñán, P., & Moreno-Piraján, J. C. (2019). Isosteric heat: Comparative study between Clausius-Clapeyron, CSK and adsorption calorimetry methods. *Processes*, *7*(4). https://doi.org/10.3390/pr7040203

Go--, D. O. E. (2016). *Biodiesel Handling and Use Guide* (Issue November).

Gonfa Keneni, Y., & Mario Marchetti, J. (2017). Oil extraction from plant seeds for biodiesel production. *AIMS Energy*, *5*(2), 316–340. https://doi.org/10.3934/energy.2017.2.316

Gorgolis, G., & Galiotis, C. (2017). Graphene aerogels: A review. *2D Materials*, *4*(3). https://doi.org/10.1088/2053-1583/aa7883

Goudilyan, M. (2015). *CFD Analysis of Combustion and Emission Characteristics of Karanja Oil in Diesel Engine : A Technical Review Nandha Engineering College , Erode*. *3*(02), 2435–2437.

Gul, M., Masjuki, H. H., Kalam, M. A., Zulkifli, N. W. M., & Mujtaba, M. A. (2020). A Review: Role of Fatty Acids Composition in Characterizing Potential Feedstock for Sustainable Green Lubricants by Advance Transesterification Process and its Global as Well as Pakistani Prospective. *Bioenergy Research*, *13*(1). https://doi.org/10.1007/s12155-019-10040-7

Habte, L., Khan, M. D., Shiferaw, N., Farooq, A., Lee, M. hye, Jung, S. ho, & Ahn, J. W. (2020). Synthesis, characterization and mechanism study of green aragonite crystals fromwaste biomaterials as calcium supplement. *Sustainability (Switzerland)*, *12*(12), 1–10. https://doi.org/10.3390/su12125062

Hadi, A. S., Ahmed, O. K., & Ali, O. M. (2020). Enhancement of Gasoline Fuel Quality with Commercial Additives to Improve Engine Performance. *IOP Conference Series: Materials Science and Engineering*, *745*(1). https://doi.org/10.1088/1757-899X/745/1/012065

Hansford, G. M., Turner, S. M. R., Degryse, P., & Shortland, A. J. (2017). High-resolution X-ray diffraction with no sample preparation. *Acta Crystallographica Section A: Foundations and Advances*, *73*(4), 293–311. https://doi.org/10.1107/S2053273317008592

Hase, G. J., Deshmukh, K. K., Pokharkar, R. D., Gaje, T. R., & Phatanagre, N. D. (2017). Phytochemical Studies on Nerium oleander L. Using GC-MS. *International Journal of Pharmacognosy and Phytochemical Research*, *9*(6), 885–891. https://doi.org/10.25258/phyto.v9i6.8195

Hassan, N., Ismail, K. N., Ku Hamid, K. H., & Hadi, A. (2018). CaO Nanocatalyst for Transesterification Reaction of Palm Oil to Biodiesel: Effect of Precursor's Concentration on the Catalyst Behavior. *IOP Conference Series: Materials Science and Engineering*, *358*(1). https://doi.org/10.1088/1757-899X/358/1/012059

Hellier, P., Ladommatos, N., & Yusaf, T. (2015). The influence of straight vegetable oil fatty acid composition on compression ignition combustion and emissions. *Fuel*, *143*, 131–143. https://doi.org/10.1016/j.fuel.2014.11.021

Hibbert, S., Welham, K., & Zein, S. H. (2019). An innovative method of extraction of coffee oil using an advanced microwave system: in comparison with conventional Soxhlet extraction method. *SN Applied Sciences*, *1*(11), 1–9. https://doi.org/10.1007/s42452-019-1457-5

Hoang, D., Bensaid, S., & Saracco, G. (2013). Supercritical fluid technology in biodiesel production. *Green Processing and Synthesis*, *2*(5), 407–425. https://doi.org/10.1515/gps-2013-0046

Holechek, J. L., Geli, H. M. E., & Sawalhah, M. N. (2022). *A Global Assessment : Can Renewable Energy Replace Fossil Fuels by 2050 ?* 1–22.

Horf, M., Gebbers, R., Vogel, S., Ostermann, M., Piepel, M., & Olfs, H. (2021). *Biogas Digestates by Portable Energy-Dispersive X-ray Fluorescence Spectrometry*.

Hornak, J. (2021). Synthesis, properties and selected technical applications of magnesium oxide nanoparticles: A review. *International Journal of Molecular Sciences*, *22*(23). https://doi.org/10.3390/ijms222312752

Hou, J., Wang, Z., Xi, S., Li, S., & Xu, X. (2022). Comparative Analysis of Combustion Behaviors and Emission Characteristics of Diesel Engines Fueled with Biodiesel or Biodiesel Blends. *ACS Omega*, *7*(37), 33461–33469. https://doi.org/10.1021/acsomega.2c04254

Hu, K., & McClements, D. J. (2015). Fabrication of biopolymer nanoparticles by antisolvent precipitation and electrostatic deposition: Zein-alginate core/shell nanoparticles. *Food Hydrocolloids*, *44*(April), 101–108. https://doi.org/10.1016/j.foodhyd.2014.09.015

Hwang, N., & Barron, A. R. (n.d.). *BET Surface Area Analysis of Nanoparticles*. *Figure 1*, 1–11.

Hwidi, R. S., Tengku Izhar, T. N., & Mohd Saad, F. N. (2018). Characterization of Limestone as Raw Material to Hydrated Lime. *E3S Web of Conferences*, *34*(March). https://doi.org/10.1051/e3sconf/20183402042

Igwebike-ossi, C. D., & Igwebike-ossi, C. D. (n.d.). *World ' s largest Science , Technology &*

Medicine Open Access book publisher X-Ray Techniques X-Ray Techniques. https://doi.org/10.5772/intechopen.72447

Islam, S., Ahmed, A. S., Islam, A., Aziz, S. A., Xian, L. C., & Mridha, M. (2014). Castor Biodiesel. *Journal of Chemistry*, *2014*, 1–8. https://doi.org/10.1155/2014/451526

Ismail, S. A. E. A., & Ali, R. F. M. (2015). Physico-chemical properties of biodiesel manufactured from waste frying oil using domestic adsorbents. *Science and Technology of Advanced Materials*, *16*(3). https://doi.org/10.1088/1468-6996/16/3/034602

Istadi, I., Prasetyo, S. A., & Nugroho, T. S. (2015). Characterization of K2O/CaO-ZnO Catalyst for Transesterification of Soybean Oil to Biodiesel. *Procedia Environmental Sciences*, *23*(Ictcred 2014), 394–399. https://doi.org/10.1016/j.proenv.2015.01.056

Jabar, J. M., Lajide, L., Adetuyi, A. O., Owolabi, B. J., Bakare, I. O., & Abayomi, T. G. (2015). Yield , quality , kinetics and thermodynamics studies on extraction of Thevetia peruviana oil from its oil bearing seeds. *Journal of Cereals and Oilseeds*, *6*(June), 24–30. https://doi.org/10.5897/JCO15.0135

Jacob, R. (2019). *THERMO GRAVIMETRIC STUDIES OF FERROELECTRIC CERAMIC PbBaTiO*. https://doi.org/10.24941/ijcr.34673.03.2019

Jaji, N. D., Lee, H. L., Hussin, M. H., Akil, H. M., Zakaria, M. R., & Othman, M. B. H. (2020). Advanced nickel nanoparticles technology: From synthesis to applications. *Nanotechnology Reviews*, *9*(1), 1456–1480. https://doi.org/10.1515/ntrev-2020-0109

Jamil, F., Al-haj, L., Al-muhtaseb, A. H., Al-hinai, M. A., & Baawain, M. (2017). *Current scenario of catalysts for biodiesel production : a critical review*. https://doi.org/10.1515/revce-2016-0026

Jankovic, A., Chaudhary, G., & Goia, F. (2021). Designing the design of experiments (DOE) – An investigation on the influence of different factorial designs on the characterization of complex systems. *Energy and Buildings*, *250*, 111298. https://doi.org/10.1016/j.enbuild.2021.111298

Jonas, M., Ketlogetswe, C., & Gandure, J. (2020). Effect of Fruit Maturity Stage on Some Physicochemical Properties of Jatropha Seed Oil and Derived Biodiesel. *ACS Omega*, *5*(23), 13473–13481. https://doi.org/10.1021/acsomega.9b03965

Kandar, M. I. M., & Akil, H. M. (2016). Application of Design of Experiment (DoE) for Parameters Optimization in Compression Moulding for Flax Reinforced Biocomposites. *Procedia Chemistry*, *19*, 433–440. https://doi.org/10.1016/j.proche.2016.03.035

Karmee, S. K., Patria, R. D., Sze, C., & Lin, K. (2015). *Techno-Economic Evaluation of Biodiesel Production from Waste Cooking Oil — A Case Study of Hong Kong*. 4362–4371. https://doi.org/10.3390/ijms16034362

Kaseke, T., Opara, U. L., & Fawole, O. A. (2021). Novel seeds pretreatment techniques : effect

on oil quality and antioxidant properties : a review Novel seeds pretreatment techniques : effect on oil quality and antioxidant properties : a review. *Journal of Food Science and Technology, January*. https://doi.org/10.1007/s13197-021-04981-1

Kasina, M. M., Joseph, K., & John, M. (2020). Application of Central Composite Design to Optimize Spawns Propagation. *Open Journal of Optimization*, *09*(03), 47–70. https://doi.org/10.4236/ojop.2020.93005

Kathirvelu, B., Subramanian, S., Govindan, N., & Santhanam, S. (2017). Emission characteristics of biodiesel obtained from jatropha seeds and fish wastes in a diesel engine. *Sustainable Environment Research*, *27*(6), 283–290. https://doi.org/10.1016/j.serj.2017.06.004

Kaya, F. (2020). *A Study on the Investigation of Diffusion Coefficient for Oil Extraction from Terebinth (*. 144–153. https://doi.org/10.2174/1877946810666200129155312

Keera, S. T., El Sabagh, S. M., & Taman, A. R. (2018). Castor oil biodiesel production and optimization. *Egyptian Journal of Petroleum*, *27*(4), 979–984. https://doi.org/10.1016/j.ejpe.2018.02.007

Keneni, Y. G., Bahiru, L. A., & Marchetti, J. M. (2020). *Effects of Different Extraction Solvents on Oil Extracted from Jatropha Seeds and the Potential of Seed Residues as a Heat Provider*.

Kesic, Z., Lukic, I., Zdujic, M., Mojovic, L., & Skala, D. (2016). Calcium oxide based catalysts for biodiesel production: A review. *Chemical Industry and Chemical Engineering Quarterly*, *22*(4), 391–408. https://doi.org/10.2298/CICEQ160203010K

Khan, I., Saeed, K., & Khan, I. (2017). Nanoparticles: Properties, applications and toxicities. *Arabian Journal of Chemistry*. https://doi.org/10.1016/j.arabjc.2017.05.011

Khaw, K. Y., Parat, M. O., Shaw, P. N., & Falconer, J. R. (2017). Solvent supercritical fluid technologies to extract bioactive compounds from natural sources: A review. *Molecules*, *22*(7). https://doi.org/10.3390/molecules22071186

Kim, K. C., Yoon, T. U., & Bae, Y. S. (2016). Applicability of using CO2 adsorption isotherms to determine BET surface areas of microporous materials. *Microporous and Mesoporous Materials*, *224*, 294–301. https://doi.org/10.1016/j.micromeso.2016.01.003

Kim, S., Kang, S. W., Kim, A., Yusuf, M., Park, J. C., & Park, K. H. (2018). A highly efficient nano-sized Cu2O/SiO2 egg-shell catalyst for C-C coupling reactions. *RSC Advances*, *8*(12), 6200–6205. https://doi.org/10.1039/c7ra13490h

Kishan, S., Kumar, A. K., Vimlesh, M., Mubeen, U. S., & Alok, S. (2012). *ISSN 2230 – 8407 A REVIEW ON : THEVETIA PERUVIANA*. *3*(4), 74–77.

Kiss, F., Biljana, Š., Tomi, M., Mi, R., & Predojevi, Z. (2018). *Current state of the biodiesel production and the indigenous feedstock potential in Serbia*. *81*(June 2017), 280–291.

https://doi.org/10.1016/j.rser.2017.07.059

Klancnik, G., Medved, J., & Mrvar, P. (2010). Differential thermal analysis (DTA) and differential scanning calorimetry (DSC) as a method of material investigation. *Materials and Geoenvironmentent*, *57*(1), 127–142.

Kovalev, A. A., Tishchenko, L. A., Shashurin, V. D., & Galinovskii, A. L. (2017). Application of X-ray Diffraction Methods to Studying Materials. *Russian Metallurgy (Metally)*, *2017*(13), 1186–1193. https://doi.org/10.1134/S0036029517130110

KPLC 2022 tarr (1).pdf. (n.d.).

Kristl, M., Jurak, S., Brus, M., Sem, V., & Kristl, J. (2019). Evaluation of calcium carbonate in eggshells using thermal analysis. *Journal of Thermal Analysis and Calorimetry*, *138*(4), 2751–2758. https://doi.org/10.1007/s10973-019-08678-8

kumar, M., & Sharma, M. P. (2016). Selection of potential oils for biodiesel production. *Renewable and Sustainable Energy Reviews*, *56*, 1129–1138. https://doi.org/10.1016/j.rser.2015.12.032

Kusuma, H. S., & Mahfud, M. (2015). Preliminary study: Kinetics of oil extraction from sandalwood by microwave-assisted hydrodistillation. *ASEAN Journal of Chemical Engineering*, *15*(2), 62–69. https://doi.org/10.1088/1757-899X/128/1/012009

Laing, C., & Taylor, J. (2013). *Optimisation of Bio-Oil Extraction Process from Beauty Leaf (Calophyllum Inophyllum) Oil Seed as a Second Generation Biodiesel Source Optim misation of Bio-o il Extrac ction Proc cess from m Beauty y Leaf phyllum) Oil Seed d as a Se cond Gen neration B. December*. https://doi.org/10.1016/j.proeng.2013.03.168

Lan, K., & Zhao, D. (2022). Functional Ordered Mesoporous Materials: Present and Future. *Nano Letters*, *22*(8), 3177–3179. https://doi.org/10.1021/acs.nanolett.2c00902

Landers, J., Gor, G. Y., & Neimark, A. V. (2013). Density functional theory methods for characterization of porous materials. *Colloids and Surfaces A: Physicochemical and Engineering Aspects*, *437*, 3–32. https://doi.org/10.1016/j.colsurfa.2013.01.007

Lavina, B., Dera, P., & Downs, R. T. (2014). Modern X-ray Diffraction Methods in Mineralogy and Geosciences. *Reviews in Mineralogy and Geochemistry*, *78*(1), 1–31. https://doi.org/10.2138/rmg.2014.78.1

Legg, B. A., Zhu, M., Zhang, H., Waychunas, G., Gilbert, B., & Banfield, J. F. (2016). A Model for Nucleation When Nuclei Are Nonstoichiometric: Understanding the Precipitation of Iron Oxyhydroxide Nanoparticles. *Crystal Growth and Design*, *16*(10), 5726–5737. https://doi.org/10.1021/acs.cgd.6b00809

Li, X., Gao, Z., Fang, S., Ren, C., Yang, K., & Wang, F. (2019). Fractal characterization of nanopore structure in shale, tight sandstone and mudstone from the ordos basin of China using nitrogen adsorption. *Energies*, *12*(4). https://doi.org/10.3390/en12040583

Lim, A., Chew, J. J., Ngu, L. H., Ismadji, S., Khaerudini, D. S., & Sunarso, J. (2020). *Synthesis, Characterization, Adsorption Isotherm, and Kinetic Study of Oil Palm Trunk-Derived Activated Carbon for Tannin Removal from Aqueous Solution*. https://doi.org/10.1021/acsomega.0c03811

Liu, Y., Yang, X., Adamu, A., & Zhu, Z. (2021). Economic evaluation and production process simulation of biodiesel production from waste cooking oil. *Current Research in Green and Sustainable Chemistry*, *4*, 100091. https://doi.org/10.1016/j.crgsc.2021.100091

Lodi, F., Zare, A., Arora, P., Stevanovic, S., Jafari, M., Ristovski, Z., Brown, R. J., & Bodisco, T. (2020). Combustion Analysis of a Diesel Engine during Warm up at Different Coolant and Lubricating Oil Temperatures. *Energies*, *13*(15). https://doi.org/10.3390/en13153931

Loganathan, S., Valapa, R. B., Mishra, R., & Pugazhenthi, G. (2017). Copyright. In *Thermal and Rheological Measurement Techniques for Nanomaterials Characterization* (Issue March 2018). https://doi.org/10.1016/b978-0-323-46139-9.12001-8

Lokesh, A. C., Mahesh, N. S., Gowda, B., Kumar K, R., & White, P. (2015). Neem Biodiesel -A Sustainability Study. *Avestia Publishing Journal of Biomass to Biofuel Journal*, *1*(February), 2368–5964. https://doi.org/10.11159/jbb.2015.001

Lundstedt, C. (2019). *BET Theory and how its used to calculate surface area*.

Mahmudul, H. M., Hagos, F. Y., Mamat, R., Adam, A. A., Ishak, W. F. W., & Alenezi, R. (2017). Production , characterization and performance of biodiesel as an alternative fuel in diesel engines – A review. *Renewable and Sustainable Energy Reviews*, *72*(November 2016), 497–509. https://doi.org/10.1016/j.rser.2017.01.001

Mairizal, A. Q., Awad, S., Priadi, C. R., Hartono, D. M., Moersidik, S. S., Tazerout, M., & Andres, Y. (2020). Experimental study on the effects of feedstock on the properties of biodiesel using multiple linear regressions. *Renewable Energy*, *145*, 375–381. https://doi.org/10.1016/j.renene.2019.06.067

Mäkelä, M. (2017). Experimental design and response surface methodology in energy applications: A tutorial review. *Energy Conversion and Management*, *151*(September 2017), 630–640. https://doi.org/10.1016/j.enconman.2017.09.021

Mansfield, E. (2015). Recent advances in thermal analysis of nanoparticles: Methods, models and kinetics. *Modeling, Characterization and Production of Nanomaterials: Electronics, Photonics and Energy Applications*, 167–178. https://doi.org/10.1016/B978-1-78242-228-0.00006-5

Maroa, S., & Inambao, F. (2021). A review of sustainable biodiesel production using biomass derived heterogeneous catalysts. *Engineering in Life Sciences*, *21*(12), 790–824. https://doi.org/10.1002/elsc.202100025

McElroy, C. R., Constantinou, A., Jones, L. C., Summerton, L., & Clark, J. H. (2015). Towards a holistic approach to metrics for the 21st century pharmaceutical industry. *Green Chemistry*,

17(5), 3111–3121. https://doi.org/10.1039/c5gc00340g

Medina-Rodriguez, B. X., & Alvarado, V. (2021). Use of gas adsorption and inversion methods for shale pore structure characterization. *Energies*, *14*(10). https://doi.org/10.3390/en14102880

Mehebub, S., Chakraborty, M., Kundu, S., & Dhibar, S. (2023). Journal of Hazardous Materials Advances Controlled synthesis of samarium trifluoride nanoparticles in a water-in-oil microemulsion : Effects of water-to-surfactant ratio on particles and phosphate removal. *Journal of Hazardous Materials Advances*, *11*(March), 100348. https://doi.org/10.1016/j.hazadv.2023.100348

Mikšík, F., Miyazaki, T., & Thu, K. (2020). Adsorption isotherm modelling of water on nano-tailored mesoporous silica based on distribution function. *Energies*, *13*(6). https://doi.org/10.3390/en13164247

Mishra, V. K., & Goswami, R. (2018). A review of production, properties and advantages of biodiesel. *Biofuels*, *9*(2), 273–289. https://doi.org/10.1080/17597269.2017.1336350

Mmusi, K. C., Odisitse, S., & Nareetsile, F. (2021). Comparison of CaO-NPs and Chicken Eggshell-Derived CaO in the Production of Biodiesel from Schinziophyton rautanenii (Mongongo) Nut Oil. *Journal of Chemistry*, *2021*. https://doi.org/10.1155/2021/6663722

Möckl, L., & Moerner, W. E. (2020). Super-resolution Microscopy with Single Molecules in Biology and Beyond-Essentials, Current Trends, and Future Challenges. *Journal of the American Chemical Society*, *142*(42), 17828–17844. https://doi.org/10.1021/jacs.0c08178

Mofijur, M., Rasul, M. G., Hyde, J., Azad, A. K., Mamat, R., & Bhuiya, M. M. K. (2016). Role of biofuel and their binary (diesel-biodiesel) and ternary (ethanol-biodiesel-diesel) blends on internal combustion engines emission reduction. *Renewable and Sustainable Energy Reviews*, *53*, 265–278. https://doi.org/10.1016/j.rser.2015.08.046

Mohan, O., Kumar, C., & Simhadri, K. (2021). Exploration Of Mahua Oil (Madhucaindica Seed Oil) Biodiesel As A Fuel In Compression Ignition Engine: A Review. *Volatiles & Essent. Oils*, *8*(4), 11609–11627.

Mohd, F., Universiti, F., Mara, T., Nwabanne, J. T., Science, P., Mohd, F., Universiti, F., & Mara, T. (2017). *Kinetics and Thermodynamics Study of Oil Extraction from Fluted Pumpkin Seed*. *August*, 11–15. https://doi.org/10.11113/jt.v78.4946

Mohiddin, M. N. Bin, Tan, Y. H., Seow, Y. X., Kansedo, J., Mubarak, N. M., Abdullah, M. O., Chan, Y. S., & Khalid, M. (2021). Evaluation on feedstock, technologies, catalyst and reactor for sustainable biodiesel production: A review. *Journal of Industrial and Engineering Chemistry*, *98*, 60–81. https://doi.org/10.1016/j.jiec.2021.03.036

Momin, M., & Deka, D. C. (2015). Fuel property of biodiesel and petrodiesel mix : experiment with biodiesel from yellow oleander seed oil. *Biofuels*, *6*(5–6), 269–272. https://doi.org/10.1080/17597269.2015.1092102

Mosaddegh, E. (2013). Ultrasonic-assisted preparation of nano eggshell powder: A novel catalyst in green and high efficient synthesis of 2-aminochromenes. *Ultrasonics Sonochemistry*, *20*(6), 1436–1441. https://doi.org/10.1016/j.ultsonch.2013.04.008

Motlagh, S. R., Khezri, R., Harun, R., Biak, D. R. A., Hussain, S. A., Chee, C. Y., & Kheawhom, S. (2022). Kinetic and thermodynamic studies of eicosapentaenoic acid extraction from Nannochloropsis oceanica using tetramethyl ammonium chloride and microwave irradiation. *PLoS ONE*, *17*(5 May), 1–20. https://doi.org/10.1371/journal.pone.0267626

Mourabet, M., El Rhilassi, A., El Boujaady, H., Bennani-Ziatni, M., & Taitai, A. (2017). Use of response surface methodology for optimization of fluoride adsorption in an aqueous solution by Brushite. *Arabian Journal of Chemistry*, *10*, S3292–S3302. https://doi.org/10.1016/j.arabjc.2013.12.028

Mourdikoudis, S., Pallares, R. M., & Thanh, N. T. K. (2018). Characterization techniques for nanoparticles: Comparison and complementarity upon studying nanoparticle properties. *Nanoscale*, *10*(27), 12871–12934. https://doi.org/10.1039/c8nr02278j

Mukhtar, A., Mellon, N., Saqib, S., Lee, S. P., & Bustam, M. A. (2020). Extension of BET theory to CO2 adsorption isotherms for ultra-microporosity of covalent organic polymers. *SN Applied Sciences*, *2*(7). https://doi.org/10.1007/s42452-020-2968-9

Munajad, A., Subroto, C., & Suwarno. (2018). Fourier transform infrared (FTIR) spectroscopy analysis of transformer paper in mineral oil-paper composite insulation under accelerated thermal aging. *Energies*, *11*(2). https://doi.org/10.3390/en11020364

Murray, J. W. (2016). Limitations of Oil Production to the IPCC Scenarios: The New Realities of US and Global Oil Production. *BioPhysical Economics and Resource Quality*, *1*(2), 1–13. https://doi.org/10.1007/s41247-016-0013-9

Nanda, S., Rana, R., Sarangi, P. K., Dalai, A. K., & Kozinski, J. A. (2018). A broad introduction to first-, second-, and third-generation biofuels. *Recent Advancements in Biofuels and Bioenergy Utilization*, 1–25. https://doi.org/10.1007/978-981-13-1307-3_1

Nath, D., Jangid, K., Susaniya, A., Kumar, R., & Vaish, R. (2021). Composites Part C : Open Access Eggshell derived CaO-Portland cement antibacterial composites. *Composites Part C: Open Access*, *5*(February), 100123. https://doi.org/10.1016/j.jcomc.2021.100123

Nde, D. B., & Foncha, A. C. (2020). Optimization methods for the extraction of vegetable oils: A review. *Processes*, *8*(2). https://doi.org/10.3390/pr8020209

Negash, Y. A., Amare, D. E., Bitew, B. D., & Dagne, H. (2019). Assessment of quality of edible vegetable oils accessed in Gondar City, Northwest Ethiopia. *BMC Research Notes*, *12*(1), 1–5. https://doi.org/10.1186/s13104-019-4831-x

Negm, N. A., Abou Kana, M. T. H., Youssif, M. A., & Mohamed, M. Y. (2017). Biofuels from Vegetable Oils as Alternative Fuels: Advantages and Disadvantages. In *Surfactants in Tribology, Volume 5* (Issue September). https://doi.org/10.1201/9781315120829-18

Niculescu, A. G., Chircov, C., Bîrcă, A. C., & Grumezescu, A. M. (2021). Nanomaterials synthesis through microfluidic methods: An updated overview. *Nanomaterials*, *11*(4). https://doi.org/10.3390/nano11040864

Niculescu, R., Clenci, A., & Iorga-Siman, V. (2019). Review on the use of diesel-biodiesel-alcohol blends in compression ignition engines. *Energies*, *12*(7), 1–41. https://doi.org/10.3390/en12071194

Niju, S., Balajii, M., & Anushya, C. (2019). A comprehensive review on biodiesel production using Moringa oleifera oil. *International Journal of Green Energy*, *16*(9), 702–715. https://doi.org/10.1080/15435075.2019.1619565

Nomanbhay, S., & Ong, M. Y. (2017). A review of microwave-assisted reactions for biodiesel production. *Bioengineering*, *4*(2). https://doi.org/10.3390/bioengineering4020057

Ntalikwa, J. W. (2021). Solvent Extraction of Jatropha Oil for Biodiesel Production: Effects of Solvent-to-Solid Ratio, Particle Size, Type of Solvent, Extraction Time, and Temperature on Oil Yield. *Journal of Renewable Energy*, *2021*(c), 1–8. https://doi.org/10.1155/2021/9221168

OA, A., AO, A., & SE, A. (2019). Process Parameter Estimation of Biodiesel Production from Waste Frying Oil (Vegetable and Palm oil) using Homogeneous Catalyst. *Journal of Food Processing & Technology*, *10*(10), 25–35. https://doi.org/10.35248/2157-7110.19.10.811

Ofori-Boateng, C., & Lee, K. T. (2011). Feasibility of Jatropha Oil for Biodiesel: Economic Analysis. *Proceedings of the World Renewable Energy Congress – Sweden, 8–13 May, 2011, Linköping, Sweden*, *57*, 463–470. https://doi.org/10.3384/ecp11057463

Ogunkunle, O., & Ahmed, N. A. (2019). A review of global current scenario of biodiesel adoption and combustion in vehicular diesel engines. *Energy Reports*, *5*, 1560–1579. https://doi.org/10.1016/j.egyr.2019.10.028

Oladipo, B., & Betiku, E. (2019). Biocatalysis and Agricultural Biotechnology Process optimization of solvent extraction of seed oil from Moringa oleifera : An appraisal of quantitative and qualitative process variables on oil quality using D-optimal design. *Biocatalysis and Agricultural Biotechnology*, *20*(May), 101187. https://doi.org/10.1016/j.bcab.2019.101187

Olanrewaju, B. T., & Olubusoye, O. E. (2020). *Reduction of Petroleum Consumption*. *January*, 0–11. https://doi.org/10.1007/978-3-319-71057-0

Olderay, M., Xie, M., Strand, B. L., Flaten, E. M., Sikorski, P., & Andreassen, J. P. (2009). Growth and nucleation of calcium carbonate vaterite crystals in presence of alginate. *Crystal Growth and Design*, *9*(12), 5176–5183. https://doi.org/10.1021/cg9005604

Oleshko, V. P. (2014). *Electron Microscopy , Nanoscopy , and Scanning Micro- and Nanoanalysis* (Issue September 2012). https://doi.org/10.13140/2.1.3852.8966

Oliveira, P. F. M. De, Torresi, R. M., & Camargo, P. H. C. (2020). *Challenges and opportunities in the bottom-up mechanochemical synthesis of noble metal nanoparticles*. 16114–16141. https://doi.org/10.1039/d0ta05183g

Ong, H. C., Mahlia, T. M. I., Masjuki, H. H., & Honnery, D. (2012). Life cycle cost and sensitivity analysis of palm biodiesel production. *Fuel*, *98*, 131–139. https://doi.org/10.1016/j.fuel.2012.03.031

Onukwuli, D. O., Emembolu, L. N., Ude, C. N., Aliozo, S. O., & Menkiti, M. C. (2017). Optimization of biodiesel production from refined cotton seed oil and its characterization. *Egyptian Journal of Petroleum*, *26*(1), 103–110. https://doi.org/10.1016/j.ejpe.2016.02.001

Oseni, M. I., Agbi, B. E., & Ogamenyi, I. O. (2014). *Extraction and Analysis of Chemo-physical Properties of Yellow Oleander Oil as Lubricant*. *4*(6), 1020–1029.

Ouedraogo, N. S. (2017). Africa energy future: Alternative scenarios and their implications for sustainable development strategies. *Energy Policy*, *106*(April), 457–471. https://doi.org/10.1016/j.enpol.2017.03.021

Owolabi, R. U., Usman, M. A., & Kehinde, A. J. (2018). Modelling and optimization of process variables for the solution polymerization of styrene using response surface methodology. *Journal of King Saud University - Engineering Sciences*, *30*(1), 22–30. https://doi.org/10.1016/j.jksues.2015.12.005

Owusu, P. A., & Asumadu-Sarkodie, S. (2016). A review of renewable energy sources, sustainability issues and climate change mitigation. *Cogent Engineering*, *3*(1), 1–14. https://doi.org/10.1080/23311916.2016.1167990

Oyegoke, T., & Geoffrey, T. T. (2022). *Sensitivity Analysis of Selected Project Parameter on the Feasibility of Converting Maize Cob to Bioethanol as a Means of Promoting Biorefinery Establishment in Nigeria*. *12*(1).

Ozturk, I. (2016). *Utilizing biofuels for sustainable development in the panel of 17 developed and developing countries*. 826–836. https://doi.org/10.1111/gcbb.12287

Palencia, M. (2018). Functional transformation of Fourier-transform mid-infrared spectrum for improving spectral specificity by simple algorithm based on wavelet-like functions. *Journal of Advanced Research*, *14*, 53–62. https://doi.org/10.1016/j.jare.2018.05.009

Pan, Y., Shen, X., Yao, L., Bentalib, A., & Peng, Z. (2018). Active Sites in Heterogeneous Catalytic Reaction on Metal and Metal Oxide: Theory and Practice. *Catalysts*, *8*(10), 478. https://doi.org/10.3390/catal8100478

Panchal, B. (2014). Optimization of Oil Extraction and Characterization from Tamarindus Indica Linn Seed Oil. *International Journal of Oil, Gas and Coal Engineering*, *2*(1), 1. https://doi.org/10.11648/j.ogce.20140201.11

Pandit, P. R., & Fulekar, M. H. (2017). Egg shell waste as heterogeneous nanocatalyst for

biodiesel production: Optimized by response surface methodology. *Journal of Environmental Management*, *198*, 319–329. https://doi.org/10.1016/j.jenvman.2017.04.100

Papanikolaou, S., Rontou, M., Belka, A., Athenaki, M., Gardeli, C., Mallouchos, A., Kalantzi, O., Koutinas, A. A., Kookos, I. K., Zeng, A. P., & Aggelis, G. (2017). Conversion of biodiesel-derived glycerol into biotechnological products of industrial significance by yeast and fungal strains. *Engineering in Life Sciences*, *17*(3), 262–281. https://doi.org/10.1002/elsc.201500191

Parashar, M., Shukla, V. K., & Singh, R. (2020). Metal oxides nanoparticles via sol–gel method: a review on synthesis, characterization and applications. *Journal of Materials Science: Materials in Electronics*, *31*(5), 3729–3749. https://doi.org/10.1007/s10854-020-02994-8

Pareek, V., Bhargava, A., Gupta, R., Jain, N., & Panwar, J. (2017). Synthesis and Applications of Noble Metal Nanoparticles: A Review. *Advanced Science, Engineering and Medicine*, *9*(7), 527–544. https://doi.org/10.1166/asem.2017.2027

Pasha, M. K., Dai, L., Liu, D., Guo, M., & Du, W. (2021). An overview to process design, simulation and sustainability evaluation of biodiesel production. *Biotechnology for Biofuels*, *14*(1), 1–23. https://doi.org/10.1186/s13068-021-01977-z

Patel, A., Arora, N., Mehtani, J., Pruthi, V., & Pruthi, P. A. (2017). Assessment of fuel properties on the basis of fatty acid profiles of oleaginous yeast for potential biodiesel production. *Renewable and Sustainable Energy Reviews*, *77*(March), 604–616. https://doi.org/10.1016/j.rser.2017.04.016

Patra, J. K., & Baek, K. (2014). *Green Nanobiotechnology : Factors Affecting Synthesis and Characterization Techniques*. *2014*.

Pattanaik, L., Pattnaik, F., Saxena, D. K., & Naik, S. N. (2019). Biofuels from agricultural wastes. In *Second and Third Generation of Feedstocks* (Issue May). Elsevier Inc. https://doi.org/10.1016/b978-0-12-815162-4.00005-7

Pattnaik, M., Pandey, P., Martin, G. J. O., Mishra, H. N., & Ashokkumar, M. (2021). *Innovative Technologies for Extraction and Microencapsulation of Bioactives from Plant-Based Food Waste and Their Applications in Functional Food Development*.

Paz-Ferreiro, J., da Luz, L. R. Q. P., Lado, M., & Vázquez, E. V. (2013). Specific Surface Area and Multifractal Parameters of Associated Nitrogen Adsorption and Desorption Isotherms in Soils from Santa Catarina, Brazil. *Vadose Zone Journal*, *12*(3), vzj2012.0203. https://doi.org/10.2136/vzj2012.0203

Perera, F. (2018). Pollution from fossil-fuel combustion is the leading environmental threat to global pediatric health and equity: Solutions exist. *International Journal of Environmental Research and Public Health*, *15*(1). https://doi.org/10.3390/ijerph15010016

Pickl, M. J. (2019). The renewable energy strategies of oil majors – From oil to energy? *Energy Strategy Reviews*, *26*(June), 100370. https://doi.org/10.1016/j.esr.2019.100370

Piechocka, J., Wieczorek, M., & Głowacki, R. (2020). *Gas Chromatography – Mass Spectrometry Based Approach for the Determination of Methionine-Related Sulfur-Containing Compounds in Human Saliva*.

Pikula, K., Zakharenko, A., Stratidakis, A., Razgonova, M., Nosyrev, A., Mezhuev, Y., Tsatsakis, A., & Golokhvast, K. (2020). The advances and limitations in biodiesel production: feedstocks, oil extraction methods, production, and environmental life cycle assessment. *Green Chemistry Letters and Reviews, 13*(4), 11–30. https://doi.org/10.1080/17518253.2020.1829099

Piskulich, Z. A., Mesele, O. O., & Thompson, W. H. (2019). *Activation Energies and Beyond*. https://doi.org/10.1021/acs.jpca.9b03967

PMI. (2008). Cost of construction labour and equipment. *Project Management Body of Knowledge*.

Poddar, T., Jagannath, A., & Almansoori, A. (2015). Biodiesel Production using Reactive Distillation: A Comparative Simulation Study. *Energy Procedia*, *75*, 17–22. https://doi.org/10.1016/j.egypro.2015.07.129

Polte, J. (2015). Fundamental growth principles of colloidal metal nanoparticles - a new perspective. *CrystEngComm*, *17*(36), 6809–6830. https://doi.org/10.1039/c5ce01014d

Premi, M., & Sharma, H. K. (2013). *Oil Extraction Optimization and Kinetics from Moringa Oleifera (PKM 1) Seeds*. *4*(4), 371–378.

Qi, L. (2015). Reverse Micelles: Synthesis of Inorganic Nanostructures. *Encyclopedia of Surface and Colloid Science, Third Edition*, 6451–6474. https://doi.org/10.1081/e-escs3-120023694

Qiu, P., Ma, B., Hung, C. Te, Li, W., & Zhao, D. (2019). Spherical Mesoporous Materials from Single to Multilevel Architectures. *Accounts of Chemical Research*, *52*(10), 2928–2938. https://doi.org/10.1021/acs.accounts.9b00357

Quinn, G., Connolly, R., & Connolly, M. (2020). Energy and Climate Policy — An Evaluation of Global. *Energies*, *13*(18).

Rabiu, A., Elias, S., & Oyekola, O. (2018). Oleochemicals from Palm Oil for the Petroleum Industry. *Palm Oil, September*. https://doi.org/10.5772/intechopen.76771

Raheman, H., Jena, P. C., & Jadav, S. S. (2013). Performance of a diesel engine with blends of biodiesel (from a mixture of oils) and high-speed diesel. *International Journal of Energy and Environmental Engineering*, *4*(1), 1–9. https://doi.org/10.1186/2251-6832-4-6

Raj, B., & Singh, O. (2012). Global Trends of Fossil Fuel Reserves and Climate Change in the 21st Century. *Fossil Fuel and the Environment, October 2016*. https://doi.org/10.5772/38655

Razon, L. F., Khang, D. S., Tan, R. R., Aviso, K. B., Yu, K. D. S., & Promentilla, M. A. B. (2019). Life-cycle costing: Analysis of biofuel production systems. In *Biofuels for a More*

Sustainable Future: Life Cycle Sustainability Assessment and Multi-Criteria Decision Making. Elsevier Inc. https://doi.org/10.1016/B978-0-12-815581-3.00008-7

Reddy, A. N. R., Saleh, A. A., Islam, M. S., Hamdan, S., Rahman, M. R., & Masjuki, H. H. (2018). Experimental evaluation of fatty acid composition influence on Jatropha biodiesel physicochemical properties. *Journal of Renewable and Sustainable Energy*, *10*(1). https://doi.org/10.1063/1.5018743

Renewable, I., & Agency, E. (2017). *RENEWABLE ENERGY PROSPECTS FOR THE RUSSIAN FEDERATION* (Issue April).

Rodrigues, E. S., Gomes, M. H. F., Duran, N. M., Cassanji, J. G. B., da Cruz, T. N. M., Sant'Anna Neto, A., Savassa, S. M., de Almeida, E., & Carvalho, H. W. P. (2018). Laboratory microprobe X-ray fluorescence in plant science: Emerging applications and case studies. *Frontiers in Plant Science*, *871*(November), 1–15. https://doi.org/10.3389/fpls.2018.01588

Rohim, R., Ahmad, R., Ibrahim, N., Hamidin, N., & Azner Abidin, C. Z. (2014). Characterization of calcium oxide catalyst from eggshell waste. *Advances in Environmental Biology*, *8*(22), 35–38.

Rupasianghe, C. P., & Gunathilaka, K. S. S. (2018). Disaster Risk Reduction through biodiesel from yellow oleander (Thevetia peruviana). *Procedia Engineering*, *212*(2017), 591–597. https://doi.org/10.1016/j.proeng.2018.01.076

Sakthivel, R., Ramesh, K., Purnachandran, R., & Mohamed Shameer, P. (2018). A review on the properties, performance and emission aspects of the third generation biodiesels. *Renewable and Sustainable Energy Reviews*, *82*(November), 2970–2992. https://doi.org/10.1016/j.rser.2017.10.037

Sangeetha, K., Ramyaa, R. B., Mousavi, A., & Radhakrishnan, M. (2023). Extraction , characterization , and application of tomato seed oil in the food industry : An updated review. *Journal of Agriculture and Food Research*, *11*(January), 100529. https://doi.org/10.1016/j.jafr.2023.100529

Santos, S. B. Dos, Martins, M. A., Caneschi, A. L., Aguilar, P. R. M., & Coimbra, J. S. D. R. (2015). Kinetics and Thermodynamics of Oil Extraction from Jatropha curcas L. Using Ethanol as a Solvent. *International Journal of Chemical Engineering*, *2015*. https://doi.org/10.1155/2015/871236

Santoso, H., Iryanto, & Inggrid, M. (2014). Effects of Temperature, Pressure, Preheating Time and Pressing Time on Rubber Seed Oil Extraction Using Hydraulic Press. *Procedia Chemistry*, *9*, 248–256. https://doi.org/10.1016/j.proche.2014.05.030

Sarangi, P. K., Nanda, S., & Mohanty, P. (2018). Recent advancements in biofuels and bioenergy utilization. In *Recent Advancements in Biofuels and Bioenergy Utilization* (Issue September). https://doi.org/10.1007/978-981-13-1307-3

Sarrai, A. E., Hanini, S., Merzouk, N. K., Tassalit, D., Szabó, T., Hernádi, K., & Nagy, L. (2016). Using central composite experimental design to optimize the degradation of Tylosin from aqueous solution by Photo-Fenton reaction. *Materials*, *9*(6). https://doi.org/10.3390/ma9060428

Saxena, P., Jawale, S., & Joshipura, M. H. (2013). A review on prediction of properties of biodiesel and blends of biodiesel. *Procedia Engineering*, *51*(NUiCONE 2012), 395–402. https://doi.org/10.1016/j.proeng.2013.01.055

Schramm, R. (2016). Use of X-ray fluorescence analysis for the determination of rare earth elements. *Physical Sciences Reviews*, *1*(9), 1–17. https://doi.org/10.1515/psr-2016-0061

Scimeca, M., Bischetti, S., Lamsira, H. K., Bonfiglio, R., & Bonanno, E. (2018). Energy dispersive X-ray (EDX) microanalysis: A powerful tool in biomedical research and diagnosis. *European Journal of Histochemistry*, *62*(1), 89–99. https://doi.org/10.4081/ejh.2018.2841

Shah, S. R., Vyas, A. P., Scholar, P. D., & Supervisor, P. D. (2018). Determination of Cetane Number for Palm Based Biodiesel and Petro-Diesel Blends. *International Journal for Research in Engineering Application & Management (IJREAM)*, *04*(04), 2454–9150. https://doi.org/10.18231/2454-9150.2018.0534

Sharma, S., & Ganguli, A. K. (2014). Spherical-to-cylindrical transformation of reverse micelles and their templating effect on the growth of nanostructures. *Journal of Physical Chemistry B*, *118*(15), 4122–4131. https://doi.org/10.1021/jp500697j

Sharma, S. K., Verma, D. S., Khan, L. U., Kumar, S., & Khan, S. B. (2018). Handbook of Materials Characterization. *Handbook of Materials Characterization*, *September*, 1–613. https://doi.org/10.1007/978-3-319-92955-2

Sharmin, M. (2016). *Synthesis of Binary and Ternary Metal Oxide Thin Films by Spray Pyrolysis and Study of Antibacterial Effects and Their Suitability for Optoelectronic Applications Presented By- Mehnaz Sharmin Ph . D . Student Department of Physics Bangladesh University of. November*. https://doi.org/10.13140/RG.2.2.33264.05120

Siddiqui, A., Rahman, Z., Korang-Yeboah, M., & Khan, M. A. (2015). Development and validation of X-ray diffraction method for quantitative determination of crystallinity in warfarin sodium products. *International Journal of Pharmaceutics*, *493*(1–2), 1–6. https://doi.org/10.1016/j.ijpharm.2015.07.051

Silva, G. F., Camargo, F. L., & Ferreira, A. L. O. (2011). *Application of response surface methodology for optimization of biodiesel production by transesteri fi cation of soybean oil with ethanol*. *92*, 407–413. https://doi.org/10.1016/j.fuproc.2010.10.002

Singh, O. (2018). *Evaluation of Energy Ratios for Karanja and Neem Biodiesel Life Cycles*. *July*. https://doi.org/10.18090/samriddhi.v1i1.1579

Siregar, K., Sholiati, S., Sofiah, I., Miharza, T., Hendroko Setyobudi, R., Anne, O., Wahyudi, A.,

Gamawati Adinurani, P., & Mel, M. (2020). Review of Implementation Life Cycle Assessment for Biodiesel Production from Palm Oil (Elaeis guineensis Jacq.) in Indonesia. *E3S Web of Conferences*, *190*(October). https://doi.org/10.1051/e3sconf/202019000021

Solomon, P. R., Ranganathan, S., Muniyandi, B., Thangaraj, B., & Lin, L. (2018). Catalysis in biodiesel production—a review. *Clean Energy*, *3*(1), 2–23. https://doi.org/10.1093/ce/zky020

Srivastava, N., Srivastava, M., Gupta, V. K., Manikanta, A., Mishra, K., Singh, S., Singh, S., Ramteke, P. W., & Mishra, P. K. (2018). Recent development on sustainable biodiesel production using sewage sludge. *3 Biotech*, *8*(5). https://doi.org/10.1007/s13205-018-1264-5

Stamenkovi, O. S., Veljkovi, V. B., & Bankovi, I. B. (2012). *Biodiesel production from non-edible plant oils*. *16*, 3621–3647. https://doi.org/10.1016/j.rser.2012.03.002

Stashenko, E., & René Martínez, J. (2014). *Gas Chromatography-Mass Spectrometry*. https://doi.org/10.5772/57492

Strategy, C. (1975). *Note on Life Cycle Analysis*.

Subroto, E., Manurung, R., Jan, H., & Augustinus, A. (2015). Optimization of mechanical oil extraction from Jatropha curcas L . kernel using response surface method. *Industrial Crops & Products*, *63*, 294–302. https://doi.org/10.1016/j.indcrop.2014.08.050

Suresh, M., Jawahar, C. P., & Richard, A. (2018). A review on biodiesel production, combustion, performance, and emission characteristics of non-edible oils in variable compression ratio diesel engine using biodiesel and its blends. *Renewable and Sustainable Energy Reviews*, *92*(March), 38–49. https://doi.org/10.1016/j.rser.2018.04.048

Susi, T. (2021). Other spectroscopic methods for graphene characterization: X-ray and electron spectroscopies. *Graphene*, *January*, 413–436. https://doi.org/10.1016/b978-0-08-102848-3.00011-6

Suwari, Kotta, H. Z., & Buang, Y. (2018). Extraction and Characterization of Crop Oil from Seed Kernels of Feun Kase (Thevetia peruviana). *Journal of Physics: Conference Series*, *1093*(1). https://doi.org/10.1088/1742-6596/1093/1/012043

Takase, M., Kipkoech, R., & Essandoh, P. K. (2021). A comprehensive review of energy scenario and sustainable energy in Kenya. *Fuel Communications*, *7*, 100015. https://doi.org/10.1016/j.jfueco.2021.100015

Talha, N. S., & Sulaiman, S. (2016). *Overview of Catalysts in Biodiesel Production*. *11*(1), 439–448.

Tan, Y. H., Omar, M., Kansedo, J., & Saptoro, A. (2018). *Optimization of Ostrich Eggshell Catalyst in Transesterification Using Waste Cooking Oil via Response Surface Methodology*. *5*(2), 277–285.

Toldra-Reig, F., Mora, L., & Toldra, F. (2020). applied sciences Trends in Biodiesel Production from Animal Fat Waste. *Applied Science*, *10*(3644), 1–17.

Tsagkari, M., Couturier, J. L., Kokossis, A., & Dubois, J. L. (2016). Early-Stage Capital Cost Estimation of Biorefinery Processes: A Comparative Study of Heuristic Techniques. *ChemSusChem*, *9*(17), 2284–2297. https://doi.org/10.1002/cssc.201600309

Tziourtzioumis, D. N., & Stamatelos, A. M. (2017). Experimental investigation of the effect of biodiesel blends on a DI diesel engine's injection and combustion. *Energies*, *10*(7). https://doi.org/10.3390/en10070970

Ul-Hamid, A. (2018). A Beginners' Guide to Scanning Electron Microscopy. In *A Beginners' Guide to Scanning Electron Microscopy*. https://doi.org/10.1007/978-3-319-98482-7

Uo, M., Wada, T., & Sugiyama, T. (2015). Applications of X-ray fluorescence analysis (XRF) to dental and medical specimens. *Japanese Dental Science Review*, *51*(1), 2–9. https://doi.org/10.1016/j.jdsr.2014.07.001

Usman, L. a., Oluwaniyi, O. O., Ibiyemi, S. a., Muhammad, N. O., & Ameen, O. M. (2009). The potential of Oleander (Thevetia peruviana) in African agricultural and industrial development: a case study of Nigeria. *Journal of Applied Biosciences*, *2004*(Usda 2004), 1477–1487.

Valério, A., & Morelhão, S. L. (2019). Usage of Scherrer's formula in X-ray diffraction analysis of size distribution in systems of monocrystalline nanoparticles. *ArXiv*, 1–9.

van Gelderen, L., Alva, U. R., Mindykowski, P., & Jomaas, G. (2017). Thermal Properties and Burning Efficiencies of Crude Oils and Refined Fuel Oil. *International Oil Spill Conference Proceedings*, *2017*(1), 985–1005. https://doi.org/10.7901/2169-3358-2017.1.985

Venkateshaiah, A., Padil, V. V. T., Nagalakshmaiah, M., Waclawek, S., Černík, M., & Varma, R. S. (2020). Microscopic techniques for the analysis of micro and nanostructures of biopolymers and their derivatives. *Polymers*, *12*(3). https://doi.org/10.3390/polym12030512

Verran, J., Redfern, J., Burdass, D., & Kinninmonth, M. (2014). Using Soxhlet Ethanol Extraction to Produce and Test Plant Material (Essential Oils) for Their Antimicrobial Properties †. *Journal of Microbiology & Biology Education*, *15*(1), 45–46. https://doi.org/10.1128/jmbe.v15i1.656

Vijayakumar, M., & Mukesh Kumar, P. C. (2019). Performance and emission characteristics of compression-ignition engine handling biodiesel blends with electronic fumigation. *Heliyon*, *5*(4), e01480. https://doi.org/10.1016/j.heliyon.2019.e01480

Volume, B., & Dallatu, D. (2017). *the Influence of Physicochemical Characteristics of a Non-Edible Non*. *10*(2), 283–291.

Wahyono, Y., Hadiyanto, H., Budihardjo, M. A., & Widayat. (2019). Energy Balance Calculation with Life Cycle Assessment for Production of Palm Biodiesel in Indonesia. *E3S*

Web of Conferences, *125*(201 9), 3–7. https://doi.org/10.1051/e3sconf/201912510005

Wu, G., Ge, J. C., & Choi, N. J. (2020). A comprehensive review of the application characteristics of biodiesel blends in diesel engines. *Applied Sciences (Switzerland)*, *10*(22), 1–31. https://doi.org/10.3390/app10228015

Wu, S. C., Tsou, H. K., Hsu, H. C., Hsu, S. K., Liou, S. P., & Ho, W. F. (2013). A hydrothermal synthesis of eggshell and fruit waste extract to produce nanosized hydroxyapatite. *Ceramics International*, *39*(7), 8183–8188. https://doi.org/10.1016/j.ceramint.2013.03.094

Xing, Y., Zheng, Z., Sun, Y., & Agha Alikhani, M. (2021). A Review on Machine Learning Application in Biodiesel Production Studies. *International Journal of Chemical Engineering*, *2021*. https://doi.org/10.1155/2021/2154258

Xiong, Q., Baychev, T. G., & Jivkov, A. P. (2016). Review of pore network modelling of porous media: Experimental characterisations, network constructions and applications to reactive transport. *Journal of Contaminant Hydrology*, *192*, 101–117. https://doi.org/10.1016/j.jconhyd.2016.07.002

Yadav, A. K., Khan, M. E., Pal, A., & Dubey, A. M. (2017). Performance , Emission and Combustion Characteristics of an Indica Diesel Engine Operated with Yellow Oleander (Thevetia Peruviana) Oil Biodiesel Produced Through Hydrodynamic Cavitation Method. *International Journal of Ambient Energy*, *0*(0), 1–20. https://doi.org/10.1080/01430750.2017.1303631

Yadav, A. K., Pal, A., Ghosh, U., & Gupta, S. K. (2017). Comparative Study of Biodiesel Production Methods from Yellow Oleander Oil and its Performance Analysis on an Agricultural Diesel Engine. *International Journal of Ambient Energy*, *0*(0), 1–18. https://doi.org/10.1080/01430750.2017.1381152

Yadav, A., & Singh, O. (2010). Energy estimations for life-cycle analysis of jatropha, neem, and karanja biodiesels - A parametric study. *Proceedings of the Institution of Mechanical Engineers, Part A: Journal of Power and Energy*, *224*(8), 1049–1057. https://doi.org/10.1243/09576509JPE939

Yadav, M., Chavan, S. B., Singh, R., Bux, F., & Sharma, Y. C. (2019). Experimental study on emissions of algal biodiesel and its blends on a diesel engine. *Journal of the Taiwan Institute of Chemical Engineers*, *96*(December), 160–168. https://doi.org/10.1016/j.jtice.2018.10.022

Yao, M., Wang, D., & Zhao, M. (2015). Element Analysis Based on Energy-Dispersive X-Ray Fluorescence. *Advances in Materials Science and Engineering*, *2015*(1). https://doi.org/10.1155/2015/290593

Yarkasuwa, C. I., Wilson, D., & Michael, E. (2013). Production of biodiesel from yellow oleander (thevetia peruvian) oil and its biodegradability. *Journal of the Korean Chemical Society*, *57*(3), 377–381. https://doi.org/10.5012/jkcs.2013.57.3.377

Yaşar, F. (2019). Biodiesel production via waste eggshell as a low-cost heterogeneous catalyst: Its effects on some critical fuel properties and comparison with CaO. *Fuel*, *255*(June), 115828. https://doi.org/10.1016/j.fuel.2019.115828

Yi, S., Dai, F., Zhao, C., & Si, Y. (2017). A reverse micelle strategy for fabricating magnetic lipase-immobilized nanoparticles with robust enzymatic activity. *Scientific Reports*, *7*(1), 1–9. https://doi.org/10.1038/s41598-017-10453-4

Yusuf, M., & Widyanie, L. (2019). Effect of storage time on moisture content of Reutealis trisperma seed and its effect on acid value of the isolated oil and produced biodiesel Effect of storage time on moisture content of Reutealis trisperma seed and its effect on acid value of the isola. *Energy Reports*, *5*(October), 1375–1380. https://doi.org/10.1016/j.egyr.2019.09.066

Yusuff, A. S., Adeniyi, O. D., Olutoye, M. A., & Akpan, U. G. (2017). A Review on Application of Heterogeneous Catalyst in the Production of Biodiesel from Vegetable Oils. *Journal of Applied Science & Process Engineering*, *4*(2), 142–157. https://doi.org/10.1177/1077546316636361

Zahan, K. A., & Kano, M. (2018). Biodiesel production from palm oil, its by-products, and mill effluent: A review. *Energies*, *11*(8), 1–25. https://doi.org/10.3390/en11082132

Zaher, F. A., & Soliman, H. M. (2015). Biodiesel production by direct esterification of fatty acids with propyl and butyl alcohols. *Egyptian Journal of Petroleum*, *24*(4), 439–443. https://doi.org/10.1016/j.ejpe.2015.10.007

Zainal, N. F. A., Saiter, J. M., Halim, S. I. A., Lucas, R., & Chan, C. H. (2020). Thermal analysis: basic concept of differential scanning calorimetry and thermogravimetry for beginners. *Chemistry Teacher International*, *0*(0). https://doi.org/10.1515/cti-2020-0010

Zhang, Q. W., Lin, L. G., & Ye, W. C. (2018). Techniques for extraction and isolation of natural products: A comprehensive review. *Chinese Medicine (United Kingdom)*, *13*(1), 1–26. https://doi.org/10.1186/s13020-018-0177-x

Zhang, Q., Yang, J., Gao, Y., Li, C., & Sun, L. (2015). The preparation of Mg–Al spinels through the method of using templates. *Applied Petrochemical Research*, *5*(4), 247–253. https://doi.org/10.1007/s13203-015-0134-x

Zhao, C., Zhang, Y., Wang, C. C., Hou, M., & Li, A. (2019). Recent progress in instrumental techniques for architectural heritage materials. *Heritage Science*, *7*(1), 1–50. https://doi.org/10.1186/s40494-019-0280-z

Zuleta, E. C., Baena, L., Rios, L. A., & Calderón, J. A. (2012). The oxidative stability of biodiesel and its impact on the deterioration of metallic and polymeric materials: A review. *Journal of the Brazilian Chemical Society*, *23*(12), 2159–2175. https://doi.org/10.1590/S0103-50532012001200004

Zulqarnain, Ayoub, M., Yusoff, M. H. M., Nazir, M. H., Zahid, I., Ameen, M., Sher, F.,

Floresyona, D., & Budi Nursanto, E. (2021). A comprehensive review on oil extraction and biodiesel production technologies. *Sustainability (Switzerland)*, *13*(2), 1–28. https://doi.org/10.3390/su13020788

Zuorro, A., Moreno-Sader, K., & González-Delgado, A. (2020). Economic Evaluation and Techno-Economic Sensitivity Analysis of a Mass Integrated Shrimp. *Polymers*, *12*, 2397.

APPENDICES

Table 4.1: Effect of solid/solvent ratio (n = 3)

Ratio	Yield %		
	< 1mm	Unsieved	>1mm
0	0	0	0
2	27.6	31.8	35.4
3	50.3	54.5	57.3
6	60.4	63.3	65.4
9	59.3	62.2	64.3

Table 4.2 Effect of particle size and temperature on yield (n =3)

Temp/K	Yield %		
	< 1mm	Unsieved	> 1mm
298	33.8	34.3	34.6
313	45.6	44.6	44.2
333	56.5	56.6	56.4
343	66.2	65.3	65.9
353	62.6	61.8	60.7

Table 4.3: Effect of particle size and time on yield

Time/Min	Yield %		
	< 1 mm	Unsieved	> 1 mm
30	39.7	41.1	44.5
60	44.6	46.8	48.9
90	50.9	52.3	54.6
120	58.4	59.6	61.3
150	63.5	64.2	65.6
180	62.4	63.9	65.3

Table 4.4: Kinetics of extraction of yellow oleander oil

Time/Minute	Yield (%)	Vol/L	Conc (g/L)	t/Ct
30	41.8	418	453.36	0.0662
60	46.8	468	507.59	0.1182
90	54.6	546	592.19	0.1519
120	59.8	598	648.59	0.1850
150	64.4	644	698.48	0.2148
180	63.9	639	693.06	0.2597

Table 4.5: Summary of the kinetics of the extraction of yellow oleander oil

T	1/T	% Yield (Y_t)	% Yield (Y_u)	k	lnk
303	0.0033	23.14	76.86	0.3011	-1.200
313	0.00319	26.02	73.98	0.3517	-1.045
323	0.0031	31.41	68.59	0.4579	-0.781
333	0.003	40.41	59.58	0.6782	-0.388
343	0.00292	52.14	47.86	1.0894	0.086
353	0.00283	65.92	34.08	1.9343	0.659

Table 4.15: Effect of the reusability of nanocatalyst on the biodiesel yield

No. of Runs	CaO	Incinerated eggshells	Synthesized nanocatalyst
1	96.2 ± 4.73	98.3 ± 3.72	99.4 ± 3.11
2	94.1 ± 5.23	96.4 ± 4.31	97.2 ± 4.74
3	92.3 ± 2.11	93.8 ± 5.62	95.2 ± 6.18
4	85.8 ± 6.88	87.6 ± 4.43	89.4 ± 5.73
5	84.2 ± 4.11	85.8 ± 6.73	87.2 ± 4.54

Appendix 2: Plagiarism report

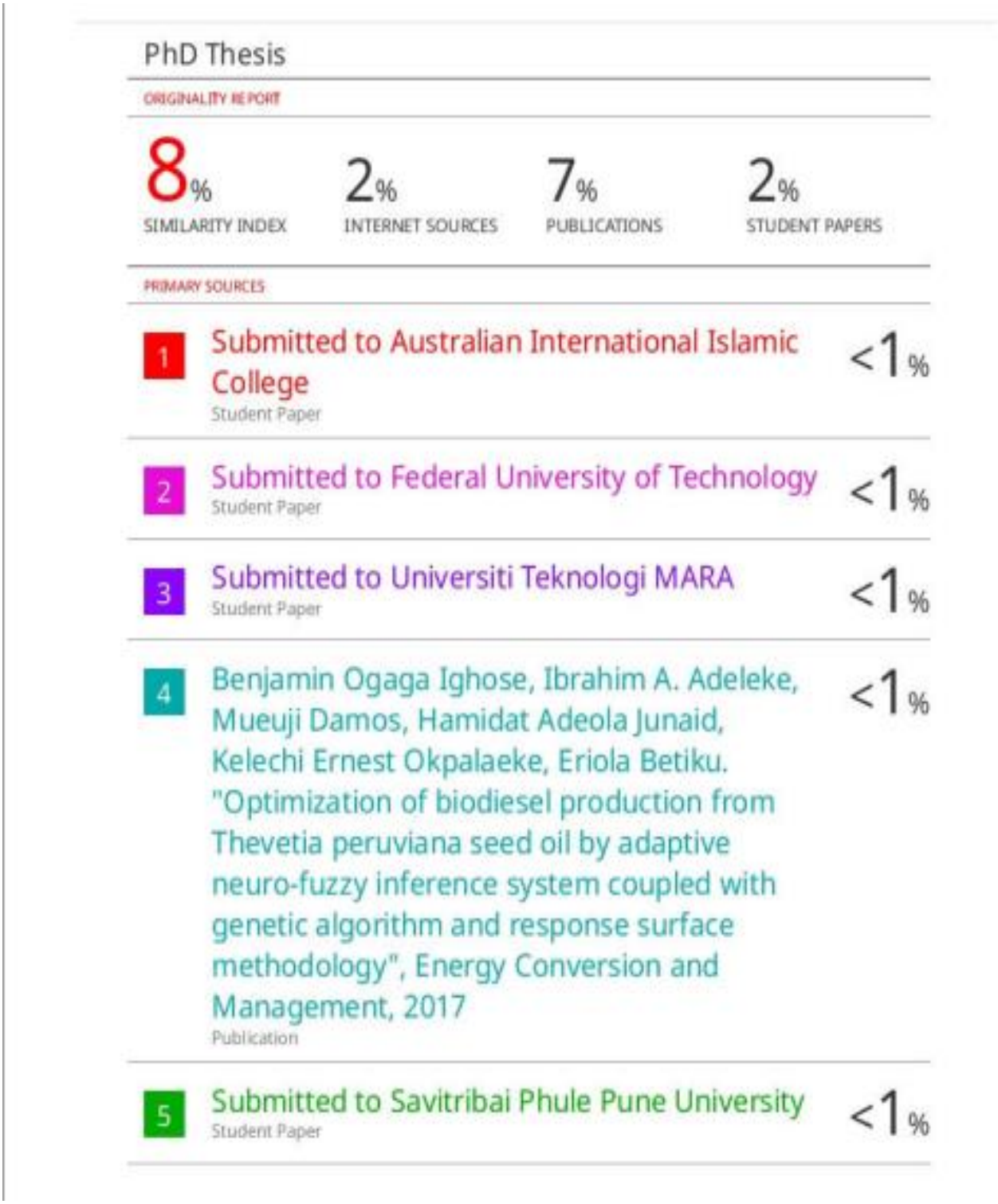

PhD Thesis

ORIGINALITY REPORT

8%	2%	7%	2%
SIMILARITY INDEX	INTERNET SOURCES	PUBLICATIONS	STUDENT PAPERS

PRIMARY SOURCES

1	Submitted to Australian International Islamic College Student Paper	<1%
2	Submitted to Federal University of Technology Student Paper	<1%
3	Submitted to Universiti Teknologi MARA Student Paper	<1%
4	Benjamin Ogaga Ighose, Ibrahim A. Adeleke, Mueuji Damos, Hamidat Adeola Junaid, Kelechi Ernest Okpalaeke, Eriola Betiku. "Optimization of biodiesel production from Thevetia peruviana seed oil by adaptive neuro-fuzzy inference system coupled with genetic algorithm and response surface methodology", Energy Conversion and Management, 2017 Publication	<1%
5	Submitted to Savitribai Phule Pune University Student Paper	<1%